This work is dedicated to my
beloved mother, my wife Khalida
and my children Hala and Muhanned

UNIVERSITY OF SOUTHAMPTON

PERFORMANCE OF SMALL CENTRIFUGAL PUMPS WITH WATER AND MIXED POLAR LIQUIDS

by

Ayad Ali Mohammad Chalaby

DEPARTMENT OF MECHANICAL ENGINEERING

Submitted for the Degree of Doctor of Philosophy

June 1983

UNIVERSITY OF SOUTHAMPTON

ABSTRACT

FACULTY OF ENGINEERING AND APPLIED SCIENCE

MECHANICAL ENGINEERING

Doctor of Philosophy

PERFORMANCE OF SMALL CENTRIFUGAL PUMPS WITH WATER AND MIXTURES OF POLAR LIQUIDS

by Ayad Ali Mohammad Chalaby

This research deals with the performance of small, automotive type centrifugal pumps handling both water and Ethylene glycol-water mixtures at temperatures up to 120°C.

Poorly designed hydraulic flow channels of these pumps render them highly inefficient machines. This research looks into the factors which may improve their performance, and examines the various power and scale-up losses. Reynolds number effects due to surface finish, pump speed and liquid viscosity are examined in the light of the numerous non-cavitating test data.

Because of the unfavourable inlet conditions arising at least in part from space limits, most of the small size pumps have a poor suction performance. This research looks into the various design and operational aspects which may influence the suction performance. This includes the inlet pipe design, the type of impeller shroud, the size of the axial tip clearance, and the shape and number of the blades. Also of importance is the test flow ratio Q_{cav}/Q_{opt} which is of special importance here because of the Re Number influence of the inlet hub vortex at low flows. [The shaft passes through the inlet chamber].

The use of Ethylene glycol-water mixture necessitates the measurement of the gas content during pump cavitation because of the strong gas content effect of the mixture on pump cavitation performance. An amperometric oxygen monitor was used to measure the oxygen content directly and continuously during the test. Gas content effects on pump cavitation were analysed with respect to rig and pump geometry, fluid properties and initial percentage saturation.

Gas filled bubbles of appreciable numbers were found to be recirculating around the system when EG/W mixture is being handled. These bubbles act as cavitation nuclei and increase the cavitation tendency of these mixtures.

Thermodynamic effect of cavitation for the test pumps is investigated in the range 20 - 120°C for the mixture 50/50 EG/W and compared to some data on water. Several influences such as impeller geometry and test flow ratio Q_{cav}/Q_{opt} are investigated.

Correlation of the thermodynamic effect test data making use of the B-factor is attempted. Suggestions are made to improve the correlation for the mixture to include the mass and heat transfer properties of binary mixtures as well as the number of cavitation nuclei involved in the cavitation process.

Finally, visual observation of the flow field at impeller inlet and the fixed cavity was made and some photographs taken to support the discussion.

ACKNOWLEDGEMENTS

The work represented in this thesis was conducted under the direction of Mr. M.T. Thew, to whom the author is grateful for his help, encouragement and advice throughout the research.

The author also acknowledges the advice given by Professor S.P. Hutton in the field of pump cavitation, and would like to thank him on my and Mr. Thew's behalf for presenting our paper to the IAHR Conference in Amsterdam.

The author would like to thank the Mechanical Workshop staff, Mr. C.R. Peach and P.G. Wheeler for their readiness to help with the rig modification and preparation of material for the tests. My thanks go also to the technical staff of the Electronic Workshop for their assistance.

A special thank goes to Mrs. G. North for her excellent typing of the thesis.

Finally, the author would like to express his gratitude to the Iraqi government and the Iraqi National Oil Company whose financial support throughout the research programme made this work possible.

CONTENTS

NOTATION

A	Area (m^2)
A_w	Cavity surface area (m^2)
a	Laplace constant $a = \sqrt{\frac{S}{g(\rho_\ell - \rho_v)}}$
b	Impeller channel depth (m)
B	Cavitation parameter $B = V_v/V_\ell$
BEP	Best efficiency point
C	Coefficient
C	Absolute flow velocity
C_a	Area coefficient ($c_a = A_w/D^2$)
C_d	Discharge coefficient for leakage flow
C_f	Frictional coefficient
C_h	Film heat transfer coefficient
C_L	Lift coefficient
C_m	Meridional component of the absolute velocity (m/sec)
C_n	Impeller contraction coefficient
CP	Pfleiderer slip factor
C_p	Pressure coefficient ($C_p = \frac{p_\infty - p_\ell}{\frac{1}{2}\rho\ V_\infty^2}$)
$C_{p\ell}$	Liquid specific heat at constant pressure KJ/kg°C
C_q	Flow coefficient ($C_q = q_v/V_\infty D^2$)
C_s	Saturation gas concentration of the liquid
C_T	Temperature coefficient ($C_T = \Delta p_v/\frac{1}{2}\rho V_\infty^2$)
C_u	Tangential component of the absolute velocity (m/sec)
ΔC_u	Slip component of C_u (m/sec)

D,d	Diameter (m)
E	Energy (Joule)
e	Disc clearance (m)
EG	Ethylene glycol (supplied by DOW company under the name D979)
EG/W	Ethylene glycol/water mixture
ΔE_v	Measured thermal cooling of cavitation (J/kg) (= $NPSE_{20°c}$ - $NPSE_{hot}$) for the same liquid (see also figure 8.8)
f	Frictional factor
F	Bubble growth factor ($m/°K\ sec^{\frac{1}{2}}$)
Fr	Froud number $V_\infty/\sqrt{gD}$
g	Gravitational acceleration (m/sec^2)
G	Vapourized mass fraction
H	Head generated by the pump (m)
ΔH	Head loss due to the presence of the tip clearance (m)
H_e	Theoretical (Euler) head of the machine (m)
H_i	Theoretical (input) head corrected for slip ($H_i = \sigma H_e$) m
H_o	Pump head at zero tip clearance
H_v	Theoretical volute head (m)
h	Heat transfer coefficient ($W/m^2\ °K$)
Δh_f	Change of fluid enthalpy (J/kg)
h_q	Heat flux (J/sec)
i	Incidence angle at blade inlet (degrees)
Ja	Jacobs number ($\rho_\ell\ C_{\rho\ell}\ \Delta T / \rho_v\ L$)
K	Constant
K	Bulk modulus (N/m^2)
k	Thermal conductivity ($J/s\ m\ °K$)
K_p	Furness cavitation parameter ($(p_\infty - p_i)/\frac{1}{2}\rho V_\infty^2$)
L	Latent heat of vapourization (J/kg)
ℓ_c	Cavity length (m)

ℓ	Length of blade (m)
m	Mass (kg)
Ma	Mach number $K/\omega^2 D^2 \rho$
MW	Molecular Weight
N	Speed of rotation (rpm)
n_s	Specific speed $\omega\ Q^{\frac{1}{2}}/(gH)^{0.75}$
n_{ss}	Suction specific speed $\omega\ Q^{\frac{1}{2}}/NPSE^{0.75}$
NPSE	Net positive suction energy (J/kg)
NPSH	Net positive suction head NPSE/g (m)
Nu	Nusselt number $C_h\ D/k$
p	Pressure (N/m^2)
Δp	Pressure rise inside the pump (N/m^2)
p_c	Cavity pressure (N/m^2)
p_g	Gas pressure inside the bubble (N/m^2)
p_v	Vapour pressure (N/m^2)
Δp_v	Reduction in vapour pressure due to local cooling (N/m^2)
Δp_{TR}	Pressure increment due to turbulence and surface roughness (N/m^2)
P	Power (Watts)
P_d	Disc power loss (Watts)
P_h	Hydraulic power loss (Watts)
P_{hyd}	Hydraulic output power of the machine (Watts)
P_i	Input power (Watts) $P_i = P_s - P_m$
P_m	Mechanical (external) power loss (Watts)
P_{rec}	Recirculatory flow power loss (Watts)
P_s	Shaft input power (Watts)
Pe	Péclét number $V_\infty\ D/\alpha$
Pr	Prandtl number ν/α

Q,q	Flow rate (m^3/sec)
Q_{bep}	Flow rate at best efficiency point of the particular pump speed (m^3/sec)
Q_{cav}	Cavitating constant test flow (m^3/sec)
Q_i	Input flow rate $Q + Q_L$ (m^3/sec)
Q_L	Leakage flow inside the pump (m^3/sec)
Q_{nc}	Non-cavitating flow (m^3/sec)
Q_o	Flow rate at zero tip clearance (m^3/sec)
Q_{opt}	Flow rate at optimum efficiency within the range of pump speed of the pump (m^3/sec)
r	Radius (m)
R	Bubble radius (m)
r_c	Vortex core radius (m)
Re	Pipe Reynolds number $\ell W/\nu$
Re_ω	Rotational Reynolds number $\omega r^2/\nu$
S	Surface tension (N/m)
t	time (sec)
t	Thickness of blade (m)
T	Temperature (°K)
T_s	Saturation temperature (°K)
ΔT	Temperature depression due to thermodynamic effect (°K)
U,u	Tangential velocity (m/sec) $U = \omega r$
V	Flow velocity (m/sec)
V	Volume (m^3)
w	Restriction width at impeller inlet (m)
W	Relative flow velocity (m/sec)
We	Weber number $V_\infty \sqrt{D\rho/S}$
X	Mole fraction

x	Mixture concentration at bubble wall
x_o	Bulk mixture concentration
Δx	Axial tip clearance (mm)
Z	Number of blades
Z	Number of bubbles entering the low pressure region
α	Proportionality factor for the leakage flow
α	Thermal diffusivity $(k/C_{p\ell}\rho_\ell)$
α	Bunsen solubility coefficient
α_m	Mass diffusivity of the volatile component into less volatile component
β	Impeller vane angle, trailing edge (°)
β	Henry's law constant
β	Proportional factor for tip clearance head loss
β	Thermal parameter of cavitation $C_{p\ell}\ T\ (\rho_\ell/\rho_v L)^2$
ϕ	Flow coefficient C_{m2}/U_2
ϕ	Bubble dynamic parameter
ϕ_p	Flow coefficient (external characteristics) $Q/\omega D^3$
ϕ_{mix}	Heat transfer correction factor for the binary mixture *(const. heat flux)*
ψ	Head coefficient
ψ_e	Theoretical (Euler) head coefficient gH_e/U_2^2
ψ_i	Input head coefficient gH_i/U_2^2
ψ_p	Head coefficient (external characteristics) $gH/\omega^2 D^2$
ψ_{mix}	Temperature depression correction factor for the binary mixture
λ	Tip clearance ratio $\Delta x/b$
λ_p	Power coefficient (external characteristics) $P_s/\rho\omega^3 D^5$
η	Overall pump efficiency $\rho gHQ/P_s$

η_m	Mechanical efficiency $(P_s-P_m)/P_s$
η_h	Hydraulic efficiency H/H_i
η_v	Volumetric efficiency $Q/(Q + Q_L)$
$\Delta\eta$	Efficiency drop due to tip clearance
δ	Overall scale up losses $1 - \eta$
δ_f	Frictional scale up losses
δ_m	Mechanical scale up losses P_m/P_s
δ_h	Hydraulic scale up losses P_h/P_s
δ_v	Volumetric scale up losses P_v/P_s
δ_{rec}	Recirculation flow scale up losses P_{rec}/P_s
δ_λ	Scale up losses at high pump speeds
μ	Absolute liquid viscosity (cP)
ν	Kinematic liquid viscosity (m^2/s)
ω	Rotational velocity (rad/sec)
θ	Liquid super heat (°K)
ε	Effective surface roughness (m)
ε_{CLA}	Surface roughness as measured by the Talysurf machine (m)
T	Reaction effect
ρ	Mass density (kg/m^3)
Δ	Specific diameter $D(gH)^{1/4} / Q^{1/2}$
γ	Proportionality factor for the efficiency drop due to tip clearance
γ	Ostwald absorption coefficient V_g/V_ℓ
σ	Slip factor
σ	Cavitation number $(p_\infty-p_v)/\frac{1}{2}\rho V^2$
σ_i	Incipient cavitation number
σ_n	Cavitation number at n% head drop

σ_{BD}	Cavitation number at breakdown
σ_b	Blade cavitation number $(p_1-p_v)/\frac{1}{2}\rho W_1^2$
σ_u	Inlet cavitation number $NPSE/\frac{1}{2} U_1^2$
σ_{TH}	Thoma sigma $NPSE/gH$
κ	Bubble growth factor $R/2\sqrt{\alpha t}$
τ	Growth factor $\Delta T/\kappa$
Γ	Vortex circulation (m^2/sec)

Subscripts

1	Impeller blade inlet
2	Impeller blade exit
cav	Cavitating condition
g	Gas
i	Internal
in	Inlet
ℓ	Liquid
L	Leakage
mix	Mixture
nc	Non-cavitating condition
o	Initial
opt	Optimum performance
p	Pure
R	Bubble wall
s	Saturation
v	Vapour
∞	Reference

LIST OF TABLES

LIST OF FIGURES

Chapter 4

CHAPTER 1

INTRODUCTION

1.1 Ground for the Research

Small size, commercial centrifugal pumps are used in great numbers for the heating and cooling systems as well as for other industrial purposes. To cut down on first cost and in some cases to save space, as it is usually the case for automotive cooling systems, these pumps tend to be rather inefficient machines. Tests in the Department of Mechanical Engineering [42, 57] on several automotive type pumps have shown that overall efficiencies were normally in the range 20 - 30%. Unfavourable inlet and discharge pipe layout, poor pump and impeller channel design and relatively high mechanical losses do contribute one way or another to this low overall efficiency. The various losses and their influence on the scale-up procedure provides the opportunity to examine the suitability of the present theories and practices to these highly inefficient hydraulic devices.

Most pumps in this category operate at or near the boiling point of the circulated liquid. High pump speeds and low local static pressures are likely to increase the susceptibility of these pumps to cavitate. Raising the local pressure or using liquids of higher boiling point are some of the ways usually applied to minimize this possibility. Ethylene glycol is one such liquid which if mixed with water gives a higher boiling temperature and lower freezing point than pure water and therefore it can serve as an excellent all year round coolant [4], and if properly inhibited against corrosion, cavitation damage can be minimized compared to water [35, 149].

Research prospects for the binary mixture EG/W arose from the fact that during pump cavitation at elevated temperatures, these mixtures do not exhibit significant thermodynamic effects similar to water and other liquids [42, 57]. Thew and Hadji-Sheikh [167] related this behaviour to several factors such as reduced surface tension effect, increased gas content effect and perhaps most significantly, due to vapour bubble growth restraints of the mixture as a

result of the depletion of the liquid adjacent to the wall of the volatile component (water), which constitute the major part of the vapour phase. These suggestions, however, were only tentative and could not be supported by conclusive test results or theoretical analysis.

Other relevant works in the cavitation of binary mixture in hydraulic machinery is not known to the author. Numerous bench tests on boiling heat transfer of binary mixture are available in the literature [150, 160, 172, 173, 175]. Some tests on commercial Ethylene glycol-water mixtures [98] also provides some insight in the nucleate heat transfer properties of these mixtures. In all cases, the heat transfer rate for nucleate boiling is increased because of the bubble growth restraints mentioned earlier.

Thermodynamic effect test data for hydrocarbon (non-polar) liquid mixtures in a hydraulic system were investigated by few authors [145, 154]. Using a direct method to measure the inlet NPSE to the centrifugal pumps [79], these authors were able to show that these mixtures exhibited some improved thermodynamic effect over that obtained with single component liquids.

The controversy between these two types of mixtures can be related to the association via hydrogen bonding of the polar mixture molecules compared to the independent molecules of the non-polar mixture components, with the result of different thermodynamic behaviour.

1.2 Aims and Objectives

This research deals with the performance of three small automotive type centrifugal pumps under non-cavitating and cavitating flow conditions, where both inhibited water and EG/W solutions of different concentrations are handled in the temperature range 20° - 120°C. Experimental and theoretical investigations of all pertinent parameters are presented in graphical form and discussed in detail. The main objectives of the research are listed briefly below:

1. To investigate the influence of geometry such as inlet and outlet pipe layout, impeller design, type of shroud and axial tip clearance size on generated head, overall efficiency and suction performance of the test pumps.

2. To examine the various losses and try to establish successful scaling factors with respect to change in speed and liquid viscosity.

3. Attempt to find some correlations with respect to gas content effect on pump suction performance for water and EG/W mixtures using an oxygen analyser.

4. By eliminating undesirable factors such as gas content effect, pump geometry and test flow rate (Q_{cav}/Q_{opt}), the thermodynamic effect for water and EG/W mixture is to be investigated in the range 20 - 120°C. Correlation of test results to the B-factor is to be attempted for both types of fluids.

5. Try to support the experimental and theoretical investigation by visual observations of the fixed cavity.

Timetable for the experimental work is done in the following order:

a. Examination of the various geometrical influences on pump performance, mid 1979 to end 1980.
b. Examination of the thermodynamic effect for the three pumps, end 1980 to end 1981.
c. Gas content effect experimentation, early 1982 to mid 1982.
d. Observation and photography, end 1982.

1.3 Layout of Thesis

The present work is split into two main sections. The first deals with the non-cavitating performances of the test pumps. These are outlined in Chapter 3 and 4, and include the analysis of the generated head, the overall efficiencies, the various losses and their influence on the scaling procedure.

In the second part, the cavitating flow performances of the pumps are analysed in detail. Suction performance is discussed in Chapter 5 and with respect to the gas content effect in Chapter 7. In Chapter 6, a theoretical review of the mechanism and the thermodynamic effect of cavitation is presented for the pure and the binary mixtures. The reason why it was inserted between the two chapters on suction performance was the need to give the reader some background to the subject of bubble formation and growth before discussing the gas content effect.

Thermodynamic effect of cavitation was analysed in Chapters 8 and 9. The first chapter was devoted to the discussion of the test results while the second was concerned with the correlation of the test results to the B-factor theory and its modifications, made to suit the binary mixtures.

Apart from Chapter 6, literature review was performed in each chapter and where the need arises.

Concluding remarks are made at the end of each chapter. A summary of these remarks is made in Chapter 11.

Experimental techniques and test material descriptions are made in Chapter 2. Emphasis was given to the installation and operation description of the amperometric oxygen monitor. Experimental techniques for the observation of the fixed cavity is given separately in Chapter 10.

Suggestions for future work are made in Chapter 12. References and Apendices are located at the end of the work.

CHAPTER 2

EXPERIMENTAL WORK

2.1 Test Rig

The test rig is described in some more detail in a departmental report [28]. The following brief description of the rig is intended to give the reader a general idea about its operation.

The rig circuitry is drawn schematically on figure 2.1. The main hydraulic circuit consists of the test pump, the inlet line, the discharge piping and the main reservoir.

The rig was originally designed to test small, high speed (up to 7000 rpm) automotive pumps of low flow capacities [42]. Therefore, several modifications were necessary to convert the rig to a general purpose pump testing facility. This included mainly the replacement of most of the piping network by a larger diameter size, and the addition of a second, larger size (38 mm) turbine type flow meter. This modification allowed for nearly 50% increase in the flow capacity of the rig for similar head losses in the systems [28].

The new 50 mm diameter inlet line which runs straight from the reservoir to the test pump, allowed to introduce a larger size glass viewing section (ϕ 50 mm x 30 mm long) which replaces the old 25 mm size short piece. In addition to its low frictional losses, this new pyrex window makes it easier to observe the formation and size distribution of the cavitation (and gas) bubbles upstream the pump inlet at low inlet pressures.

The main reservoir has a total capacity of $\sim$ 220 litres and it is situated $\sim$ 3 metres away from the test pump. The introduction of a large reservoir in the system is intended to provide a reasonably good stabilizing factor for the flow and allow for acceptable repeatability of the test.

System pressure is normally controlled through the main reservoir. Expansion air bellows are provided to allow for system pressurization. To reduce the pressure in the system below atmosphere, the reservoir is fitted with a vacuum pump and piping which allows for efficient pressure reduction inside the main reservoir down to $\sim$ 0.3 bar, abs.

Heating of the liquid in the system can be done automatically. To do this the reservoir is fitted with a 6 KW heater (which replaced the old 3 KW element), 2 thermostats, a vent, an expansion tank and a relief valve in case of accidental over-pressurization.

Apart from the main hydraulic circuit, the rig is provided with a secondary liquid change-over system which allows for the storage and transfer of different types of liquids and liquid mixtures. This includes 3 sets of barrels, piping and a small positive displacement transfer pump.

The drive system to the pump consists of a 6 KW electric motor, a magnetic coupling, a step-up spur gear pair, a drive shaft fitted with a strain gauge torque meter, and a step-up toothed belt linking the test pumps to the drive shaft. Theoretically the power input to the pump could reach the nominal motor capacity. However, the magnetic coupling torque rating and the spur gear ratio limit the maximum pump shaft input power to nearly half that of the electric motor at present.

The instruments layout is given on figure 2.2. It consists mainly of 2 different sections. The first deals with the measurement and control of the flow variables such as flow, pressure, power and liquid temperature. The second deals with the safety of the rig operation.

Flow measurements are performed by two turbine flow meters which can be operated individually for single discharge pumps, or in parallel for twin discharge pumps such as the automotive pump J. This setting allows for accurate flow measurements down to 25 litre per minute and a maximum total flow capacity of about 800 litre per minute (only of theoretical

value here because of the flow rate limitations of the test rig given in table 2.1).

Pressure around the hydraulic system is measured by a precision Bourden tube pressure gauge via three 6-way valves. The rig is also provided with a scanivalve transducer and control and drive unit which can measure the liquid pressure and transmit it as an analog signal, which can be stored through a data logger or converted to a digital signal.

A Westland Aircraft (now British Hovercraft Corporation) strain gauge torque transducer is used to measure the torque in the rotating shaft. It is axially mounted with two flexible couplings connecting it to both sides of the drive shaft.

Torque meter shaft speed and hence pump speed is controlled by the Tasc magnetic coupling. A magnetic impulse pick-up is situated near a wheel mounted on the drive shaft with 60 teeth machined on its periphery. The pick-up sends its signals to a digital counter set to read cycles per second, thus indicating revolutions per minute.

To monitor the fluid temperature at the location of the test pump, a manually switched five-way temperature recorder with matched thermistor probes and digital display is used.

Flow, torque, speed and temperature are displayed in digital form and by choosing the right amount of gain the digital signal can be transformed to any desired unit and read directly from the relevant display units. Litres per minute, Nm, rpm, and °C are usually displayed during this research programme. Since the torque meter reading includes the parasitic torques needed to overcome the frictional losses in the torque meter shaft bearing, the actual input torque to the pump is less than that recorded on the instrument by an amount determined from the test [28].

The safety system is described in some detail in ref. [28]. Its' main function is to shut-down the rig in case of emergency and hence minimise

the amount of spillage or damage to the rig. It is actuated by a Lo-Hi pressure switch sensing the fluid pressure at pump discharge. Too high pressure as a result of pump overspeed or malfunctioning air regulator, or too low system pressure as a result of damage to the inlet line (or glass) will activate the pressure switch, and rig shut-down will follow.

A photograph of the rig is presented in figure 2.3. In table 2.1 the rig operation limits are listed.

2.2 Direct Monitoring of O_2 in the Liquid

One of the main objectives of this research is to examine the effect of the amount of dissolved air in the liquid on the cavitating flow performance of the pump. To do so, an oxygen meter was used which monitors the oxygen saturation level continuously during the test. This type of instrument although may not give a perfect indication of the total air content at the time of the test, but it has the advantage of being easy to calibrate, operate and maintain. Dissolved gas level may also change during the test and it is therefore desirable to obtain an indication of these changes.

The introduction of the O_2-monitor into the test hydraulic system had to take into account the following 2 main requirements.

1. Since the O_2-sensor cannot respond to sub-atmospheric pressures, the location of this sensor had to be made at a point downstream the pump discharge.

2. The maximum allowable temperature of the sensor is in the range of $\sim$ 45°C, which is far below that of the normal test temperature of 90-100°C. Therefore, a special loop had to be installed which runs parallel to the discharge pipe and provides sufficient flow for the operation of the sensor. This loop was also provided with a cooler to reduce the liquid temperature to the operating temperature of the sensor.

The O_2-monitor loop and details are shown on figure 2.4. A picture of the front panel of the O_2-monitor is presented on figure 2.5

The principle of operation of the oxygen monitor is based on the ability of the sensor to respond to the partial pressure of dissolved oxygen. An amplifier measures the magnitude of the sensor signal and thus provides a direct readout on a pannel.

With the sensor placed in the process stream, a potential of 0.725 volt d.c. is applied across the gold cathode and silver anode. Oxygen in the stream diffuses through a teflon membrane and is reduced at the cathode. The reduction of oxygen results in a current flow proportional to the partial pressure of oxygen in the sample. If an alkaline electrolite is used in the electrochemical cell then the following reactions are considered to happen [62];

At the Cathode:

$$O_2 + 2H_2O + 4e^- \rightleftarrows 4OH^-$$

At the Anode:

$$4Ag + 4Cl^- \rightarrow 4AgCl + 4e^-$$

The solubility of O_2 in the liquid is temperature dependent. For pure water exposed to atmospheric air at 20°C, the O_2 solubility is 9.1 ppm. This corresponds to $\sim$ 25.3 ppm air in water for equilibrium condition. As the temperature changes, the O_2 concentration will change although the partial pressure of O_2 may remain unchanged [62].

By using an amperometric sensor, the effect of temperature is to change the diffusion rate through the membrane. A 3% error with a change of 1°C must be considered [5]. To avoid such large errors, these instruments are

normally fitted with temperature compensation devices which account for the effect of changing temperatures. A temperature dependent resistance or thermistor having a negative temperature coefficient is installed in the circuit of the sensor, hence balancing out the signal to the amplifier.

For a reliable temperature compensation, the partial pressure of oxygen does not change with temperature, although the concentration does vary. However, most temperature compensations are not completely reliable due to changes in membrane permability and temperature. Also at temperatures above 20°C the vapour pressure of the liquid becomes more important and will influence the partial pressure of the dissolved oxygen [5, 62]. Therefore, for accurate measurements the automatic temperature compensation should be not relied on, and calibration should be carried out at a temperature close to that of the sample temperature [62].

Sensor details and electronic measuring circuitry are shown on figure 2.6.

2.3 Test Procedures

Small centrifugal pumps are usually designed according to the simple one-dimensional methods and procedures [92]. If the performance of a model pump is known, then the similarity rules can be applied to estimate the performance of the production type with a reasonable accuracy. If a model pump is not available, then the first thing the pump manufacturer wants to know is to find out the non-cavitating performance relating the flow rate to the developed head and input power. This is normally done with cold water, which is the standard liquid.

Because one of the main purposes of this research is to look at the pump performance when handling a mixture of liquids, all pumps included in this research are tested both with inhibited water and Ethylene glycol water mixtures, both for the non-cavitating and the cavitating performance. This will allow us to study the effect of fluid properties on pump performance and to try to assess the differences which are bound to occur.

Non-cavitating performance tests are simple and straightforward. To achieve high enough NPSE at pump inlet, the main reservoir can be pressurised using the air bellows. The amount of pressurisation depends largely upon the flow rate and the liquid vapour pressure. Normally pump inlet pressure is raised far above that required to suppress cavitation. For the small pumps being tested here, pump inlet pressures of 0.4 - 0.5 bar (gauge) are normally applied, up to a temperature of $\sim$ 90°C.

The discharge flow is controlled by valves 19 and 20 (figure 2.1) and in testing for the effect of discharge split ratio (for dual discharge pumps), valves 14 and 15 are used simultaneously.

Cavitating flow performance tests are more complicated and require more attention and effort. The tests start normally from the non-cavitating conditions and proceed by gradually reducing the NPSE, keeping both pump speed and liquid temperature constant, until performance break-down is reached. Two methods are usually applied, a) by keeping the flow rate constant, and b) by keeping the system geometry (including valves setting) constant.

Method (a) allows us to study the pump cavitation at the same pump inlet velocity measure at the suction flange (V_{in}) and hence scale effect due to flow velocity is avoided. By using the cavitation number σ ($= NPSE/\frac{1}{2}V_{in}^2$) as the cavitation parameter describing the tendency of the pump cavitation, the head drop in the pump or the head rise ratio (ψ/ψ_{nc}) would indicate the cavitation state of the pump. A head loss of 1-5% (ψ/ψ_{nc} = 0.99-0.95) is normally specified for conventional pumps to compare the suction ability or suction requirement of the pump for the same head drop, if flow conditions and fluid properties are varied. The cavitation gradient $d\psi/d\sigma$ for a given pump speed and liquid temperature is likely to depend on the test flow (Q_{cav}), and has been shown to be largest at low discharge flows [90]. For a given Q_{cav} and pump speed, $d\psi/d\sigma$ is likely to depend on temperature due to the thermal cooling and for water is likely to be a maximum at ambient temperatures [155].

To avoid further complexity, pump cavitating correlations are made at the optimum (best efficiency point) flow ($Q_{cav} = Q_{opt}$), thus minimizing other effects like inlet shock losses and pre-rotation. However, because of the increasing importance of pump cavitating performance at partial dishcarges, the present research includes several test runs at flows away from the optimum point. With the present rig piping, a cavitating flow as high as 1.2 Q_{opt} can be achieved for all pumps tested.

Testing a pump at a constant Q_{cav} and reduced NPSE is done by reducing the reservoir pressure and at the same time by opening up the discharge valves slightly (valves 19 or 20) to compensate for the reduced suction capacity, until the head breakdown occurs. Liquid temperature must be kept constant especially at high temperatures with increasing vapour pressure gradient (dP_v/dT). For liquid temperatures above 80°C, the temperature variation is not to exceed ± 0.2°C. To achieve this small tolerance, the cooler and the reservoir heater are operated at the same time, with the cooling water regulated as required (see figure 2.1).

Method (b) which describes the cavitating behaviour of the pump at fixed geometry but varied NPSE represents a real life condition, whereby the pressure level in the pump suction reduces, while the system is unchanged. (For example, a cooling system with fully open thermostat). This will allow us to correlate the pump flow capacity (or flow coefficient ϕ) to the suction capacity (or cavitation parameter σ). Again here $d\phi/d\sigma$ is a function of temperature for any given pump speed and geometry.

The constant geometry test method is simpler than the constant Q_{cav} method because it involves the reduction of the suction tank pressure only. Geometry setting is normally done to give Q_{opt} at the non-cavitating condition.

Reading errors during the test can result either from instruments or test inaccuracies. The average error margins for the most important test parameters are listed below.

Test Parameter	Instrument Error	Reading Error
Flow rate	± 0.5%	± 0.5 L/min
Pressure (Bourdon tube)	± 0.1%	± 0.005 bar
Speed (Torque shaft)	± 0.05%	± 3 rpm
Torque	± 1.0%	± 0.03 Nm
Temperature	± 0.5 - ± 1.5%	± 0.2°C

The combined effects of these errors on the performance estimation of the centrifugal pump is analysed in Appendix III.

The oxygen monitor has been described in the last section. Its use and interpretation of the test results are discussed fully in Chapter 7. However, it is worth noting here that its use has been limited to ambient temperatures (∿ 20°C) for 2 reasons.

1. Because of the inaccuracy of the temperature compensation of this device which is perhaps related to the ineffectiveness of its thermistor due to long storage time. The liquid temperature was kept similar to the calibration temperature which is normally done on ambient air of ∿ 20°C and ∿ 750 mm Hg barometric pressure.

2. In order to cool down the loop flow of ∿ 2 L/min from the standard temperature of 90°C to the maximum allowable of the sensor of 45°C, 8 KW cooling power is required. Compared to 6 KW maximum heat input into the system, this meant that a combined use of the cooler and the heater still cannot provide a stable temperature of the test, bearing in mind that heat dissipation from the system must be also accounted for.

Test temperature at the sensor was kept reasonably constant within ± 0.2°C. Including the instrument error, a combined error of the O_2-monitor at 20°C is not expected to exceed ± 3%.

2.4 Test Pumps and Impellers

Three automotive type centrifugal pumps were available for the test. They are termed H, J and K according to their sequence in the test programme. Both pumps H and K have aluminium bodies whereas pump J has a cast iron body. The impellers of pumps H and J are made of cast iron, whereas that of pump K is made of pressed metal sheet. Pump J is the only one which is provided with a simple volute. The other two discharge the flow immediately into a square cavity for simplicity. In table 2.2 all relevant specifications of the three pumps are listed.

Each of the 3 pumps was tested with different version of impeller design in order to investigate the influence of impeller geometry on pump performance (both cavitating and non-cavitating). To distinguish the various impellers, the following impeller nomination is followed.

	Pump type		Number of blades		Discharge angle (β_2°)
Example:	J	-	8	-	48

Pump H has been tested in the department before [57]. In addition to the production type impeller H-6-90, the present researcher had the opportunity to test 5 additional impeller geometries supplied by the same pump user. In figure 2.7, a picture of the pump body together with the standard impeller are shown. On figure 2.8 the detail and dimensions of the various impellers are presented.

Pump J is by far the most important one of the three pumps tested. Because of its larger size, the more reasonable inlet and outlet piping layout, the more conventional impeller design and the presence of a proper volute, made this pump more suitable for a thorough investigation in the field of cavitation of this type of pump.

This pump was originally supplied with 2 different versions of pump casing designs (phase 1 and phase 2). These are virtually similar with regard to inlet geometry and volute design. The only difference being the discharge channels and ports, which have been modified to allow for higher flow rate in the cooler branch (figure 2.9). Since phase 2 type body is the one with the better hydraulic design, all tests included here are made exclusively with this body type. The flow split ratio between the two discharges of the pump is determined by the total resistance of each branch. In the present pump installation with both valves 14 and 15 fully open, the ratio of the flow in the cooler branch (through valve 14) to the total flow rate through the pump is maintained at $\sim$ 38% throughout the test. To avoid the influence of the twin discharges flow distortion on the pump performance estimation, the outlet pressure was recorded before the flow splits at the discharge channel (see figure 3.3).

Two semi-open impellers of the same diameter and channel height but of different blade design were supplied with phase 2 version of pump J. Four more impellers were designed by the author and were also supplied later on by the same pump manufacturer [29]. Furthermore, the production type semi-open impeller J-8-48 was modified to produce a 7th, closed version of this impeller after the addition of a front shroud. This was done in order to assess the difference in pump performance with regard to the type of shrouding, both for the cavitating and non-cavitating flow conditions.

In figure 2.10, the details and dimensions of all 7 impellers of pump J are presented. In figure 2.11, a photograph is presented showing three versions of the semi-open impellers of similar blade numbers for both pumps H and J.

The third pump (K) is similar to pump H in that it has no proper volute. Two versions of pump body were supplied for the test, both fitted with the same standard impeller K-6-90 (std.).

Unlike pump J, these two pump casing versions are significantly different in that the inlet pipe design is changed to allow for a higher through flow and developed head. The two versions are shown on figure 2.12 together with the discharge cavity, which has been manufactured to simulate the actual engine cylinder block as nearly as possible.

The standard impeller of this pump is cut out of pressed metal sheet (figure 2.12). This type of cheaply produced impeller proved to be highly inefficient mainly because of the holes in the back shroud. To improve on this, 2 additional improved versions of the same impeller were produced and tested during the programme. The first K-6-90 (so) is obtained by simply covering the back shroud by a thin plate, thus eliminating the influence of the holes, and therefore becomes truly semi-open. The second version, K-6-90 (c1) is obtained by adding a second shroud to the first modified version, hence a closed type impeller is produced.

2.5 Test Data Processing

Use is made of the departmental mini computer (Cromemco), to process all test results. Bascially all processing programmes consist of the following main steps;

1. Input matrix: This, usually represents the test results in tabulated form, either by inputting the results directly into the programme or better by extracting them from a data file. Data files can be stored on tape or on the main disc of the computer.

2. Test constants: Particular flow constants like pump speed, fluid temperature, etc. are either inserted directly into the main programme or extracted from the data file.

3. Fluid properties: Properties like vapour pressure, density, viscosity etc., can be presented in equation form or tabulated as a function of the

temperature of the liquid or liquid mixture. The equation form is prefered because small variations in temperature could be accounted for. Properties data are usually contained in a sub-routine of the main programme.

4. Calculation: By using 1, 2 and 3 the required parameters can be calculated using the available equations.

5. Output matrix: Calculated values like developed head, efficiency, NPSE, etc., are presented in matrix form which allows easy read-out for any test point.

6. Graph plotting: An X-Y Digi-Plot facility was available for use. A special programme is required to feed the output matrix into the Digi-Plot and hence the results can be plotted, using 2-dimensional co-ordinates.

In Appendix IV to VI , the main computer programmes used in this research are presented in skeleton form. Numerical examples are included to clarify their use.

TABLES 2.1 and 2.2

FIGURES 2.1 to 2.12

Table 2.1 Rig operation ranges and limits

Test parameter	Limits
Flow throughput capacity (lit/min)	0 - 400
Minimum liquid circulation time (sec)	30
Pressure rise across the pump (bar)	0 - 4
Liquid temperature (degrees Celcius)	20 - 120°
Pump revolutions per minute	500 - 6500
Main reservoir pressure (bar, abs)	0.3 - 3.0
Pump inlet pressure (bar, abs)	0.15 - 2.5
Electric motor power (KW)	6.0 max
Magnetic coupling output torque (Nm)	0 - 14.8
Pump shaft torque (Nm)	0 - 5.0
Strain gauge torque transducer (Nm)	0 ± 20.0
25 mm flow meter linear range (lit/min)	27 - 270
38 mm flow meter linear range (lit/min)	57 - 570
Oxygen monitor flow rate (lit/min)	0.2 - 3.0
Oxygen monitor sensor pressure (bar, abs)	1.0 - 4.0
Oxygen monitor sensor temperature (deg. cent)	20 - 44°

Table 2.2 Pump specifications

Pump design	H	J	K
Pump type	Radial, semi-open impeller		
Impeller diameter (mm)	56.6	90.0	68.0
Impeller material	cast iron	cast iron	Pressed steel sheet
Pump body	cast aluminium	cast iron	cast aluminium
Design maximum speed (rpm)	6500	5000	6500
Inlet type	Side suction (flow past shaft)		
Bearing and shaft	Ball bearing cantilever shaft		
Seal	Mechanical face seal		

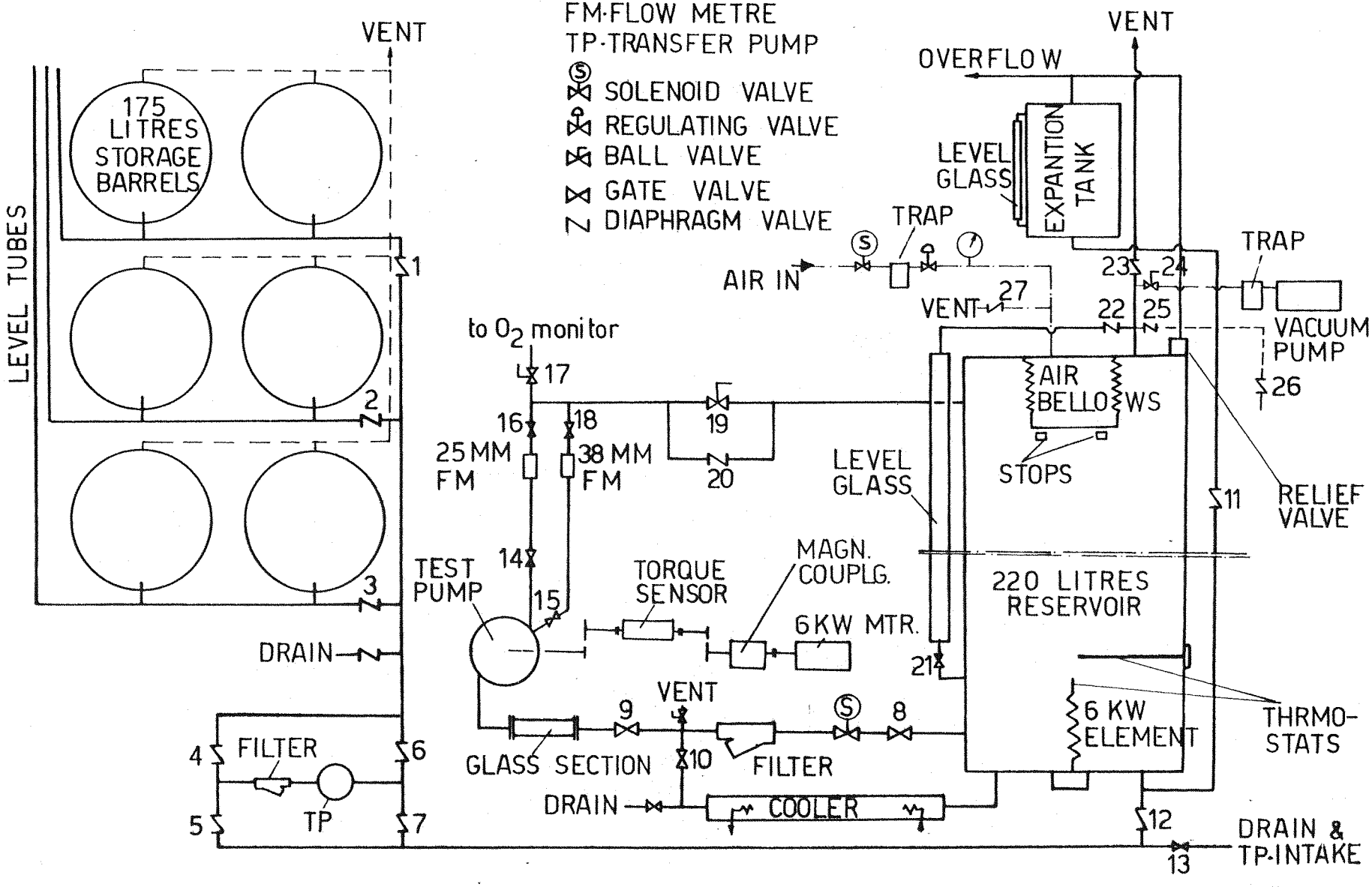

FIG. 2.1 RIG LAYOUT SCHEMATIC

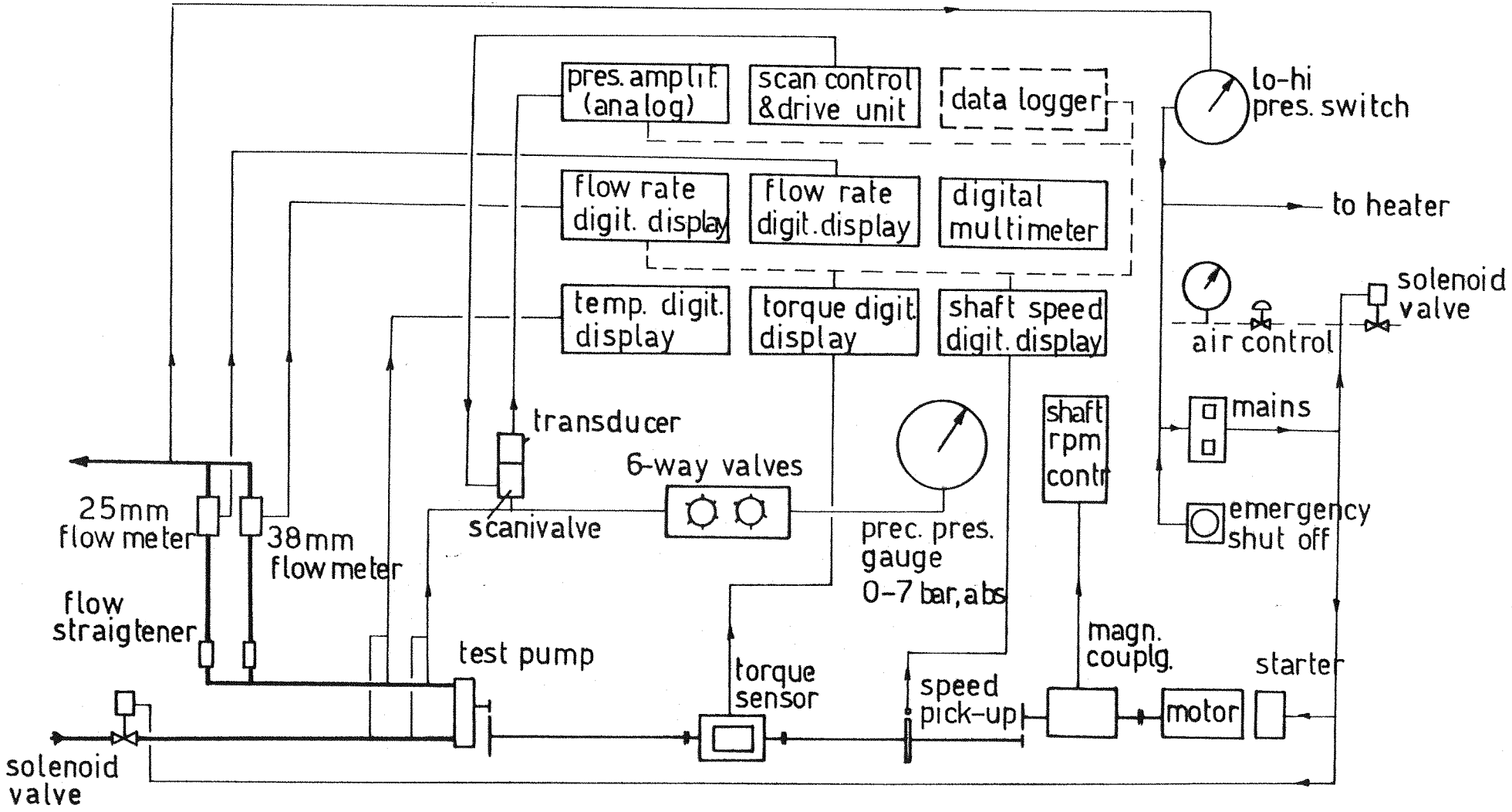

FIG. 2.2 RIG INSTRUMENTATION LAYOUT

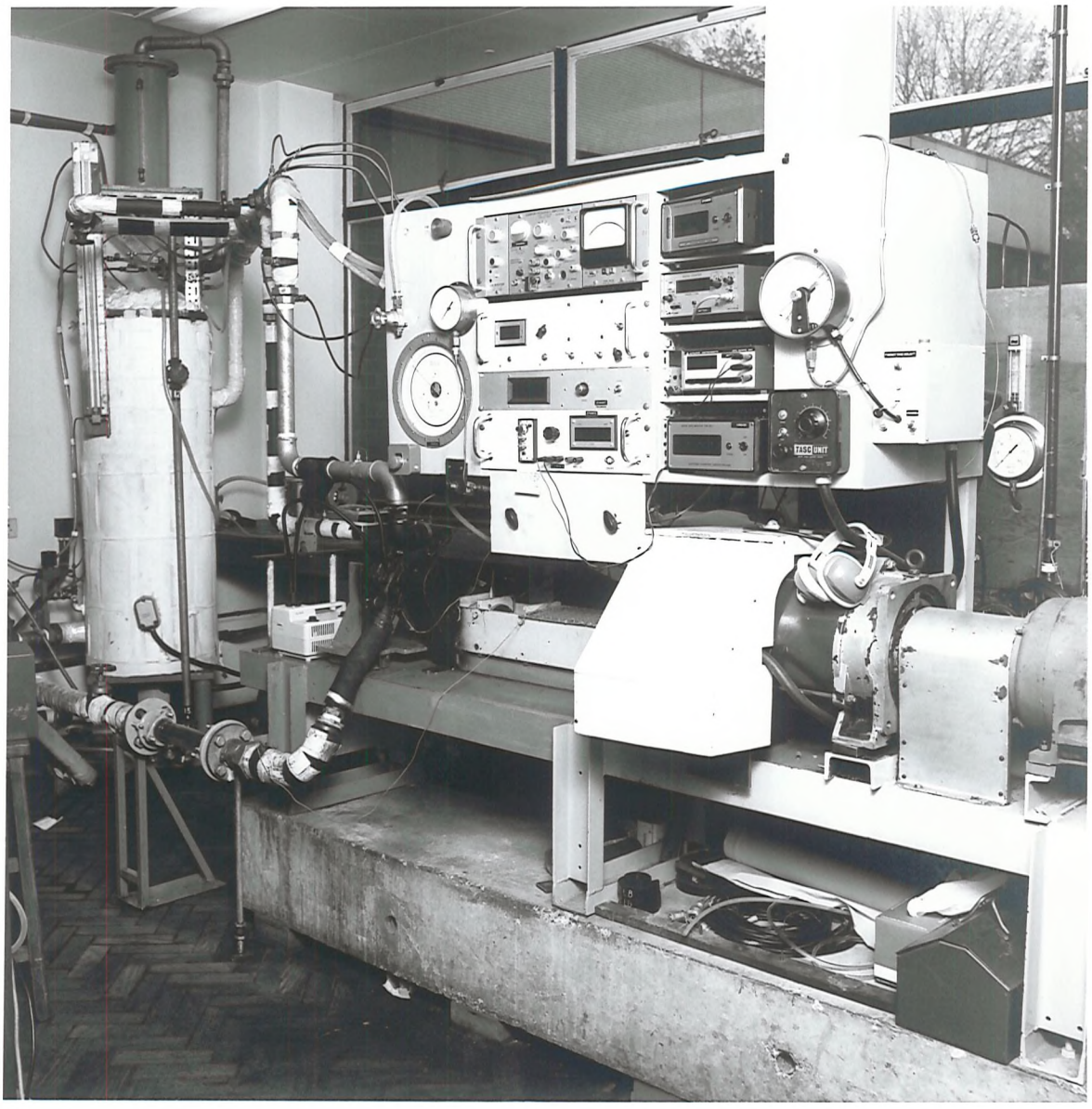

Figure 2.3 Test rig photograph.

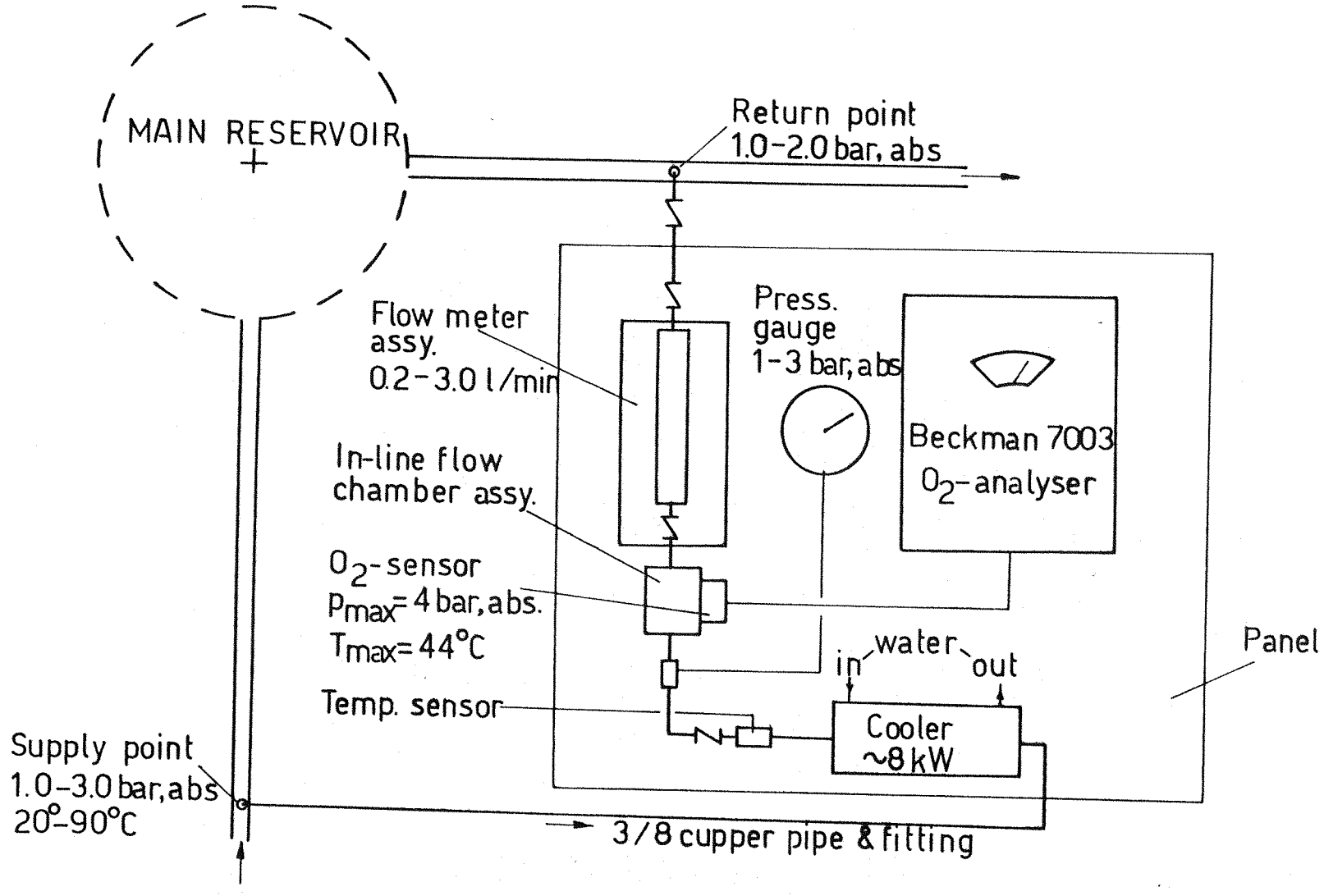

FIG 2.4 IN LINE INSTALLATION OF O_2-MONITOR AND INSTRUMENTATION

Figure 2.5 Oxygen monitor front panel.

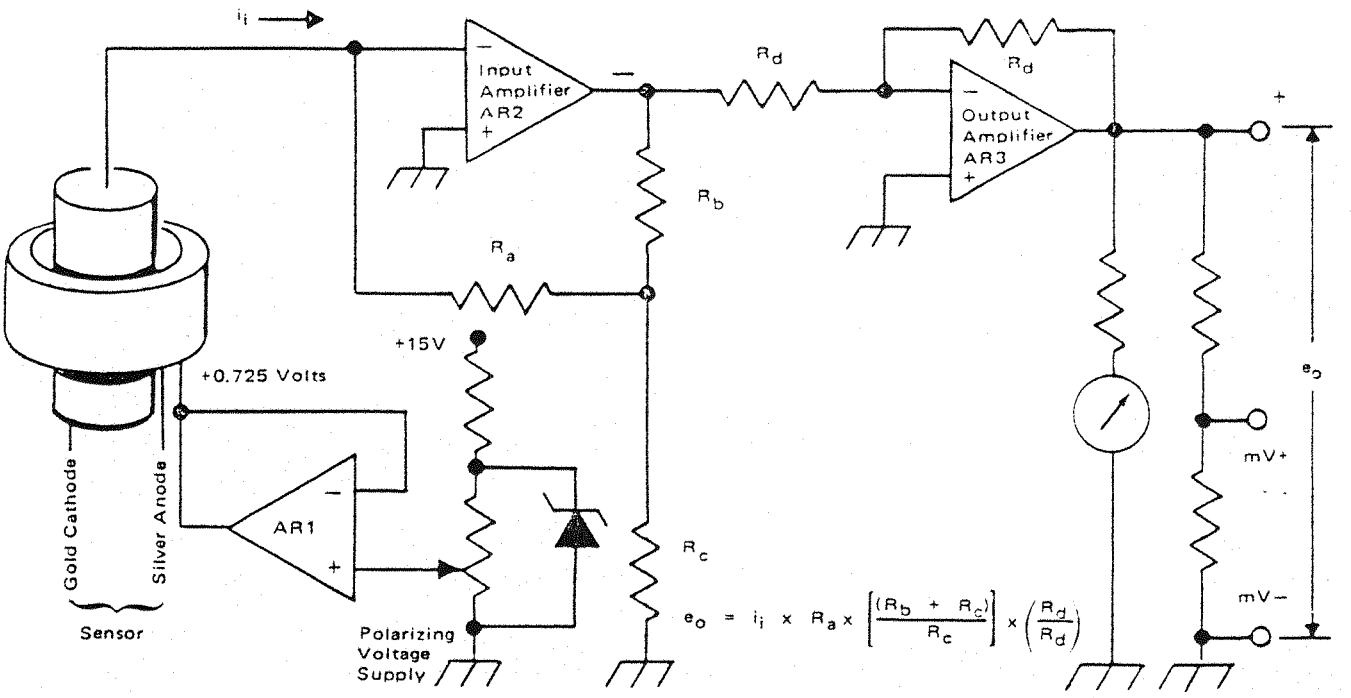

a. Functional diagram of electronic measuring circuitry.

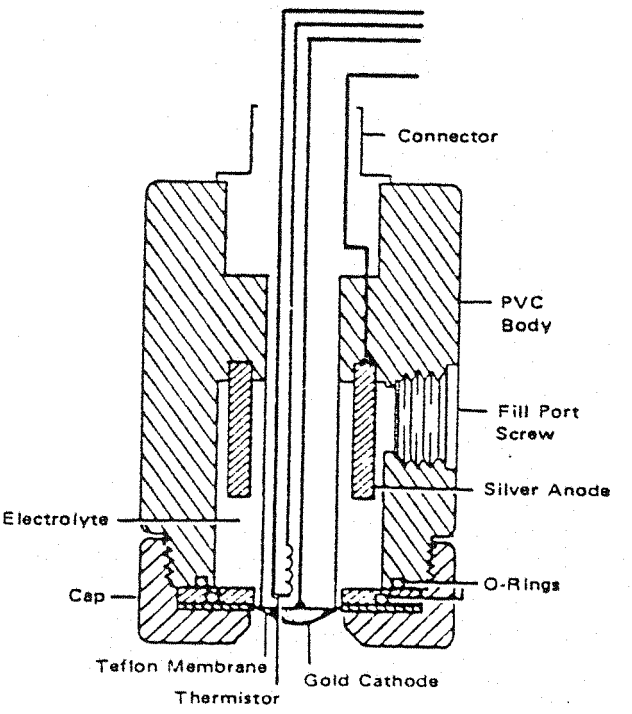

b. Amperometric oxygen sensor.

Fig. 2.6 Electronic measuring circuitry and amperometric sensor of Beckmann's 7003 oxygen monitor.

2.7

Figure 2.7 Pump H with the standard impeller.

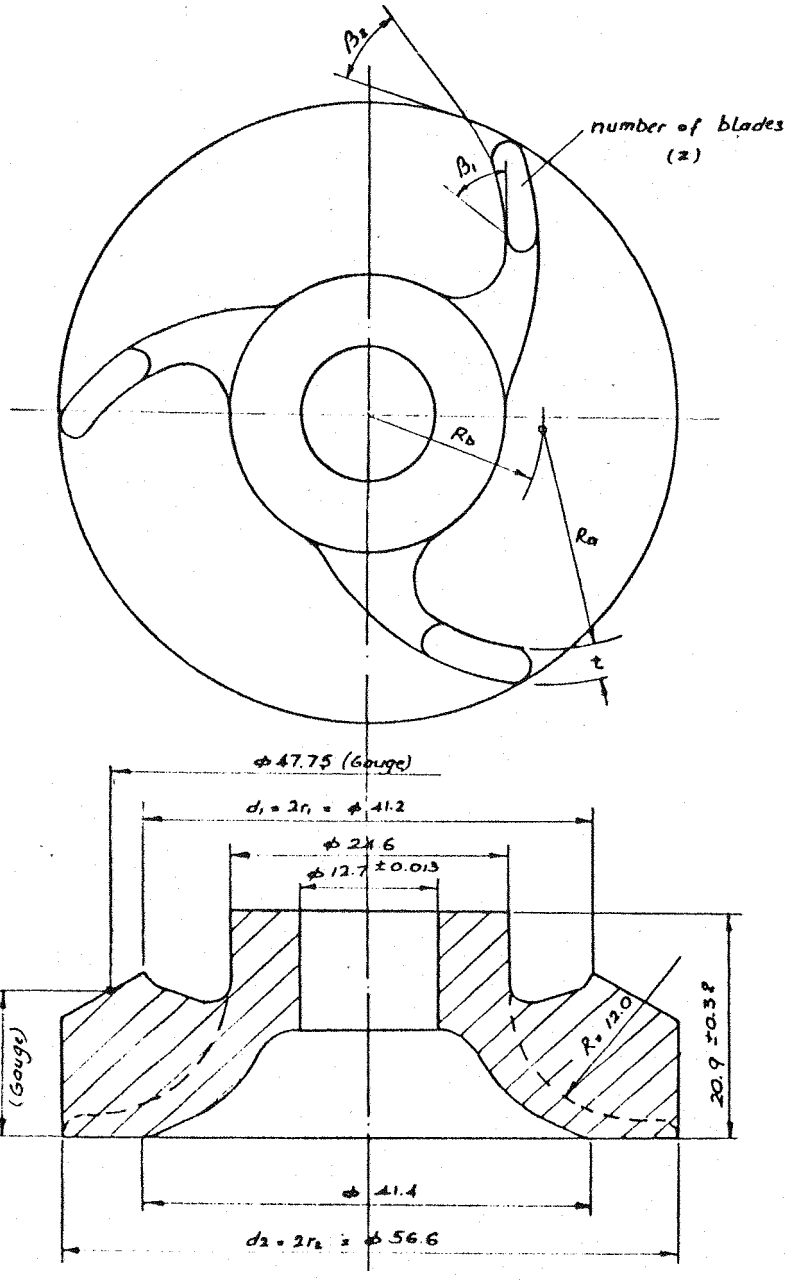

Impeller	z	β_1°	β_2°	d_1	d_2	b_1	b_2	t	R_a*	R_b
H-8-90	8	90	90	41.2	56.6	13.0	9.0	3.3	∞	∞
H-8-60	8	60	60	↓	↓	↓	↓	3.3	20.0	22.5
H-8-40	8	40	40	↓	↓	↓	↓	4.3	20.0	16.0
H-6-90	6	90	90	↓	↓	↓	↓	4.3	∞	∞
H-6-60	6	60	60	↓	↓	↓	↓	4.0	20.0	22.5
H-6-40	6	40	40	↓	↓	↓	↓	4.0	20.0	16.5

* $R_a = \frac{1}{2} \frac{r_2^2 - r_1^2}{(r_2 \cos\beta_2 - r_1 \cos\beta_1)}$

Dimensions in mm
Scale - 2:1
Material - cast iron
Average roughness - 8 μm

FIG 2.8 DETAILS AND DIMENSIONS OF IMPELLERS FOR PUMP H

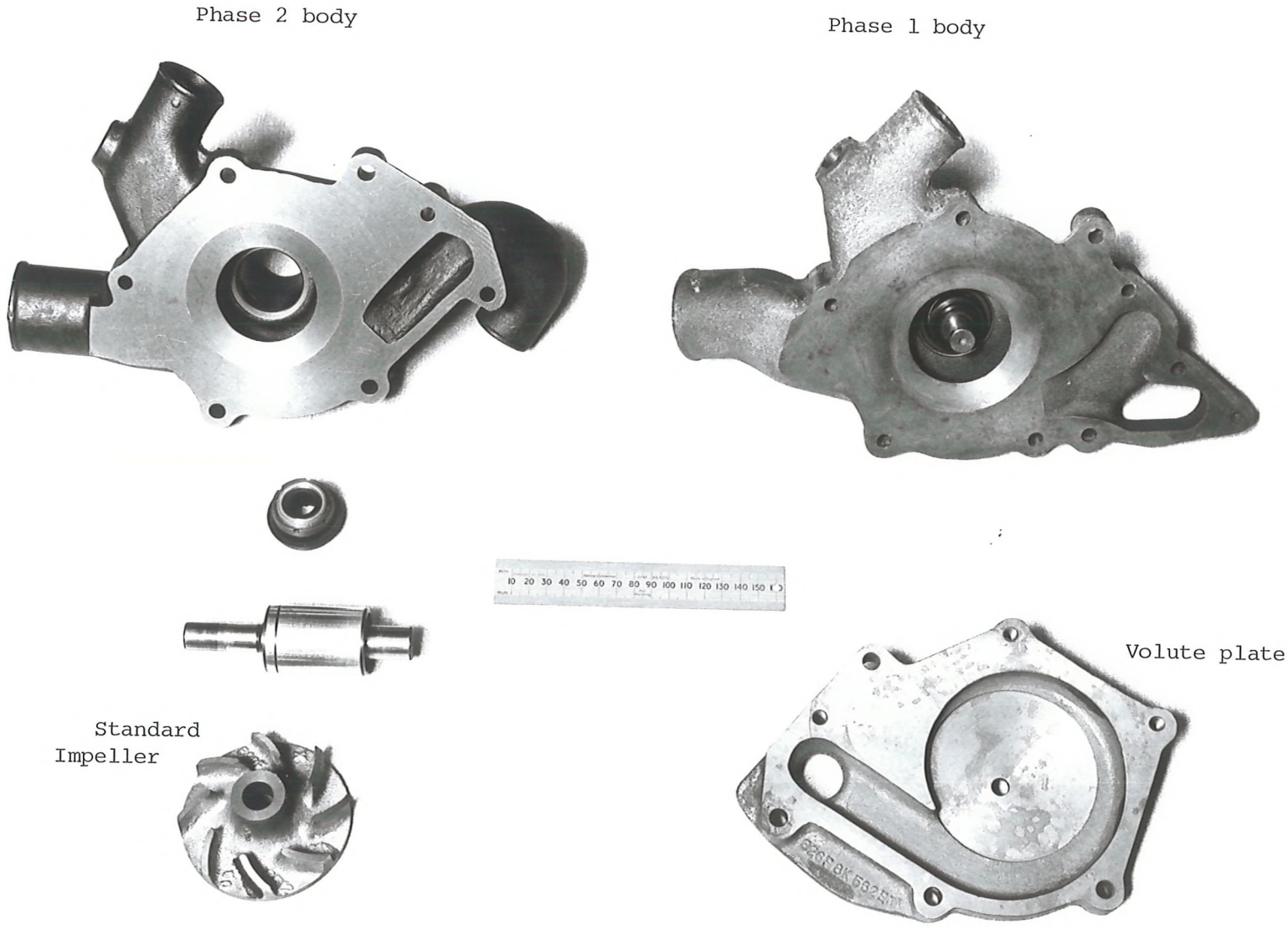

Figure 2.9 Pump J's mechanical parts with two types of pump body.

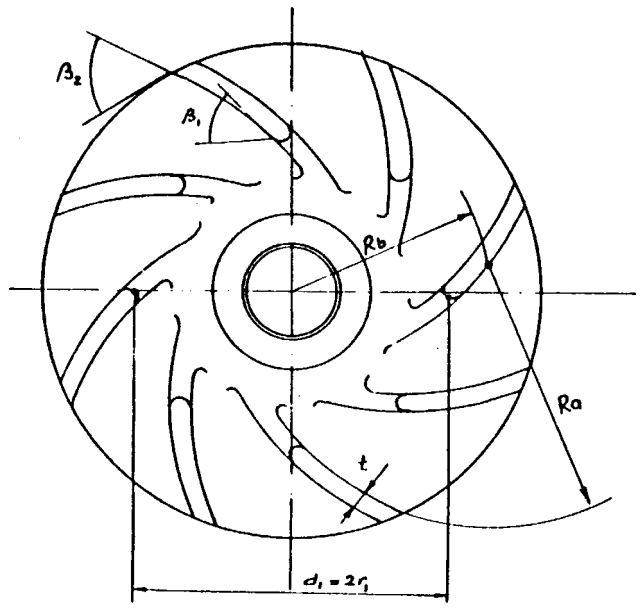

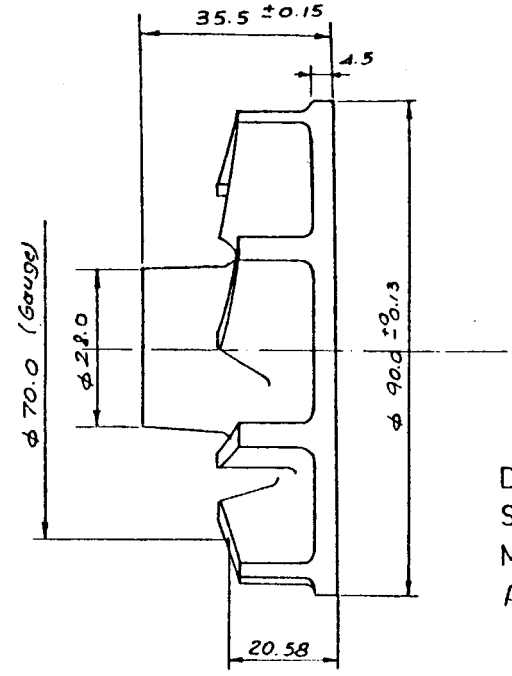

Dimensions in mm
Scale : 2:1
Material : cast iron
Average roughness : 9 μm

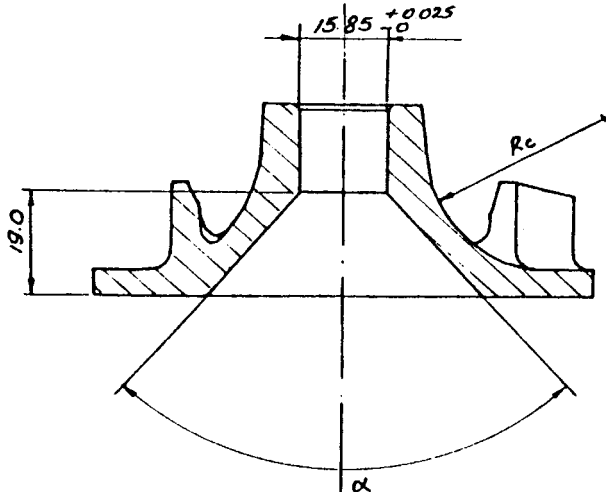

Impeller	z	β_1°	β_2°	α°	d_1	d_2	b_1	b_2	t	R_a*	Rb	Rc
J-8-70	8	70	70	70	54.0	90.0	13.0	9.0	3.5	105.0	98.0	18.0
J-8-48	8	48	48	84	56.5	↓	↓	↓	3.5	47.0	36.0	22.0
J-8-48 cl	8	48	48	84	56.5	↓	↓	↓	3.5	47.0	36.0	22.0
J-8-30	8	20	30	84	56.5	↓	↓	↓	4.5	35.0	20.0	22.0
J-6-70	6	70	70	70	54.0	↓	↓	↓	3.5	105.0	98.0	18.0
J-6-50	6	25	50	70	56.5	↓	↓	↓	4.0	90.0	68.0	18.0
J-6-38	6	30	38	70	56.5	↓	↓	↓	4.0	36.0	20.0	18.0

* see fig 2.8 for definition

FIG. 2.10 DETAILS AND DIMENSIONS OF IMPELLERS FOR PUMP J

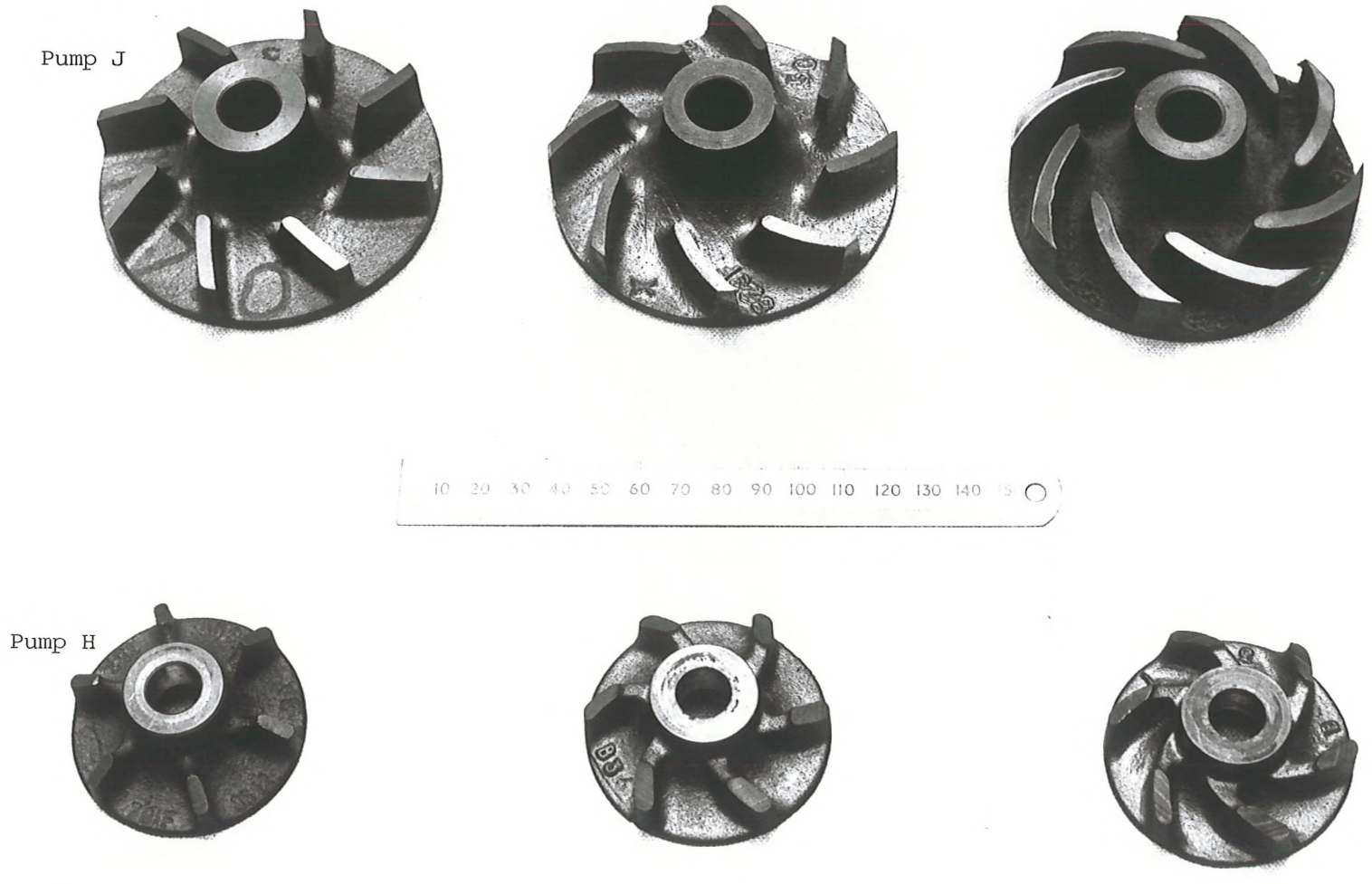

Figure 2.11 Impellers of different blade shape for pumps H and J.

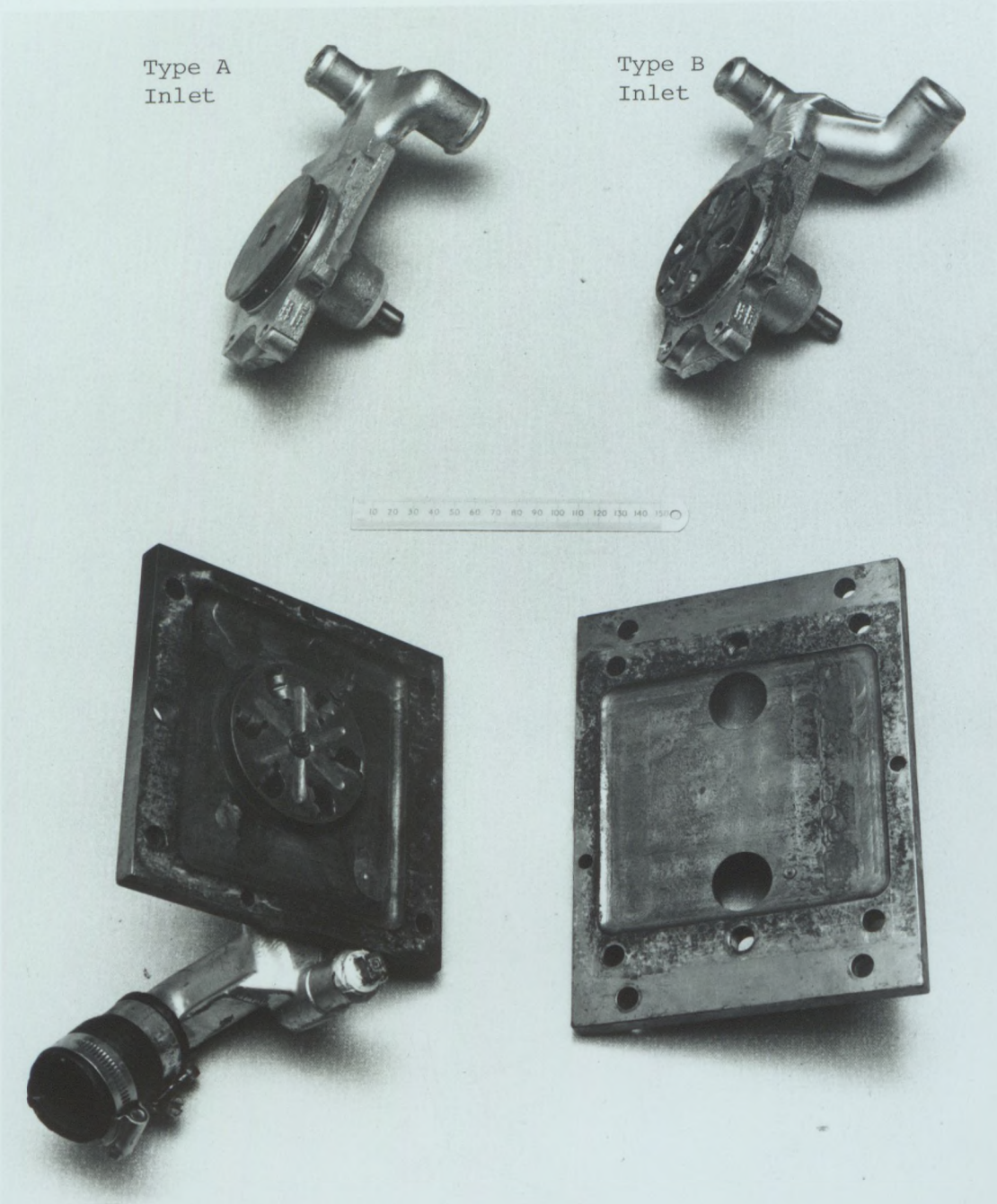

Figure 2.12 Pump K with two versions of inlet designs with the discharge cavity.

CHAPTER 3

NON CAVITATING PERFORMANCE: GENERATED HEAD

3.1 Theoretical and Actual Developed Head

The energy transfer across the centrifugal impeller is most conveniently described by the one-dimensional momentum theory for the mean stream line of the flow. If one assumes an infinite number of blades with a finite passage width which allows for a perfect guidance of the flow without any deviations, then from the inlet and outlet velocity triangles of figure 3.1, the theoretical (Euler) energy transfer per unit mass can be expressed by the equation:

$$g H_e = U_2 C_{u2} - U_1 C_{u1} \qquad (3.1)$$

The Euler head is of theoretical value only. Its significance lies in the comparison of this head to the actual developed head of the machine. Well designed, large centrifugal pumps are expected to give a high H/H_e ratio, as compared to the poorly designed, small size pumps used for coolant circulation.

Mass produced, low cost centrifugal pumps used for the automotive industry have several features in common which can be summarized as follows:

1. Cramped inlet pipe layout to save space.
2. Poorly designed semi-open impellers (mostly radial) of inadequate blade number and length, to reduce cost.
3. The replacement of the volute (in most cases) by a square cavity for simplicity and low cost.
4. High manufacturing tolerances to cut down on assembly costs.

All these factors are likely to promote high losses with respect to the generated head. Earlier tests on several automotive centrifugal

pumps [42, 57] have shown that H/H_e ratios of all tested pumps are far below those expected from similar size, conventionally designed centrifugal pumps.

To demonstrate this, 2 pumps of different designs tested during this programme are compared on figure 3.2*. Pump J has a simple volute, a reasonably well designed closed impeller of backward curved blades and a more acceptable inlet and outlet piping layout (figure 2.9). Pump K on the other hand, has no volute at all but rather an irregular square cavity of impeller discharge, a closed impeller of poor design, and inconveniently laid inlet pipe and flow chamber (figure 2.12). The theoretical head coefficient ψ_e is estimated according to equation (I.4) in Appendix I.

The results of figure 3.2 indicate clearly that pump J of the better design, produces an ψ/ψ_e ratio almost twice that of the poorly designed pump K, as a result of the enormous hydraulic losses associated with the latter pump.

To analyse the results of figure 3.2 in some more detail, the reaction effect and the slip factor outlined in Appendix I are to be estimated for both pumps J and K.

The term $(C_2^2 - C_1^2)/2$ of the Euler equation (I.5) represents the dynamic part of the energy transfer, and theoretically it can be converted into static pressure rise energy in the volute or diffuser of the pump [41]. Therefore good pump design requires this term not to be excessively high. If however, C_2 is kept high as it is the case with pump K, then the absence of the volute could only mean a high degree of energy wastage.

---

*The standard test liquid in this research programme is 50/50 EG/W at 90°C. Since this mixture at this temperature has a viscosity nearly similar to that of cold water, developed head is likely to be also similar to that of cold water. In fact hot 50/50 EG/W mixtures produces slightly higher head than cold water for similar flowrate and pump speed (See also next chapter).

As mentioned earlier, the theoretical energy transformation assumes an infinite number of blades with perfect guidance of the flow and without any deviations. In reality, this cannot be achieved since a finite number of blades has to be used, which makes the guidance of the flow more difficult, and is expected to deteriorate with decreased number of blades.

Assuming a loss-free constant total energy transfer, the presence of a finite number will result in a higher discharge relative velocity at the suction side of the blade and a lower one at the pressure side, hence creating a velocity gradient in the passage with the result of a flow deflection allowing the average relative velocity to leave at an angle smaller than the geometrical angle β_2. The result of this is a reduction in the absolute exit velocity and thus the whirl component of this absolute velocity is reduced by an amount equal to ΔC_{u2} (figure 3.1c), a phenomenon known as the head slip. Noorbachsh [112], in a recent work analysed the head slip as a function of several variables, such as

$$\Delta C_{u2} = f\ (Z,\ \beta_2,\ r_1/r_2,\ b_2/b_1,\ \phi,\ Re,\ \nu) \qquad (3.2)$$

This author concluded that slip is theoretically predictable near the optimum flow condition, but at flows away from that point, deviation from the real slip value is significant especially at low flows, where a reverse flow at impeller exit sets in, inducing pre-rotation at impeller inlet. Since Noorbachsh results implicitly consider time-average velocity, flows away from the BEP are likely to be highly unsteady. In fact his results show that ΔC_{u2} takes a minimum value near the BEP.

Using a laser double focus velocimeter, Eckandt [190] was able to show that the potential, one dimensional energy transfer theory is only partially applicable for the centrifugal impeller at the BEP because of the flow separation followed by a wake growth at the suction side of the flow channel. At flows away from the BEP these secondary effects are likely to increase.

From his own experience, and from many other results by several authors, Wiesner [181] modified equation (I.14) of Appendix I to suit most results and it was found to agree well with Busemann's [26] approach, hence he suggested the following expression for the slip factor;

$$\sigma' = 1 - \frac{\sin \beta_2}{Z^{0.7}} \left[1 - \left(\frac{r_1/r_2 - \xi}{1 - \xi}\right)^2\right] \qquad (3.3)$$

The limit ξ divides the region of constant and variable slip factor and is given by the equation;

$$\xi = \frac{r_1}{r_2} \cong \frac{1}{\ln^{-1} \frac{8.16 \sin \beta_2}{Z}} \qquad (3.4)$$

For $r_1/r_2 \leqq 0.5$ the ξ limit approaches the value of r_1/r_2 and the bracket in equation (3.3) is reduced to unity, and the slip factor is constant for given values of Z and β_2. For higher values of r_1/r_2 it is likely to have changing slip factors.

More recent test results [82, 120, 174], showed a fairly good agreement with Wiesner's modified slip factor.

Applying the slip factor to modify the theoretical head for a finite number of blades, the theoretical (input) head H_i is obtained from the following equation [120];

$$H_i = \sigma' \frac{U_2^2}{g} - \frac{U_2 C_{m2}}{g \tan \beta_2} \qquad (3.5)$$

The reaction effect of equation (I.7) of Appendix I, can also be modified with respect to the input head as follows;

$$T_i = 1 - \frac{1}{2} \psi_i \qquad (3.6)$$

Using equation (3.5) and applying the slip factor according to Wiesner (equation 3.3), the input head coefficient ψ_i for both pumps J

and K was plotted on figure 3.2 against flow coefficient. Furthermore, assuming that the dynamic energy part of the generated head of pump K is nearly all dissipated because of the absence of the volute, the reaction effect T_i was estimated according to equation (3.6) and the product $T_i\psi_i$ was also plotted on figure 3.2 for pump K.

Examination of figure 3.2 reveals that the exceptionally low ψ/ψ_e of pump K can be related to the following 2 main reasons;

1. The head slip at the BEP (Section AB) is far larger for pump K than pump J. This can be attributed to the poor design of pump K's impeller with only 6, short, radial blades.

2. The hydraulic head losses at the BEP (Section BC) is significantly larger for pump K. Whereas these losses are more or less frictional for pump J (in the impeller and volute channels), two types of losses can be distinguished for pump K. The first is friction (Section EC) and the second is due to the wastage of the dynamic energy part of the input head (Section BE).

Therefore it should be obvious that for the small size, commercially produced, low cost, centrifugal pumps, most of the head energy is wasted to overcome the various internal hydraulic losses. In addition to that, the design and layout of the inlet pipe plays a crucial role in reducing the developed head, as we shall see in Chapter 5.

3.2 The Influence of the Type of Shroud and the Tip Clearance

To avoid high manufacturing and installation costs, most modern commercially produced pumps for coolant circulation are fitted with semi-open impellers of relatively simple geometrical design. The presence of an axial clearance between the blade tip and the pump body, would mean an increased internal leakage from the high pressure to the low pressure side of the blade, which is inevitably proportional to the size of this clearance and the Re number across the gap [111]. This leakage produces some lift and drag upon the blade with the result of reduced blade loading

and total energy rise through the impeller.

Myles [109, 110] noted that the energy loss across the mixed flow blade is a function of the cord length ℓ, the tip clearance Δx, the blade tip lift C_L and the relative velocity W, in the form;

$$E = \frac{2\sqrt{2}}{5} \rho \, \Delta x \, \ell \, W^3 \, C_L^{3/2} \qquad (3.7)$$

A more useful method is to compare the head coefficient of the semi-open impeller to that of a zero tip clearance condition. Myles [110] puts it in the general form;

$$\psi = \psi_o - \Delta\psi_d - \Delta\psi_L \qquad (3.8)$$

ψ_o denotes the head coefficient at zero clearance, $\Delta\psi_d$ the head losses due to the drag and $\Delta\psi_L$ that due to tip lift. Pfleiderer [126] simplifies the same idea by introducing a head drop proportional to the tip clearance/channel depth ratio (λ);

$$\Delta H = \beta \lambda H_o \qquad (3.9)$$

Whereby β is a proportionality factor and H_o is the developed head at zero tip clearance.

All 3 pumps available for this research were fitted with semi-open impellers with relatively large tip clearance. To reach a comprehensive understanding of the various factors influencing both non-cavitating and cavitating behaviour of the small size pumps, one impeller of each pump (J and K) was fitted with a second shroud to become a closed impeller and tested at the same speed. The results of these tests are shown on figure 3.3 for pump J and on figure 3.4 for pump K and the design values at BEP are listed in Table 3.1. If the assumption is made that the developed head at zero tip clearance is nearly equal to the head developed by the closed impeller (normally semi-open impellers of zero clearance are expected to perform better than the closed impeller [106]), then equation (3.9) can be applied with the result of the proportionality factor β taking the value of

$\sim$ 1.8 for pump J and 0.3 for pump K at the shut-off point. These values of β are not in agreement with those suggested by Pfleiderer [126] (β = 1) and Rütchi [143] (β = 0.9).

Variation in the tip clearance of pump J gave a proportional decrease in the generated head and efficiency, to Δx (and λ). On figure 3.5, the performances of the closed and the semi-open impeller with 3 different Δx are shown. On figure 3.6a the proportionality factor β of equation (3.9) takes the average value of $\sim$ 1.3 at zero flow.

At the optimum flow rate, a relationship of β to the optimum head is to be established from the following empirical equation [106];

$$H_{opt} = (1 - \beta\lambda)\, H_o \qquad (3.10)$$

and by the combination of both equations (3.9) and (3.10) we obtain;

$$\Delta H = \beta\lambda / (1 - \beta\lambda)\, H_{opt} \qquad (3.11)$$

The change in the developed head ΔH must mean a similar change in the input head to the impeller, an assumption confirmed from actual tests [184] and from passage velocity measurements [70]. The corrected input heads for the various clearances of pump J are plotted on figure 3.6b by using the relationship of equation (3.11). A good agreement between the theoretical and actual head losses exists at the higher values of Δx, but to a less extent for $\Delta x < 1$ mm. Hence it can be said for this pump that the presence of the clearance is more important than its size with respect to generated head, for the range of Δx tested.

Tests performed on pump K with the standard (perforated) impeller showed a similar tendency (figure 3.7) with the effect of the clearance on the developed head greatly reduced at clearances above 1 mm, although the efficiency is slightly reduced. It should be noted here, however, that the tip clearance of this pump is not constant over the whole length of the blade, thus complicating the picture further.

For the same pump (K) also, the comparison between the closed and the semi-open impeller (with holes covered) seems to indicate, that the effect of the tip clearance is to reduce the dynamic losses due to reduced input head (figure 3.8), other losses on the other hand are only marginally effected.

3.3 The Influence of the Impeller Geometry

One way to improve the relatively poor performance of small, commercial centrifugal pumps is by improving the design of the impeller such as blade curvature and blade number. For this reason, several impeller geometries were included in the test programme for both pumps H and J, the dimensions of which are listed on figs. 2.8/10 . Typical photographs of pump J's and pump H's impellers are shown on figure (2.11).

On figure 3.9 the test results for pump J with 6 semi-open impellers of different designs, but with the same pump body and volute, are shown in non-dimensional form. To gain a better understanding of these results, the performances of pump J were plotted in dimensional form on figure 3.10 for 8-bladed impellers and on figure 3.11 for the 6-bladed impellers. On figure 3.12, the test results for 3 impellers of pump H of the same number of blades are plotted in dimensional form.

From these figures it should be obvious that the change in the impeller geometry produces only insignificant improvement in both generated head and overall efficiency of pump H. The main reason behind this lies in the exceptionally high dynamic losses associated with the absence of the volute which makes any improvement in the impeller geometry rather ineffective. This is not the case for the volute type pump J, where the impeller geometry seems to produce significant performance changes. This is more clearly seen on figure 3.13, where the pump performances at the BEP are plotted against the discharge angle β_2. On this figure, the general trend seems to indicate an increase in both Q_{opt} and H_{opt} with increased β_2. The influence of the number of blades, Z, however, is less obvious on this figure.

In designing the centrifugal impeller, the optimum number of blades takes the experimental value [124, 126, 181];

$$Z = K \left(\frac{d_2 + d_1}{d_2 - d_1}\right) \sin\left(\frac{\beta_1 + \beta_2}{2}\right) \qquad (3.12)$$

K = 5.65 for cast iron impellers [126] (surface finish dependent)

This suggests that the pump performance is related to the impeller solidity in a higher degree than simply to the discharge angle. Such a correlation is attempted on figure 3.14 for pump J with 6 different impeller geometries. The results seem to indicate a clear improvement in performance with reduced impeller solidity due to a combination of adequate guidance to the flow and reduced skin friction losses. This improvement, however, seems to reach a maximum at a certain low solidity, below which the pump performance starts to deteriorate, mainly due to greatly reduced guidance to the flow.

The concept of the solidity seems to provide the explanation for the higher generated head produced by the 6-bladed J-6-50 impeller compared to impeller J-8-48 of nearly similar β_2 but of higher number of blades. Reducing the inlet angle β_1 of impeller J-6-50 helps to increase the blade length considerably, which in turn more than compensates for the reduction of the number of blades. This however does not mean a similar improvement in efficiency, largely due to increased skin friction.

In table 3.1 all the relevant theoretical and actual performance figures at the Q_{opt} are listed for all impellers tested in the programme. Of particular interest is the ratio of H/H_e. This ratio seems to improve with increased β_2 and number of blades for any one pump. Otherwise it is significantly larger for the volute type pump J.

For the semi-open, radial impeller of pump H, the effect of increasing the number of blades from 6 to 8 does not produce a significant improvement compared to that obtained for the theoretical (Euler) head. On figure 3.15, an increase of 17% in H_e results in less than 10% improvement in the actual

head. The obvious reason behind this is the higher skin friction combined with similar dynamic losses of the 6-bladed impeller.

3.4 Impeller to Volute Matching of Pump J

Pump J is fitted with a spiral casing of simple design (figure 2.9). Six semi-open impellers of various designs but of the same outside diameter and blade height, were tested in conjunction with the same casing. In this section we shall try to use quasi-theoretical analysis to find the best suited impeller of those tested to the same casing.

The impeller is regarded as a source of radial flow on which is super-imposed a vortex so that emerging from its outlet there is a spiral flow whose circumferential component C_u is related to the head while the radial component C_m is related to the delivery. Therefore the angle of spiral flow depends on the rate of discharge through the impeller [185]. Volutes are designed in such a way as to accommodate and guide the flow as smooth as possible to avoid excessive disturbance to the flow streams. This is normally done by matching the spiral flow angle at the operating point (or at BEP) to that of the spiral casing.

The free vortex theory of the flow in the volute is given by [126];

$$C_u.r = \text{Const} \qquad (3.13)$$

For the whirl component at impeller discharge, which after considering the slip factor is C_{u2}', then $C_u.r = C_{u2}' r_2$ and from figure 3.16 the flow rate passing the area element dA at any cross section of the volute of depth a is given by;

$$dQ = dA\, C_u = adr \frac{C_{u2}' r_2}{r} \qquad (3.14)$$

At the volute throat where the total flow rate passes, Q can be found by integrating equation (3.14) between the limit r_2 and $r_2 + b$, b being the throat height;

$$Q = ar_2 C_{u2}' \int_{r_2}^{r_2+b} \frac{dr}{r} = ar_2 C_{u2}' \ln\left(1 + \frac{b}{r_2}\right) \quad (3.15)$$

According to Worster [185], the volute characteristic at BEP is defined by the ratio of the average throat velocity C_3 to the circumferential velocity U_2, or

$$\frac{C_3}{U_2} = \frac{Q}{ab\,U_2} = \frac{ar_2 C_{u2}' \ln\left(1 + \frac{b}{r_2}\right)}{ab\,U_2} \quad (3.16)$$

Replacing C_{u2}' by gH_i/U_2 in the above equation and solving for H_i, the following equation is obtained for the input head [185];

$$H_i = \frac{Q}{ab}\frac{U_2}{g}\frac{\frac{b}{r_2}}{\ln\left(1 + \frac{b}{r_2}\right)} \quad (3.17)$$

If the input head of equation (3.17) is assumed to be fully transmitted through the volute without significant disturbance and with full recovery of the dynamic head of equation (I.5), then both the impeller input head and volute input head meet together at BEP [185], or $H_i = H_v$.

The input head of the impeller is found from equation (I.10), by the application of a proper slip factor, σ.

To extend the investigation further, two options for the estimation of the slip factor are considered. The first is that due to Wisener (equation 3.3), and the second is that due to Pfleiderer in equation (I.17) of Appendix I. For volute type, radial pumps, the constants of equation (I.18) are given the values a = 0.68 and b = 0.6 [126]; hence

$$CP = \frac{0.68 + 0.6 \sin\beta_2}{Z\left(1 - (r_1/r_2)^2\right)} \quad (3.18)$$

and for the input head;

$$H_i = \frac{H_e}{(1 + CP)} \quad (3.19)$$

On figure 3.17, the head curve of the closed impeller of pump J was plotted against flow rate. Using both equations (3.5) and (3.19), the input head for the same pump was estimated and plotted on this figure. The volute head line H_v is plotted according to equation (3.17). It crosses the impeller input lines H_i at point A and B. The down projection of these two points meets the head curve at C and D respectively. Point C is nearer to the BEP at the speed of the pump in consideration which may indicate that the slip factor is crucial in deciding upon the impeller to volute matching. In this case it seems that Wiesner's slip factor (upper curve) produces too high H_i thus pushing the BEP further to the right.

To look at this problem in more depth, three semi-open impellers of the same number of blades but of different blade curvatures were investigated on figure 3.18. The volute line H_v was plotted according to equation (3.17) and the line joining the BEP points with the origin was drawn. The projection of the BEP's on the volute line are B, D and F corresponding to A, C and E. On figure 3.19 the head curves for the same BEP's and their respective volute points are plotted against discharge angle β_2. Also on the same figure the impeller input head values for the different impellers at their BEP are plotted using both Wiesner's slip factor (equation 3.3) and Pfleiderer's slip factor (equation 3.18), and joined together. The resulting picture seems to indicate that at low discharge angle, the difference between H_v and H_i is significant indicating high losses, and that is more pronounced if Wisener's slip factor is used for the input head. At large β_2 the difference between H_v and H_i is much smaller and the Pfleiderer's slip factor may be under-rated.

These results may indicate that the design of the same casing of pump J is more suited for impellers of large dishcarge angle β_2. Also, the Wiesner slip factor is a more reliable source to be used for estimating H_i. The excessively high H_i-H_v for lower β_2 values is perhaps more generally connected with high discharge losses in the volute, due to greater mis-matching of the spiral angle.

3.5 Concluding Remarks

Small, high speed*, commercially produced centrifugal pumps are known to perform poorly with respect to the generated head across the impeller [42, 57]. Size effect, large head slip and excessively high internal losses are among the reasons behind this behaviour, not to mention the high dynamic losses associated with the absence of the proper volute in most cases.

The present research, among other things looked into several factors influencing the generated head of these small pumps. These included the type of discharge cavity, the type of shroud and the size of the tip clearance, and the impeller geometry (inlet conditions to be dealt with in a later chapter). Test results were numerous and the following conclusions can be drawn:

1. The effect of the nature of the discharge cavity has been demonstrated by comparing a volute type pump J, with pump K, which has no volute but rather a square cavity. The ratio of the actual to the theoretical Euler head H/H_e for pump J has been shown to be nearly twice that of pump K. Beside the low slip factor of pump K, the main reason behind the high head losses was found to be due to the poor recovery of the dynamic part of the generated head, in the discharge cavity of this pump.

2. The influence of the type of shroud was found to be especially pronounced with the two pump versions tested (pump J and K). The presence of the tip clearance for the semi-open impeller helps to reduce the developed head, in proportion to the tip clearance/channel depth ratio λ. However, test results on pump J showed that the proportionality does not hold well over the range of clearances tested and it may reach a value as high as 2.3 at very small clearances. Compared to a suggested ratio of 0.9 [143], the results indicate a highly sensitive operation of the small size pumps to the introduction of the tip clearance.

---

*Nominal operating speeds 4000-7000 rpm.

3. The effect of the discharge angle β_2 on the mass and energy transfer is quite significant for the volute type pump J. For the 8-bladed impellers, a change of β_2 from 25° to 70° gave an increase in Q_{opt} of $\sim$ 24%, and in H_{opt} of $\sim$ 20%. For the volute-less pump H, on the other hand, an increase in β_2 from 40° to 90° gave an increase of only $\sim$ 10% in Q_{opt} and $\sim$ 12% in H_{opt}. High hydraulic losses of the poorly designed pump H, seem to render changes in the impeller geometry less effective.

4. Developed head increases by increasing β_2 for the same number of blades as one would expect from the Euler equation. Increasing the number of blades for nearly the same β_2 did not necessarily mean an increased developed head. This is evident from tests on 2 impellers of pump J, where the 6-bladed impeller J-6-50 produces higher head than the 8-bladed impeller J-8-48. The reason behind this is simply smaller inlet angle β_1 of impeller J-6-50, which increases the length of the blade with the result of improved blade loading. Using the solidity concept which takes the length and the number of blades into account, seems to give a better correlation between geometry and performance.

5. The matching of different impellers to the same pump casing of pump J seems to suggest that impellers of high β_2 bring the volute characteristics H_v nearer to the input head H_i of the impeller at the BEP, which means an optimization of performance for the matching impeller. Using Wiesner's slip factor to obtain H_i seems more appropriate at high β_2. The slip factor according to Pfleiderer on the other hand, seems to give better results at low values of β_2 but is too low at high β_2 and hence is not appropriate to use.

TABLE 3.1

FIGURES 3.1 to 3.19

Table 3.1 Theoretical and actual design figures at Q_{opt}** for pumps H, J and K.

Impeller	Q (L/min)	H (m)	$\phi = Cm_2/U_2$	$\psi = gH/U_2^2$	$H_e = U_2^2(1 - \frac{\phi}{\tan\beta_2})$	Pfleiderer		Wiesner			H/H_e
						σ	H_i (m)	σ'	H_i (m)	$\tau = 1 - \frac{\sigma'}{2}\frac{Cu_2}{U_2}$	
J-8-70	290	22.4	0.073	0.488	44.6	0.66	28.6	0.72	31.1	0.66	0.5
J-8-48 cl	280	19.6	0.072	0.427	42.6	0.69	29.2	0.77	32.8	0.64	0.46
J-8-48*	250	19.0	0.063	0.415	43.0	0.69	28.6	0.77	32.3	0.65	0.44
J-8-30	230	17.3	0.066	0.378	40.6	0.71	28.1	0.81	32.3	0.68	0.42
J-6-70	280	21.8	0.067	0.473	44.7	0.60	25.6	0.64	27.4	0.70	0.48
J-6-50	260	19.6	0.065	0.427	43.3	0.62	25.8	0.68	28.5	0.69	0.45
J-6-38	240	17.6	0.062	0.384	42.2	0.64	26.1	0.73	29.8	0.67	0.42
H-8-90	105	5.6	0.081	0.175	32.2	0.60	18.6	0.62	19.4	0.70	0.174
H-8-60	100	5.3	0.079	0.166	30.8	0.61	18.2	0.65	19.3	0.70	0.172
H-8-40	96	5.0	0.084	0.157	29.0	0.64	18.0	0.72	20.3	0.69	0.172
H-6-90*	101	5.2	0.073	0.163	32.2	0.52	16.3	0.53	16.6	0.74	0.160
H-6-60	100	5.2	0.075	0.163	30.8	0.54	16.1	0.55	16.4	0.74	0.169
H-6-40	98	4.8	0.078	0.150	29.2	0.57	16.1	0.62	17.6	0.73	0.164
K-6-90 cl	100	9.7	0.061	0.208	46.5	0.60	27.9	0.64	29.9	0.68	0.21
K-6-90 so	80	9.7	0.050	0.206	46.5	0.60	26.0	0.64	28.0	0.70	

* Standard impeller

** At pump speeds - 6000 rpm for pumps H and K and 4500 for pump J.

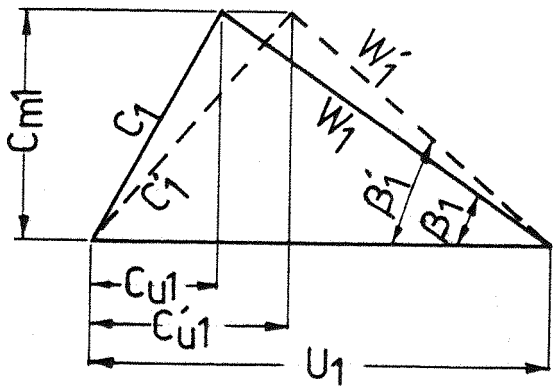

a – Inlet velocity triangle

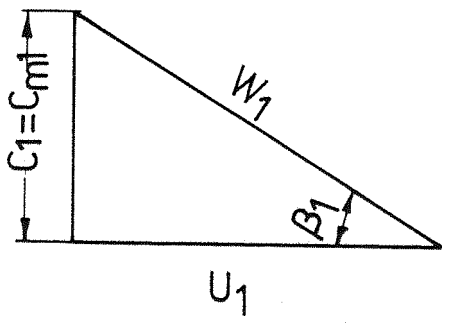

b – Inlet velocity triangle
(no pre-swirl)

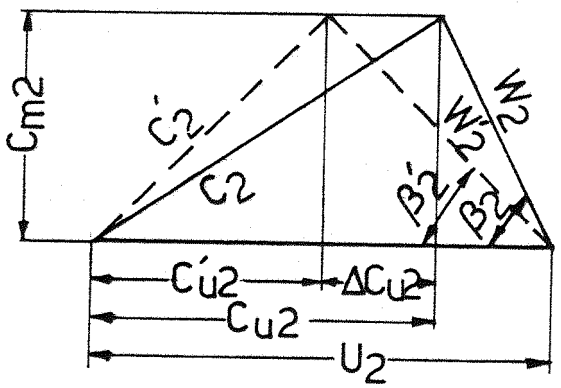

c – Outlet velocity triangle

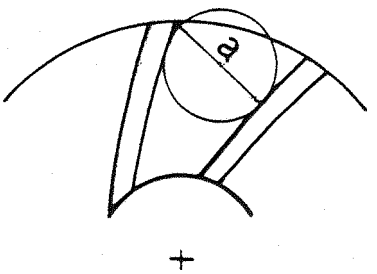

d – Discharge slip diameter

FIG 3.1 INLET AND OUTLET VELOCITY TRIANGLE AND THE SLIP DIAMETER

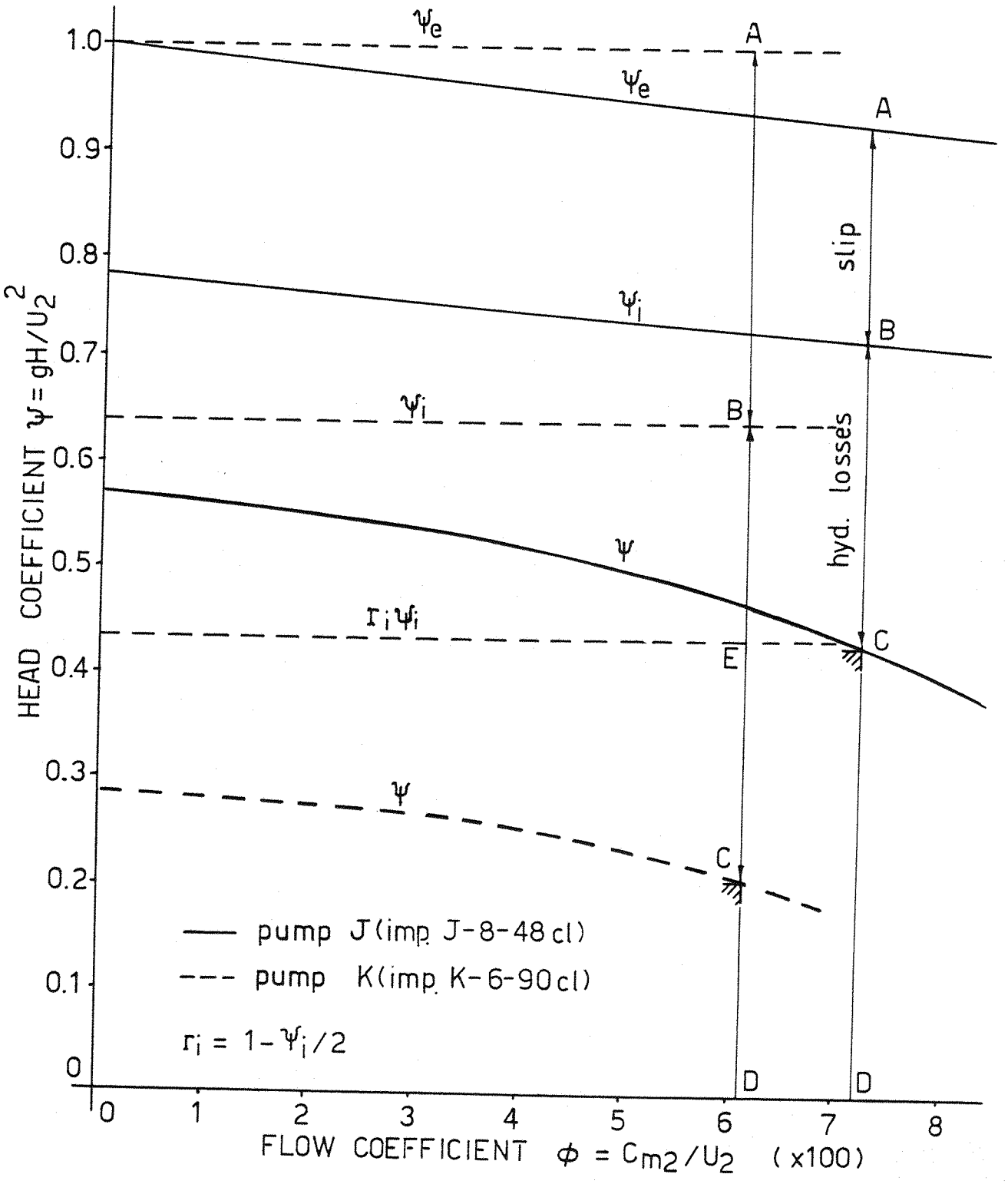

FIG.3.2 THEORETICAL AND ACTUAL HEAD FOR 2 CENTRIFUGAL PUMPS WITH CLOSED IMPELLERS

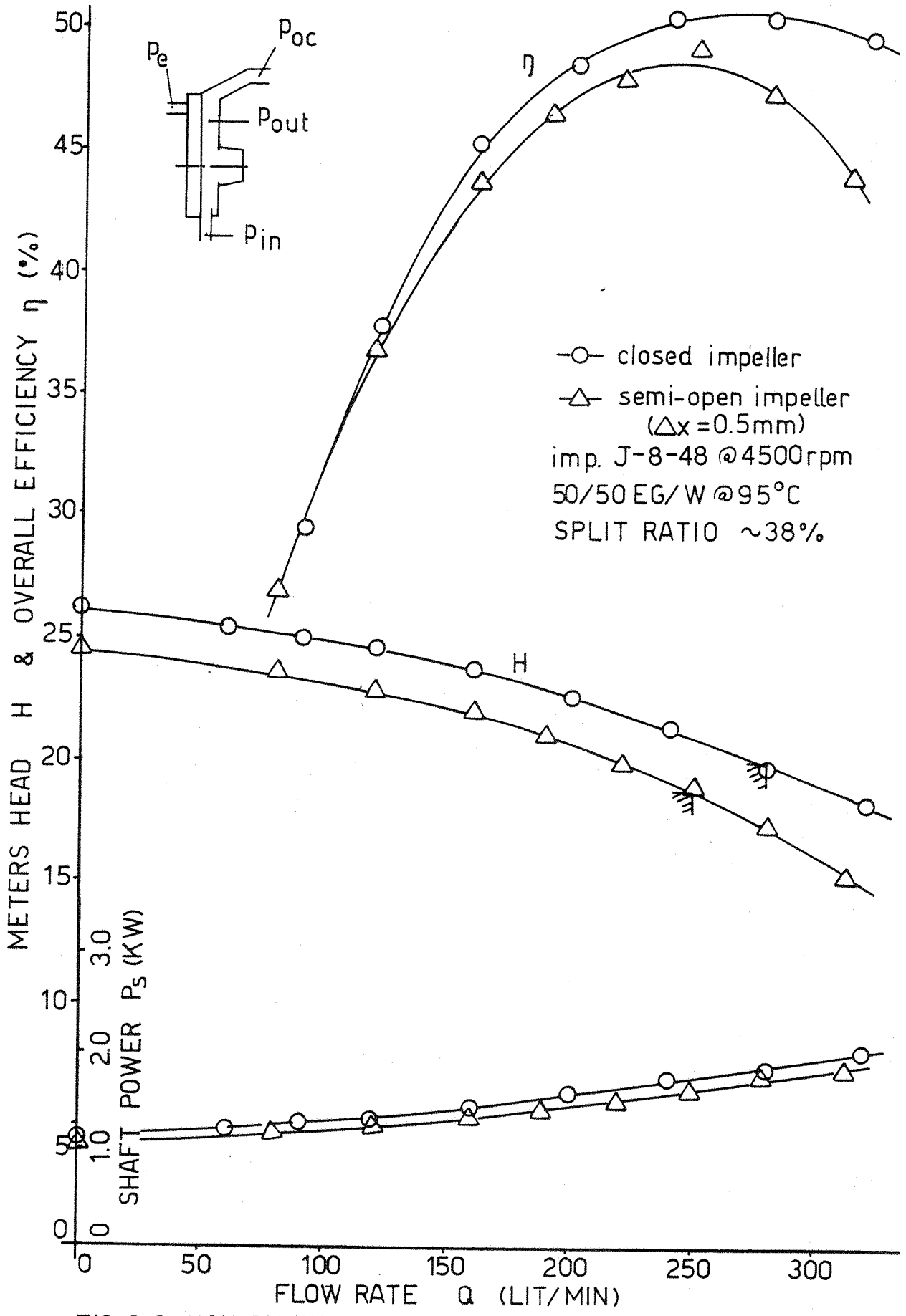

FIG. 3.3 NON CAVITATING PERFORMANCE FOR PUMP J WITH 2 IMPELLER GEOMETRIES

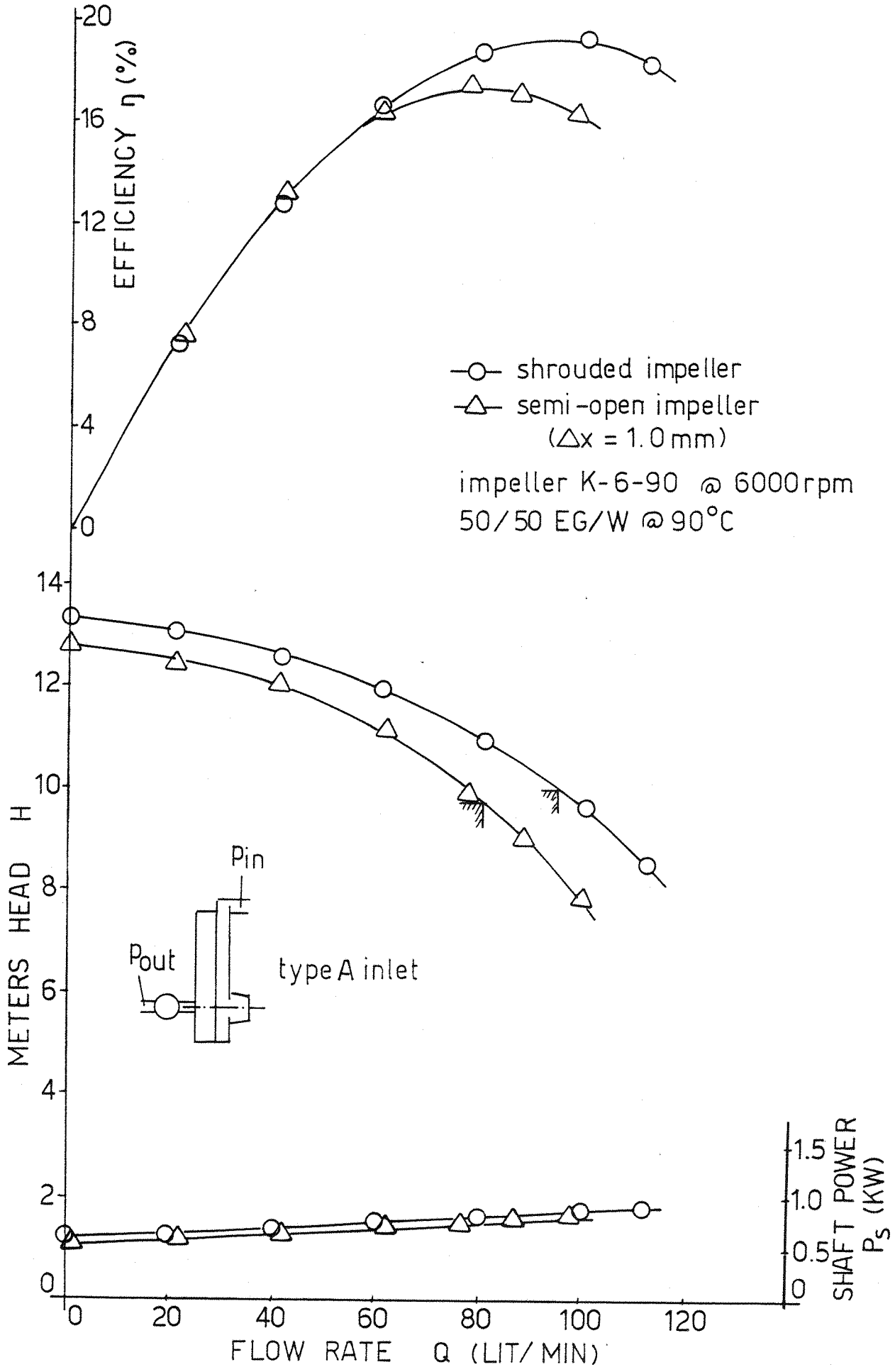

FIG 3.4 NON-CAVITATING PERFORMANCE FOR PUMP K WITH 2 IMPELLER GEOMETRIES

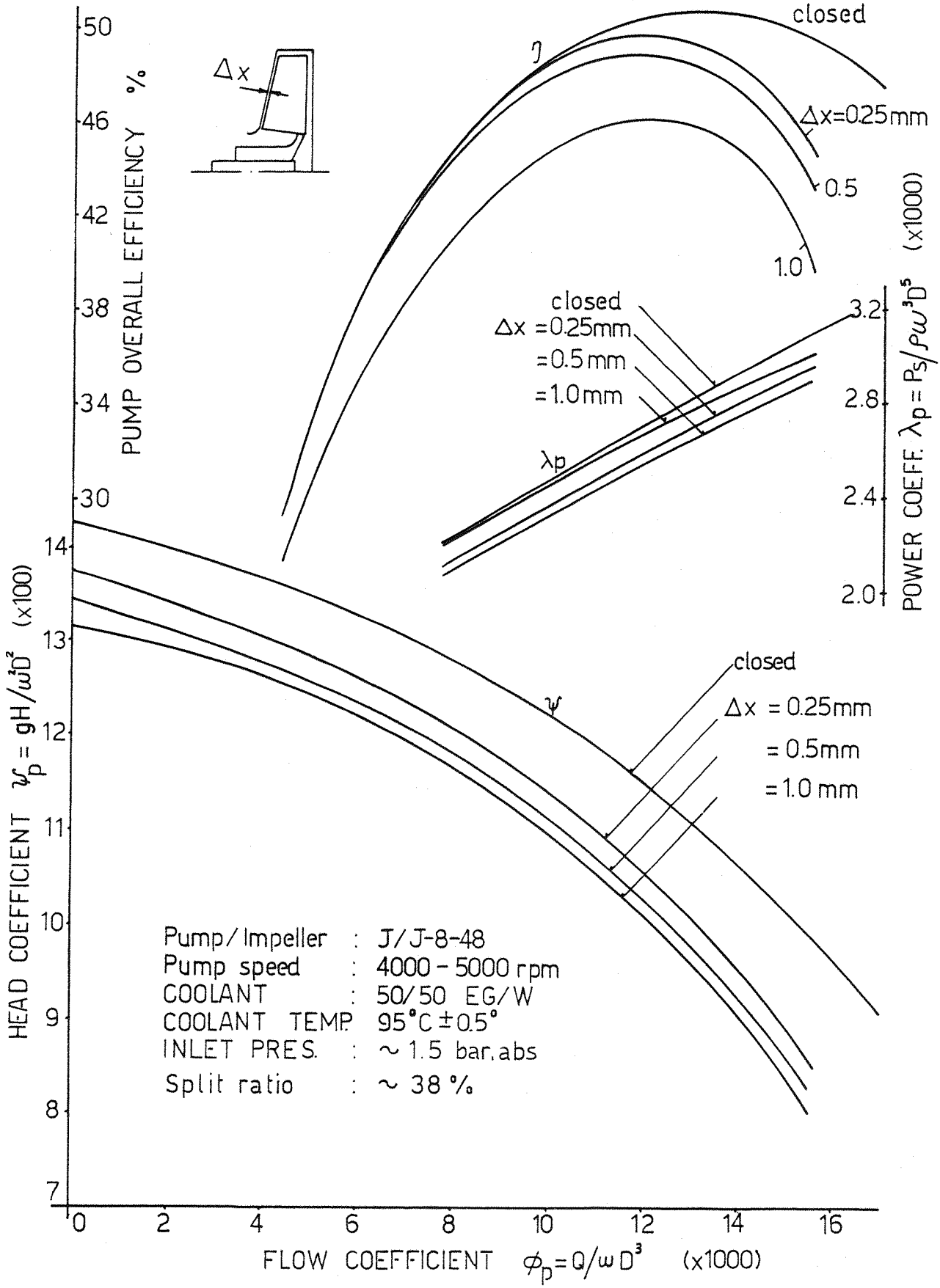

FIG. 3.5 NON-CAVITATING PERFORMANCE OF PUMP J WITH THE CLOSED AND SEMI-OPEN IMPELLERS

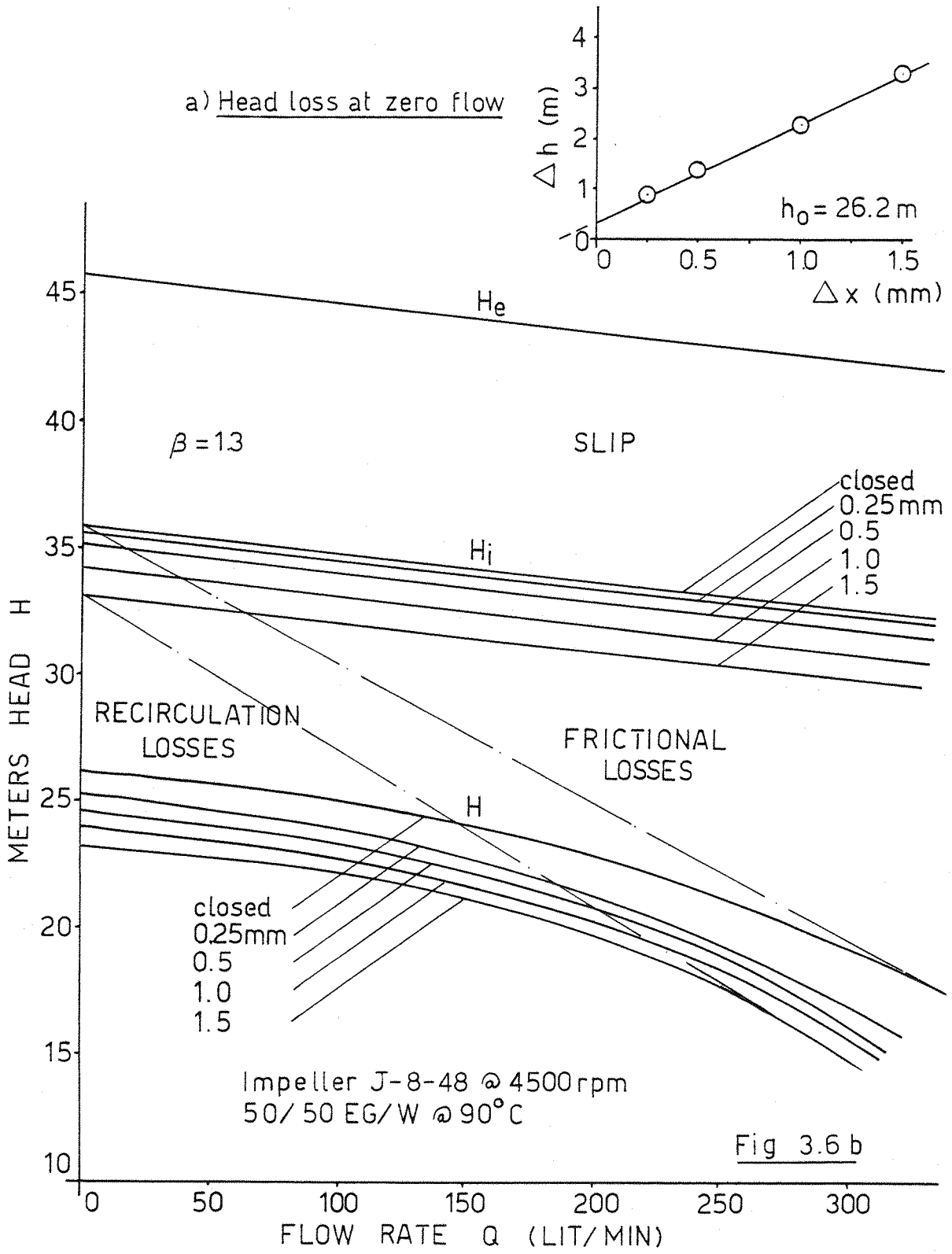

FIG 3.6 THEORETICAL AND ACTUAL HEAD FOR PUMP J WITH THE CLOSED AND SEMI-OPEN IMPELLERS OF DIFFERENT TIP CLEARANCE

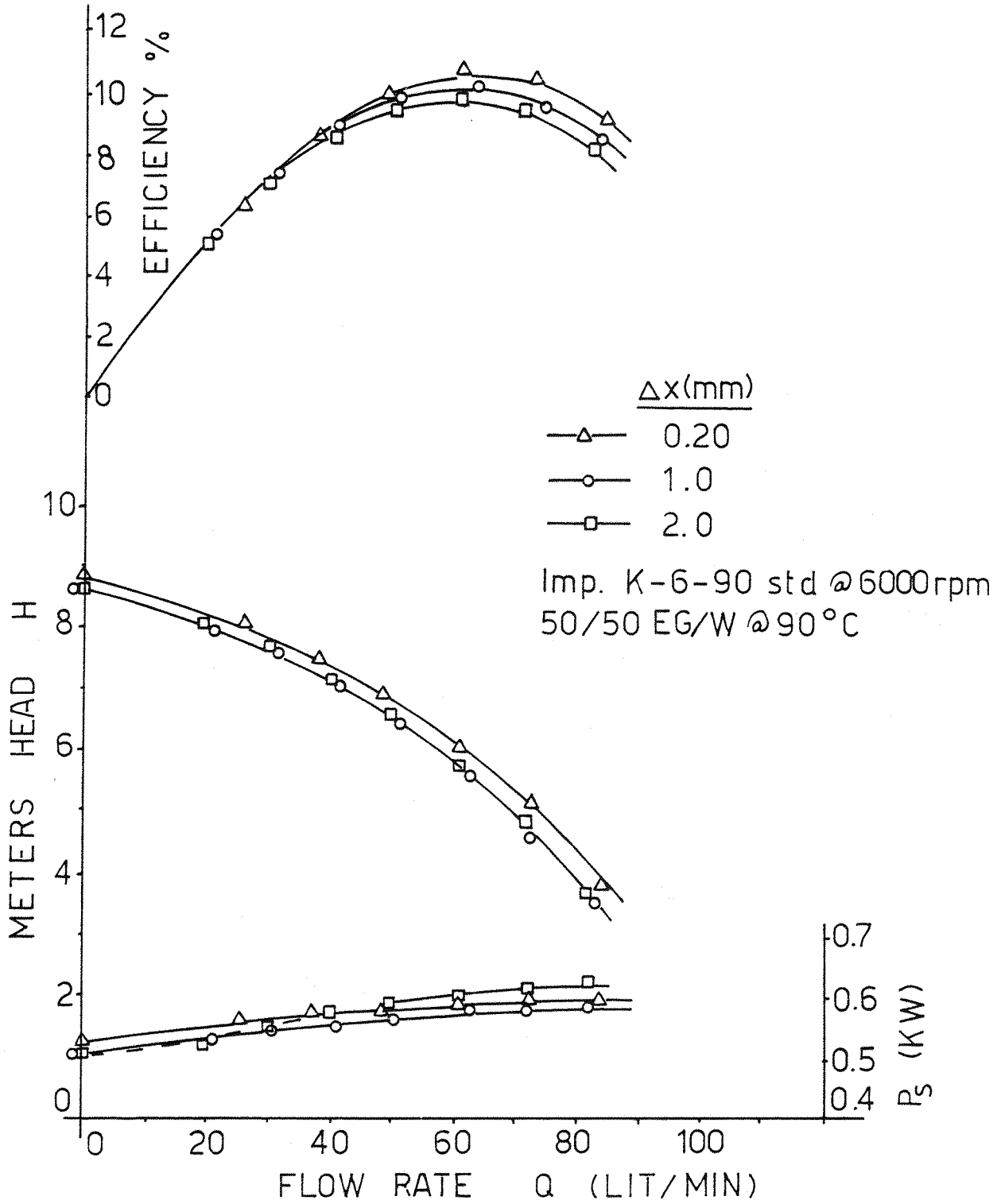

FIG 3.7 THE EFFECT OF THE TIP CLEARANCE ON PUMP K PERFORMANCE WITH THE PRODUCTION TYPE IMPELLER

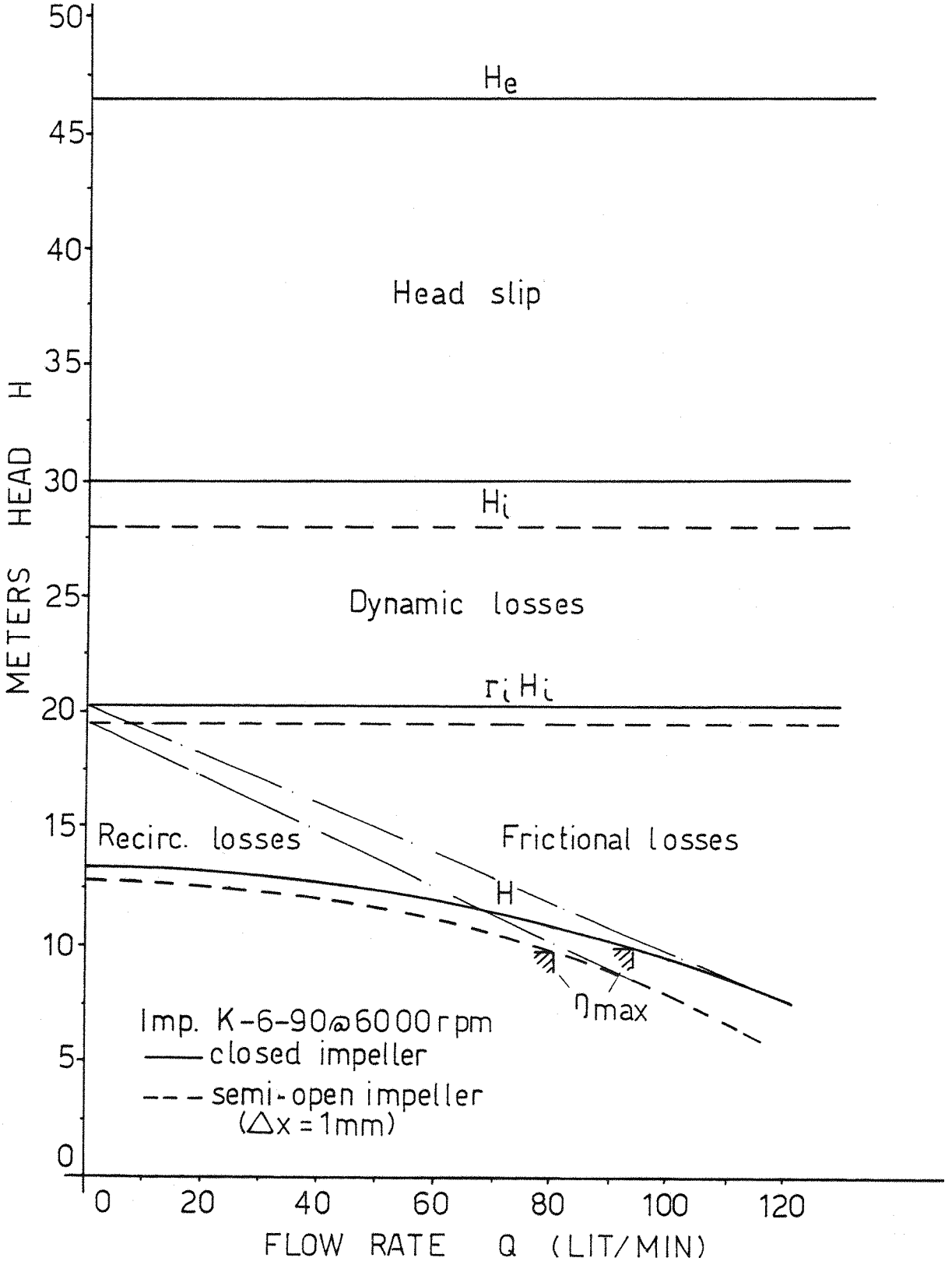

FIG 3.8 THEORETICAL & ACTUAL HEAD FOR PUMP K WITH 2 IMPELLER GEOMETRIES

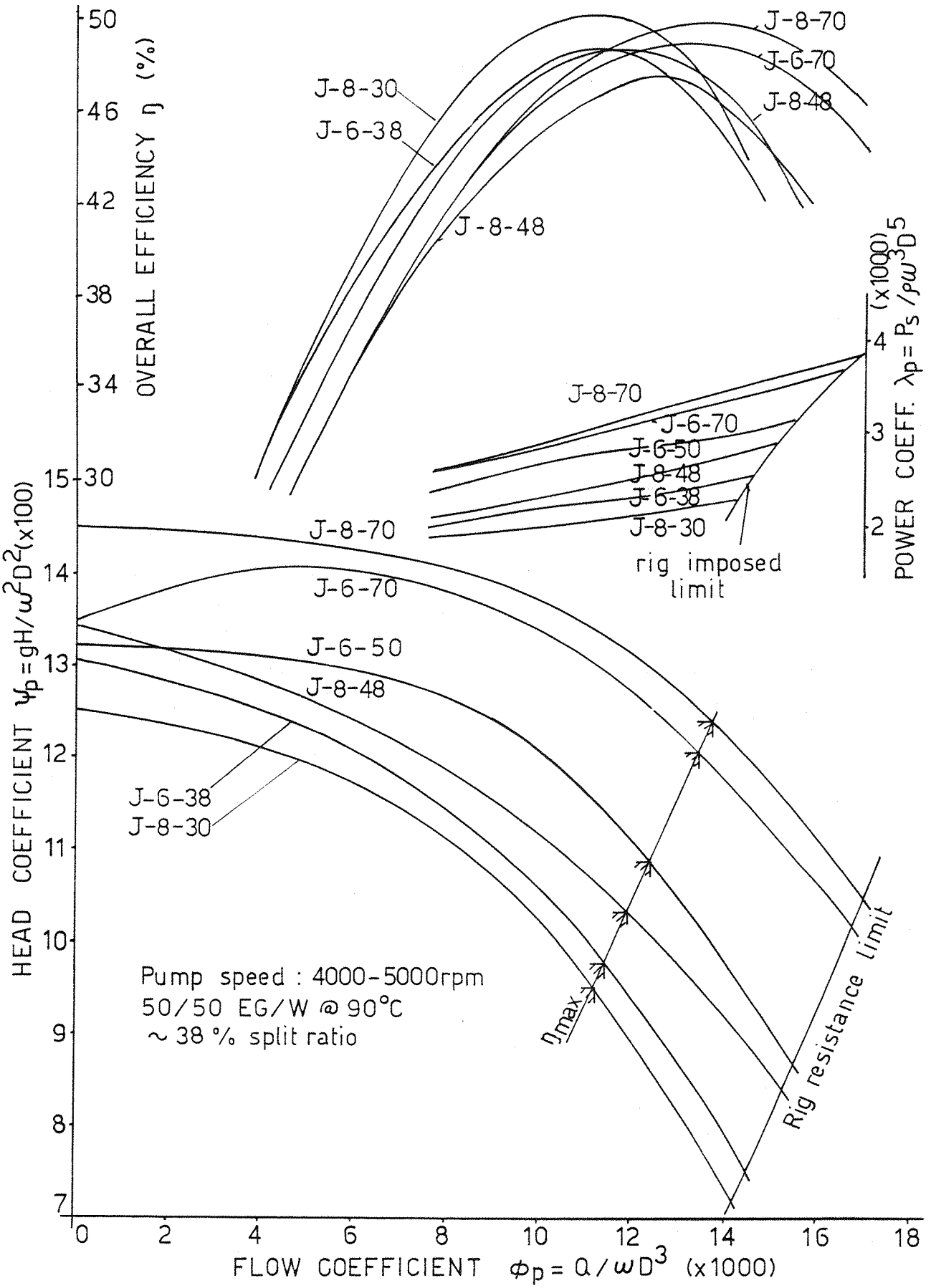

FIG 3.9 NON-DIMENSIONAL PARAMETERS FOR PUMP J WITH 6 IMPELLER GEOMETRIES & 3 PUMP RPM'S

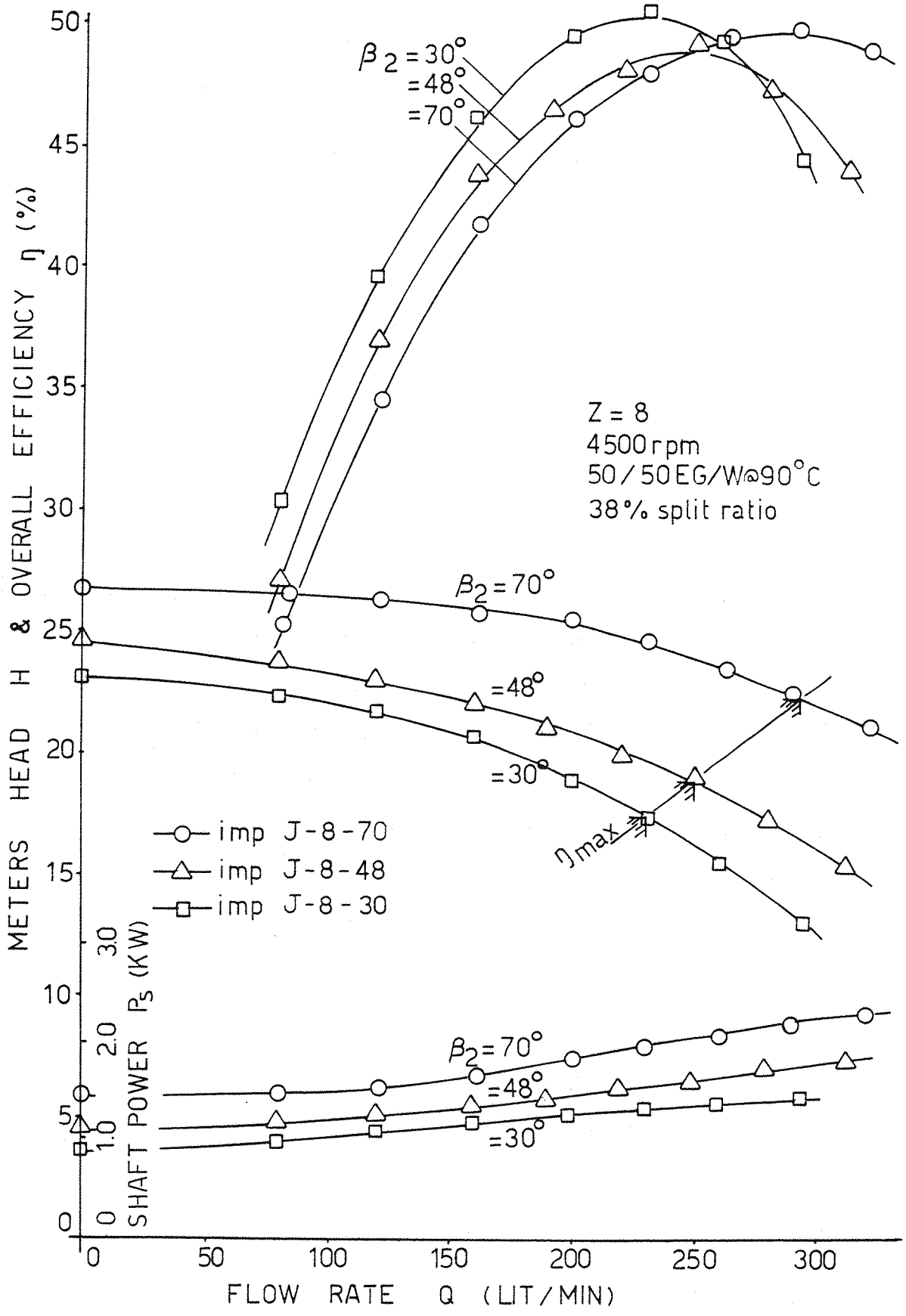

FIG 3.10 NON-CAV. PERFORMANCE OF PUMP J WITH 8-BLADED SEMI OPEN IMPELLERS OF DIFFERENT OUTLET ANGLE β_2

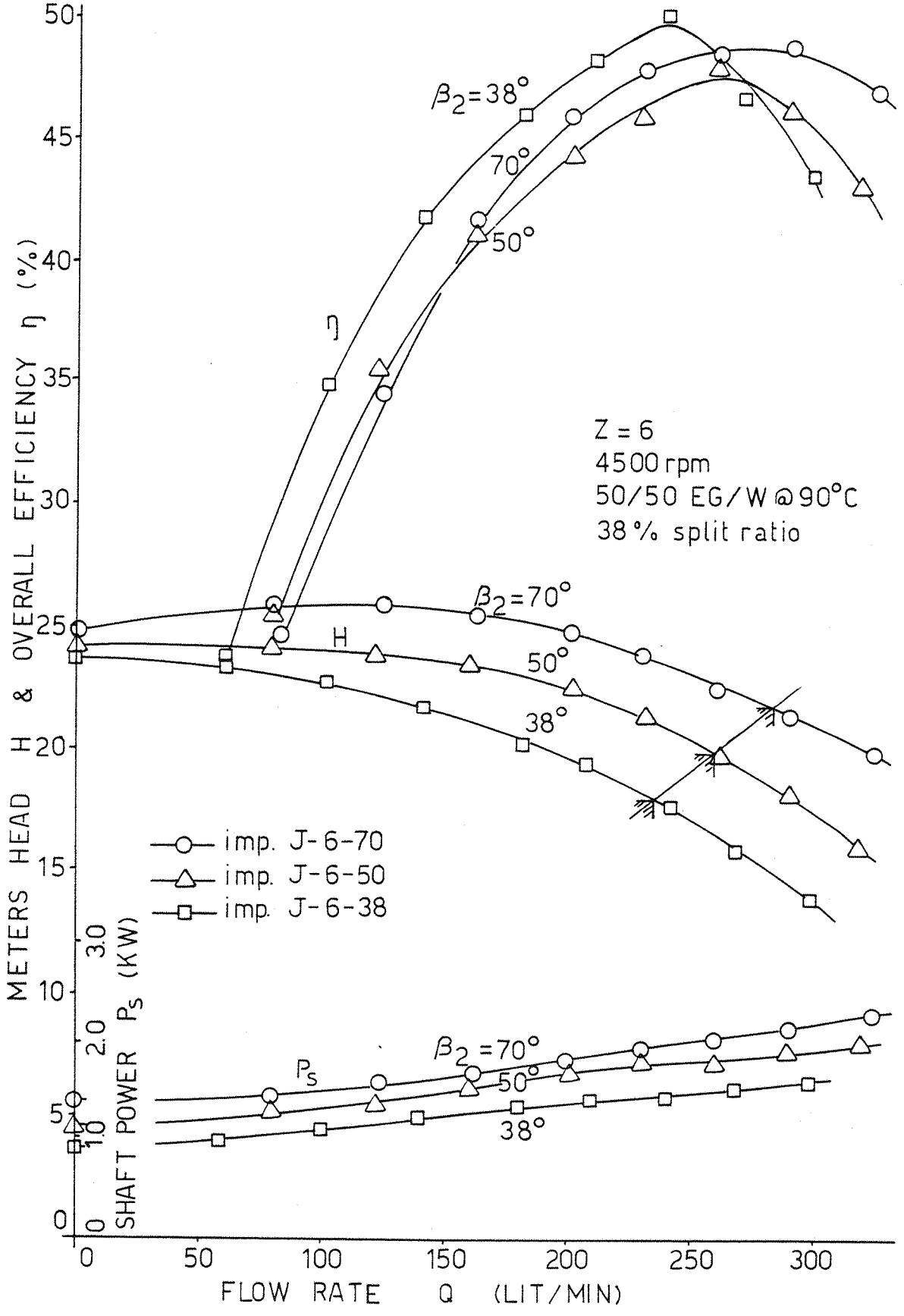

FIG 3.11 NON CAV. PERFORMANCE OF PUMP J WITH 6-BLADED SEMI OPEN IMPELLERS OF DIFFERENT OUTLET ANGLE β_2

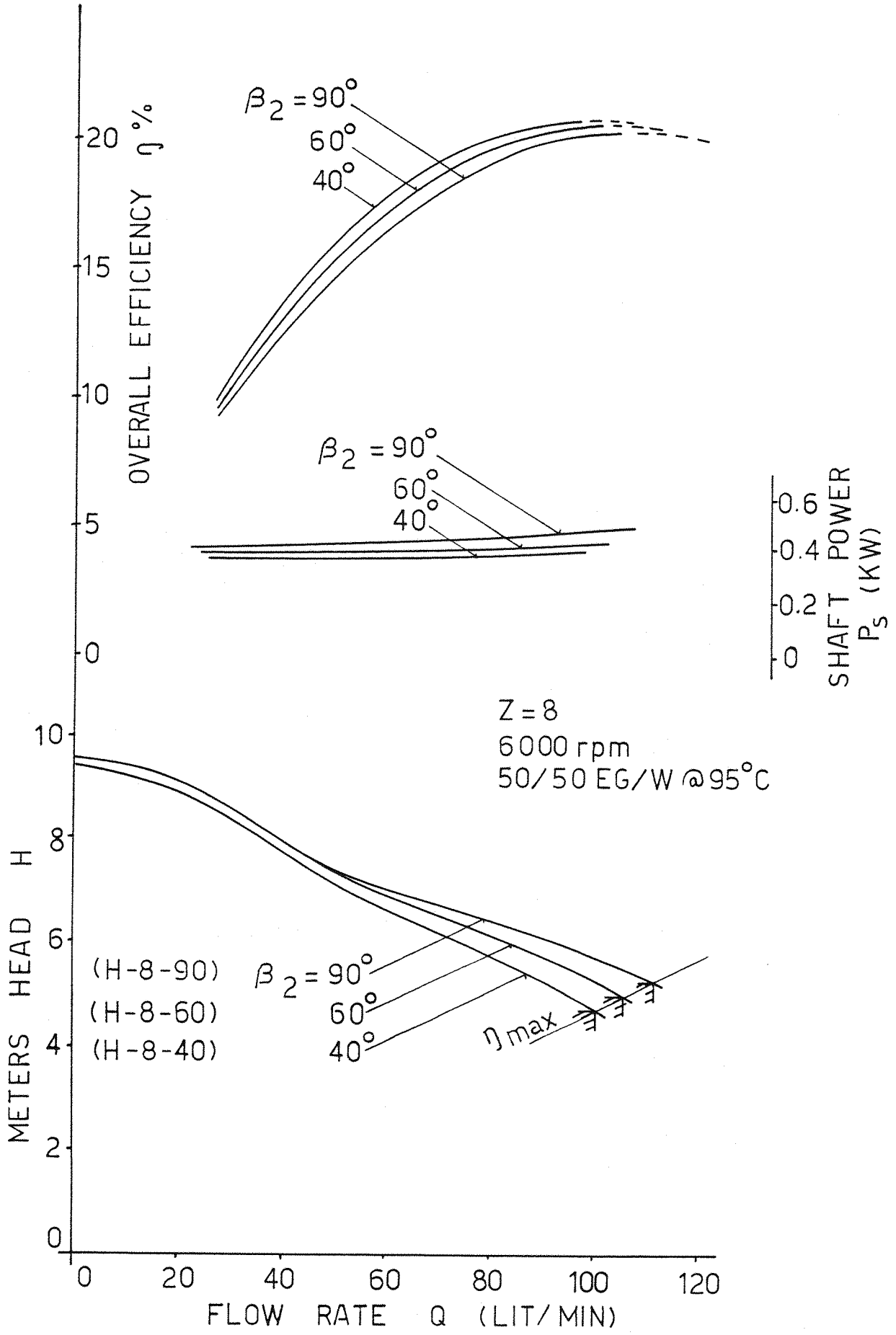

FIG. 3.12 NON-CAV. PERFORMANCE OF PUMP H WITH 8 BLADED SEMI OPEN IMPELLERS OF DIFFERENT OUTLET ANGLES β_2

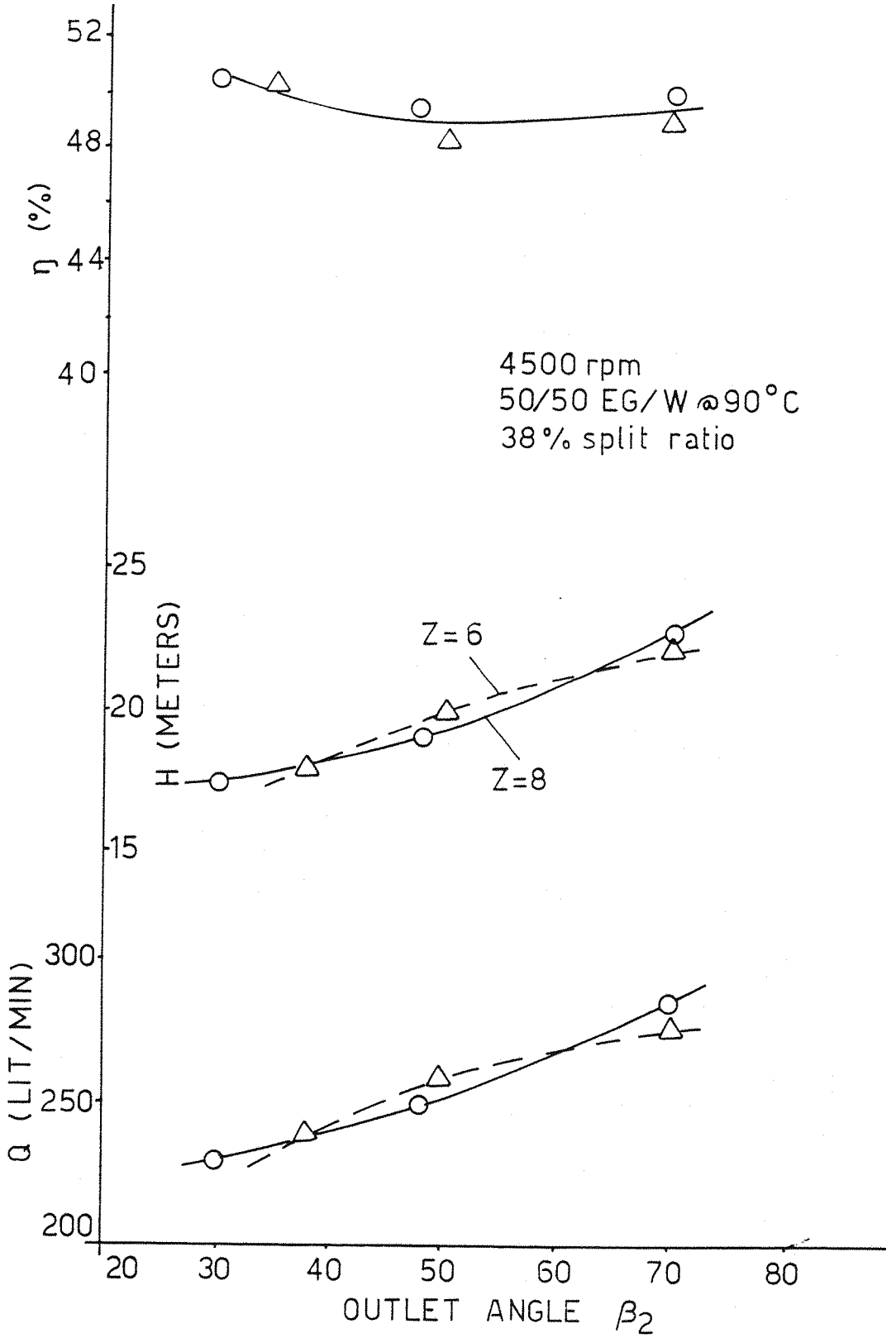

FIG 3.13 THE EFFECT OF NUMBER OF BLADES AND OUTLET ANGLE ON THE PERFORMANCE OF PUMP J AT BEP

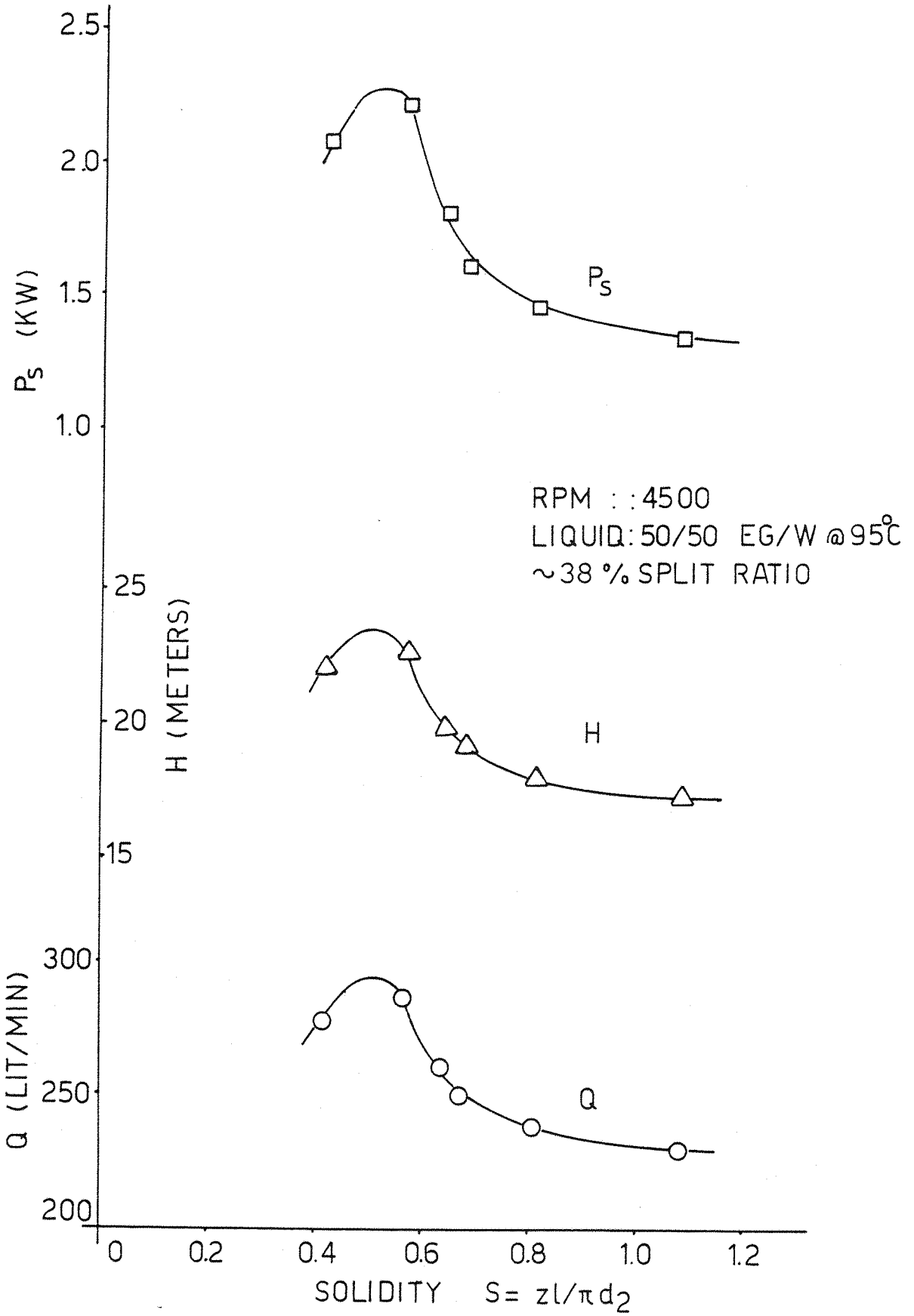

FIG. 3.14 IMPELLER SOLIDITY INFLUENCE ON THE PERFORMANCE OF PUMP J AT BEP

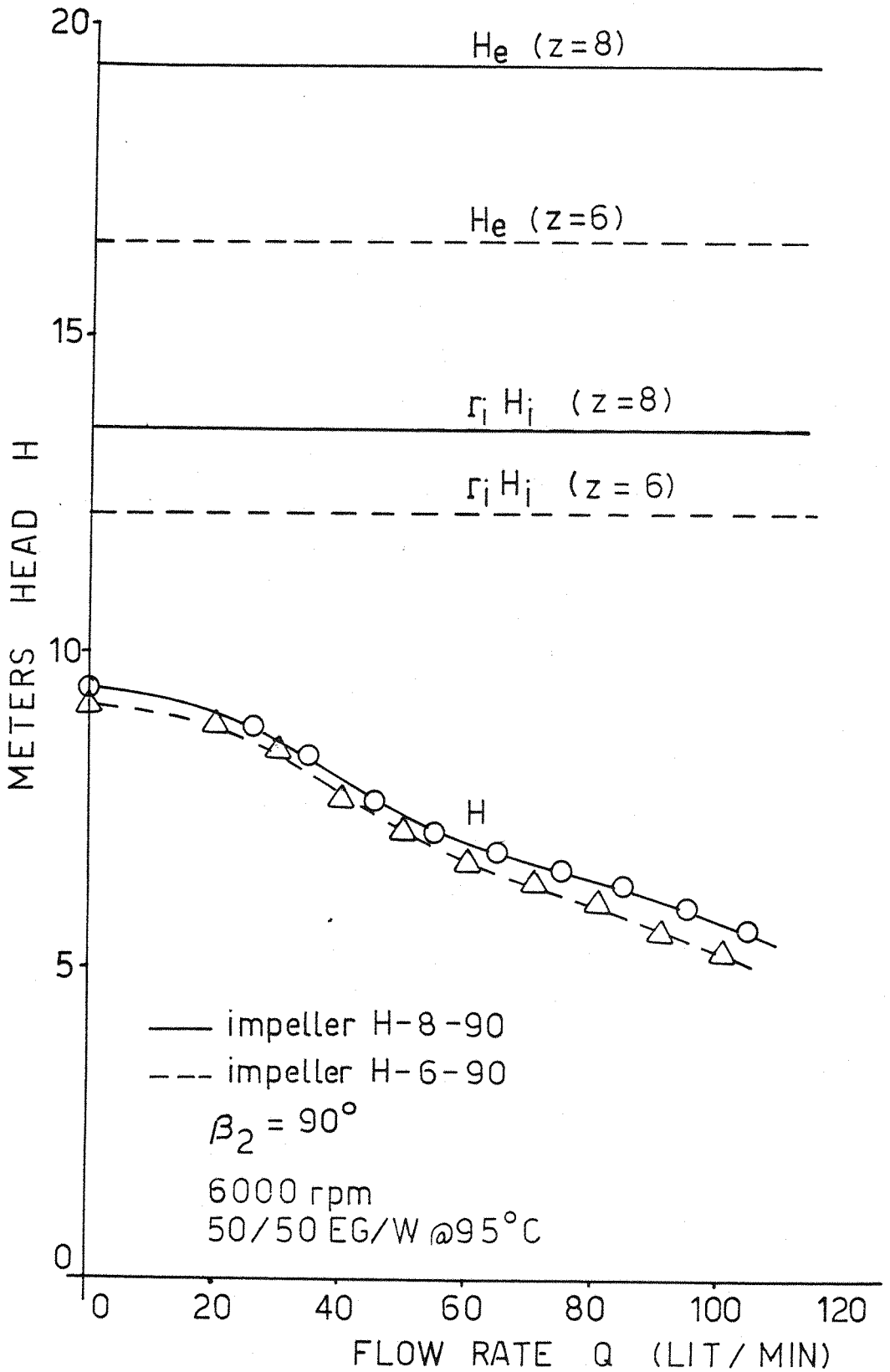

FIG 3.15 ACTUAL AND INPUT HEAD FOR 2 RADIAL IMPELLERS OF PUMP H WITH DIFFERENT NUMBER OF BLADES

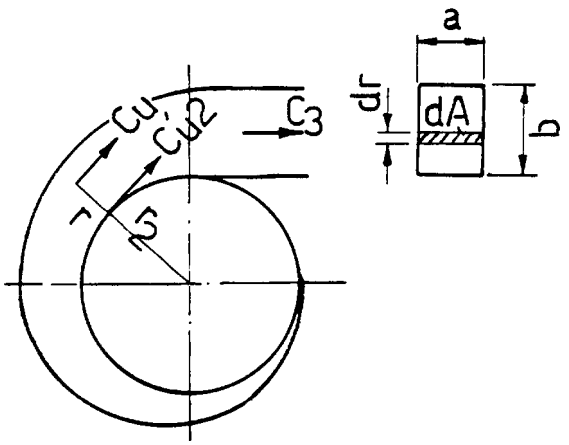

FIG 3.16 VORTEX FLOW VELOCITIES AT THE DISCHARGE OF CENTRIFUGAL PUMPS

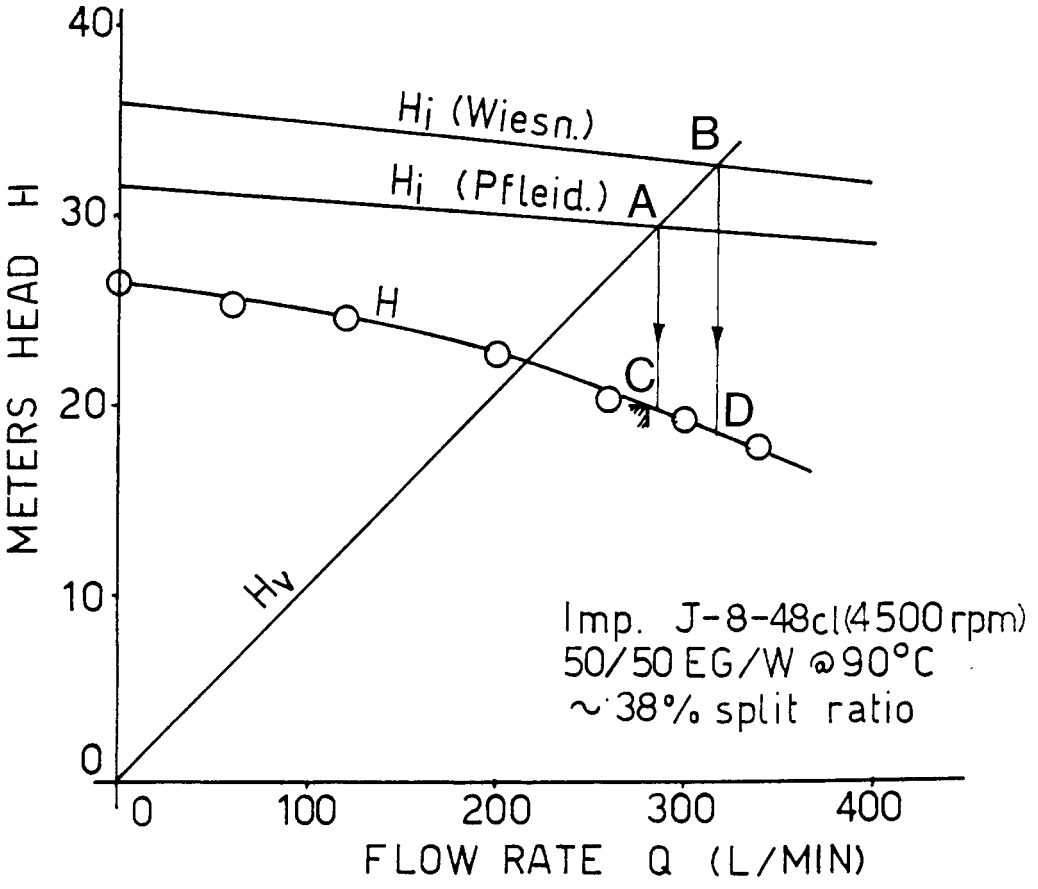

FIG. 3.17 VOLUTE TO IMPELLER MATCHING OF PUMP J WITH THE CLOSED IMPELLER

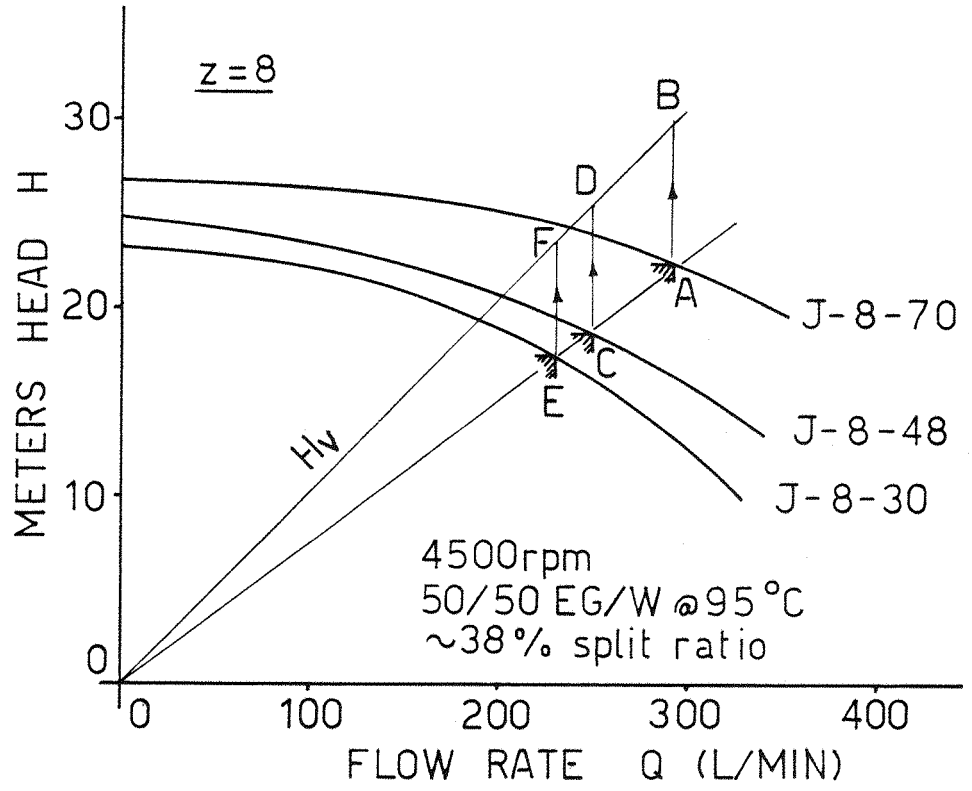

FIG. 3.18 IDEAL IMPELLER TO VOLUTE MATCHING FOR 3 IMPELLER GEOMETRIES OF PUMP J

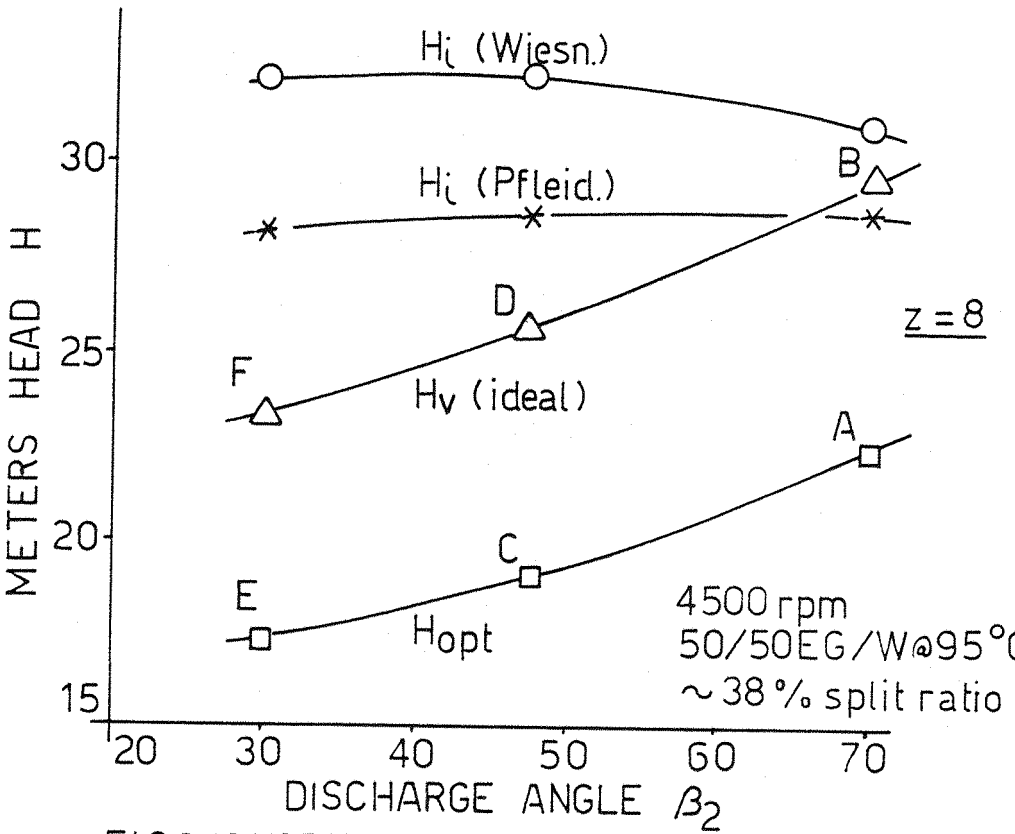

FIG.3.19 VARIATIONS IN THE IMPELLER TO VOLUTE MATCHING OF PUMP J WITH RESPECT TO IMPELLER DISCHARGE ANGLE

CHAPTER 4

PUMP LOSSES AND SCALE EFFECTS

4.1 Efficiencies and the Various Losses

The overall efficiency of the centrifugal pump is the ratio of the net hydraulic power gain P_{hyd} to the total shaft input power P_s, and is known to be a function of the type and size of the machine [61, 156]. Pumps of high specific speed n_s and delivering large quantities of liquid, usually have high efficiencies. Small radial pumps of low n_s and delivering only small amounts of liquid, on the other hand, are expected to have considerably lower overall efficiency because of the larger wetted area to mass flow ratio, which is associated with high hydraulic and disc friction losses.

Pump J with a simple volute and a closed (double shrouded) impeller of reasonable design produces an overall efficiency of $\sim$ 50% (figure 3.3). Considering the unfavourable suction condition (side suction with the flow passing over the shaft seal) and the absence of the wearing rings, this efficiency is close to the expected value from the more conventionally designed straight inlet centrifugal pump in this range ($\sim$ 60%).

Pump K with a closed impeller, on the other hand, barely produces an overall efficiency of 20% (figure 3.4), which gives an indication of the amount of losses associated with many of the mass produced small centrifugal pumps. Insufficient, short, radial impeller blades, large clearance inside the pump and relatively oversized mechanical seals are some of the factors contributing to the bad performance of these pumps, but more significantly is the poor design of both inlet and outlet flow channels which help to dissipate a great part of the generated head thus making life more difficult for the hydraulic performance of these pumps.

Ignoring the change in the velocity energy between pump inlet and outlet, the hydraulic power P_{hyd} is given by the total energy gain of the mass flow rate through the pump (ρgQH). The difference between this hydraulic power and the input shaft power P_s is wasted to overcome the different types of losses involved in the hydrodynamic machines, and it is relatively a minimum at the point of best efficiency of the machine (BEP).

In general there are four major types of losses at a given flow rate (see figure 4.1) and these are: a) external (mechanical) losses P_m which include frictional losses in the bearing and seals P_{bs}, and frictional losses in the disc of the impeller (P_d); b) volumetric losses P_v due to the leakage of high pressure liquid through gaps and clearances to the low pressure region of the pump; c) hydraulic losses of the flow P_h which are mainly frictional but also are due to changes of flow direction inside the pump, and finally d) recirculation losses P_{rec} due to the reverse flow setting in at exit which induces pre-rotation and recirculatory flow inside the flow channels, and is most pronounced at low flows.

At the optimum flow rate, the recirculatory flow losses are normally ignored for being negligible [117], and hence the overall efficiency of the pump can be expressed in this form;

$$\eta = \eta_m \ \eta_v \ \eta_h \qquad (4.1)$$

Hydraulic losses are perhaps the most difficult ones to estimate and it is customary to assume that the total hydraulic head loss is equivalent to the difference between the input head and the actual developed head ($H_h = H_i - H$). If the volute design is such as to allow for full recovery of the dynamic energy of equation (I.5), then at the optimum point with little separation loss, the hydraulic head loss is merely frictional. If however such a recovery is not complete then part of the hydraulic losses are dynamic. If the volute is replaced by a square cavity for economical reasons, then some small pressure recovery is still possible. However, if

this small regain is ignored, then the maximum dynamic head wasted could be obtained by using equation (3.6) or;

$$H_{dyn} = H_i (1 - T_i) \qquad (4.2)$$

Paint spot check tests [42] have shown that for a pump with a square cavity replacing the volute, a strong closed recirculatory pattern of the flow could be traced behind the back shroud of the impeller near the housing well. This can be attributed to the energy dissipation of H_{dyn} (or some great part of it) which is understandably converted into uselsss flow recirculation, and is therefore a hydraulic power loss.

Volumetric losses are determined by the amount of leakage Q_L across the gaps. Because the leakage flow is coming from the highest pressure to the lowest pressure in the system, the power lost is given by $P_v = \rho g H_i Q_L$ [156]. The estimation of the leakage flow Q_L for the closed impeller is based on the modified Bernelli equation across the gap and can be represented in the following form [126, 156];

$$Q_L = C_d A_L \sqrt{2gH_L} \qquad (4.3)$$

The head change across the gap H_L can be estimated using Stepanoff's empirical formula [156];

$$H_L = 0.75 \left(\frac{u_2^2 - u_1^2}{2g}\right) \qquad (4.4)$$

Test results by Varley [174] show good agreement with equation (4.4). However, a more detailed method was proposed by Pfleiderer [126]; taking into consideration the fluid rotational velocity of the vortex between the impeller disc and casing (ω_d);

$$H_L = \frac{1}{g} \left(T_i gH - \omega_d^2 \frac{r_2^2 - r_1^2}{2}\right) \qquad (4.5)$$

ω_d is less than the rotational velocity at r_2 and for very small disc clearance it could reach half of it.

The constant C_d in equation (4.3) is a discharge coefficient of the gap, and according to Stepanoff [156], for an annular gap, it takes the form;

$$C_d = \frac{1}{\sqrt{f \frac{L}{2s} + 1.5}} \qquad (4.6)$$

L is the length of the gap, and s is the gap thickness. f is a frictional factor, which is a function of both the linear Re number through the gap and the rotational Re_ω of the liquid upstream the gap [126]. Well designed neck rings can have C_d value as small as 0.35 [156, 174].

For the semi-open impeller, the determination of Q_L is more complex because the rate of flow across the blade tip clearance is expected to be non-uniform with respect to radius. Equation (3.7) expresses the general form of energy loss due to the presence of the tip clearance for one blade. For practical purposes however, a simplified relationship like that expressed in equation (3.9) for the head reduction, the leakage flow can be also related to zero clearance flow rate [126];

$$Q_L = \alpha \lambda Q_o \qquad (4.7)$$

The proportionality factor α can be found from experiments and is normally smaller than β of equation (3.9) [106, 126, 143].

Mechanical losses in the bearing and seals contribute only to a small percentage of the input power (1 - 2%) in large pumps [156]. Losses in the stuffing box were found to be nearly a square law function of pump speed ($T \sim \omega^2$), and in the bearing it takes the form ($T \sim \omega^n$), with n between zero and one [109, 156]. Losses in the mechanical seal are a combination of friction and the effect due to the drag action of the fast rotating seal in the sealed medium [96]. Considering the frictional

resistance only*, the power losses in the seal can be presented in the form;

$$P_{seal} = r_m \times A \times f \times p \times \omega \qquad (4.8)$$

r_m is the mean radius, and A is the effective area of the sealing surface. p is the contact pressure at the sealing face and f is a friction factor depending on the shear stress produced by the hydrodynamic action of the sliding surfaces, and is therefore viscosity dependent. The friction factor is also a function of the hydrodynamic pressure and decreases with increased contact pressure [96].

Disc friction losses are produced by the vortex created in the space between the rotating pump shroud and stationary casing wall. The general equation defining the power losses to overcome these losses is given by [126, 156];

$$P_d = K\, 2\pi \int_o^r V^3\, r dr = K\omega^3 D^5 \qquad (4.9)$$

K is a factor depending on the clearance to diameter (e/d_2) ratio, on the rotational Reynolds number Re_ω and on surface roughness. Pfleiderer [126], modified equation (4.9) to accommodate these factors:

$$P_d = K_1\, \rho\, U_2^3\, d_2\, (d_2 + 5e) \qquad (4.10)$$

In this equation K_1 is a function of the rotational Reynolds number and surface roughness only. For closed impellers with a smooth machined surface for the disc, equation (4.10) takes the form [126];

$$P_d \cong 7.3 \times 10^{-4} \left(\frac{10^6}{Re_\omega}\right)^{1/6} \rho\, U_2^3\, d_2^2 \left(\frac{d_2 + 5e}{d_2}\right) \qquad (4.11)$$

---

*Most mechanical seals are situated in the flow channel of the pump and therefore prevent leakage of the liquid to the outside. In the case of the fast moving automotive pumps with pump speeds reaching 7000 rpm or more, the fluid drag on the seals is likely to be of some significance.

Stepanoff [156] plotted the constant K of equation (4.9) against Re_ω and e/d_2 ratios, using the relationships of equation (4.10) and (4.11). This plot showed that disc friction contributes to a large portion of the input power for large (e/d_2) ratios, low n_s and low Re_ω values.

Deducting the mechanical power loss P_m from the shaft power P_s will yield the input (internal) power P_i (figure 4.1). If no recirculation in the impeller channel is assumed in theory (at BEP), the input power P_i will be consumed by raising the total mount of input mass flow ρQ_i to the total input energy level gH_i, or $P_i = \rho Q_i \times g\, H_i$. Consider the mechanical efficiency as P_i/P_s, the volumetric efficiency as Q/Q_i and the hydraulic efficiency by H/H_i, then equation (4.1) will reduce to;

$$\eta = \frac{P_i}{P_s} \times \frac{Q}{Q_i} \times \frac{H}{H_i} = \frac{\rho g Q H}{P_s} \qquad (4.12)$$

The above equation is only valid if $P_i = \rho g H_i Q_i$. Tests performed by Varley [174] showed that at BEP, the calculated values of $P_i = P_s - P_m$ agree with the hydraulic input power using input head estimation according to Busemann [26], [slip factor equivalent to that of equation (3.3)], only at small discharge angles β_2 and moderate number of blades (4-6) and is normally higher than that in most other cases. Osterwalder [117] using a conventional straight inlet centrifugal pump, showed that the excess of P_i over the theoretical hydraulic value is wasted in useless circulatory flows inside the flow channel, and is only significant at low flows.

4.2 Loss Analysis and the Effect of the Tip Clearance

On figure 4.1 the power flow in the centrifugal pump is shown schematically. The mechanical losses in the bearing and seal were determined experimentally for pump J with the impeller removed and by allowing some form of circulation [29]. The results were plotted on figure 4.2 as a function of the pump speed. Making use of equation (4.8) and by using a similar frictional factor, the power losses for pumps H and K are roughly estimated and plotted on the same figure.

The disc friction losses for all pumps tested were estimated using equation (4.11) for the closed impeller with two shrouds whereby the gap dimension e taking an average value between the two shrouds. For the semi-open impeller, because of the presence of one shroud only the disc friction power losses is only half that mentioned in equation (4.11).

Volumetric losses are more difficult to estimate for the small size pumps dealt with here. For the closed impeller, the determination of the discharge coefficient C_d of equation (4.2) is uncertain, because of the absence of any wearing rings. Both pumps J and K were fitted with a closely fitted second shroud, and therefore the assumption was made to treat this close clearance as a cylindrical gap with the length $L = (r_2 - r_1)$ and a clearance s of 0.25 mm. Hence equation (4.3) could be used in conjunction with equations (4.4) and (4.6) with reasonable accuracy.

The volumetric losses for the various semi-open impellers were estimated according to equation (4.7). To obtain an expression for the zero clearance flow Q_o, a similar approach to that of H_o of equation (3.9) is applied [106];

$$Q_{opt} = (1 - \alpha\lambda)\, Q_o \qquad (4.13)$$

and by combining with equation (4.7);

$$Q_L = (\alpha\lambda/(1 - \alpha\lambda))\, Q_{opt} \qquad (4.14)$$

The proportionality factor α is less than β of equation (3.9). Some authors [126, 143] suggested that $\alpha = 0.5 - 0.75\ \beta$. From our experiments, β was found to take the average value of 1.3 for pump J and hence an average value of $\alpha = 1$ seemed to give reasonable agreement with the test results.

The hydraulic losses contribute to most of the losses at the BEP. The head losses due to the hydraulic action of the flow, which is mostly

frictional at the BEP, is defined by the difference between the input head of the impeller H_i, and the actual developed head H. The determination of H_i from the theoretical Euler head H_e is limited to the determination of the slip factor. In the last chapter it was shown for pump J that the Wiesner slip factor according to equation (3.3) is more appropriate to use over a wide range of impeller designs. The Pfleiderer slip factor according to equation (3.18) was found to give higher slip and is used for comparison in this chapter.

Head slip of the semi-open impellers is lower than that of the closed impellers of similar design. A correction factor to the head slip equivalent to that mentioned in equation (3.11) is applied.

Losses were analysed according to the above mentioned approaches for various pumps and impellers tested in the programme. On figures 4.3 and 4.4, the power breakdown for the closed impellers of pumps J and K are shown respectively. Wiesner's slip factor was used in both cases to estimate the input head H_i. The predicted total power consumption ΣP for pump J seems to approach the actual shaft power P_s near the BEP. This indicates a good agreement between the theoretical approach and the actual power consumption for this particular pump. The difference $P_s - \Sigma P$ is obviously wasted in the recirculatory flow.

As for the radial impeller of pump K, the same prediction indicates a significant difference between ΣP and P_s, which suggests a much higher rate of recirculatory flows for this particular pump. Also of significance for this impeller the exceptional high hydraulic losses due to the absence of the volute, and the high mechanical losses in the mechanical seal which consumes nearly 12% of the total input shaft power at the test speed. (This is related to an over-sized seal used for this pump).

The effect of the shroud type and tip clearance is shown on figure 4.5 for pump J. The presence of one shroud only reduces the disc friction and therefore the mechanical efficiency of the closed impeller is lower on this figure. On the other hand, the hydraulic efficiency is better with

the closed impeller. This is perhaps due to the shear forces associated with the leakage flow across the blade tip. Howard [70] found from velocity measurements on a semi-open impeller, that the flow entering the passage through the tip clearance strongly influences the secondary flow pattern, with the result of increased head slip. The volumetric efficiency is expected to be better for the closed impeller. This is only true if compared to the semi-open impeller of large tip clearance on figure 4.5. Small tip clearance seems to give better volumetric efficiency. This is mainly because of the absence of the neck rings of the closed impeller of pump J.

On figure 4.6 the various efficiencies of figure 4.5 were plotted for the BEP as function of the tip clearance ratio λ. The overall efficiency η seems to take a linear function of λ, or

$$\Delta\eta = \gamma\lambda\eta_o \qquad (4.15)$$

with $\gamma \cong 1.3$ from the figure. This means that $\gamma \cong \beta$ of equation (3.9) which is normally assumed to be true in the literature [106, 126, 143].

Results obtained with two modified impellers of pump K (figure 4.7) seems to give similar effect of the shroud to those obtained with pump J. The exceptional low hydraulic efficiency of this pump (for both impeller types) is greatly attributed to the dynamic head losses of equation (4.2) as a result of poor recovery of this head in the discharge cavity of this pump. These hydraulic losses appear in a recirculatory flow pattern behind the back shroud. Poor impeller design of pump K is another factor contributing to low η_h.

4.3 Real and Predicted Input (Internal) Power

The input (internal) power P_i is the total input power at impeller entrance, and from figure 4.1, is equal to $P_s - P_m$. This input power is necessary to raise the head energy of the total input mass flow (ρQ_i) by

an amount equal to the input energy of the impeller (gH_i). If Q_i and H_i are estimated with reasonable accuracy and with negligible recirculatory flow inside the impeller channel, then P_i will be equal to $\rho g Q_i H_i$. If however, P_i is found to be appreciably higher than $\rho g Q_i H_i$ then this power defficiency is lost in the recirculatory flow, or;

$$P_{rec} = P_i - \rho g Q_i H_i \qquad (4.16)$$

Well designed pumps using small discharge angle ($\sim 20°$) have been shown to allow good prediction of input power at the BEP, with no recirculatory flow losses present [117]. Test results by Varley [174] showed however, that the impeller geometry influences the accuracy of prediction with impellers of high β_2 giving lower predicted values at the BEP, which may suggest that impellers of lower guidance to the flow (higher β_2 or low number of blades) do produce some circulatory flows inside the impeller channel, even at the BEP.

To obtain a clear picture of the effect of impeller geometry on the predicted input power at the BEP, the actual input power, P_i, of 6 semi-open impellers of pump H were plotted on figure 4.8 against the discharge angle β_2. The predicted input power $\rho g Q_i H_i$ was estimated using the approach discussed previously, whereby both Wiesner's and Pfleiderer's slip factors were considered. The estimated values were plotted on figure 4.8. The resulting picture shows that for this particular pump, the Pfleiderer slip factor gives lower predicted input power and is perhaps safer to be applied. The discrepancy between the predicted and the actual input power seems to diminish at low β_2 values and is of significance at higher discharge angles. Also for the same discharge angle, the difference is much larger for impellers of lower number of blades. It is to be mentioned here that for this particular pump, P_{rec} of figure 4.8 do not include recirculation in the discharge cavity created by the uncontroled free vortex of the flow and which are considered to be part of the hydraulic losses P_h.

These results suggest that the recirculatory flow is somehow related to the solidity of the impeller. To demonstrate this the actual and

predicted input powers at the BEP for 6 semi-open impellers of pump J were plotted against the solidity on figure 4.9. The difference between those two power values was assumed to be consumed as recirculation power losses P_{rec}, and was plotted against the solidity on the same figure. The result seems to indicate clearly that the discrepancy between the predicted and the actual input power increases with reduced solidity of the impeller, and is negligible only for impellers of low β_2.

4.4 Scale Effect Due to Changes in Pump Speed

In comparing the performance of hydraulic machines of the same family but of different speed or size, non-dimensional groups have been developed to provide the similarity laws governing the relationship within the family. In general, it can be said that the power of any machine is dependent on the following variables;

$$P = f(Q, H, D, \rho, \mu, K, \varepsilon) \qquad (4.17)$$

By solving this equation by dimensional analysis using M for mass, L for length and T for time, it will result in the following non-dimensional relationship [40];

$$\frac{P}{\rho\omega^3 D^5} = f\left[\left(\frac{Q}{\omega D^3}\right);\ \left(\frac{gH}{\omega^2 D^2}\right);\ \left(\frac{\mu}{\rho\omega D^2}\right);\ \left(\frac{K}{\rho\omega^2 D^2}\right);\ \left(\frac{\varepsilon}{D}\right)\right] \qquad (4.18)$$

or simply;

$$\lambda_p = f(\phi_p, \psi_p;\ Re, Ma;\ \varepsilon/D) \qquad (4.19)$$

The Mach number Ma can be ignored for incompressible liquids and therefore if ε/D is kept constant, similarity can be achieved if Re number is high in the turbulent region. This implies that for any particular λ_p there exist similar ϕ_p and ψ_p for the whole range of pumps of the same

family, and therefore if these coefficients are known for one particular pump (model), the performances of other pumps of similar hydraulic design can be easily predicted.

Similarity laws are based on the assumption that the pipe Reynolds number Re and relative roughness ε/D have no significant effect on the general pump performances. In reality however, Re increases with size and speed and for the same roughness ε, ε/D decreases with size. These in effect tend to push the flow higher in the turbulent region with a decreasing friction factor. Hence an improvement of performance (higher H and Q and lower P_s) is expected with increase in N and D. These are termed scale effects, and are usually small for water, because Reynolds number for water is usually very high [40].

In figures 4.10 and 4.11 the non-dimensional flow parameters at different pump speeds are shown for pump J and H respectively. Pump J of relatively reasonable design seems to follow the similarity concept only at speeds over 4000 rpm. Below that, significant scale effects in λ_p and ψ_p appear which reduce the pump efficiency considerably. Pump H of poorer hydraulic design shows some sign of similarity with respect to ψ at high speeds. However, the similarity with regard to λ_p (and η) is hardly obtainable even at speeds as high as 6000 rpm.

The reason behind these large scale effects are apparently very high mechanical and hydraulic losses which can be in some sort R_e dependent but at different rate [12, 111, 156]. Defining the scale-up losses by the following;

$$\delta = \frac{P_s - P_{hyd}}{P_s} = 1 - \eta \qquad (4.20)$$

then the Hutton formula [72] can be applied to obtain a first hand approximation;

$$\frac{\delta}{\delta_m} = (1 - C) + C \left(\frac{Re_m}{Re}\right)^{\frac{1}{f}} \qquad (4.21)$$

The terms δ and δ_m refer to hydraulically smooth prototype and model respectively. C is the portion of the losses which are considered to be caused by skin friction effect and is therefore Re number dependent. (1 - C) is the portion caused by inertia or diffusion losses and these are assumed to remain unchanged within the family [111]. The value of C is an experimental one in the range 0.5 - 1.0. For well designed, high efficiency pumps, it takes the value of 0.7 - 0.76 [74, 117]. The frictional factor f is accepted to take the value of $\sim$ 5 [74, 111].

Osterwalder [117, 118] analysed the scale-up losses in a more simplified way by summing up all type of losses but excluding those in the bearing and seals, or;

$$\delta' = \delta_h + \delta_d + \delta_v + \delta_{rec} \qquad (4.22)$$

Nixon and Cairney [111] neglected the indeterminate recirculating losses part δ_{rec} at the BEP and related all three remaining types of losses as functions of the Reynolds number. Fay [45] assumes this component loss to take the general form corresponding to equation (4.21);

$$\delta_i = K_i + F_i \left(\frac{Re_m}{Re}\right)^{\frac{1}{f_i}} \qquad (4.23)$$

$$i = 1, \ldots, n$$

For the hydraulic losses δ_h, f_i takes the value 5 - 6 as before [118]. For the disc friction K_i is zero and f_i varies between 5 and 6 [111, 126]. As for the volumetric losses δ_v, Nixon and Cairney [111] found from their own experience that contrary to the hydraulic and disc friction losses, the volumetric losses increase with increased Re number, with f_i ranging between -13 and -19 for the closed impeller. Similar results were obtained by Osterwalder [117].

Applications of equations (4.21) and (4.23) for the small centrifugal pumps when operated at different speeds is of no practical use, because they involved constants which are very difficult to estimate, if one bears

in mind the additional shock and recirculation losses which are to be considered. A further complication arises from the fairly rough surface ($\sim$ 10 μ) of the cast iron impeller and casing of pumps H and J, which necessitate a correction factor for these two equations [45], (see section 4.6).

A more appropriate way of thinking is to find the scale effect associated with the various losses defined by equations (4.20) and (4.22). If the minimum power coefficient at the higher speed and Re number is used as a reference, then a scaling factor δ_λ for other pump speeds can be obtained from the following expression;

$$\delta_\lambda = \frac{\lambda_p - \lambda_{pmin}}{\lambda_{pmin}} \qquad (4.24)$$

In table 4.1, the scaling factor for pump H and K are estimated with reference to the power coefficient at 6000 rpm. Three types of power coefficients were used in this table. The first λ_p corresponds to the total input shaft power P_s (and therefore to δ). The second λ_p' corresponds to the input power p_i after deducing all mechanical losses including those due to disc friction from P_s. The third λ_p'' is that corresponding to the predicted input power $Q_i p_i$. On figure 4.12 the scale effects of table 4.1 are plotted against pump speed.

The most striking thing to realise from this figure is the exceptionally high scale effects based on the total losses in the pump as shown by the upper curve. This is especially pronounced with the smaller diameter pump H. Removing the mechanical scale effect (including the disc friction) brings the scaling factor within reasonable limits for the closed impeller pump K, which means that the mechanical losses are perhaps mainly responsible for the large scale effects of this pump, and in the range of pump speeds tested. Pump H, on the other hand, although giving less mechanical scale effects because of the ommission of one shroud which helps to cut down on the disc friction, it appears that still high scale effects are present and to be reckoned with.

Applying the predicted input power $Q_i P_i$ as the scaling power (section 4.3) seems to remove all scale effects for both pumps in the range of speeds tested with reasonable accuracy. Following the assumption of equation (4.16), the scale effects appearing between the two lower curves of figure 4.12 are those due to the recirculatory flow losses. These losses seem to be of much more significance with pump H and rather less important with pump K. The explanation is found from figure 4.13, where recirculation power losses were estimated at different speeds as a percentage of the total shaft power for both pumps. Here it appears that δ_{rec} is larger for pump K, but it remains relatively constant over the whole pump speed range. For pump H on the other hand, δ_{rec} increases almost three-fold in going from a pump speed of 6000 to 4000 rpm, and therefore a significant scale effect is produced.

From figures 4.12 and 4.13 it can be therefore concluded that for the small size high speed centrifugal pumps, scale effect due to the hydraulic losses δ_h (including the dynamic losses in the discharge cavity), and volumetric losses δ_v are only minor in the pump speed range 3000 - 6000, which is a reasonable assumption to make, because Re_ω number is quite high ($Re_\omega = 0.5 \times 10^6$ to 1.0×10^6), and therefore the scale-up losses are mainly those due to mechanical (including disc friction) and due to recirculatory flow inside the pump channels, or;

$$\delta_\lambda \cong \delta_m + \delta_{rec} \qquad (4.25)$$

4.5 Liquid Viscosity Scale Effects

For the same pump diameter, changes in the Re number can be as a result of changes in the flow velocity which is related to pump speed, or due to changes in the viscosity of the circulated liquid.

The effect of pump speed on pump performance was discussed in the previous section. Large scale effects were evident, which are partly attributed to Re number dependent losses. Hence changes in the liquid

viscosity are expected to yield similar scale effects, although of a different nature.

Consider first the effect of the fluid viscosity on the performance of pump K with both the closed and the semi-open impeller. On figure 4.14, the viscosity is reduced $\sim$ 10 fold by increasing the liquid temperature (in this case 50/50 EG/W) from 20° to 120°C. The test was performed at the same flow velocity so that the Re number is viscosity dependent only.

The general feature of the resultant curves (ψ_p and η) seem to indicate a decline in pump performance with increased viscosity, which is in line with the general viscous effect theory [61, 110, 156]. On the other hand, there seems to be a certain optimum viscosity below which the pump performance shows some sign of decline (part AB on the efficiency curves of figure 4.14). Some earlier results by Stepanoff [156] suggest that a slight increase of liquid viscosity helps to suppress the re-circulatory flow in the pump channel. An improved hydraulic friction factor inside the turbulent flow region was also found to be responsible [119].

If one pump (model) is operating with varying Re number due to changes in viscosity, then the value of the constant C of equation (4.21) is likely to change according to the following relationship [45];

$$(1 - C_1)\ \delta_1 = (1 - C_2)\ \delta_2 \qquad (4.26)$$

Results obtained by Stepanoff [156] for 9 pumps working on a wide range of viscosities showed that C_2 of the viscous liquid can reach a value of 0.9 or more, compared to $C_1 = 0.75$ for water. Applying similar value of C_1 to point B in figure 4.14, then for 2% drop in the overall efficiency at point C, the value of C_2 becomes $\sim$ 1% higher than that of C_1.

Further examination of the viscosity effect was performed on pump J with a closed and a semi-open impeller operated with water and 50/50 EG/W

at different temperature. The results are shown on figure 4.15, whereby the flow coefficient is kept constant near the BEP for each impeller, and therefore the Re number is viscosity dependent only.

A similar trend can be established here to that observed with pump K, although the increase in liquid viscosity produces less significant performance drops. As a matter of fact, the head coefficient of the closed impeller is improving throughout the viscosity range. This may be attributed to the better hydraulic design of this pump.

From figure 4.15 it is also worth mentioning that since 50/50 EG/W mixture at 90°C has similar viscosity to that of cold water ($\sim$ 0.8 cP), pump J's performance is likely to be similar for both conditions. In fact test results showed that in almost all cases 50/50 EG/W at 90°C produces higher H and η than cold water for the same flow rate and pump speed; a phenomenon also found to be true by previous investigators [42, 57].

A better understanding of the viscous effect on pump J is, by plotting the various scaling losses of equations (4.20) and (4.22) as a function of the viscosity. This is done on figure 4.16 for the shrouded impeller, and on figure 4.17 for the semi-open impeller. Test results are also listed in table 4.2

As for the closed impeller, the hydraulic losses δ_h seems to reduce with increased viscosity, obviously due to improved generated head. The disc friction δ_d increases steadily with viscosity. The volumetric losses δ_v is remaining almost constant and cannot be expected to change significantly over the range of viscosities encountered here. The fall of δ at a viscosity of 1 m^2/sec can be thus related to both improved δ_h and δ_{rec}. Further increase in viscosity will render the improved δ_h less effective against rising δ_{rec} and δ_d, with the result of reduced overall efficiency.

This is especially pronounced for the semi-open impeller of figure 4.17. Here, the improvement in δ_h is only slight. On the other hand, both δ_{rec} and δ_d increase steadily with increased viscosity, with the result of a minor drop in δ at point B.

Losses in the mechanical seal were assumed to remain nearly constant over the range of viscosities tested and therefore they were not included in figures 4.16 and 4.17. In reality however, the increase in liquid viscosity is likely to increase the sealing film thickness with improved hydrodynamic and cooling action of the seal, and therefore some improvement in the power consumption is expected [96]. Some experimental results on a coolant pump seal [57] seem to confirm this concept.

4.6 Surface Finish Effect

The hydraulic losses within the pump are a combination of skin friction, shock and diffusion losses [156]. Skin friction losses δ_f caused by surface drag on fluid in the impeller passages and volute casing are known to depend upon pipe Reynolds number under certain flow conditions. Nixon and Cairney [111] put it in the form;

$$\delta_f = C_f W^2 \qquad (4.27)$$

where W is the relative velocity and C_f is a function of pipe Re number and surface roughness.

Nixon and Cairney found from their extensive studies on centrifugal pump scale losses, that for the disturbed flow in an impeller, C_f is likely to remain independent of pipe R_e number for considerably lower values of R_e than for a flat plate. The stage where a strong dependence of C_f on R_e number is obtained at;

$$Re_{crit} \simeq 25 \frac{\ell}{\varepsilon} \qquad (4.28)$$

where ℓ is the length of the blade and ε is the surface roughness. Below the critical Re of equation (4.28) the skin friction is likely to be influenced by Re, otherwise it will be solely a function of ℓ/ε.

The effective surface roughness takes the form [99];

$$\varepsilon = K \frac{\nu}{W} \qquad (4.29)$$

The range of K for the transitional flow in an impeller is K = 28 - 224. Below this range the flow regime is smooth and above it, it is fully rough and therefore C_f becomes independent of Re.

For the random type of finish (no grain in any particular direction), such as for cast or well-polished surfaces, the effective roughness takes the value [111];

$$\varepsilon = 1.7\ \varepsilon_{CLA} \qquad (4.30)$$

where ε_{CLA} is the surface roughness of the impeller, as measured on the Talysurf machine.

Talysurf test values for the impeller passages gave an approximate value of 8 - 9 μm for the cast iron impellers of pumps H and J and about 2 μm for the pressed sheet metal impeller of pump K (because of other irregularities produced by the pressing procedure, this figure cannot be expected to be representative for the surface roughness of this impeller, ε is likely to be higher).

Using ε_{CLA} of ∿ 9 μm, equation (4.29) was applied for the closed impeller of pump J at the BEP. In table 4.3, the results are listed for water and 50/50 EG/W mixture at 2 temperatures each.

From this table it is possible to conclude that in the range of viscosities and pump speeds tested, pump J operates in or close to the transitional flow regime. Since ε does not exceed the upper limit of 224 ν/W, fully rough flow is never obtained for this impeller in the normal operating range, and hence C_f (and δ_f) are likely to depend on Re number.

Since the hydraulic scale loss δ_h is mainly frictional at the BEP and since δ_f was found to be Re number dependent, the decrease in δ_h for pump J for both the closed and the semi-open impeller, with increased viscosity (figures 4.16 and 4.17) cannot be explained in this context.

Other factors such as reduced secondary flows inside the flow channel with reduced head slip may be operative here.

A strong Re number effect was found to influence the developed head of all pumps tested at pump speeds below 3000 rpm (see figures 4.10 and 4.11). Pump H has a measured surface roughness ε_{CLA} of $\sim$ 8 μm and therefore ε is 13.6 x 10^{-6}. At 3000 rpm the upper range of the transitional flow regime is 288 x 10^{-6} for cold water, and therefore a strong Re number dependency of C_f (and δ_h) is expected with a pronounced influence on the developed head.

Similar Re number influence with pump speed were found also on several other small size pumps tested in the Department of Mechanical Engineering [42, 57, 99].

4.7 Cordier Correlations

The flow coefficient ϕ and the head coefficient ψ of the hydraulic machines are of major importance for the determination of similarity in the same family. For simplicity, they appear in equation (4.19) expressed in terms of the external characteristics of the pump and were given the suffix p; or

$$\phi_p = K_1 \phi = \frac{Q}{\omega D^3} \qquad (4.31)$$

and

$$\psi_p = K_2 \psi = \frac{gH}{\omega^2 D^2} \qquad (4.32)$$

By manipulating equations (4.31) and (4.32) for the diameter D and the angular speed ω, Cordier [36] obtained the following relationships;

$$D = (gH)^{-1/4} \; Q^{1/2} \; \psi_p^{1/4} \; \phi_p^{-1/2} \qquad (4.33)$$

$$\omega = (gH)^{3/4} \; Q^{-1/2} \; \psi_p^{-3/4} \; \phi_p^{1/2} \qquad (4.34)$$

Denoting the non-dimensional products $\psi_p^{1/4} \; \phi_p^{-1/2}$ by the specific diameter Δ and $\psi_p^{-3/4} \; \phi_p^{1/2}$ by the specific speed (n_s), we obtain;

$$\Delta = \frac{D \; (gH)^{1/4}}{Q^{1/2}} \qquad (4.35)$$

$$n_s = \frac{\omega \; Q^{1/2}}{(gH)^{3/4}} \qquad (4.36)$$

Both Δ and n_s are functions of ψ_p and ϕ_p and hence the similarity concept implies that hydraulic machines of the same family have the same Δ and n_s values and therefore the same efficiency at the BEP.

Cordier [36] plotted the Δ - n_s relationship for various hydraulic machines with the result of the optimum points falling on a narrow band, thus allocating a locus for other machines in the same range of n_s and Δ. Thew [166] replotted some more results obtained by other authors [11, 38, 144], on the same non-dimensional basis and found that these results agree well with the Cordier results especially at lower n_s values (radial impeller range).

On figure 4.18, the BEP of several small size commercial pumps tested in the Department of Mechanical Engineering, including those of the present research are plotted on the n_s - Δ scale. Here it can be seen that most of the points lie outside the Cordier band, and in fact only pump J is well inside it. Drawing iso-efficiency curves parallel to the Cordier plot and corresponding to the measured overall efficiencies, will show that the farther away from the Cordier locus, the less efficient these

pumps become. This seems to agree with Balje's [12] approach for efficiencies within a certain range of machines.

As for the same machine diameter and speed, the application of the n_s - Δ correlation was shown to give some marginal discrepancies [178]. Some differences, although of different nature, were also found for the 3 pumps tested in this research, which can be attributed to changes in pump geometry.

On figure 4.19, two different geometrical factors seem to influence the locations of the BEP with regard to the Cordier locus. The first is the effect of the discharge angle β_2, whereby decreased β_2 seems to push the BEP away from the locus, in a vertical direction to it. The second is the effect of the type of shroud, whereby the introduction of a second shroud helps to push the BEP up along the Cordier locus. In both cases these shifts are associated with some changes in the overall efficiency of the pump.

The effect of the discharge angle β_2 for pump J is further investigated on figure 4.20. Both Δ and n_s are decreasing with increased β_2. However, the rate of change in the specific diameter with respect to the discharge angle $d\Delta/d\beta_2$ is less than that of the specific speed $dn_s/d\beta_2$, thus pushing the BEP of smaller β_2 away from the Cordier locus. (Scatter on Cordier original plot is high and therefore the dislocation of the BEP of the test pumps is only considered because it provides a consistent trend with respect to impeller geometry).

From the definitions of Δ and n_s of equations (4.33) and (4.34) their ratio can be expressed for a certain range of machines by;

$$\frac{\Delta}{n_s} = \frac{\psi_p}{\phi_p} \qquad (4.37)$$

In figure 4.20 the ratios ψ_p/ϕ_p for the various impellers of pump J were plotted against discharge angle β_2. In table 4.4 these ratios are listed for nearly all pumps and impellers tested in the programme. For

the semi-open impellers of pump J and H the influence of increased discharge angle is to increase ψ_p/ϕ_p, a feature which is clearly indicated on figure 4.20. This increase in ψ_p/ϕ_p is accompanied by a similtaneous shift of the BEP towards the centre of the Cordier locus (figure 4.19).

Since ψ_p/ϕ_p is indicative of the ratio of the energy transfer to the volume transfer through the pump, then for the same pump diameter the increase in ψ_p/ϕ_p means a higher energy transfer ratio per unit volume. This in turn means a better utilization of the pump diameter for the duty it performs and therefore the shift towards the optimum BEP locus on the Cordier diagrams can be interpreted as a result of that improved utilization.

Better diameter utilization, on the other hand, does not necessarily mean higher pump overall efficiency. This is because the latter is likely to improve with reduced discharge angle β_2 due to improved hydraulic performance and reduced head slip. Therefore ψ_p/ϕ_p and η do not appear to act in the same direction on figure 4.20. This is also true for pump H in table 4.4.

4.7 Concluding Remarks

The overall efficiency of the centrifugal pump is very much a function of size and flow rate. Pumps of low specific speed, i.e. high developed head at comparatively low flows, are known to produce low efficiencies as compared to pumps of high specific speed and flow rates. In this research the efficiencies of 3 small, automotive type centrifugal pumps were studied, and the several scale effects with respect to pump speed and fluid viscosity investigated. Results discussed in detail in this chapter are summarized below.

1. The volute type pump J produces an overall efficiency of about 50% which is reasonable enough for a specific speed of $\sim$ 0.6 and a flow rate of 300 L/min. Pumps H and K on the other hand, barely produce an efficiency of $\sim$ 20%. High hydraulic losses associated with the poor impeller, inlet pipe and discharge cavity design contribute to this low efficiency of energy transfer. The disappearance of a proper volute does not give these 2 pumps

the ability to convert the dynamic head of the discharging vortex fully into useful static head. In effect most of this dynamic head is wasted in the discharge cavity as a useless circulation.

2. Closed impellers were shown to give slightly higher overall efficiency than their semi-open counterpart. Increasing the tip clearance for the semi-open impeller of pump J in the range 0.25 to 1.5 gave a proportional decrease in the overall efficiency according to $\Delta\eta = \gamma\lambda\eta_o$. The proportionality factor λ was found to take the approximate value of ~ 1.3, which is similar to the proportionality factor β for the head drop with respect to tip clearance changes.

3. In the absence of any unidentified losses the actual input power $P_i = (P_s - P_m)$ should be equal to the predicted input power found from the expression $\rho g Q_i H_i$. Using slip factors according to equations (3.3) and (3.18), the predicted input power was estimated for both pumps H and J using 6 semi-open impellers of different design for each pump. The comparison of the predicted to the actual input head showed that P_i is most of the time higher than the predicted value and the difference increases with increased β_2 and decreased number of blades. In the absence of further information the difference $P_i - \rho g Q_i P_i$ is expected to be wasted by liquid recirculation inside the impeller channel. Using the solidity concept, it is possible to show for pump J using different impeller geometries, that this recirculatory flow losses P_{rec} tend to increase with reduced impeller geometry (corresponding to reduced guidance).

4. Power scale effects due to changes in pump speed were found to be quite significant for the small size pumps. These scale effects could not be simply related to Re number effect but rather to exceptionally high losses, which are in turn more or less Re number dependent. By analysing the various losses involved in the scaling procedure of pumps H and K, it was possible to establish that in the speed range 3000 - 6000 rpm, scale effects are mainly due to mechanical losses including those in the disc friction, and due to high recirculation losses in the impeller channel. The latter being especially pronounced for pump H.

5. Fluid viscosities were found to influence the overall efficiency in two directions. A slight increase in viscosity from $\sim$ 0.3 to 0.7 cP seems to produce some improvement in the overall efficiency of nearly all pumps tested. Further increase on the other hand produces an opposite effect with the overall efficiency on the decline again. Scale effect analyses for pump J suggest that a combination of improved head generation and reduced recirculatory flow may be responsible for the improvement in η at $\sim$ 0.8 cP.

6. Analysing the frictional hydraulic losses as function of pipe Re number and relative roughness it was possible to show that for measured surface roughness of the cast iron impellers of pumps J and H, the flow regimes are transitional and therefore fully rough flows are not achieved for the operating flows of these pumps. Hence frictional losses are expected to be Re number dependent. This is much more pronounced at speeds below 3000 rpm with a pronounced scale effect on generated head.

7. $\Delta - n_s$ correlations for several small size centrifugal pumps showed that the BEP plots on the diagram produce much higher scatter than that established by Cordier. Examination of the BEP plots suggests that the lower the pump efficiency, the further away the BEP is located with respect to the optimum range of the Cordier locus.

8. The location of the BEP of the pump on the Cordier diagram was found to be marginally influenced by the impeller geometry. However a consistent trend could be established for all impellers tested with respect to changing Δ/n_s ratio according to

$$\frac{\Delta}{n_s} = \frac{\psi_p}{\phi_p}$$

For pump J, an increase in β_2 from 30 to 70° produces a simultaneous increase in ψ_p/ϕ_p of about 20% (figure 4.20) with the result of the BEP location moving closer to the centre of the Cordier locus. Similar trend

could also be found from tests on pump H. From this it is reasonable to assume that for the same pump diameter, an increase in ψ_p/ϕ_p means a better head generation per unit volume flow, and hence an optimization of the pump diameter is achieved, thus bringing the BEP nearer to the optimum range on the Δ - n_s diagram.

TABLES 4.1 to 4.4

FIGURES 4.1 to 4.20

Table 4.1 Power scale effect at $\sim Q_{bep}$

	rpm	Q l/min	Q_i l/min	H_i (meter)	P_s (Watt)	P_m (Watt)	λ_p		$\lambda_{p'}$		$\lambda_{p''}$		
							$\frac{P_s}{\rho\omega^3 D^5}$	δ_λ (%)	$\frac{P_i}{\rho\omega^3 D^5}$	δ'_λ (%)	$\frac{Q_i P_i}{\rho\omega^3 D^5}$	δ''_λ (%)	
Pump K $\phi_p = 0.0084$	6000	100.0	111.0	29.2	855	112.4	0.00229	0	0.00200	0	0.00151	0	Ref.
	5000	83.0	92.0	20.8	511	76.3	0.00237	3.5	0.00201	0.5	0.00150	-0.6	
	4000	66.4	73.7	13.3	275	49.4	0.00250	9.2	0.00204	2.0	0.00150	-0.6	
	3000	49.8	55.3	7.5	129	29.0	0.00277	20.1	0.00215	7.5	0.00150	0	
Pump H $\phi_p = 0.0154$	6000	105.3	113.0	19.4	493	96.8	0.00332	0	0.00267	0	0.00249	0	Ref.
	5000	87.6	93.8	13.5	309	68.0	0.00359	8.1	0.00280	4.7	0.00248	-0.6	
	4000	69.6	74.2	8.6	178	45.3	0.00405	22	0.00302	12.8	0.00244	-2.0	

$$\delta_\lambda = \frac{\lambda_p - \lambda_{pmin}}{\lambda_{pmin}}$$

Table 4.2 Viscosity scale-up losses of pump J*

	Liquid	Temp °C	ν (x 10^{-6}) m^2/sec	ψ_p	η (%)	δ_h (%)	δ_v (%)	δ_d (%)	δ_{rec} (%)	δ' (eq 4.22) (%)
Closed impeller ϕ = 0.014	50/50 EG/W	30	2.99	0.1090	49.6	31.8	4.0	4.1	7.4	47.3
		95	0.75	0.1069	50.4	34.0	4.1	3.4	4.8	46.3
	Inhib. Water	25	0.898	0.1065	49.7	33.8	4.1	3.4	5.7	47.0
		95	0.312	0.1035	48.5	35.4	4.1	2.9	5.6	48.0
Semi-open impeller ϕ = 0.0116	50/50 EG/W	25	3.35	0.1035	45.9	29.9	5.6	2.4	12.8	50.7
	Inhib.	28	0.843	0.1049	46.7	29.4	5.6	1.9	12.6	50.7
	Water	95	0.312	0.1035	46.7	30.5	5.7	1.6	11.6	49.4

*Impeller J-8-48 at 4500 rpm.

Table 4.3 Flow regime in pump J

Closed impeller J-8-48, Q = 280 L/min, pump rpm = 4500, W ∿ 2 m/sec, ℓ ∿ 0.02m, ε_{CLA} ∿ 9 μm

Liquid	Temperature (°C)	Viscosity ν (m^2/sec)	Re = ($W\ell/\nu$)	ε (transitional range) = $(28 - 224)\frac{\nu}{m}$ (m)	$\varepsilon = 1.7\ \varepsilon_{CLA}$* (m)
50/50	30	3×10^{-6}	0.013×10^{6}	$41 - 334 \times 10^{-6}$	15.3×10^{-6}
EG/W	95	0.75×10^{-6}	0.05×10^{6}	$10.5 - 84 \times 10^{-6}$	15.3×10^{-6}
Inhibited	25	0.9×10^{-6}	0.044×10^{6}	$126 - 101 \times 10^{-6}$	15.3×10^{-6}
Water	95	0.31×10^{-6}	0.31×10^{6}	$4.3 - 35 \times 10^{-6}$	15.3×10^{-6}

*ε_{CLA} is the surface roughness of the impeller as measured on the Talysurf machine.

Table 4.4 Pump parameters for similarity predictions.

Pumps H and K at 6000 rpm, Pump J at 4500 rpm.

Impeller	Q_{opt} L/min	H (metres)	D_2 (mm)	N (rpm)	η %	η_s	Δ	ψ_p/ϕ_p
J-8-70	290	22.4	90.0	4500	49.8	0.574	4.98	6.68
J-8-48 cl	280	19.6	90.0	4500	50.9	0.623	4.91	5.93
J-8-48*	250	19.0	90.0	4500	49.4	0.603	5.15	6.69
J-8-30	230	17.3	90.0	4500	50.4	0.620	5.25	5.72
J-6-70	280	21.8	90.0	4500	48.8	0.576	5.04	7.06
J-6-50	260	19.6	90.0	4500	48.1	0.601	5.09	6.57
J-6-38	240	17.6	90.0	4500	50.2	0.626	5.16	6.19
H-8-90	105	5.6	56.6	6000	20.3	1.303	3.68	2.16
H-8-60	100	5.3	56.6	6000	20.5	1.325	3.72	2.10
H-8-40	96	5.0	56.6	6000	20.7	1.356	3.75	1.87
H-6-90*	101	5.2	56.6	6000	18.4	1.351	3.67	2.23
H-6-60	100	5.2	56.6	6000	20.0	1.344	3.71	2.17
H-6-40	98	4.8	56.6	6000	19.9	1.413	3.67	1.92
K-6-90 cl	100	9.7	68.0	6000	19.1	0.842	5.20	3.41
K-6-90 so	80	9.7	68.0	6000	17.3	0.753	5.80	4.12

* Standard impeller.

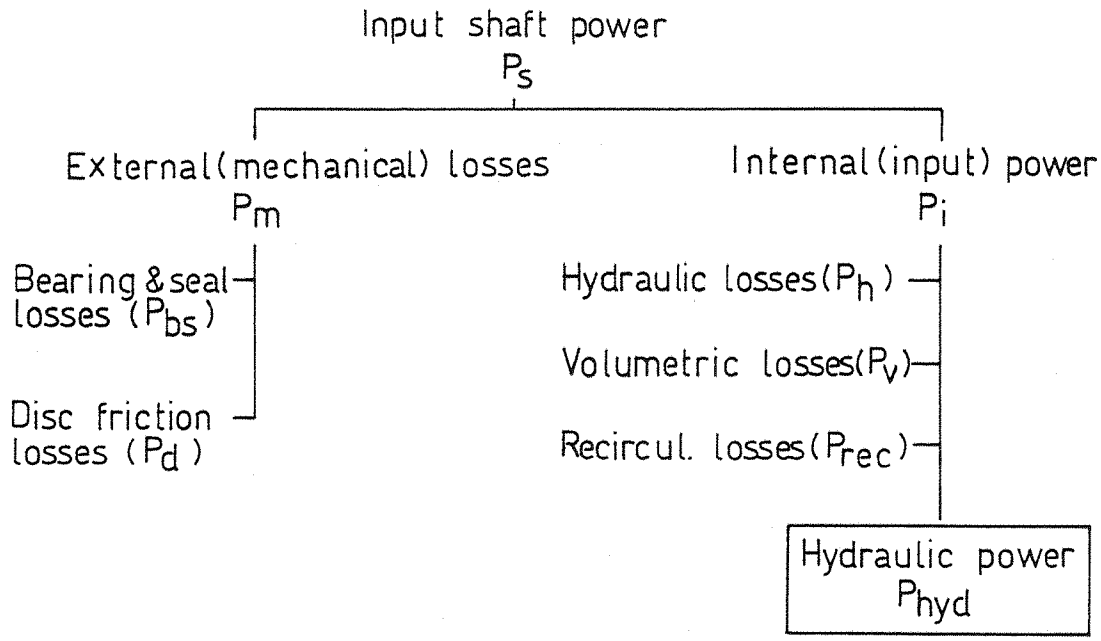

Fig. 4.1 Power flow inside the centrifugal machine

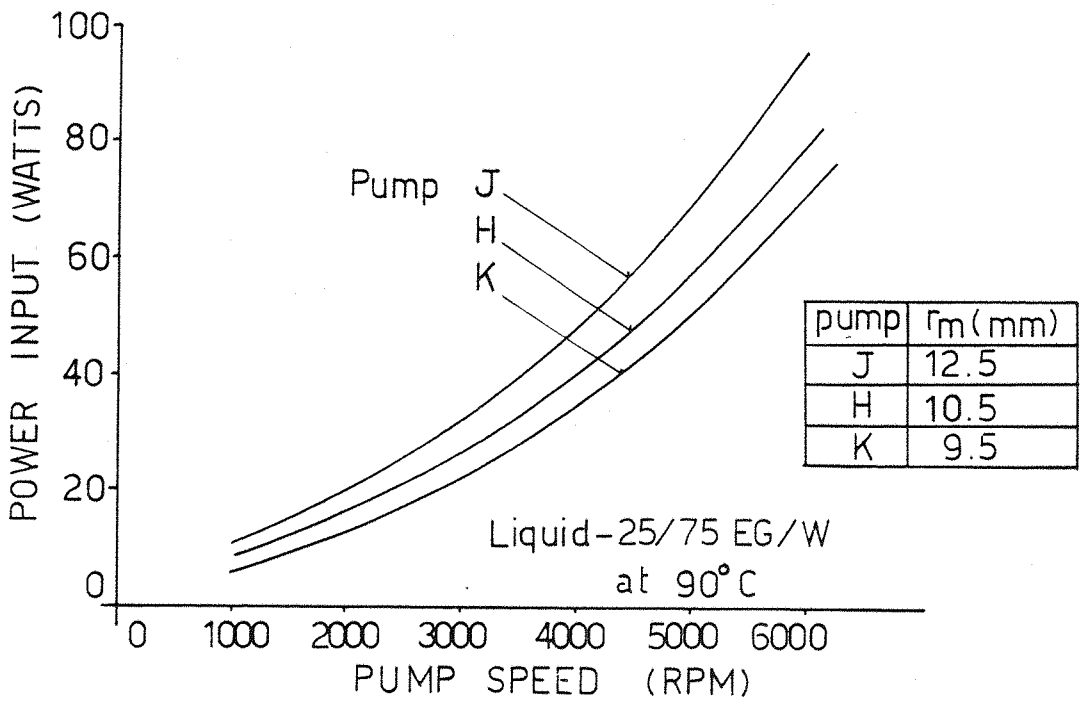

FIG 4.2 POWER CONSUMPTION IN THE MECHANICAL SEALS AND BEARINGS OF 3 SMALL PUMPS

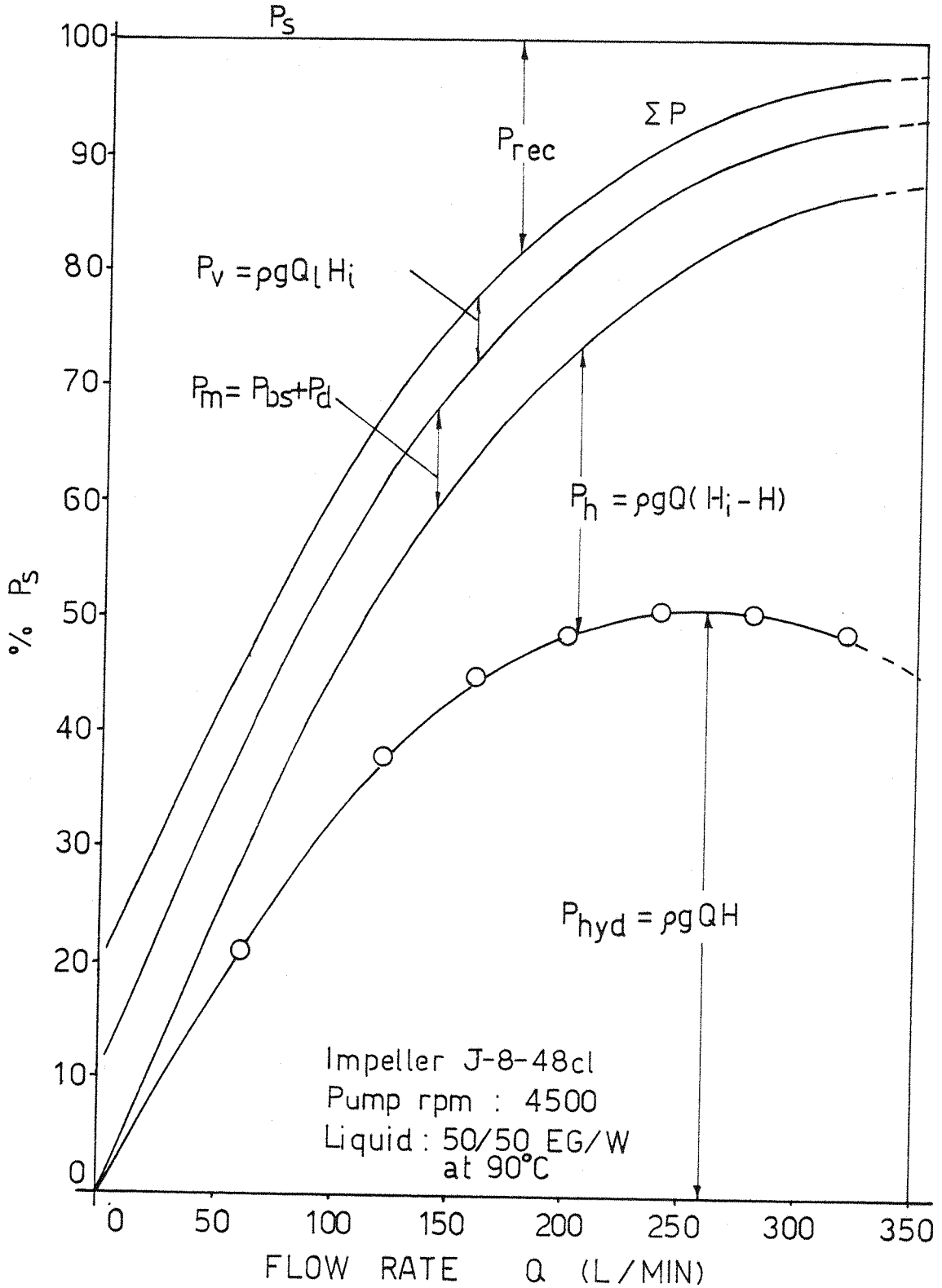

FIG 4.3 POWER BREAKDOWN FOR PUMP J WITH THE SHROUDED IMPELLER

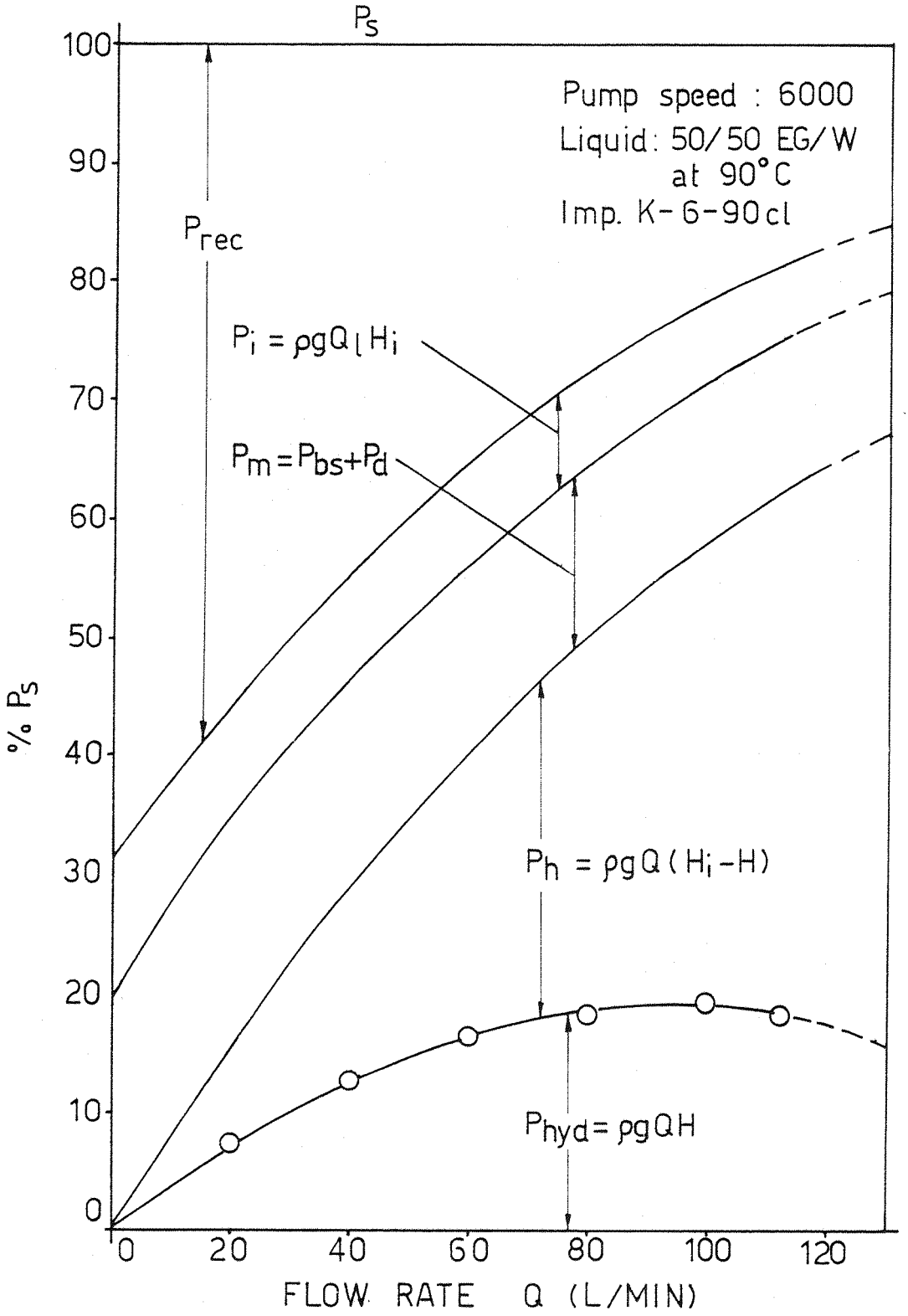

FIG. 4.4 POWER BREAKDOWN FOR PUMP K WITH THE SHROUDED IMPELLER

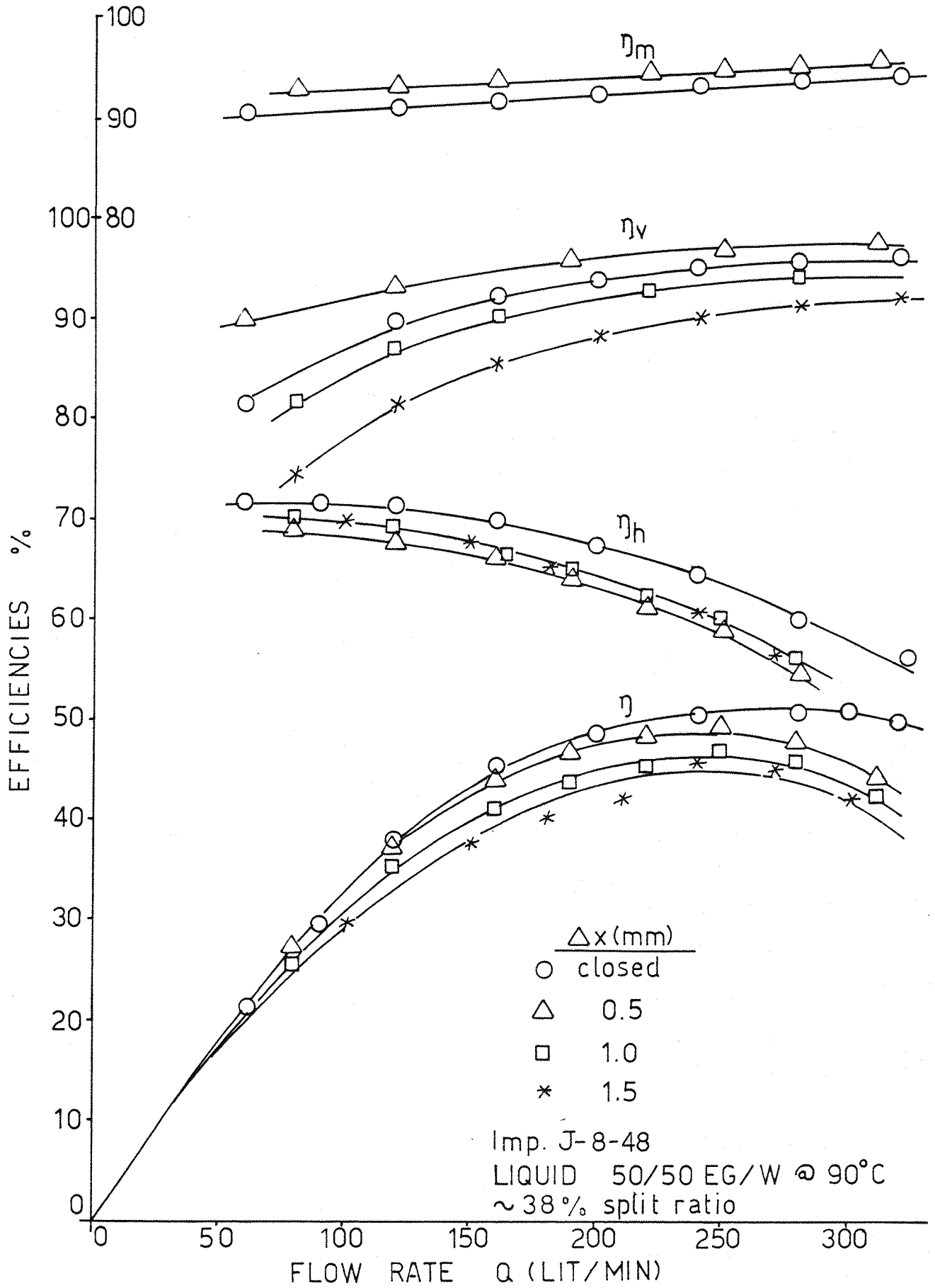

FIG. 4.5 THE EFFECT OF THE TYPE OF SHROUD AND THE TIP CLEARANCE DIMENSION ON THE VARIOUS EFFICIENCIES OF PUMP J

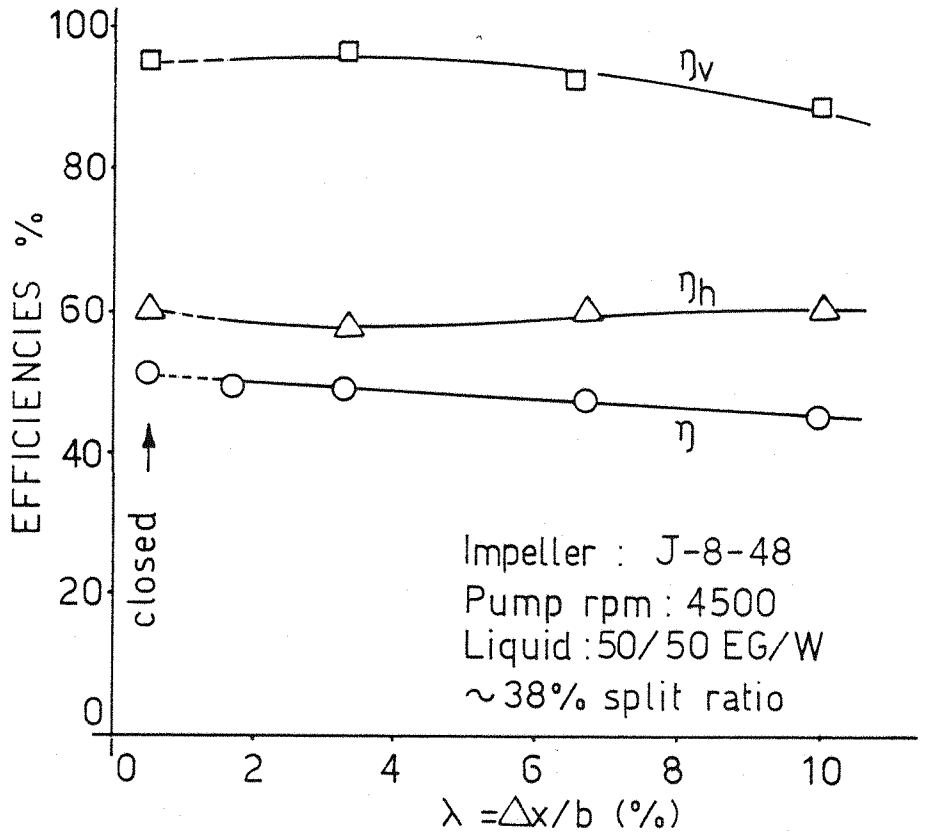

FIG 4.6 TIP CLEARANCE EFFECT ON THE EFFICIENCIES OF PUMP J

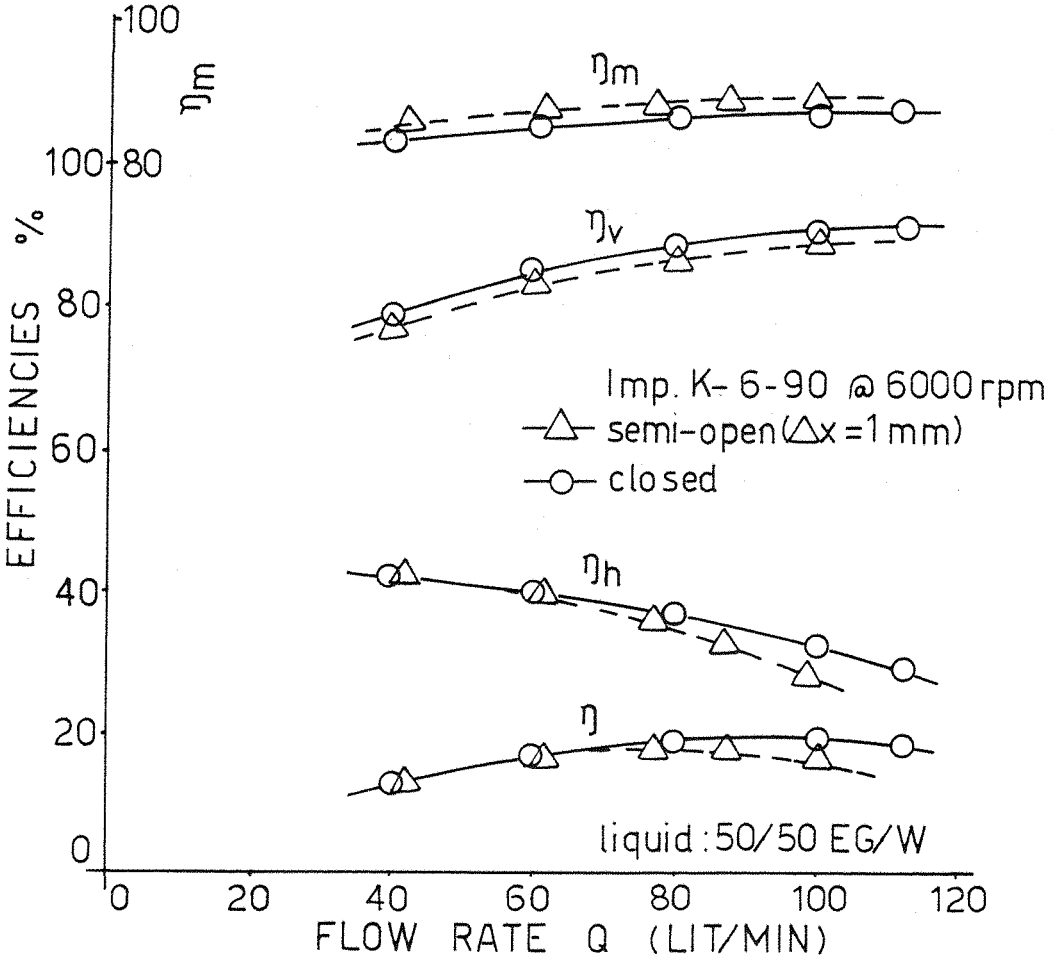

FIG 4.7 THE INFLUENCE OF THE TYPE OF SHROUD ON THE EFFICIENCIES OF PUMP K

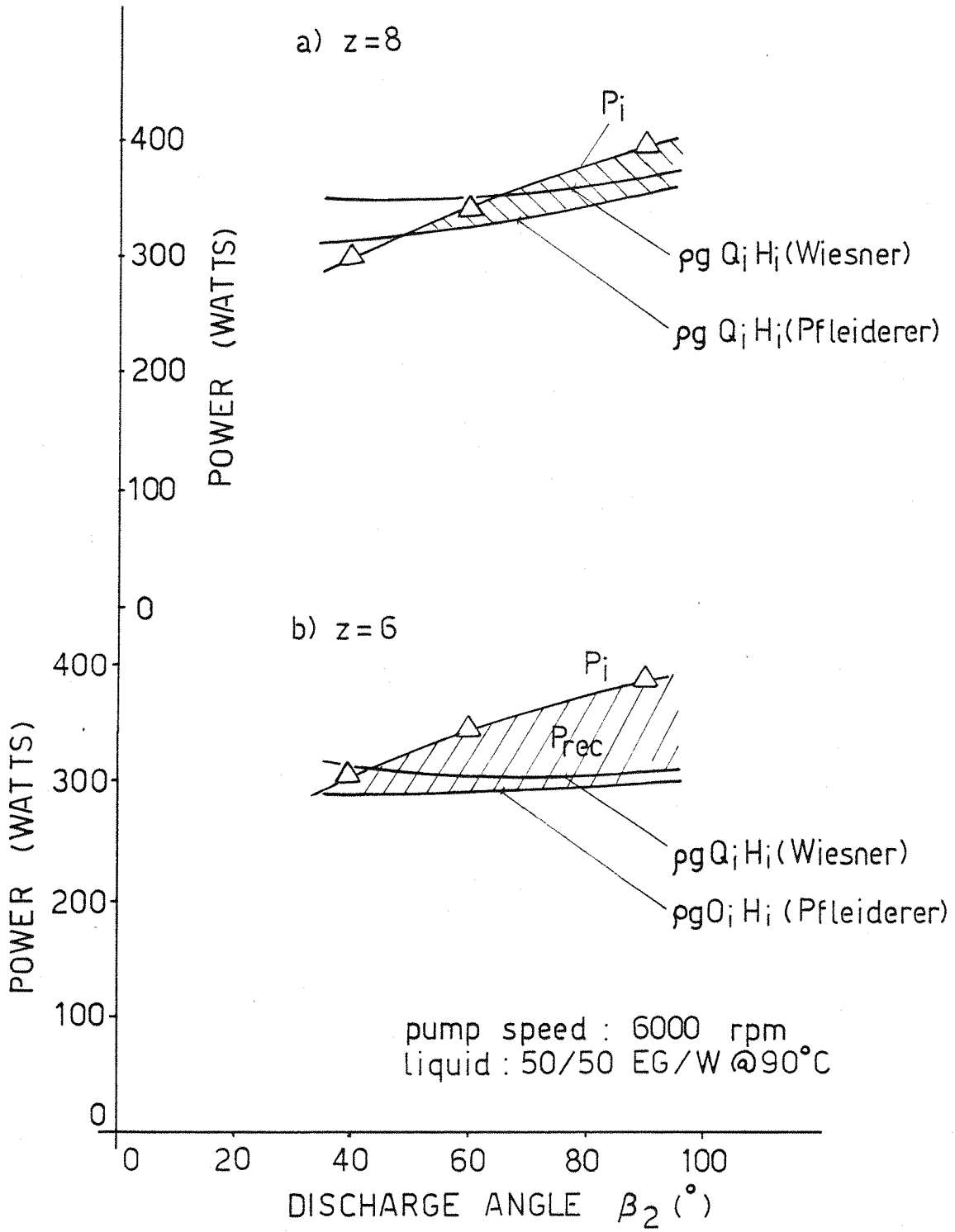

FIG 4·8 ACTUAL AND PREDICTED INTERNAL INPUT POWER FOR PUMP H AS FUNCTION OF THE DISCHARGE ANGLE β_2

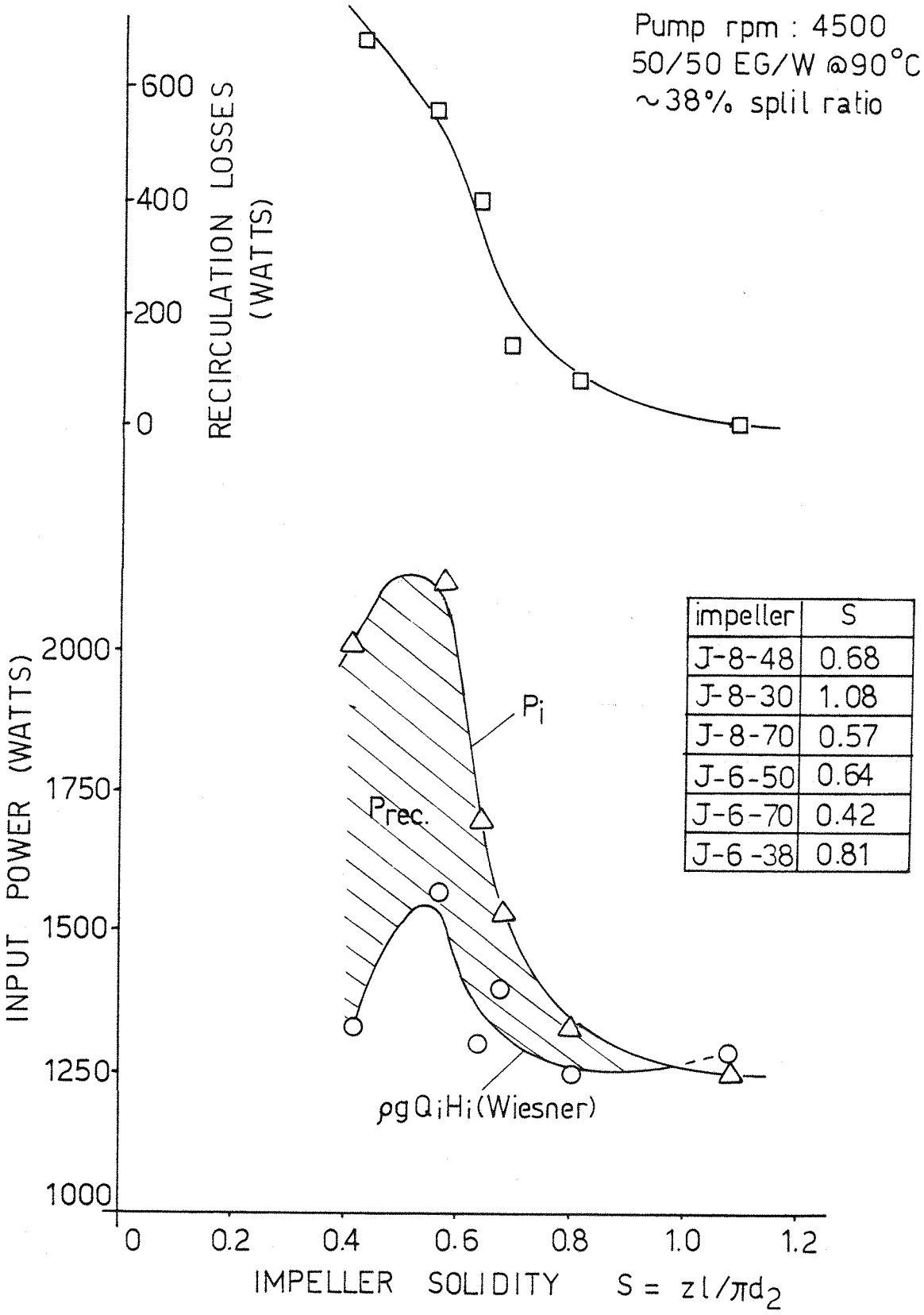

impeller	S
J-8-48	0.68
J-8-30	1.08
J-8-70	0.57
J-6-50	0.64
J-6-70	0.42
J-6-38	0.81

FIG. 4.9 ACTUAL AND PREDICTED INTERNAL INPUT POWER FOR PUMP J AS FUNCTION OF THE IMPELLER SOLIDITY

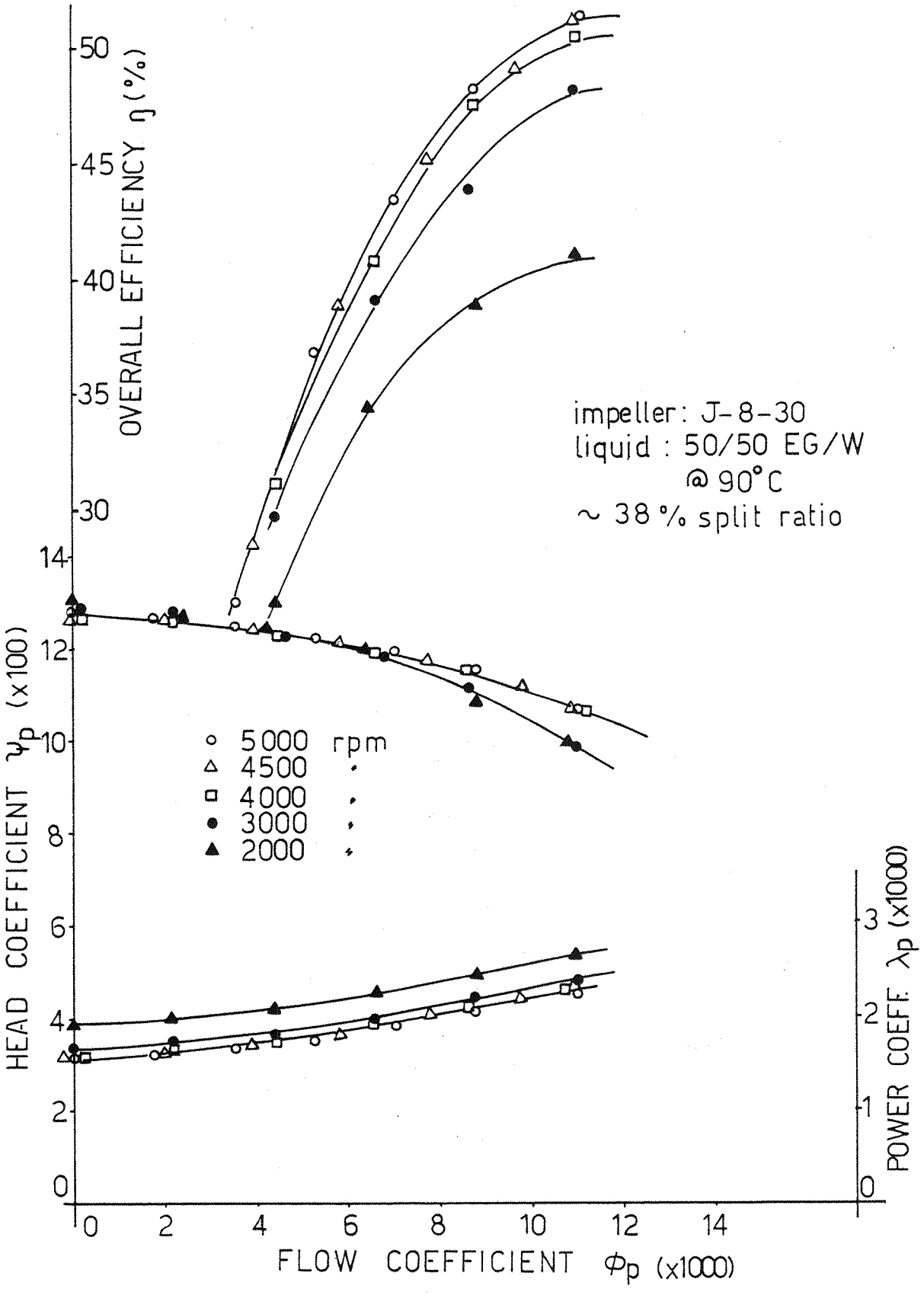

FIG. 4.10 THE EFFECT OF PUMP SPEED ON THE SCALING PARAMETERS OF PUMP J

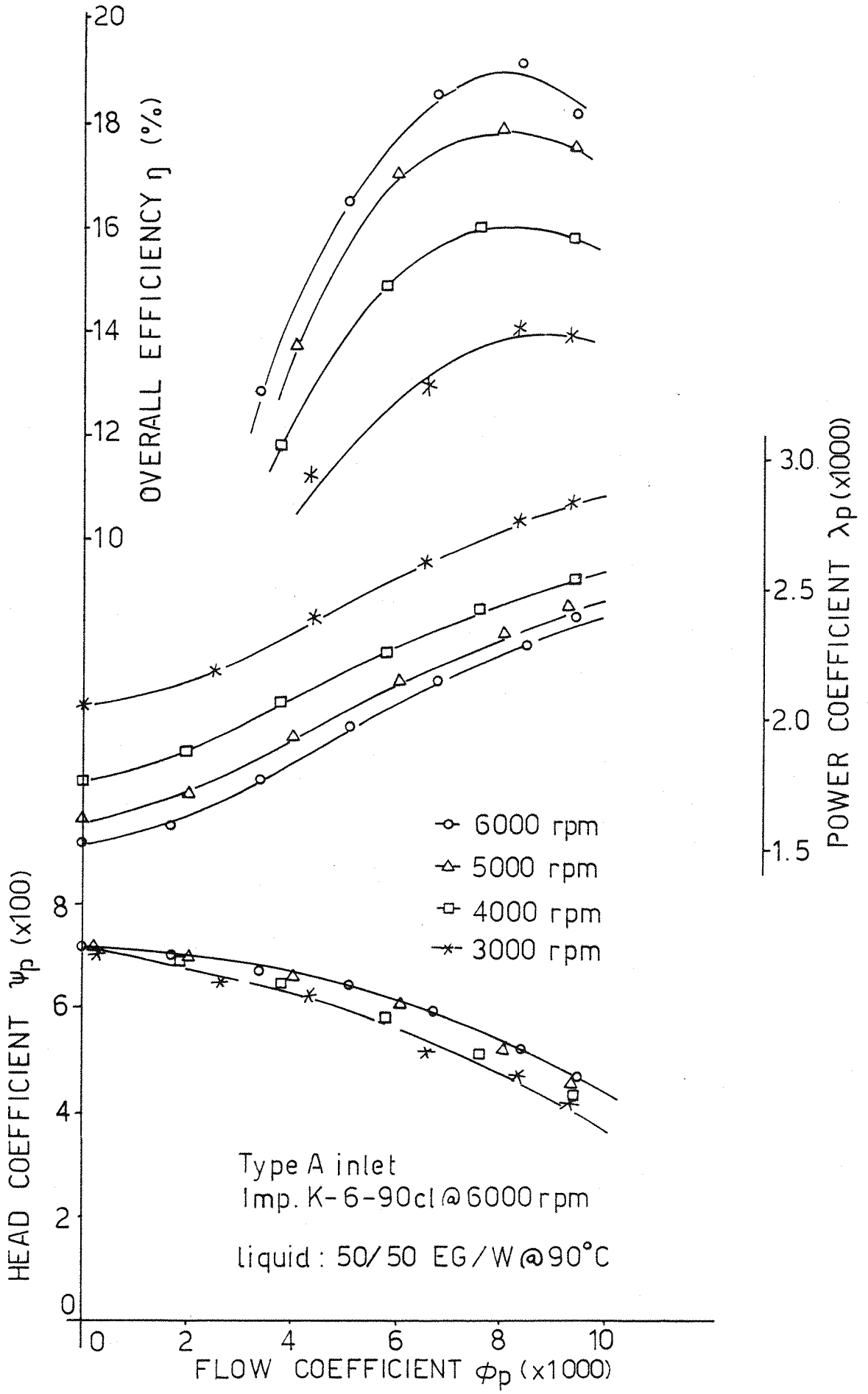

FIG. 4.11 THE EFFECT OF PUMP SPEED ON THE SCALING PARAMETERS OF PUMP K

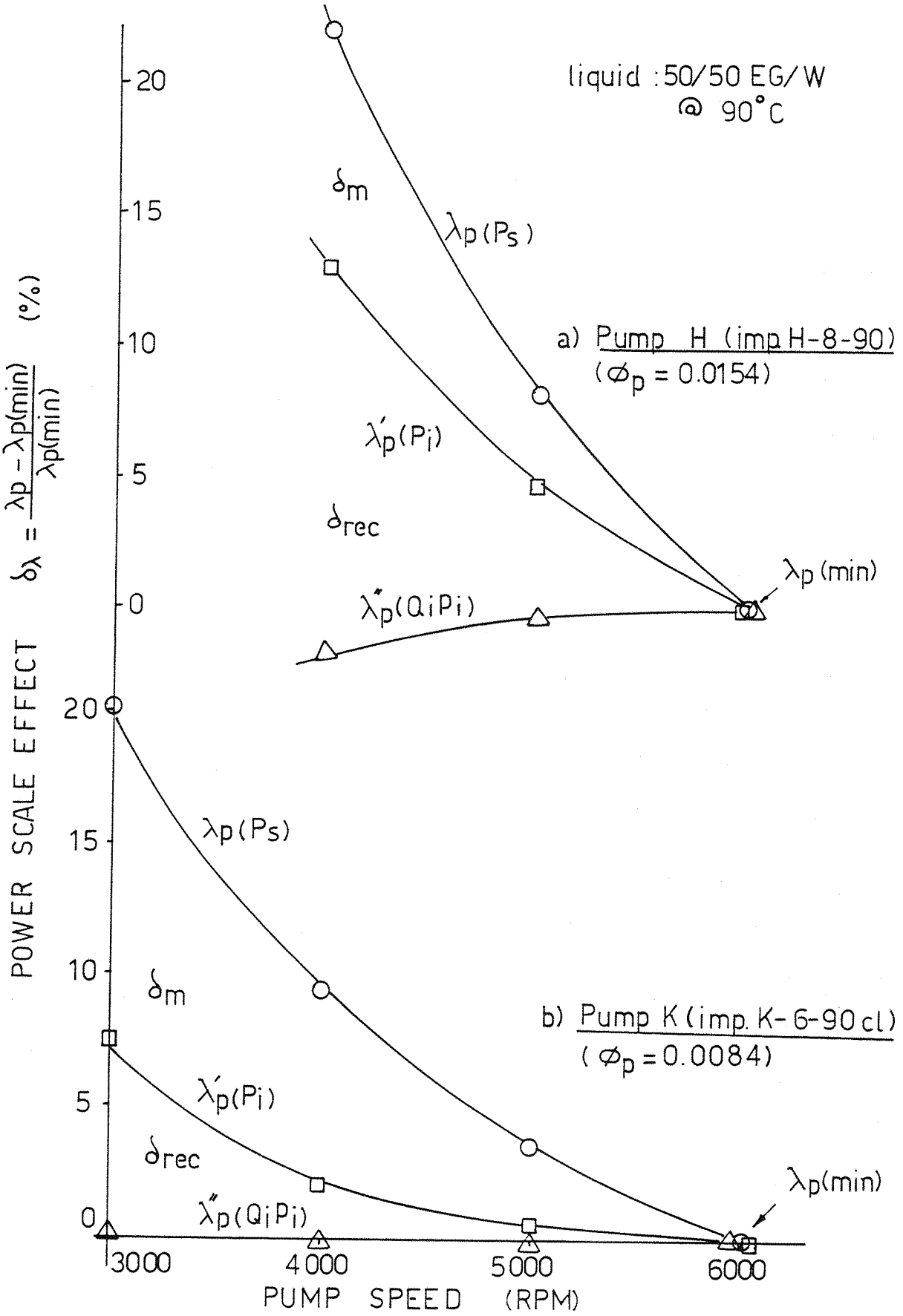

FIG 4.12 POWER SCALE EFFECT AS FUNCTION OF PUMP SPEED FOR 2 SMALL PUMPS

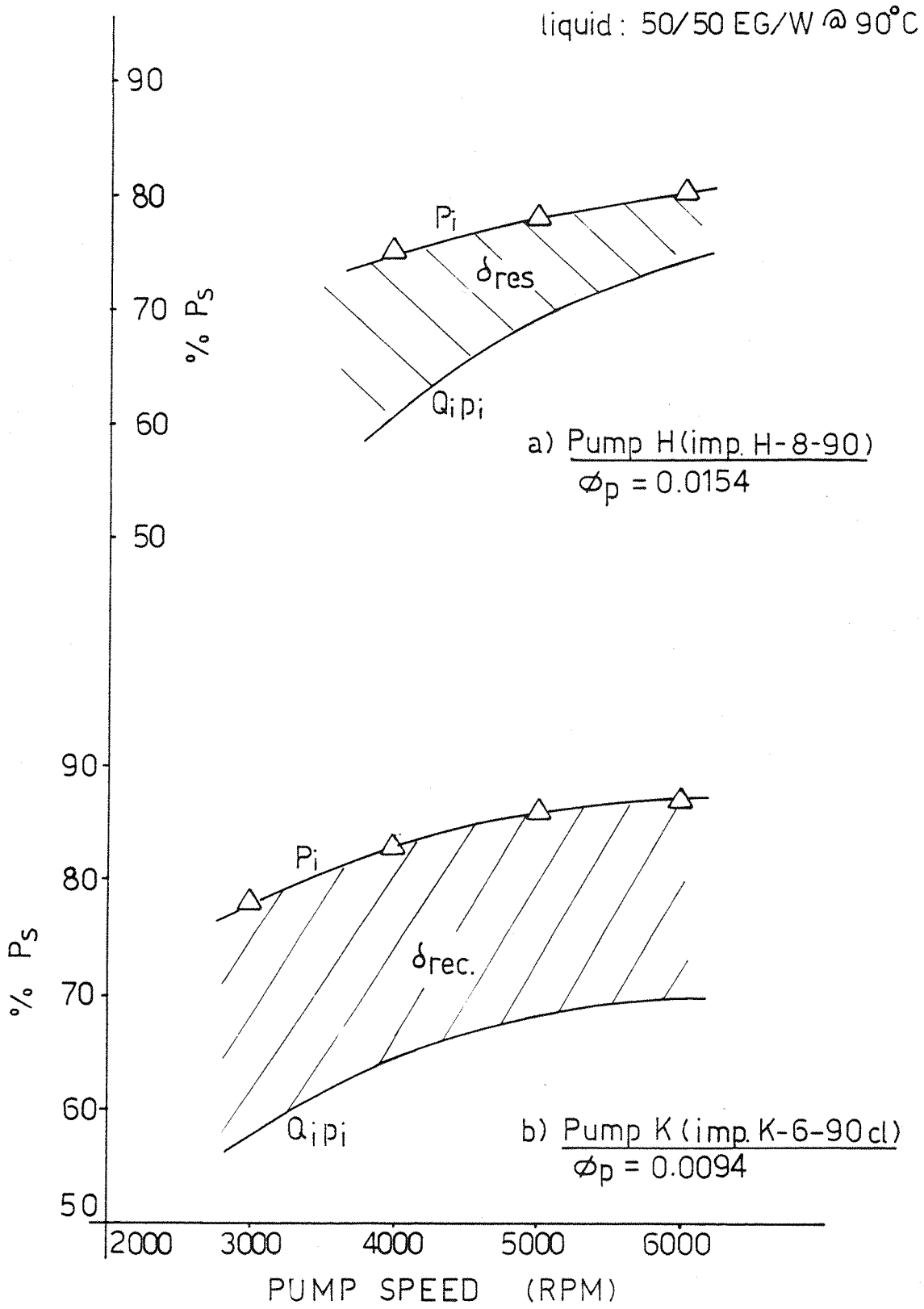

FIG 4.13 THE EFFECT OF PUMP SPEED ON THE RECIRCULATION SCALE LOSSES OF TWO SMALL PUMPS

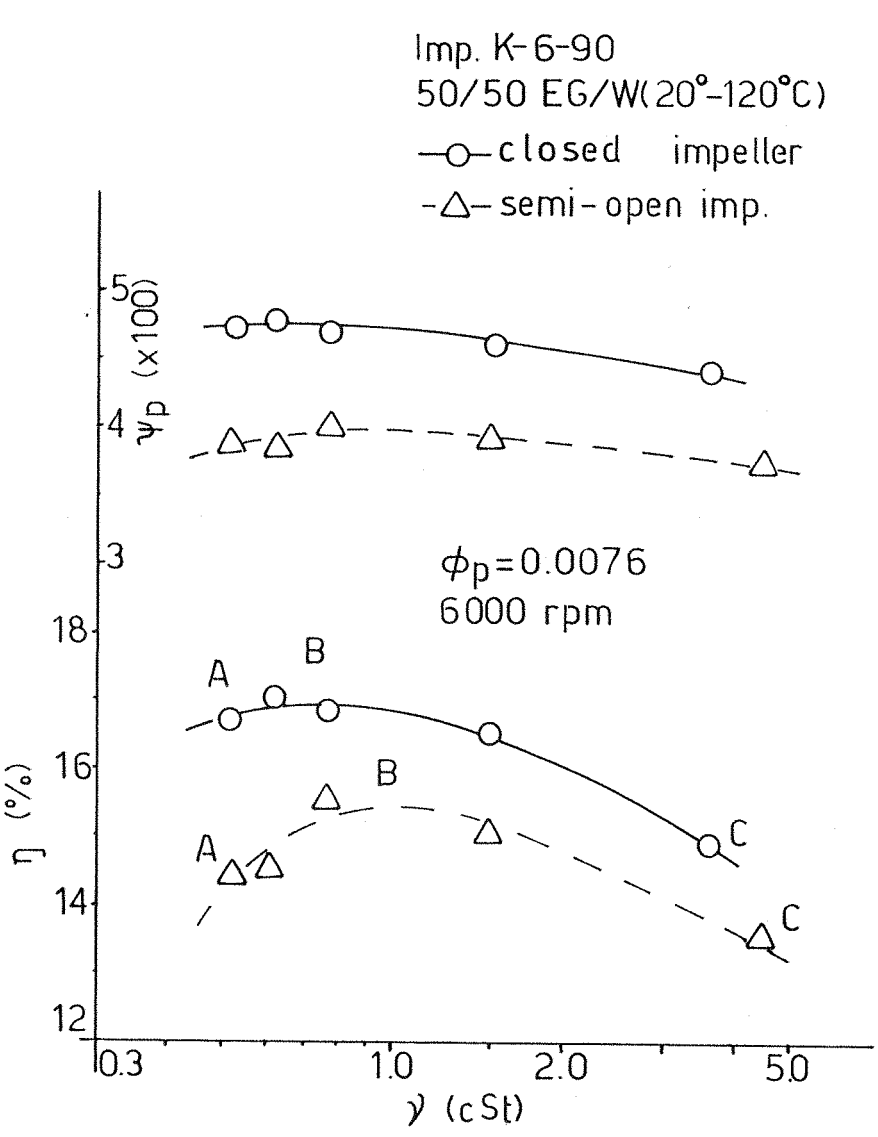

FIG 4.14 VISCOSITY EFFECT ON THE PERFORM. OF PUMP K AT THE BEP

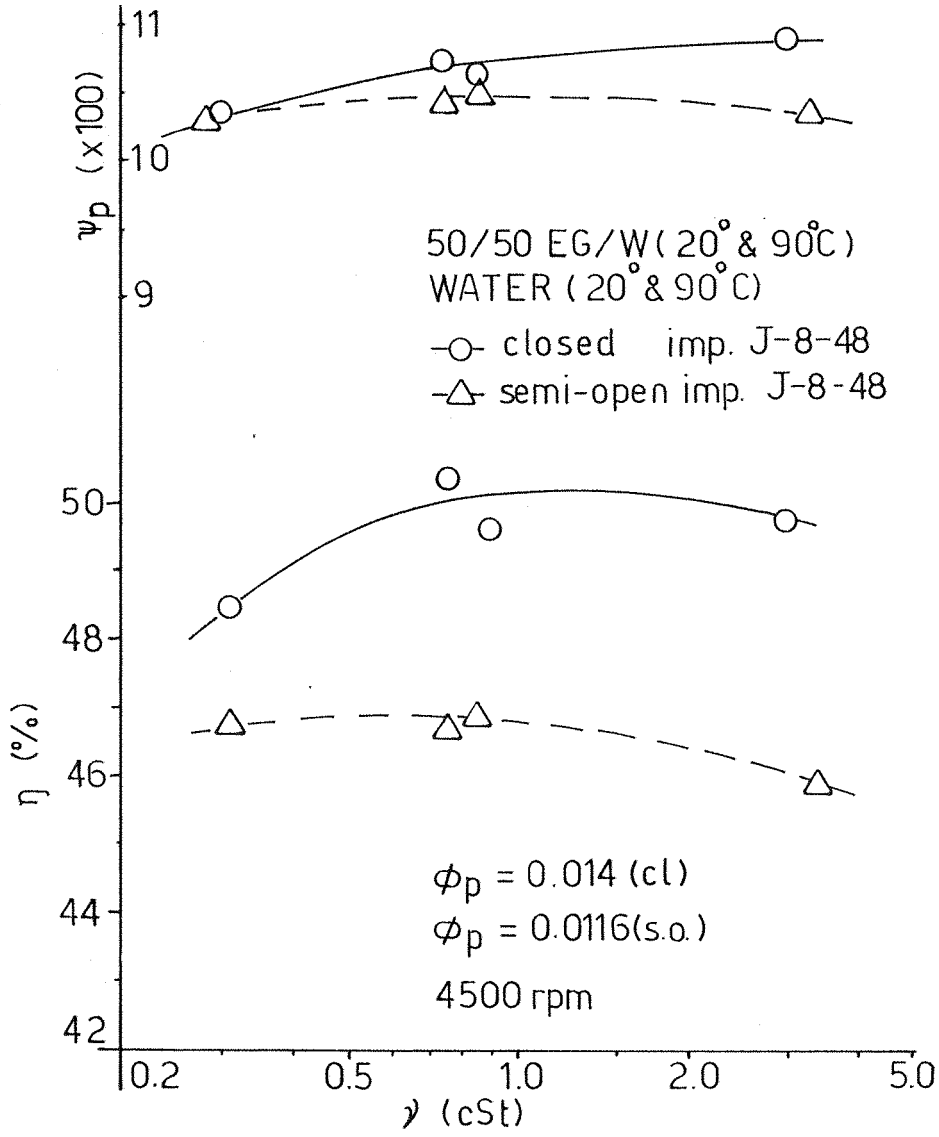

FIG 4.15 VISCOSITY EFFECT ON THE PERFORM. OF PUMP J AT THE BEP

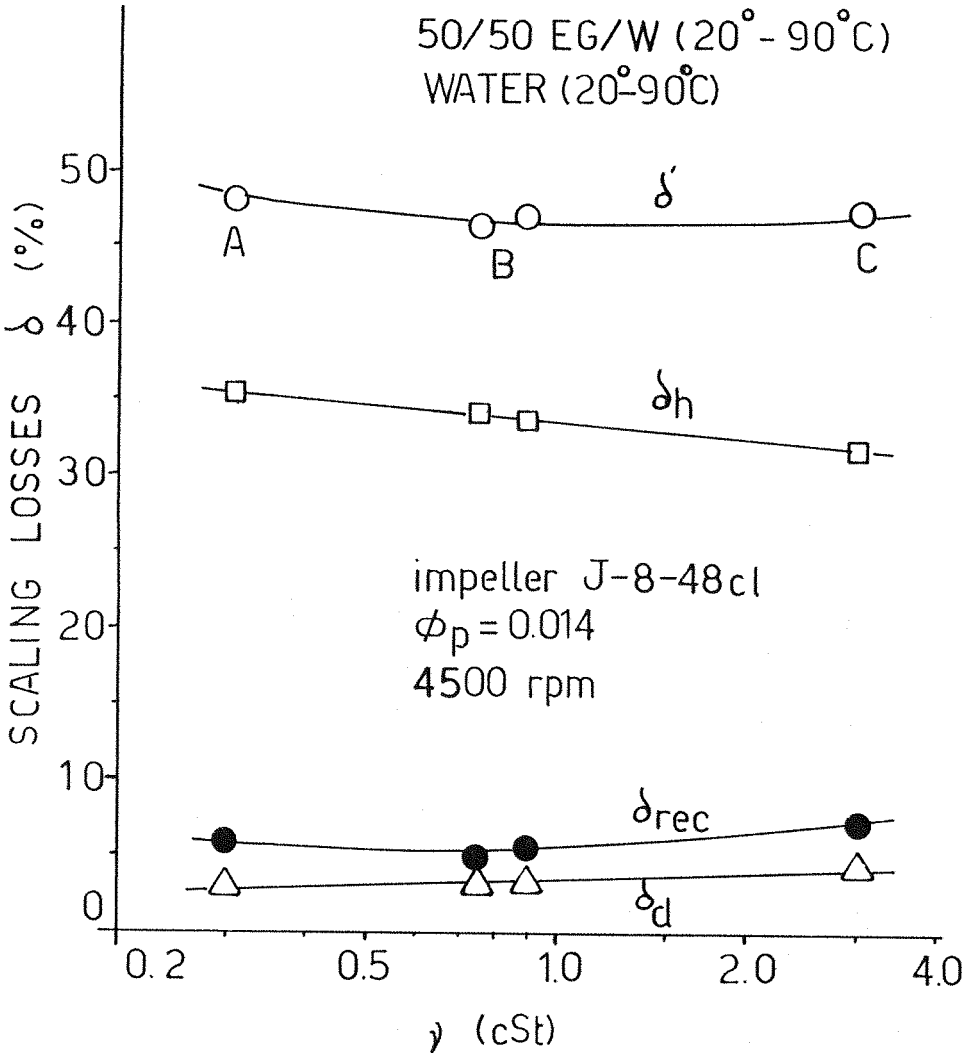

FIG. 4.16 VISCOSITY EFFECT ON THE SCALE LOSSES OF PUMP J WITH THE SHROUDED IMPELLER

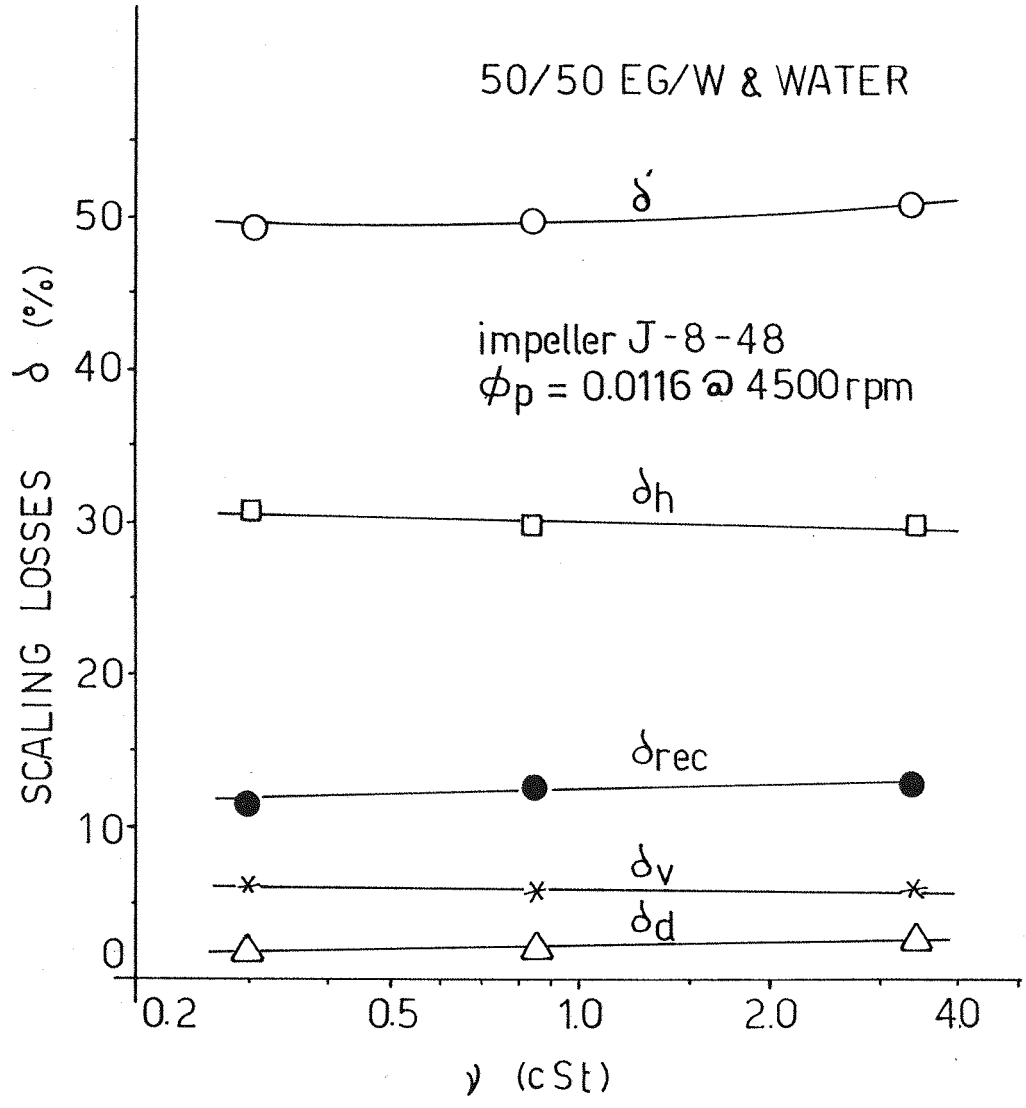

FIG. 4.17 VISCOSITY EFFECT ON THE SCALE LOSSES OF PUMP J WITH THE SEMI-OPEN IMPELLER

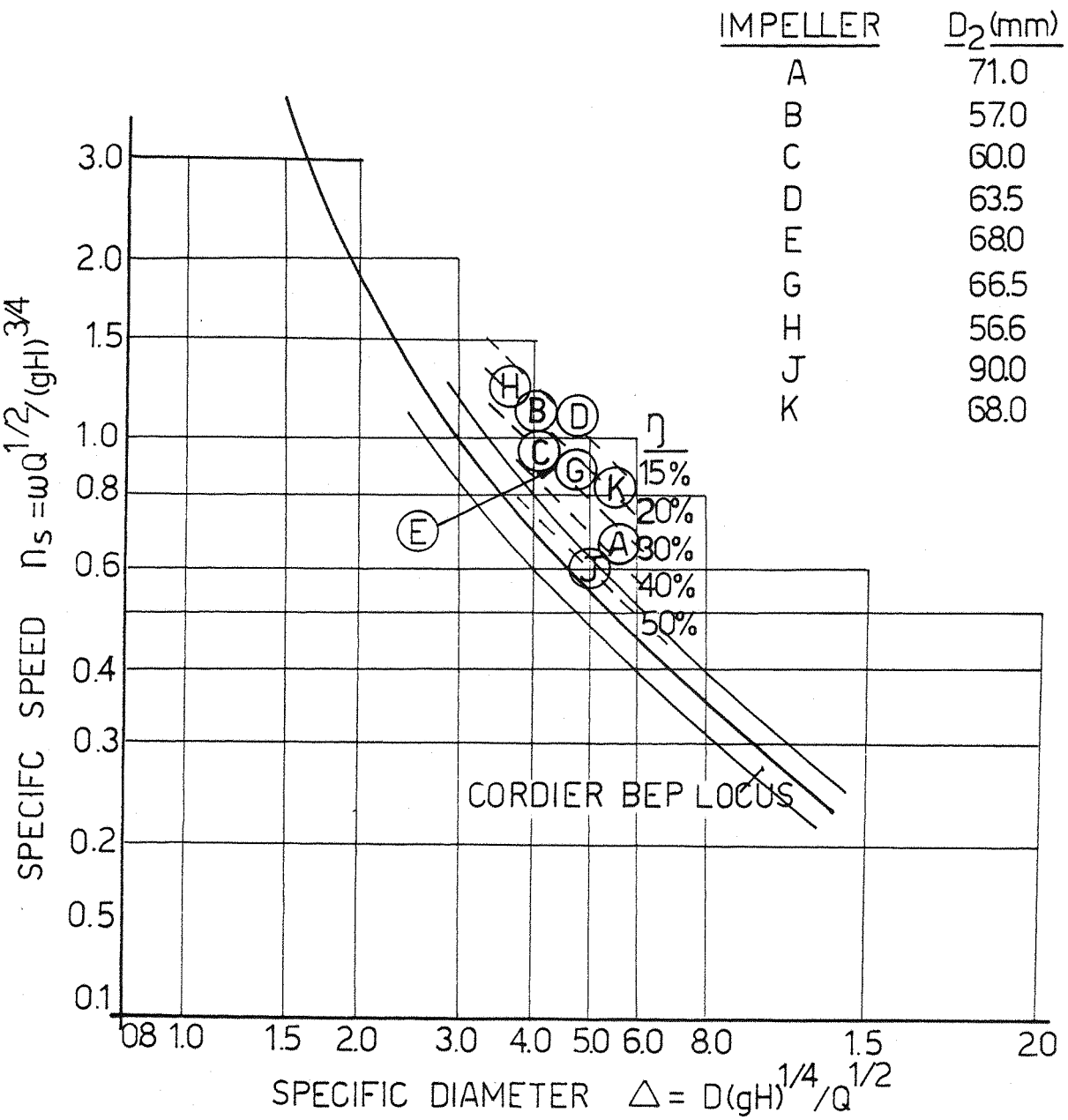

FIG 4.18 $n_s - \Delta$ CORRELATION FOR SMALL RADIAL CENTRIFUGAL IMPELLERS (ref. 29, 43, 57)

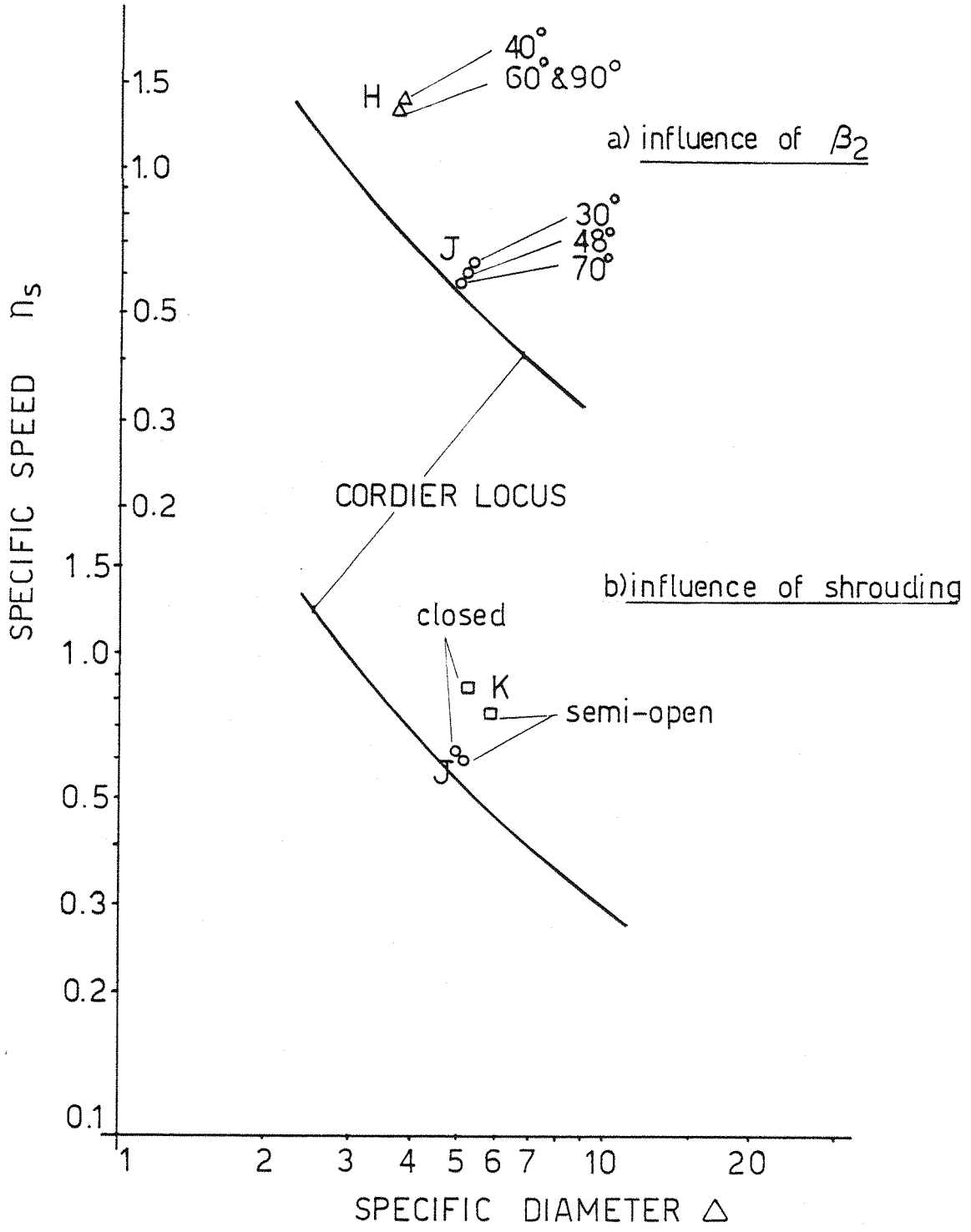

FIG. 4.19 THE INFLUENCE OF IMPELLER GEOMETRY ON ON THE LOCATION OF THE BEP ON THE CORDIER DIAGRAMME

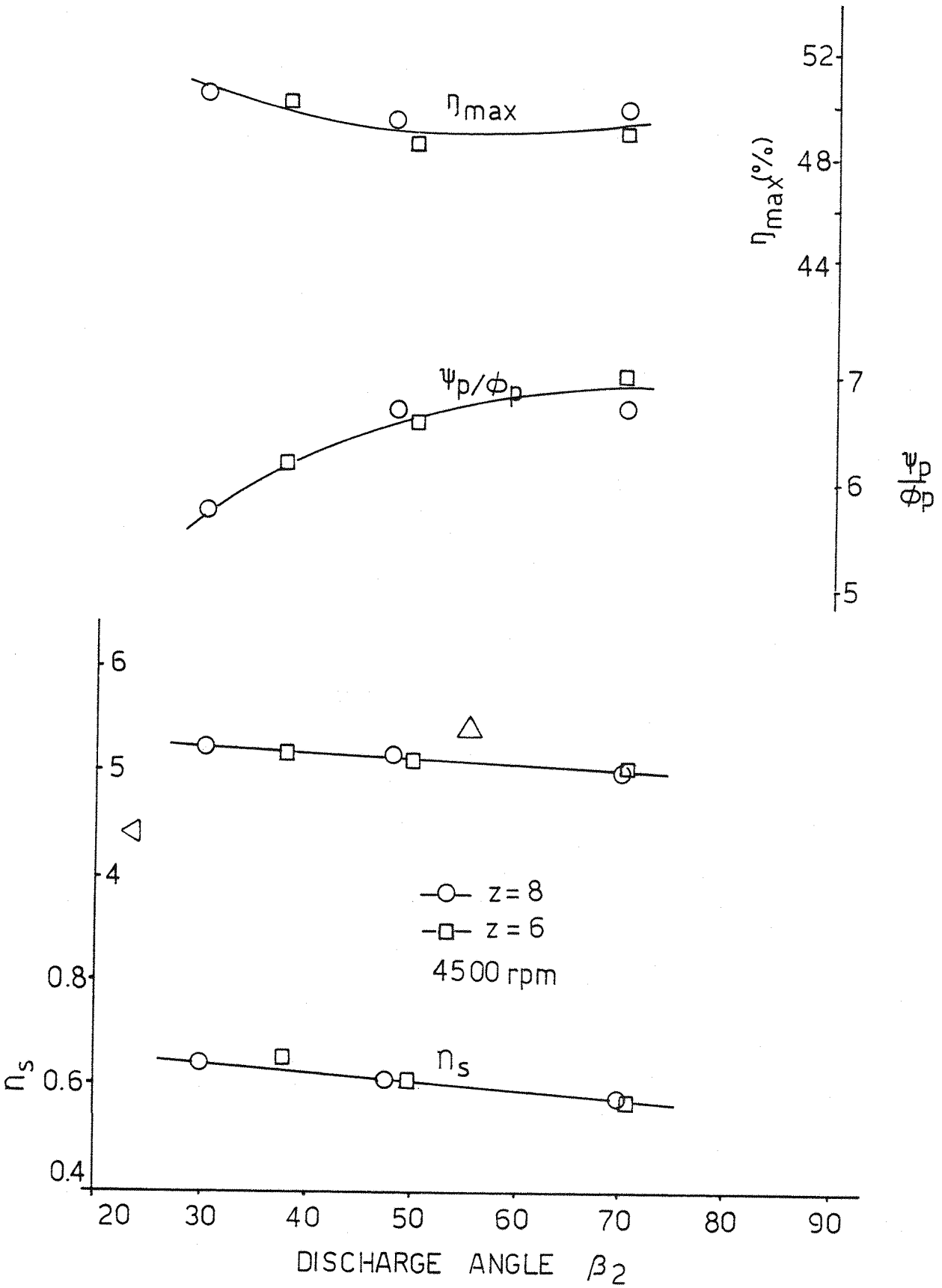

FIG 4.20 IMPELLER GEOMETRY INFLUENCE ON THE CORDIER CORRELATIONS OF PUMP J

CHAPTER 5

PUMP CAVITATION - FACTORS INFLUENCING THE SUCTION PERFORMANCE OF SMALL CENTRIFUGAL PUMPS

5.1 General Considerations

To ensure cavitation free flow at pump inlet, the total pressure of the liquid should not reach excessively low value at any location, thus approaching the vapour pressure of the liquid at the prevailing bulk liquid temperature, with the result of vapour bubbles forming and therefore reducing the blade loading of the impeller. To avoid this, a minimum pressure energy above the vapour pressure energy, known as the net positive suction energy NPSE, must be always available.

In attempting to describe a three-dimensional unsteady flow by 1-2-dimensional steady flow it will not be possible to get a comprehensive understanding of the flow inside the turbo machine. However a three-dimensional analysis of the flow is beyond the scope of this research and therefore, a steady, one-dimensional flow is assumed for practical purposes.

The net positive suction energy at a point near the suction flange is given by the following expression;

$$NPSE = \frac{p_{in}}{\rho} + \frac{V_{in}^2}{2} - \frac{p_v}{\rho} \qquad (5.1)$$

Because the area of lowest pressure normally occurs at the blade entrance (trailing face), the NPSE is best related to blade inlet parameters by using the modified Bernoulli equation between the suction flange and the blade entrance [120];

$$\frac{p_{in}}{\rho} + \frac{V_{in}^2}{2} = \frac{p_1}{\rho} + (1+K)\frac{C_{m1}^2}{2} \qquad (5.2)$$

The term $K_c \frac{C_{m1}^2}{2}$ represents the contraction loss at blade entrance. Subtracting p_v/ρ from both sides of equation (5.2) yields;

$$NPSE = (\frac{p_1}{\rho} - \frac{p_v}{\rho}) + (1 + K_c) \frac{C_{m1}^2}{2} \qquad (5.3)$$

and,

$$NPSE = \sigma_b (\frac{1}{2} W_1^2) + (1 + K_c) \frac{C_{m1}^2}{2} \qquad (5.4)$$

whereby σ_b $(= (p_1 - p_v)/\frac{1}{2} \rho W_1^2)$ is known as the blade cavitation number [120]. For radial entry, substituting for $W_1^2 = U_1^2 + C_{m1}^2$ in equation (5.4) and rearranging;

$$NPSE = (1 + K_c + \sigma_b) \frac{C_{m1}^2}{2} + \sigma_b \frac{U_1^2}{2} \qquad (5.5)$$

σ_b represents a design constant for the optimum flow rate and is a function of the inlet diameter, flow and pump speed [120]. Expressing the constants $(1 + K_c + \sigma_b)$ and σ_b by K_1 and K_2 respectively, gives;

$$NPSE = K_1 \frac{C_{m1}^2}{2} + K_2 \frac{U_1^2}{2} \qquad (5.6)$$

This is the usual form of expressing the minimum required NPSE as found in the literature [127, 156]. Yedidiah [188] showed from tests on various centrifugal pumps, that K_1 can vary from 2-3 and K_2 from 0.06 - 0.15. Pearsall [120] suggested the value of σ_b to be between 0.2 and 0.4 for conventional pumps, with K_c in equation (5.5) in the range 0.04 - 0.2. Based on optimization of NPSE and suction specific speed, Pearsall suggested the following empirical equation for the optimum inlet diameter (for given Q_{opt} and ω);

$$D_1 = 1.37 \left[\sqrt{\frac{2(1 + \sigma_b)}{\sigma_b}} (\frac{Q}{\omega}) \frac{1}{(1 - \lambda_h^2)}\right]^{1/3} \qquad (5.7)$$

Equation (5.7) is based on inlet tip values, with λ_h as the hub to tip ratio.

For readily available pump design, equation (5.7) can be rearranged to be solved for σ_b;

$$\sigma_b = 2 \left[\left\{ \left(\frac{d_1}{1.37}\right)^3 \left(\frac{\omega}{Q}\right) (1 - \lambda_h^2) \right\}^2 - 2 \right]^{-1} \qquad (5.8)$$

Equations (5.7) and (5.8) indicate that pumps with good suction capacities should have small σ_b, large inlet diameters and small hub to tip ratios λ_h for any given (Q/ω) ratio.

The preceding approach for the estimation of the minimum required NPSE for satisfactory pump operation is based on the assumption of a radial flow entry, where both pre-rotation and shock losses are minimal. Also the hydraulic losses between the suction flange and blade entrance were neglected for the straight inlet pipe design, and therefore, only contraction losses at the blade entrance were considered.

For the small pumps tested in this programme, the above appraoch is not expected to give a good prediction because of the unfavourable inlet design of the pumps. A side suction pipe discharging tangentially into a narrow suction cavity at impeller entrance (figure 2.9) will certainly promote pre-rotation and high hydraulic losses. This pre-rotation is likely to be increased by the high speed rotation of the shaft and rear part of the mechanical seal, which are placed inside the flow channel.

The importance of the inlet pipe design is demonstrated on figure 5.1. By introducing a new type B inlet, all relevant pump performance of pump K is improved over that of type A. More importantly, the flow rate capacity of the pump increased by a significant 16% for the same rig resistance.

Both inlet designs of pump K are shown schematically on figure 5.2. In both cases the impeller is fed through a narrow, rectangular channel of

similar design, which runs parallel to the impeller. The height of this channel is set by the space constraint which is a limiting factor for most automotive cooling systems. The main difference between the two designs is the situation and approach of the pipe leading to that channel. In type A design the pipe is situated to the side of the channel and approaches at a 90° angle. The flow is then forced through a rectangular contraction into the channel. This in effect will accelerate the flow, pushing it nearer to the outside wall with the result of a large flow disturbance and vortices. In type B design, the pipe is made to approach the channel directly at an angle, thus a smoother transition is provided, and disturbances are greatly reduced.

The static head losses between the inlet pipe and the channel are understandably higher for type A. However for the non-cavitating condition the difference in the differential heads of both designs is much higher than that obtained from lower losses at the inlet (at 100 ℓ/min the differential head improvement is 2.9 m corresponding to inlet loss improvement of $\sim$ 0.5 m). This will imply that suction performance is very much dependent on the inlet pipe design, a phenomenon widely accepted to be valid for all centrifugal pumps [58, 143].

To show that the suction performance of the small pumps dealt with here is far removed from the conventional design implied by equations (5.6) and (5.8), the blade cavitation number σ_b was estimated for optimum suction performance according to equation (5.8) for all impellers of pumps J and H at their Q_{opt}. Then from equation (5.6) σ_b was estimated by inserting the actual required NPSE to produce 5% drop in generated head, into that equation. The constant K_1 was given the value of $(3 + K_2)$ to account for the high losses in the pump inlet channel. In table 5.1, the theoretical and experimental results are listed for the 12 impellers. From this table it should be obvious that the actual σ_b as found from the experimental NPSE is 1.7 - 3.2 times higher than that based on optimum pump designs. This shows that for these pumps, the inlet pipe shape and the associated high entrance losses tend to reduce the suction performance far below the optimum value. Poor blade design also helps to render these pumps less efficient in that respect.

5.2 The Influence of the Test Flow

One of the many variables which influences the cavitation study of centrifugal pumps is the test flow Q_{cav} and its relationship to the best efficiency of Q_{opt}. Centrifugal pumps are usually designed to give satisfactory performance at the BEP, where the flow is assumed to enter the impeller shock-free and without great pre-whirl. Therefore most cavitation research and correlations limit themselves to the BEP flow.

For the small circulating pumps, changes of pump speed and flow requirement are so great, that one requires to know what effect the test flow bears on the cavitation of the pump. Especially if one would note that for the type of pumps tested with the flow passing around the drive shaft, the BEP does not necessarily mean that pre-whirl is a minimum or completely disappearing.

In figure 5.3, the cavitating flow test results for pump J over a wide range of test flows are shown. These tests show that the lower Q_{cav} is, the more rapidly drooping the curve becomes. At 5% head drop, the cavitation number increases from $\sim$ 9.2 at 1.2 Q_{opt} to $\sim$ 17.6 at 0.7 Q_{opt}, although the suction specific speed is only slightly changed. This is clearly shown on figure 5.4 for a different impeller of pump J. Here it is evident that the cavitation number σ is dependent both on the percentage head drop and the test flow, and the effects are most pronounced at low flows with the suction specific speed reaching exceptionally low value, especially at 2% head drop. As for the required NPSE to produce a certain head drop, there appears to be a minimum at a flow of about $\sim$ 60% Q_{opt} below which the required NPSE starts to increase again. The critical flow Q_{cr} is likely to be geometry dependent.

The effect of the test flow on the cavitation behaviour of centrifugal pumps has been investigated by several authors [46, 101, 115, 121, 163]. It has been shown that for cavitation inception, the lowest required $NPSH_i$ occurs near the optimum flow rate of the pump. For 3% head drop, on the other hand, the lowest required $NPSE_{03}$ is likely to occur somewhere between

zero flow and Q_{opt} [163]. Schiele [147], using the results of Florgancic [46] showed that although the available NPSE could prove to be sufficient for critical cavitation at low flows, the incipient cavitation could have developed much earlier with the consequences of high noise level and erosion rate.

Pearsall [120, 121] suggested that the blade cavitation number σ_b in equation (5.5) is a minimum at a low incidence angle (i), which is normally the case at a flow near the BEP. Decreased flow rates tend to increase the incidence angle and σ_b simultaneously until it reaches a stalling incidence of $\sim 12°$. After that a marked pre-rotation will probably occur. Solving equation (5.5) for the blade cavitation number for the ideal case will give;

$$\sigma_b = (NPSE - K \frac{C_{m1}^2}{2}) / \frac{W_1^2}{2} \qquad (5.9)$$

However, the application of equation (5.9) for flows away from Q_{opt} is dependent on the constant K, which is related to the entry condition at impeller inlet. Also at high pre-whirl, the relative velocity of this equation ought to be replaced by W_1' (figure 3.1). Therefore a direct application of equation (5.9) without knowing all the inlet flow parameters could be misleading.

Mansel [94] analysed the problem in a more detailed manner. By using Minami's [101] data for cold water, he arrived at the assumption that the inception $NSPH_i$ can be expressed as the sum of all static pressure changes at impeller inlet, or in equation form;

$$NPSH_i = h_a + h_r + h_t + h_\alpha \qquad (5.10)$$

whereby h_a is the static pressure changes between the reference plane and that upstream of the blade section, h_r is that due to pre-rotation, h_t is that due to blade thickness, and h_α is that due to the increase in the incidence anlge i. At flows below Q_{opt}, both h_r and h_α were found equally important.

Stepanoff [156] represented the inlet triangle for the general case for flows below or above the non shock flow. Noskievic [113, 114] used a similar, but more thorough approach to include all pertinent factors involved to construct the inlet triangle. This is shown on figure 5.5. The triangle ABF represents the condition of the shockless entry corresponding to the geometrical inlet angle β_{1s}, and U_2. At any other operating meridional velocity smaller than the shockless C_{mls}, the velocity triangle ABC would represent a new theoretical shockless condition with operating inlet angle β_1. If some pre-rotation is allowed which produces a whirl component C_{ul}, then the velocity triangle would become ABD with increased inlet angle β_1' ($\beta_1' = \beta_1 + i$). If β_1' is smaller than the geometrical angle β_{1s}, then the flow is forced to adjust itself to the geometrical boundary resulting in a shock component W_{1i}, so that it assumes the final relative velocity W_1''. Therefore we are left in this case with a trapezoid ABDE, to represent the velocity relationships at impeller inlet.

To include all these kinetic energy changes at impeller inlet, Noskievic [113] improved on equation (5.4) to obtain the following expression for the required NPSE at flows away from the shockless flow;

$$NPSE = [(1 + K_1)\frac{C_{m1}^2}{2} + K_2\frac{W_1''^2}{2}] + K_3\frac{C_{u1}^2}{2} + K_4\frac{W_{1i}^2}{2} + K_5\frac{(W_1'^2 - W_1''^2)}{2} \qquad (5.11)$$

The terms in the large bracket are equivalent to those of equation (5.4) with $K_2 = \sigma_b$, but with the exception of the relative velocity W_1 being replaced by the final W_1'' of that at the boundary. The remaining three terms, represent the kinetic energy changes due to pre-rotation, due to velocity impact, and due to those associated with the change of the relative velocity vector respectively (K_3 takes a negative value in most cases [113]).

This approach indicates that the application of equation (5.5) for flows far below that corresponding to C_{mls}, is not valid. In reality the solution for the required NPSE is far more complex and requires a more detailed knowledge of the flow parameters at impeller inlet and their associated constants.

Visual observations of the flow at the impeller entrance of the automotive type pump J (see Chapter 10) showed that a strong vortex is created around the impeller hub as a result of the side suction flow pattern enhanced by the drive shaft and seal rotation. This type of vortex examined at Q_{opt} is associated with high pre-rotation and entrance energy losses.

On figure (5.6) the inlet velocity triangle for 2 impellers of pump J is constructed. Here it should be obvious that in order to achieve shockless flow corresponding to the geometrical inlet angle β_{1s} at 4500 pump rpm, the flow rate must be increased $\sim$ 7 fold for impeller J-8-48 and $\sim$ 1.5 fold for impeller J-8-30 which is far beyond the reach of these pumps. Therefore even at flows near the optimum point, we would expect a high degree of pre-rotation and shock losses for all pumps in this design category. This is less pronounced with impeller J-8-30 than with impeller J-8-48, which contributes to the improved efficiency of impeller J-8-30 (see Chapter 4). On the other hand W_1'' is significantly higher for impeller J-8-30, which helps to push the NPSE higher. All this suggests that equations (5.5) and (5.6) should be treated with reservation if deviations from the radial entry concept are likely to be high such as for the small pumps tested here.

At high liquid temperatures similar behaviour of pump inlet performance is expected (although the cavitation number reduces due to thermodynamic effect as we shall see in a subsequent chapter). However from figure 5.7 the test flow rate seems to have much more pronounced effect, especially at a flow Q_{cr} of about 50% Q_{opt}, where both σ and NPSE reach a relatively high value, with a dip in the suction specific speed.

This suggests that the further away from Q_{opt}, the more unpredictable and unreliable the cavitation will be, and therefore tests should limit themselves to the horizontal part of the σ-Q curve for the purpose of cavitating flow test result correlations.

5.3 Type of Shroud and the Tip Clearance

In Chapter 3, the effect of the introduction of an axial tip clearance by removing one shroud, was found to reduce both generated head and the overall efficiency for any one test flow (figure 3.5). An increased re-circulated leakage flow across the clearance results in wasted power and at the same time the drag forces produced by this cross-flow help to push the impeller input head down.

As for the cavitating flow behaviour, some earlier test results on several centrifugal pumps of small inlet angles and high solidity [184] showed that for the same test flow, the semi-open impeller is superior to its shrouded counterpart in that the critical σ_{cr} is delayed.

Small centrifugal pumps used for coolant circulation are usually fitted with semi-open impellers for economical reasons. The tip clearance can vary within the tolerance limit of ∿ 2 - 15% of the impeller channel depth. To establish a reasonable relationship between the size of the clearance and pump cavitation, a better understanding and result correlation is sought. Hence both pump J and K were tested with varying clearance. Also the shrouded impeller of pump J was included in the programme.

On figure 5.8, the cavitating flow test result of pump J with both the shrouded and the semi-open impeller of various tip clearance are shown. A constant system test was applied, whereby the rig resistance is held constant to give the same Q_{nc} for all geometries ($Q_{nc} \sim Q_{opt}$), and cavitation is produced by reducing the available NPSE at pump inlet. These results indicate clearly for the liquid mixture used in this test (cold 50/50 EG/W), that both the deterioration in the flow capacity and the suction specific

speed with reduced inlet NPSE is delayed with increased tip clearance, the shrouded impeller coming off worse. A cross plot of the same test results was obtained on figure 5.9 by comparing the performance at the same inlet NPSE with regard to tip clearance ratio λ. Obviously here, the pump suction performance is increasing nearly linearly with increased clearance (within the test limit of clearances), and this is especially pronounced at low NPSE.

To obtain a more precise picture of this phenomenon, constant flow tests were performed in order to compare the pump performance at a low head drop at a wide range of test flows. Some of these test results are shown on figure 5.10 for the shrouded and the semi-open impeller of pump J of the same geometry as with a tip clearance of 1 mm. Cold inhibited water was used in this test series, and test results were compared at the same flow coefficient. From this figure, the obvious conclusion is that the semi-open impeller gives a better cavitating performance over the whole range of test flows.

Two reasons seem to contribute to this improvement. The first is hydrodynamic and follows from the presence of the leakage flow Q which constributes to the disturbance of the fixed cavity formed at the low pressure side of the impeller, and eventually reducing its size. (Cross flow is evident from photographs taken at advanced cavitation shown in Chapter 10). The second reason is purely operational, which arises from the fact that Q_{opt} of the shrouded impeller is about 12% higher than that of the semi-open impeller and therefore the same flow of the test can only be favourable to the semi-open impeller. In fact comparing the same results of figure 5.10 to Q_{cav}/Q_{opt} instead of Q, will bring all σ_{03} values on nearly the same curve. The NPSE values will then be a function of the square of the corresponding inlet velocities. However, for the general pump user, the comparison at the same flow rate is perhaps more important, than the theoretical value of Q_{cav}/Q_{opt}.

Increased tip clearance was shown to improve the suction performance of pump J (figure 5.8). To elaborate on this, the constant flow test method was used to compare the cavitation parameters at small head drop to the clearance ratio. This is shown on figure 5.11. Hot 50/50 EG/W mixture was used in these tests to avoid excessive gas solubility scale effect. These test results show that for the same Q_{cav}, the semi-open impeller gives always better performance (lower σ and higher n_{ss}). The improvement is however, not proportional to the clearance ratio λ. There seems to be a certain optimum clearance, which gives the best results. For pump J from figure 5.11, this occurs at $\lambda \cong 4\text{-}5\%$, which is equivalent to 0.5 - 0.7 mm clearance.

These results seem to explain earlier results obtained with pump K, although the tip clearance for this pump is not constant over the length of the blade. Three tip clearances were attempted with the stand. impeller K-6-90 (std.). The constant resistance tests were performed with hot 50/50 EG/W for the same reason outlined before, at a constant non-cavitating flow of 88 L/min. As it can be seen from figure 5.11, improvement of the cavitating performance of this impeller reaches a maximum at a clearance of 1 mm beyond which the improvement starts to diminish. This may indicate that large leakage flows associated with large values of Δx are less effective in breaking up the fixed cavity, perhaps because of less differential pressures across the blade tip.

5.4 Blade Geometry and Solidity

The influence of the blade shape and number is of great importance for the determination of the cavitating flow behaviour of centrifugal pumps. The influence of the number of blades is known to be two-sided [46, 147, 187]. The first is an improvement tendency with increased number of blades at the inception point and at small head drop values. This is related to the reduced blade loading with increased number of blades [187]. As the cavity increases in size, an opposite trend appears with the impeller of the fewer blades giving the improved cavitating flow performance. The

reason behind the latter is obviously a reduction in the flow restriction area (given by the restriction w in table 5.2) due to the increase in the blade number. A reduction in w means that at advanced cavitation the impeller is more readily clogged up with cavitation bubbles and therefore a fast performance deterioration is expected [187].

Tests performed on 2 impellers of pump J of exactly the same blade design but of different number of blades (figure 5.13a) shows a good agreement with this approach. The performance deterioration is delayed significantly by using an impeller of higher number of blades, but on the other hand a better performance of the lower blade number impeller at breakdown is apparent.

Improvement at advanced cavitation was also found with pump H tested in a constant resistance system, when the 8-bladed radial impeller was replaced by a 6-bladed radial impeller (figure 5.14).

The influence of the blade inlet geometry which is mainly governed by the inlet angle β_1, is known to be of decisive importance to the cavitating behaviour of centrifugal pumps. Similar to the influence of increased number of blades, the reduction of β_1 for the same number of blades would mean a reduction of the restriction width w, with the result of greater deterioration in performance at advanced cavitation.

This seems to agree well with test results obtained on both pumps J and H on figures 5.13b and 5.14, using both a constant resistance rig geometry and constant flow test methods, respectively. From both these figures it seems that the influence of increased β_1 is to improve the cavitating flow performance from the point of inception down to the breakdown.

This is also obvious on figure 5.15, whereby 3 impellers of pump J of the same number of blades were tested at a constant Q_{cav} at the BEP. The increase in the cavitation number is most pronounced at small head drops and reduces towards the performance breakdown.

From experience, Raabe [131] combined the effect of both the blade number and the inlet angle β_1 to be related to the contraction number defined by;

$$C_n = \frac{t.z}{2\pi r \sin \beta} \qquad (5.12)$$

whereby the blade thickness t, the radius r and the blade angle β are those at the point of observation.

In table 5.2 the contraction numbers for 6 impellers of pump J are listed and on figure 5.16 the cavitation number at 5% head drop is plotted for 6 different impeller geometries against their respective contraction number measured at impeller inlet. The general trend of this figure is to increase the cavitation number with increased contraction number. However the scatter is rather high especially for impeller J-6-38. The reason behind this seems to lie in the exceptionally long vanes of impeller J-6-38, with the result of higher blade loading and hence more cavitating tendency.

Introducing a new modified non-dimensional geometrical ratio (ℓ/w) which includes both the length of the channel (ℓ) and the restriction width w, and by plotting the same cavitation number values of figure 5.16 against this new ratio on figure 5.17, a better correlation could be obtained, thus suggesting that the contraction number of equation (5.12) may be less effective as a correlation factor because it neglects the channel length.

The suction specific speed is a measure of the ability of the pump to push the required mass flow rate at a certain inlet energy and pump speed. From its definition we obtain;

$$n_{ss} = \frac{\omega \sqrt{Q}}{NPSE^{3/4}} = \frac{\omega \sqrt{Q}}{(gH)^{3/4}} \left(\frac{gH}{NPSE}\right)^{3/4} \qquad (5.13)$$

by noting that the Thoma sigma is defined by (NPSE/gH), then;

$$n_{ss} = n_s/(\sigma_{TH})^{3/4} \qquad (5.14)$$

On figures 5.18 and 5.19 both σ_{TH} and n_{ss} are plotted against the specific speed for 6 impellers of pump J and 5 impellers of pump H respectively. All values are recorded at 5% head drop, using constant flow tests at $\sim Q_{opt}$. On these 2 figures it should be obvious that large inlet angles are associated with lower n_s values, lower σ_{TH} and better suction specific speeds. Impellers of lower inlet angles, however, are associated with higher n_s values, higher σ_{TH} and lower suction performance.

5.5 Concluding Remarks

In this chapter several factors influencing the cavitating flow performance of small centrifugal pumps were discussed. Inlet pipe design, test flow rate, type of shrouding and impeller geometry were found to influence the suction performance in one way or another. The main points of interest are listed here.

1. Minimum required NPSE for these pumps was found to be much higher than that obtained from the theoretical approach based on suction performance optimization. Cavitation blade numbers calculated from experiments may reach 4 times those based on theoretical approach assuming no pre-rotation or shock losses at pump entrance.

2. The influence of the test flow, in relation to the optimum flow rate (Q_{cav}/Q_{opt}), is of decisive importance for the estimation of a representative cavitation number. Flows far below the BEP flow rate were shown to give excessively high cavitation number and in some cases very low suction specific speeds, compared to those obtained at flows around the optimum flow rate. This suggests that cavitation correlation is best served by limiting tests to the horizontal part of the σ-Q curve.

3. Using a comprehensive analysis of the inlet flow triangle, a thorough understanding of the cavitating behaviour of pump J at low flows was sought. The component of pre-rotation and impact velocities at impeller entrance

were found excessively high at all flows attempted in the test. This is thought to be mainly responsible for the exceptionally low suction performance of the small centrifugal pumps tested. This suggests that the optimization theory based on shockless radial entry put forward by Pearsall [120] must be treated with reservations in our case. A better understanding can be obtained by analysing the various energy losses at pump entrance which is beyond the scope of this research.

4. Shrouded impellers were found to be less favourable than semi-open impellers in their cavitating flow performances if compared at similar flow rate, and over a wide range of test flows. The main reason behind this was thought to be related to the leakage flow across the clearance of the semi-open impeller which helps to break up the fixed cavity and reduce its size.

5. The influence of the size of the tip clearance was not immediately apparent. Some tests suggested a proportional suction improvement with increased tip clearance. A more detailed investigation at a small head drop showed however, that there exists an optimum clearance above which improvements reduce again and eventually excessive clearance thends to impair the performance pushing the cavitation number up again, at the same test flow.

6. The influence of the impeller geometry is of great importance to the cavitation study of centrifugal pumps. Increasing the number of blades for exactly similar blade design have a two sided effect, the first is to improve the cavitation performance at inception and very small head drops mainly due to reduced blade loading. The second was an opposite effect, with the impeller of lower number of blades, which gives superior cavitation performance at moderate head drops and breakdown. The reason behind the latter can be related to a reduced restriction area due to fewer number of blades, which in turn helps to reduce the blockage to the flow when the cavity is well developed.

7. The influence of increased blade inlet angle β_1 was found to favour an improvement in the cavitating performance of the pump at BEP over the

whole range of performance drops. Using a contraction number, C_n to express all the geometrical influences at impeller inlet of pump J, such as number of blades, blade thickness and inlet angle β_1, the cavitation number at the BEP was found to increase with increased C_n. However the scatter was high. It was thought that this scatter is because of the ommission of the channel length in the contraction number. Using a geometrical ratio ℓ/w according to figure 5.17 instead, was shown to give better correlation with less scatter.

8. Comparison of the different impeller geometries of pumps J and H seem to indicate that at the BEP, high inlet angles β_1 are associated with lower specific speed, lower Thoma sigma and higher suction specific speeds. The opposite can be said for lower inlet angle β_1.

TABLES 5.1 and 5.2

FIGURES 5.1 to 5.19

Table 5.1 Suction parameters for pumps H and J near the BEP
Test liquid 50/50 EG/W at 25-30°C.

	Impeller	Q_{cav} (L/min)	β_1 (°)	D_1 (tip) (mm)	U_1 m/sec	C_{m1} m/sec	W_1 m/sec	$\lambda = d_h/d_1$	σ_b Eq. 5.8	Experimental Results			
										$NPSE_{05}$ (J/kg)	K_1 (Eq. 5.6)	$K_2 = \sigma_b$ (Eq. 5.6)	$(n_{ss})_{05}$
4500 rpm	J-8-70	280	70	54.0	12.7	2.13	12.9	0.519	0.20	40.9	3.41	0.41	2.00
	J-8-48	240	48	56.5	13.3	1.84	13.4	0.495	0.12	38.1	3.37	0.37	1.93
	J-8-30	230	20	56.5	13.3	3.28	13.7	0.495	0.11	42.1	3.28	0.28	1.75
	J-6-70	280	70	54.0	12.7	2.00	12.9	0.519	0.20	41.0	3.42	0.42	2.00
	J-6-50	260	25	56.5	13.3	2.07	13.5	0.495	0.13	50.0	3.48	0.48	1.65
	J-6-38	240	30	56.5	13.3	2.10	13.5	0.495	0.12	45.2	3.43	0.43	1.68
6000 rpm	H-8-90	100	90	41.2	12.9	1.50	13.0	0.607	0.11	37.7	3.41	0.41	1.67
	H-8-60	95	60	41.2	12.9	1.50	13.0	0.607	0.10	35.5	3.38	0.38	1.70
	H-8-40	95	40	41.2	12.9	1.74	13.1	0.607	0.10	41.2	3.43	0.43	1.55
	H-6-90	95	90	41.2	12.9	1.31	13.0	0.607	0.10	36.8	3.40	0.41	1.70
	H-6-60	95	60	41.2	12.9	1.36	13.0	0.607	0.10	42.9	3.47	0.47	1.50
	H-6-40	95	40	41.2	12.9	1.50	13.0	0.607	0.10	40.1	3.43	0.43	1.57

Table 5.2 Geometrical value for pump J.*

Impeller	D_1	D_2	β_1	β_2	Z	t	ℓ/w	$C_n = \frac{tZ}{\pi D_1 \sin\beta_1}$	Solidity $(Z\ell/\pi d_2)$
J-8-70	54.0	90.0	70	70	8	4	1.1	0.2	0.57
J-8-48	56.5	90.0	46	46	8	4	1.35	0.24	0.68
J-8-30	56.5	90.0	20	30	8	4	3.18	0.53	1.08
J-6-70	54.0	90.0	70	70	6	4	0.8	0.15	0.42
J-6-50	56.5	90.0	25	50	6	4	1.6	0.32	0.64
J-6-38	56.5	90.0	30	38	6	4	2.06	0.27	0.81

* Dimensions in mm.

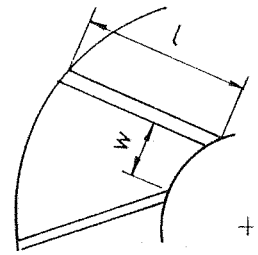

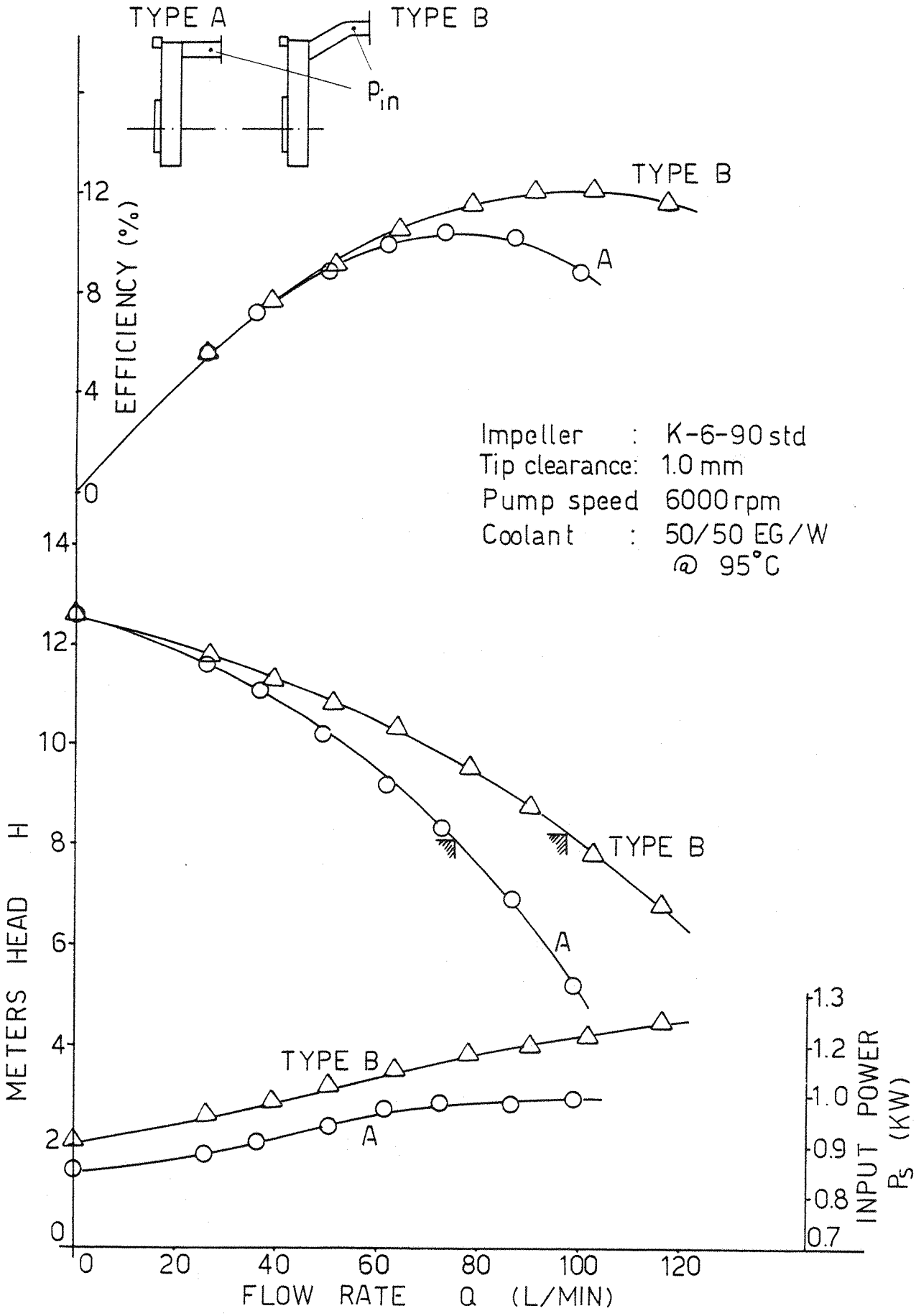

FIG 5.1 THE INFLUENCE OF THE INLET PIPE SHAPE ON THE NON-CAV. PERFORMANCE OF PUMP K

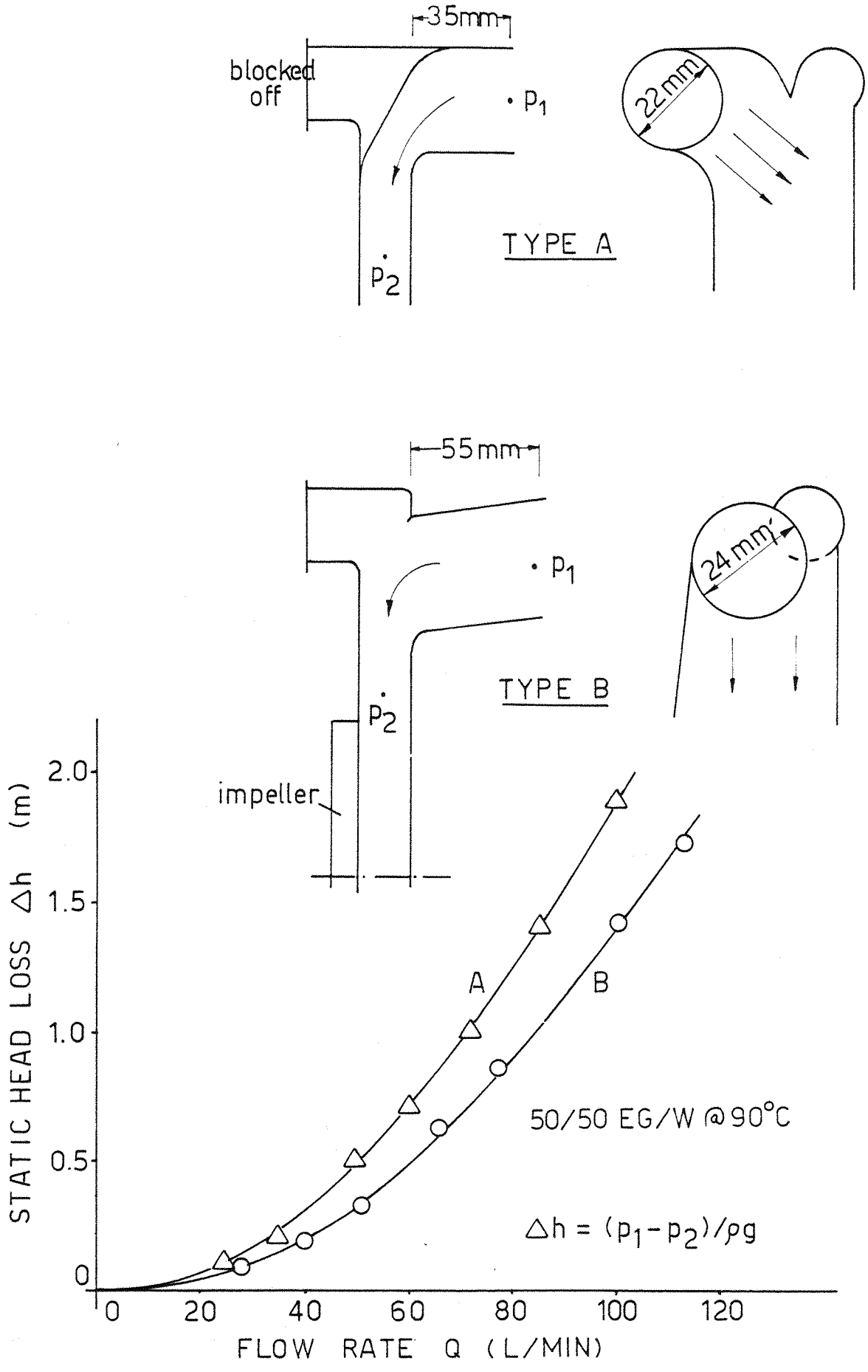

FIG 5.2 HEAD LOSSES FOR 2 INLET DESIGNS OF PUMP K

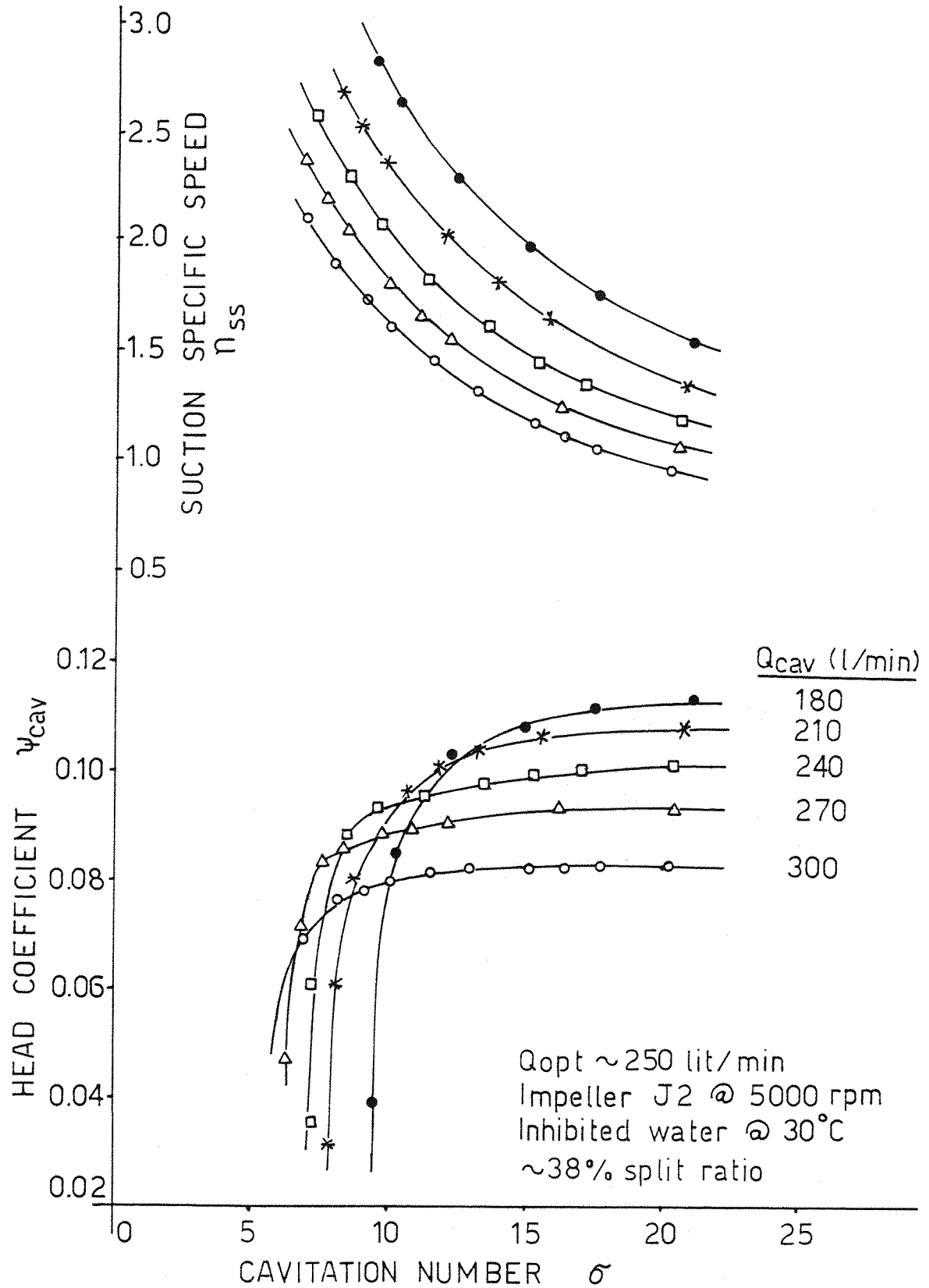

FIG. 5.3 THE INFLUENCE OF TEST FLOW ON THE CAVITATION OF PUMP J

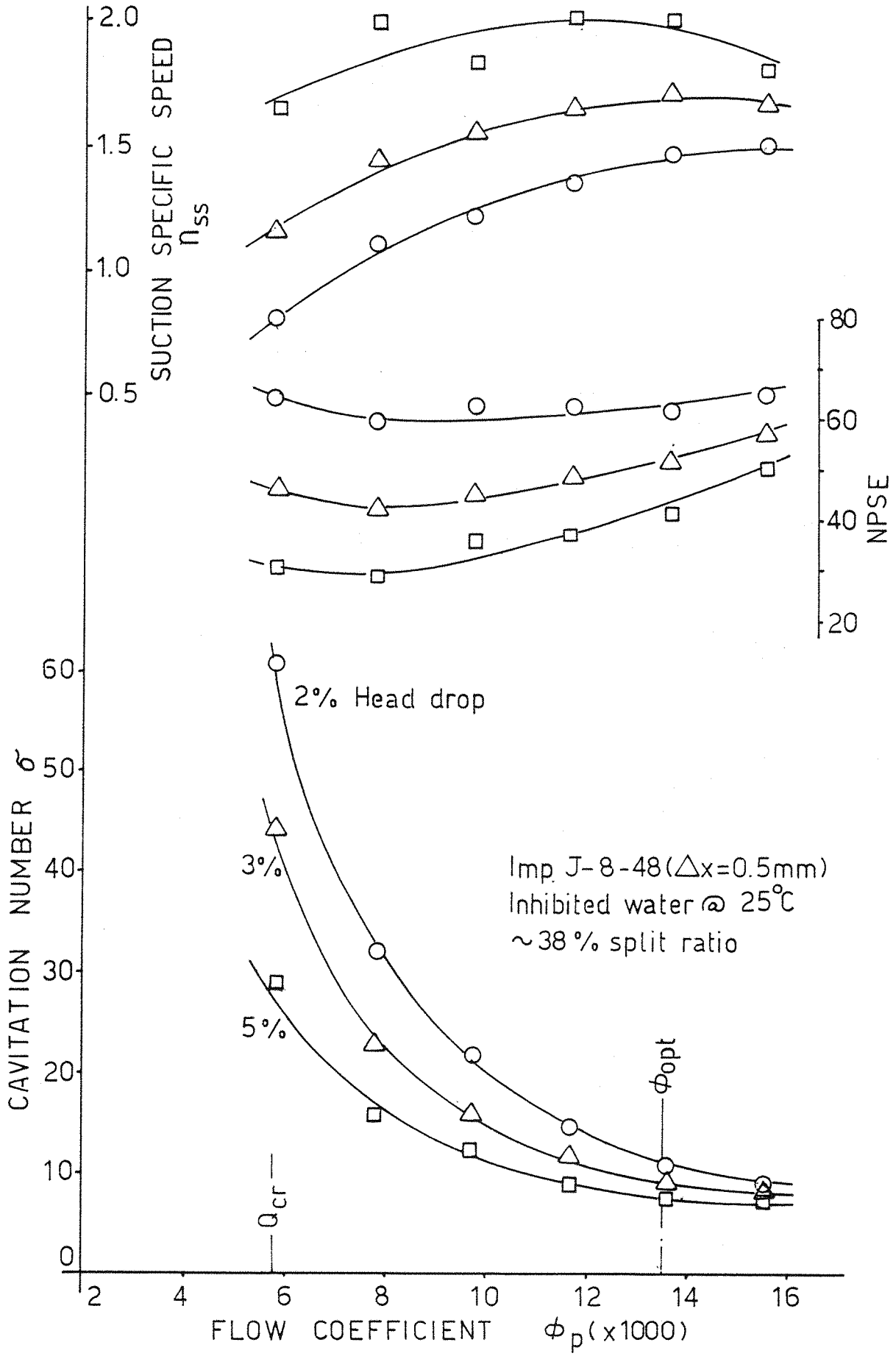

FIG 5.4 CAVITATING FLOW PERFORMANCE OF PUMP J AT VARIOUS FLOWS

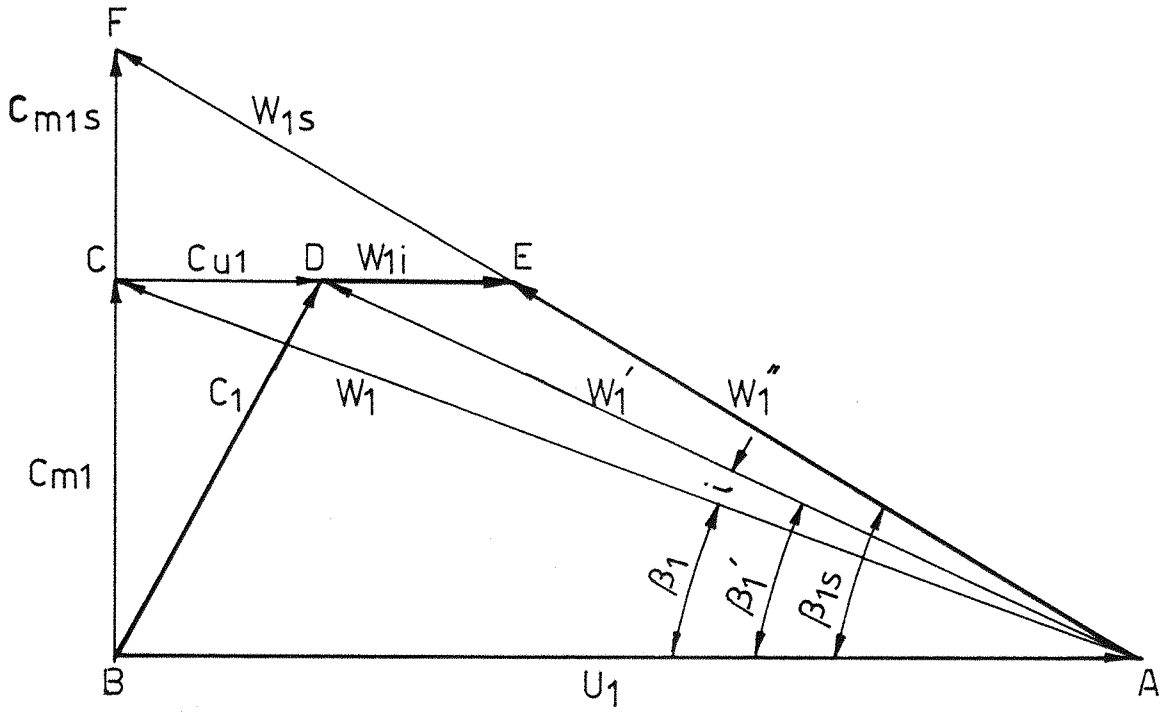

FIG 5.5 INLET VELOCITY TRIANGLE AT FLOWS BELOW SHOCK LESS AND WITH A PRE-SWIRL COMPONENT

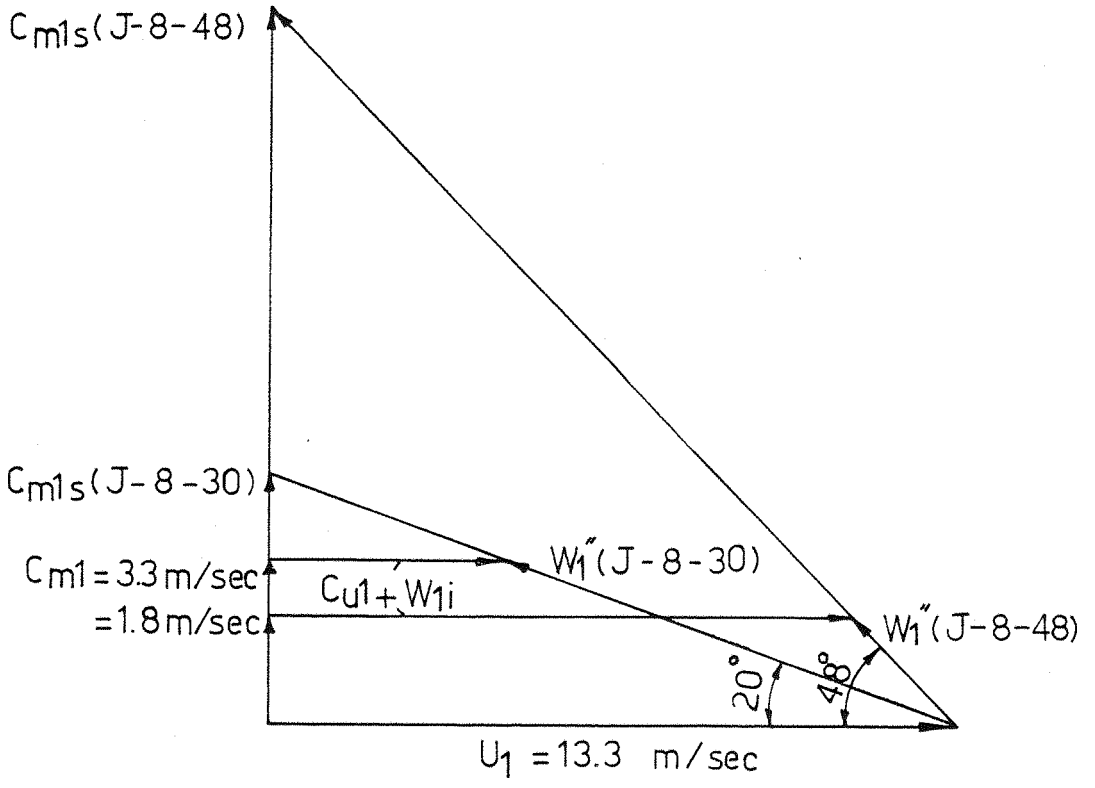

FIG 5.6 INLET VELOCITY TRIANGLE FOR 2 IMPELLERS OF PUMP J AT Qopt

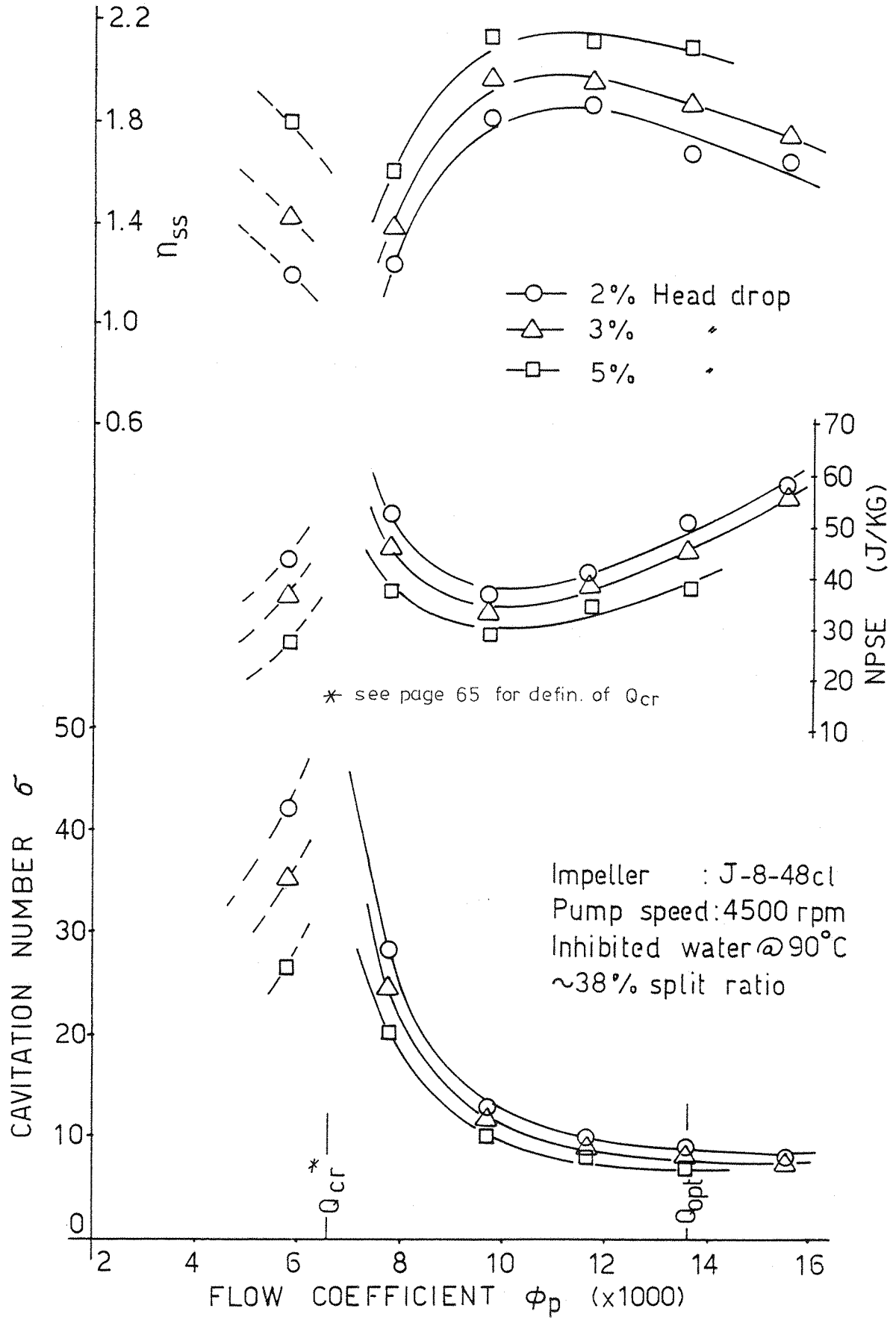

FIG 5.7 THE INFLUENCE OF THE TEST FLOW ON THE CAV. PERFORMANCE OF PUMP J WITH HOT WATER

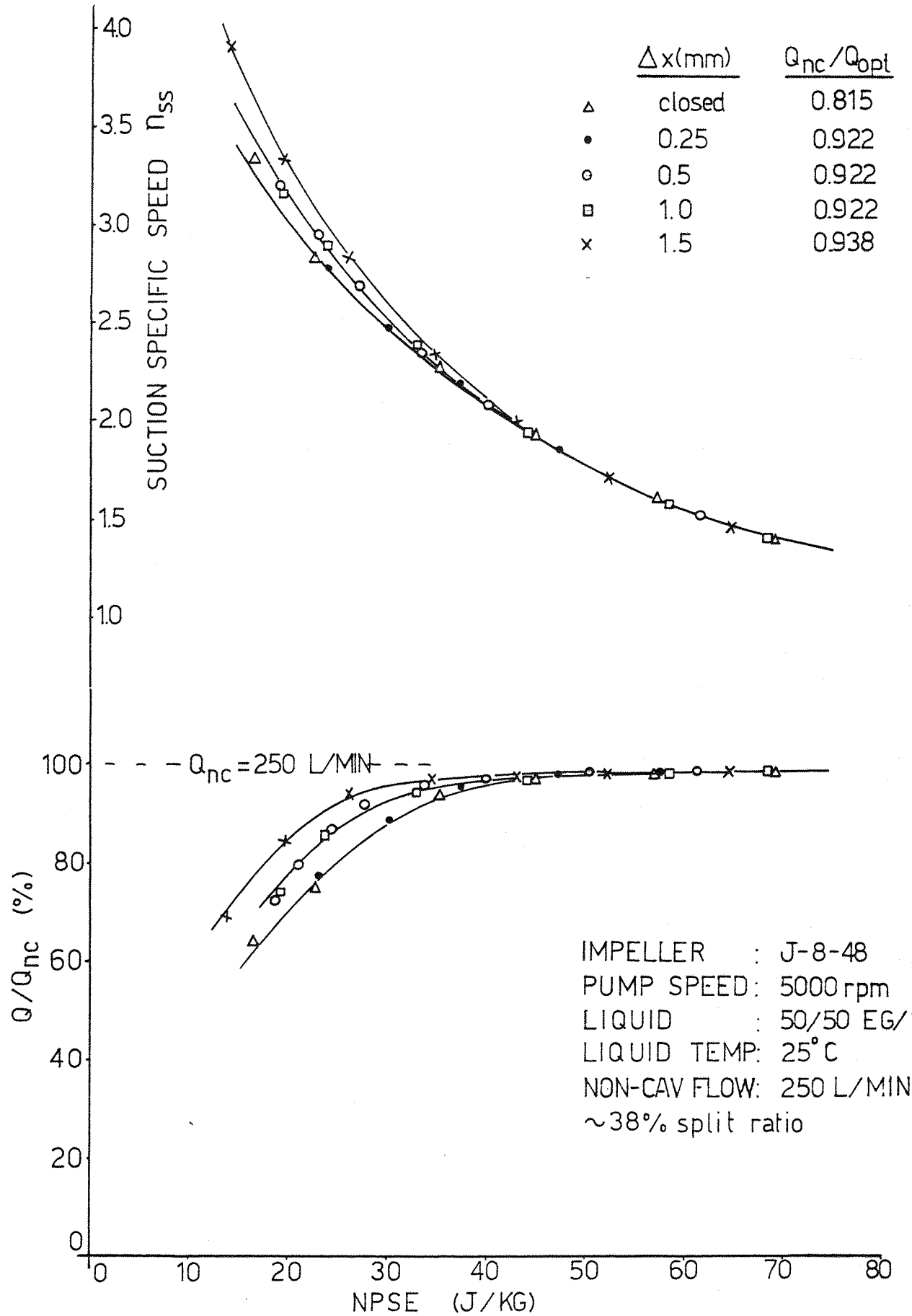

FIG. 5.8 THE EFFECT OF THE AXIAL TIP CLEARANCE ON THE CAVITATING BEHEVIOUR OF THE SEMI OPEN IMPELLER ON A CONSTANT RESISTANCE SYSTEM

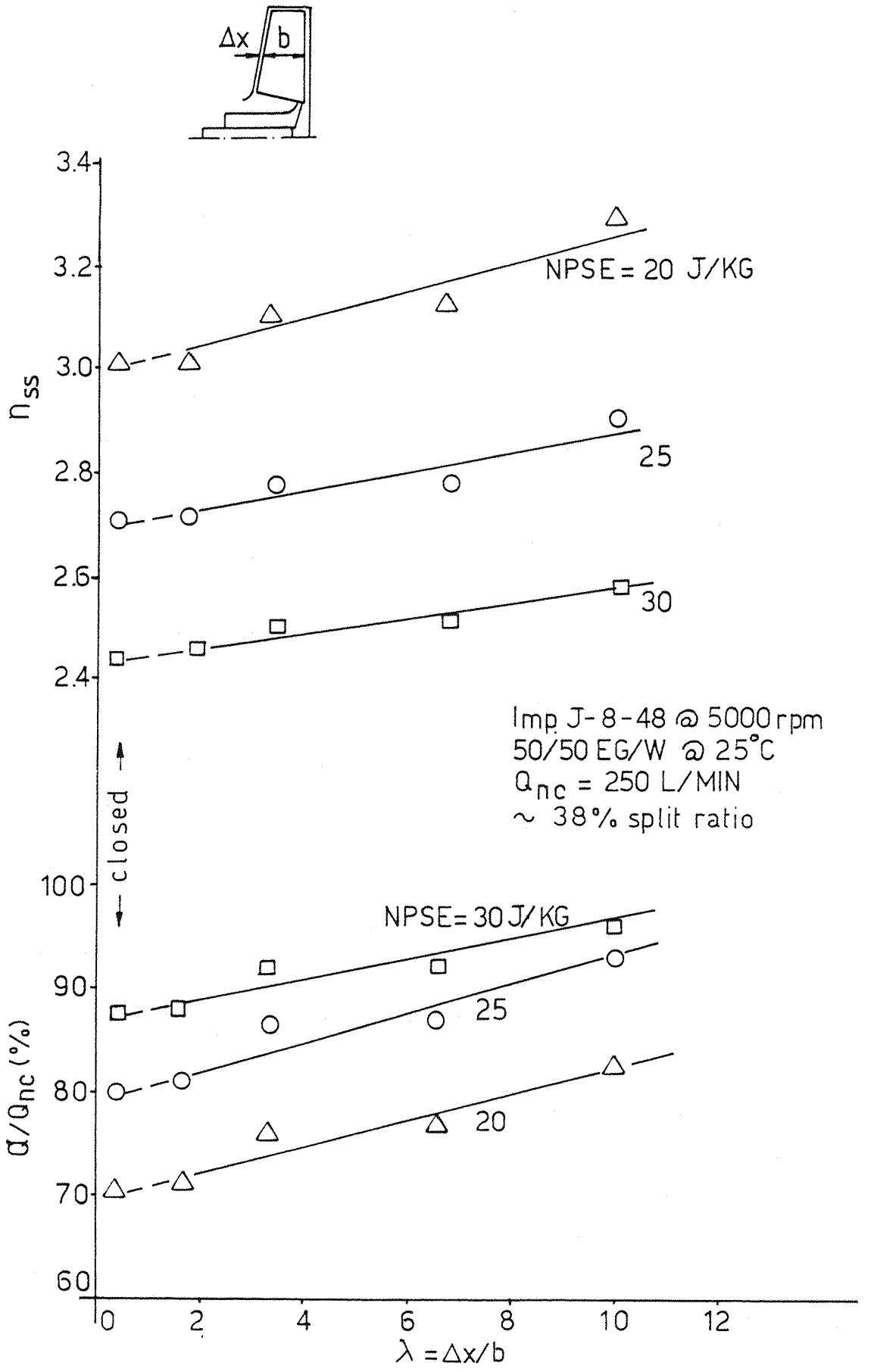

FIG 5.9 THE INFLUENCE OF THE TIP CLEARANCE ON THE CAVITATING FLOW PERFORMANCE OF PUMP J RUNNING AT A CONSTANT GEOMETRY SYSTEM

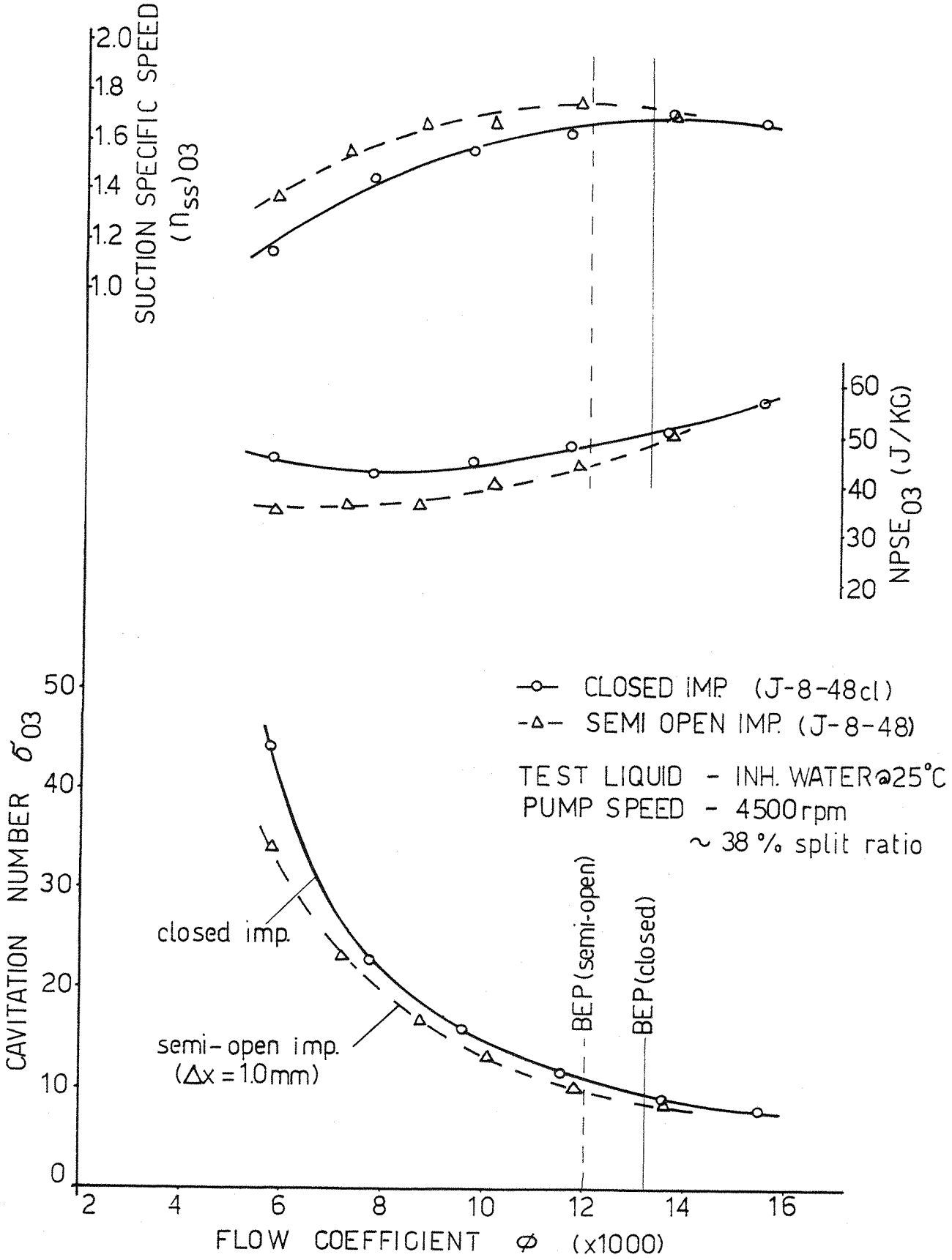

FIG. 5.10 CAVITATING FLOW PERFORMANCE OF PUMP J WITH THE CLOSED AND SEM-OPEN IMPELLER AT VARIOUS FLOWS

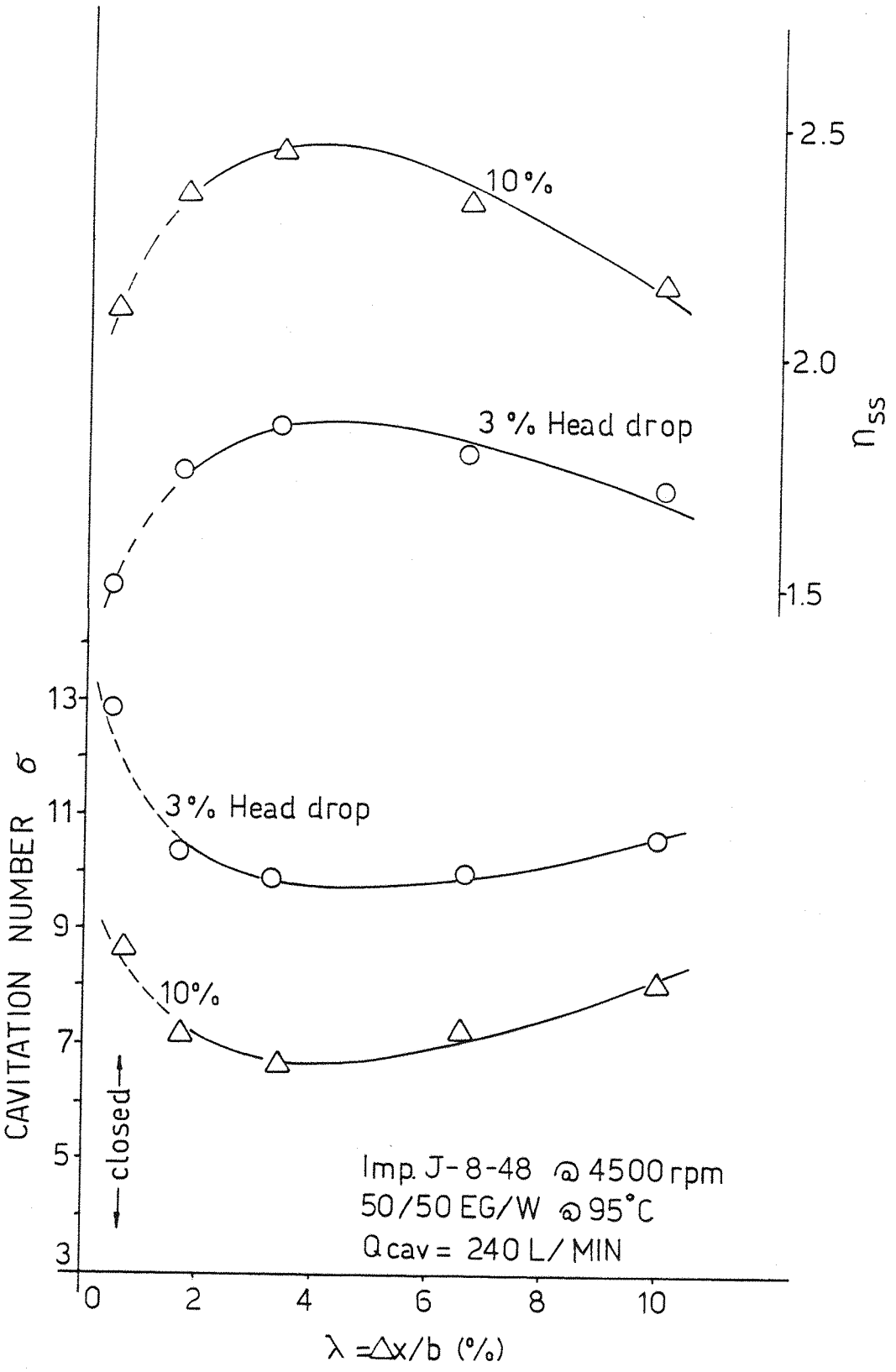

FIG 5.11 THE INFLUENCE OF THE TIP CLEARANCE ON THE CAVITATION OF PUMP J AT A CONSTANT TEST FLOW NEAR Qopt

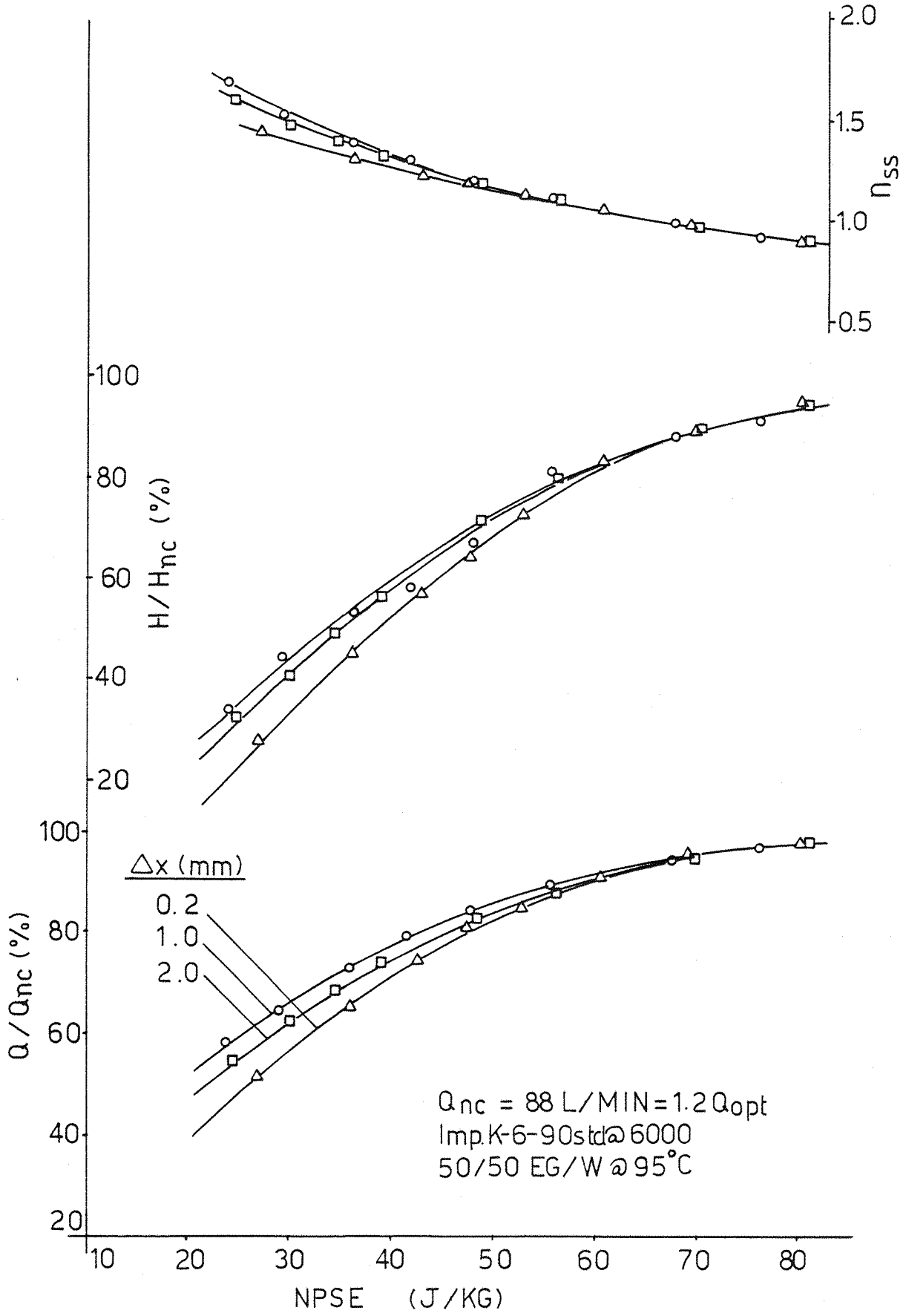

FIG 5.12 THE INFLUENCE OF THE TIP CLEARANCE ON THE CAVITATION OF PUMP K AT A CONSTANT GEOMETRY SYSTEM NEAR THE BEP

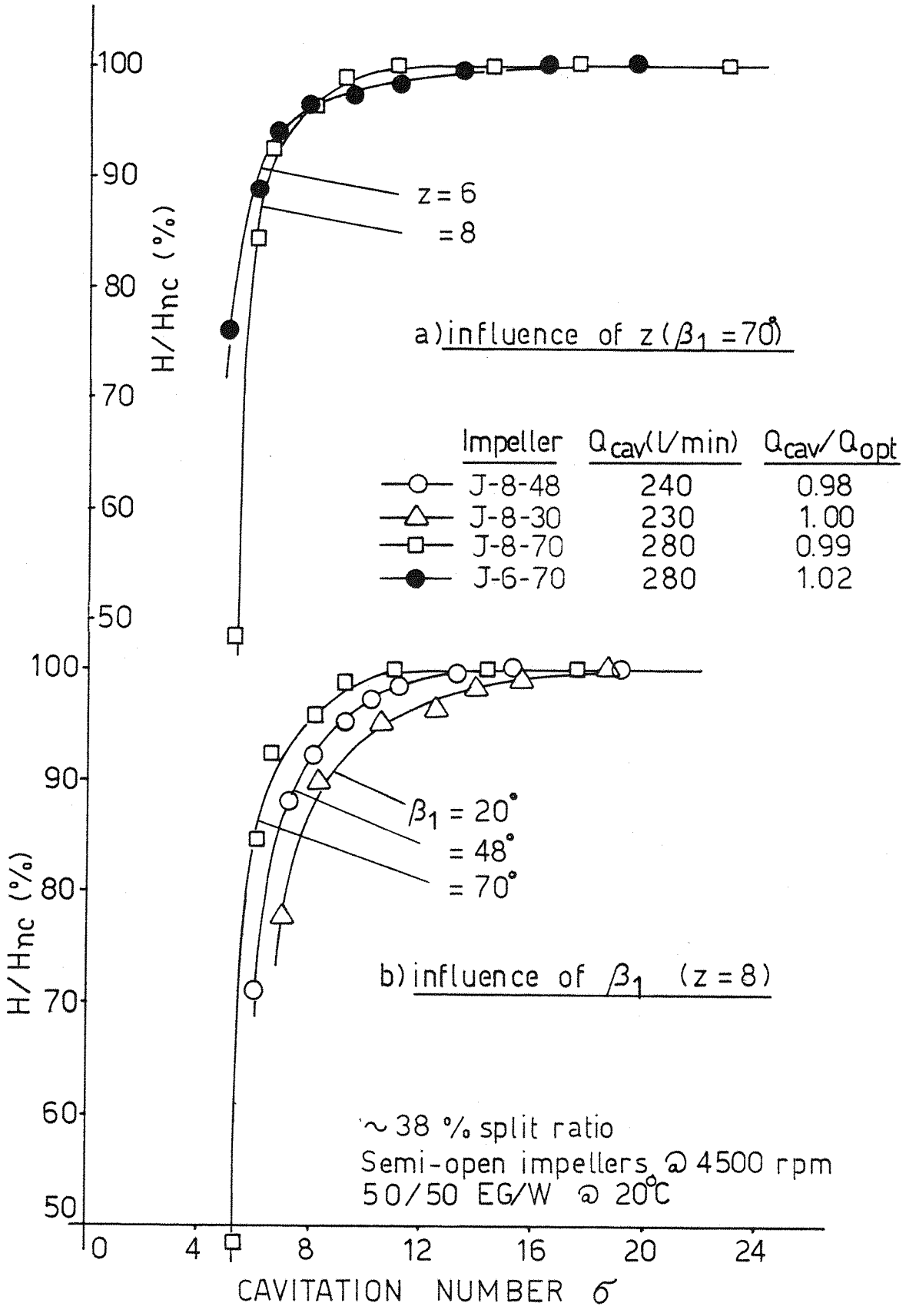

FIG 5.13 THE INFLUENCE OF IMPELLER GEOMETRY ON THE CAVITATION OF PUMP J AT A CONSTANT TEST FLOW NEAR Qopt

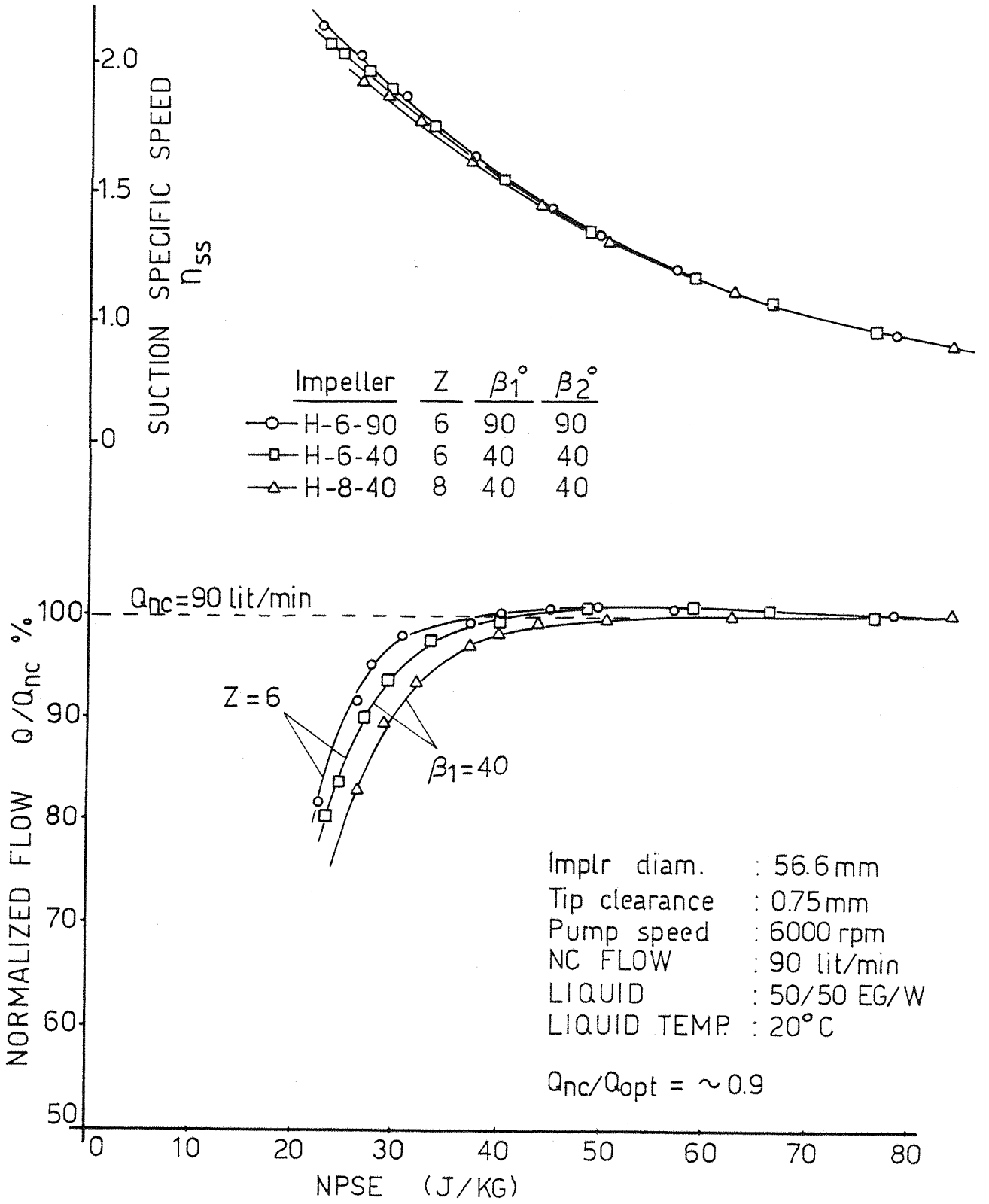

FIG.5.14 COMBINED EFFECT OF BLADE SHAPE AND NUMBER OF BLADES ON THE CAVITATING BEHAVIOUR OF PUMP H WITH A CONST RESISTANCE SYSTEM

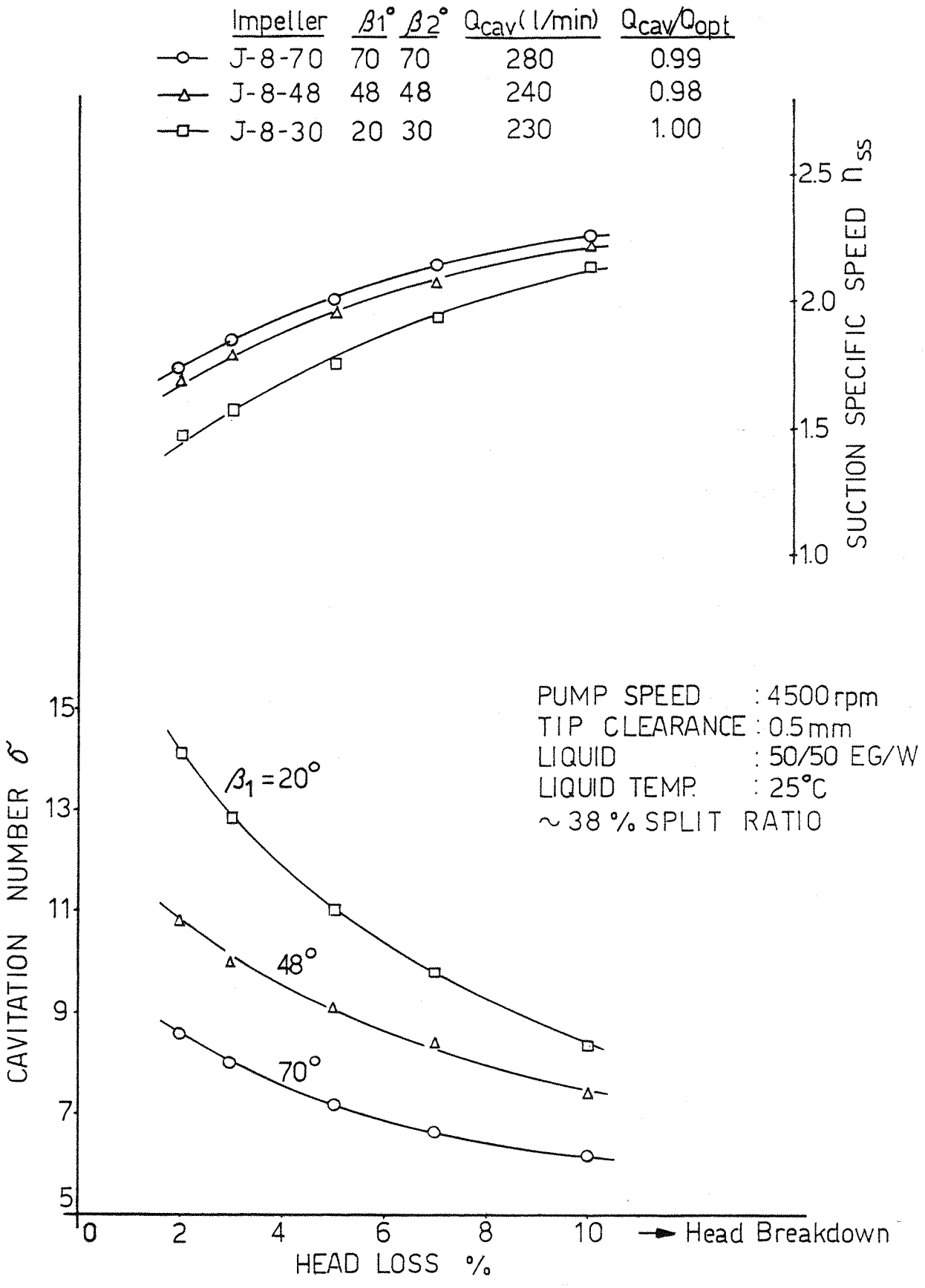

FIG. 5.15 THE EFFECT OF BLADE SHAPE ON THE CAVITATING PERFORMANCE OF PUMP J WITH 8-BLADED SEMI-OPEN IMPELLERS

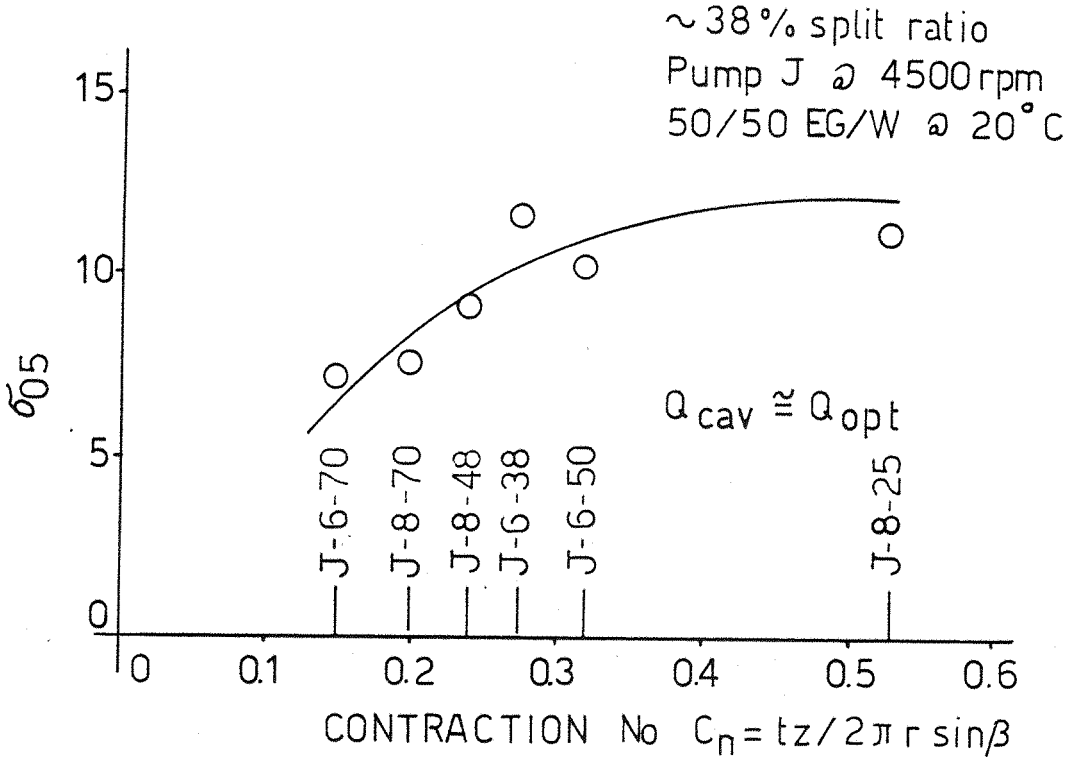

FIG 5.16 CRITICAL CAVITATION NUMBER AS FUNCTION OF THE INLET CONTRACTION NUMBER

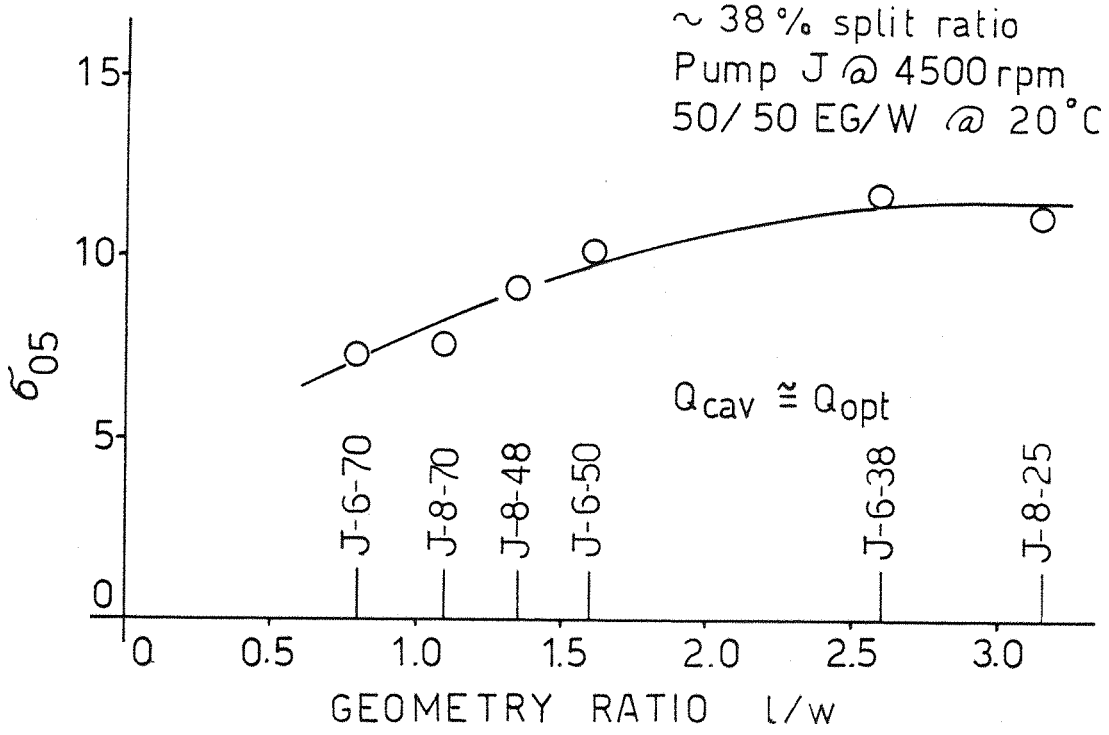

FIG 5.17 CRITICAL CAVITATION NUMBER AS FUNCTION OF THE IMPELLER GEOMETRY RATIO l/w

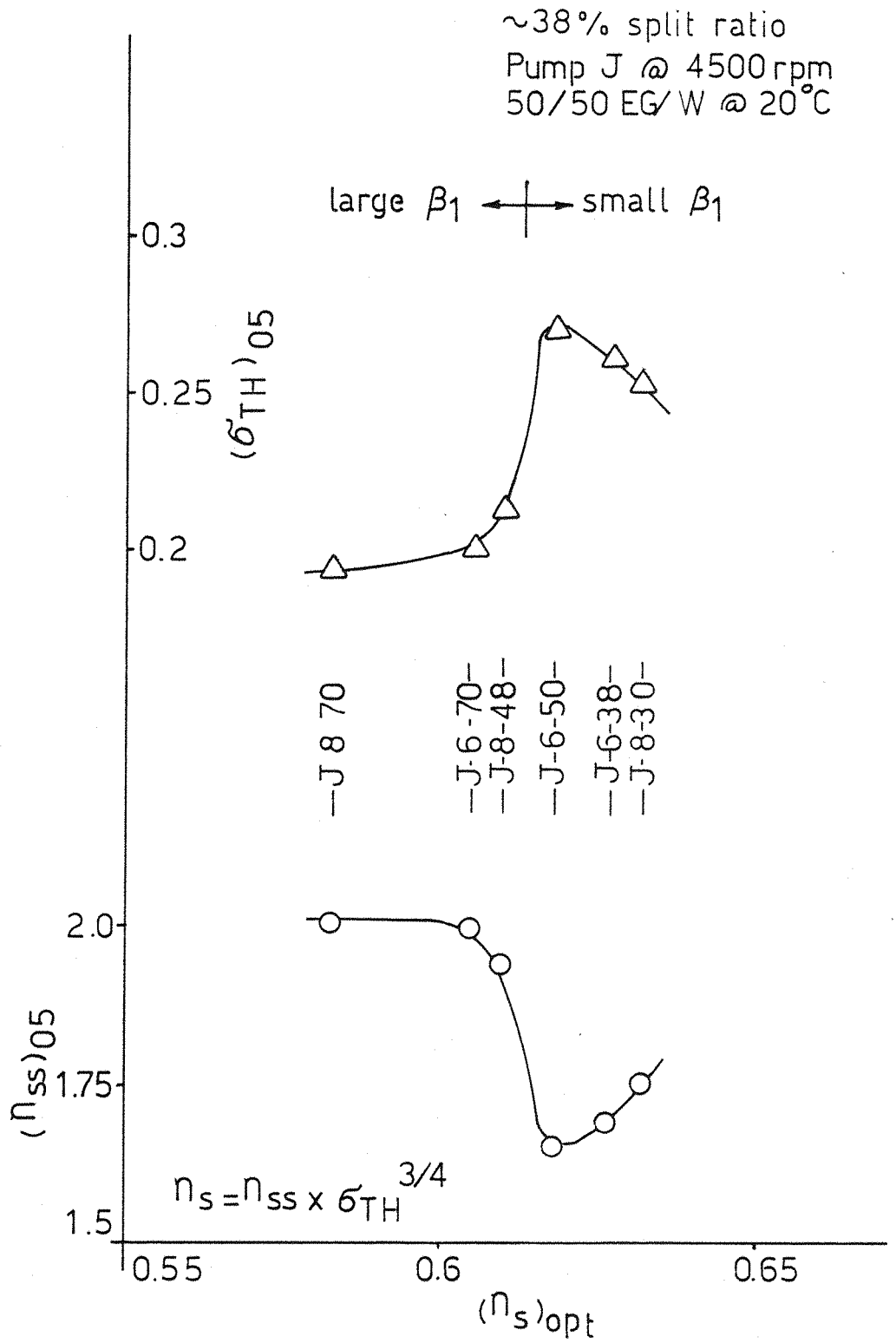

FIG 5.18 THE INFLUENCE OF IMPELLER GEOMETRY ON THE SPECIFIC SPEED AND RELATED CAVITATION PARAMETERS OF PUMP J

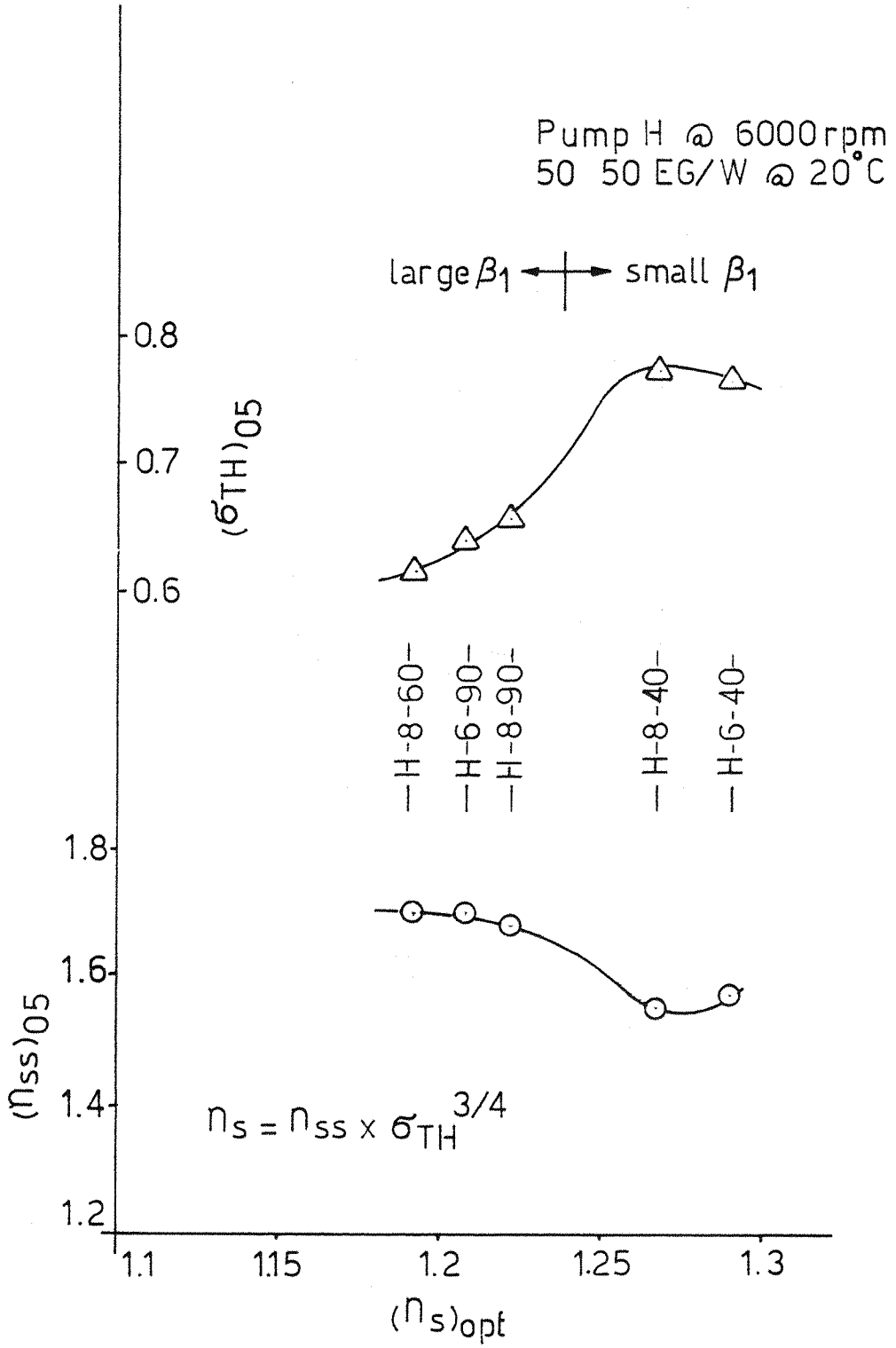

FIG 5.19 THE INFLUENCE OF IMPELLER GEOMETRY ON THE SPECIFIC SPEED AND RELATED CAVITATION PARAMETERS OF PUMP H

CHAPTER 6

REVIEW OF THE THEORY OF THE MECHANISM, SCALE EFFECTS AND THERMODYNAMICS OF CAVITATION

6.1 Nuclei and Bubble Growth

The term 'cavitation' is given to the process of development of cavities in liquids, their growth due to localized pressure drop and finally to their collapse while passing through a high pressure field.

Contrary to boiling, cavitation bubbles start to appear as a result of pressure reduction rather than temperature rise. However, in both cases, a state will be reached where the local static pressure of the liquid is equal to its vapour pressure with the result of bubble formation and growth.

For a pure homogeneous liquid, the forces tending to hold liquid particles together are external pressure and intermolecular cohesion forces. It is these cohesive forces which are known to support the tensile strength of liquids. For pure, de-aerated cold water, static tensile strengths as high as 150 atm were recorded [90]. Hall [66] reported a maximum tensile strength of 280 atm for cold water at 10°C measured by a centrifugal method. Several other tests on various pure liquids gave tensile strength varying between 0 and 20 atm [90].

Liquids encountered in most applications are far from being pure or homogeneous. Most liquids are either saturated or even super-saturated with air, and impurities such as solid particles and minerals are commonplace. All this helps to reduce the intermolecular forces considerably, and therefore, real life liquids are not expected to support any tension. However, some venturi tests [142] showed that nearly similar tensions were

required at the venturi throat to initiate the cavitation bubbles for both demineralized and tap water of similar air content.

The diminishing or complete disappearance of the tension in liquid can be related to weak spots which are commonly termed nuclei [66, 90]. For a spherical, small bubble of radius R_o, in equilibrium with the surrounding liquid, the difference between the pressure inside the bubble p_i and that of the surrounding liquid p_ℓ, is that due to the tensile force exerted by the surface tension at the bubble wall; or

$$p_{st} = \frac{2S}{R_o} = p_i - p_\ell \qquad (6.1)$$

The equilibrium of equation (6.1) cannot hold for molecular dimensions of R_o because that means extremely high p_i with the result of either condensing the vapour or pushing the trapped gas in the bubble into solution.

There are two major nucleation models [60]. The first is the stationary crevice model which applies mainly for boiling, and the second deals with entrained nuclei which are carried by flow stream and therefore are termed 'travelling nuclei'. The latter model is primarily applicable to cavitation but is also operative for boiling [60].

The reason why entrained nuclei do not disappear completely when enough liquid pressurization is present remains obscure. For liquid saturated with air Epstein and Plesset [44], found that entrained gas bubbles which can act as cavitation nuclei, need some time to disolve in water depending on the equilibrium radius R_o. Bubbles of smaller radius ($\sim 10^{-3}$ cm) need only 7 seconds to disolve in water, whereas larger bubbles ($R_o = 10^{-2}$ cm) do persist much longer (about 100 minutes).

In a flowing system, where pumps are employed to circulate the liquid in a closed loop, Ripken and Killen [135] found that vortex flows associated with the hydrodynamic impellers do act as an excellent generator of gas

bubbles which are ultimately nuclei in the region of the flow system where cavitation occurs. They also found that the amount of liberated (free) gas bubbles depend on the amount of total gas present in the liquid. The pressure field of the flowing stream and the time available for the nuclei to reach stability ($\sim$ 3 minutes maximum). Once a certain amount of free gas is established in the flowing stream, cavitation inception was found to increase with the amount of free gas present (in ppm) at any flow velocity of the test.

Detection of cavitation nuclei is of vital importance to the understanding of the cavitation process, because the size and distribution of the bubbles approaching the low pressure section could have a large effect on that process. Morgan [104] summarized all the applied methods for nuclei measurements, of which Billet [17] applied the two most favoured optical methods on the same test section at the same time for comparison reasons. His results showed that the light scattering method is suitable for detection of smaller bubbles (less than 20 micrometer in diameter) which are mainly particles, whereas the holographic method was found to detect bubbles of larger size (> 10 μm). On the whole, the holographic method was found to be more accurate with higher accumulative values (up to $\sim$ 400 nuclei/cm^3). It is also suggested that only large nuclei of 100 μm and more are involved in the cavitation process [17].

For a spherical bubble of an equilibrium initial radius R_o entrained in the flow stream, the bubble wall starts to expand in radial direction when it enters a low pressure region. The bubble growth can be expressed by the extended Rayleigh equation [60, 133] for the inviscid isothermal case, at time t;

$$\ddot{R}R + \frac{3}{2}\dot{R}^2 = \frac{1}{\rho_\ell}(p_R - p_\ell) \qquad (6.2)$$

In this equation, R is the bubble radius at time t, $\dot{R} = dR/dt$, and p_R is the pressure immediately outside the bubble wall.

For a spherical bubble growing in a viscous liquid, the pressure at the bubble wall p_R can be modified to include the surface tension and viscosity of the liquid [60, 128];

$$p_R = p_i - \frac{2S}{R} - \frac{4\mu}{R}\dot{R} \qquad (6.3)$$

The internal pressure of the bubble p_i is composed of the vapour and any entrapped gas partial pressures, or;

$$p_i = p_v + p_g \qquad (6.4)$$

Combining equations (6.4), (6.3) and (6.2) yields the so-called Rayleigh-Plesset equation [66, 71];

$$\ddot{R}R + \frac{3}{2}\dot{R}^2 = \frac{1}{\rho_\ell}\left(p_v + p_g - p_\ell - \frac{2S}{R} - 4\mu\frac{\dot{R}}{R}\right) \qquad (6.5)$$

The vapour pressure is that for the wall temperature T_R which is assumed not to vary much for the cold liquid. Otherwise the energy equation should be applied [66].

A close examination of equation (6.5) reveals that both the surface tension and the fluid dynamic viscosity restrain the growth of the bubble. If all dynamic parts of this equation are reduced to zero and the bubble is stabilized again at a new radius R, a process termed 'pseudo cavitation' by Holl [67], then equation (6.5) reduces to the equilibrium condition expressed by;

$$p_v + p_g = p_\ell + \frac{2S}{R} \qquad (6.6)$$

with $p_\ell = p_R$.

Neglecting the viscosity effect on the growth of a vapour bubble (and with $p_g \sim 0$), Plessett [128] integrated equation (6.5) to reach the following

equation for the bubble wall velocity;

$$\dot{R}^2 = \left(\frac{R_o}{R}\right)^3 \dot{R}_o^2 + \frac{3}{2}\frac{p_v - p_\ell}{\rho_\ell}\left[1 - \left(\frac{R_o}{R}\right)^3\right] - \frac{2S}{\rho_\ell R}\left[1 - \left(\frac{R_o}{R}\right)^2\right] \tag{6.7}$$

And for $R >> R_o$ and $p_v > p_\ell$, the growth velocity reduces to the approximate asymptotic value; which can be put for the radius at the end of the growth period;

$$R = \left(\frac{2}{3}\frac{p_v - p_\ell}{\rho_\ell}\right)^{\frac{1}{2}} \tag{6.8}$$

Similar results can be obtained from the isothermal bubble growth of a boiling cavity. Initial bubble size can be related to the superheat of the liquid $\theta_o = T_\infty - T_s$, which is equivalent to the tensile stress of the liquid.

Assuming homogeneous nucleation process for an initial superheat θ_o of the liquid, only vapour cluster with a radius R_o are in meta-stable equilibrium with the surrounding liquid [173], or

$$R_o = \frac{2S\ T_s}{\rho_v\ L\ \theta_o} \tag{6.9}$$

and;

$$\dot{R} = \left(\frac{2\ \rho_v\ L\ \theta_o}{3\ \rho_\ell\ T_s}\right)^{\frac{1}{2}} \tag{6.10}$$

By eliminating θ_o from equations (6.9) and (6.10) and integrating for the bubble radius;

$$R = \left(\frac{2}{3}\frac{2S}{\rho_\ell\ R_o}\right)^{\frac{1}{2}} \tag{6.11}$$

Noting that from equation (6.1) for $p_i = p_v$, the surface tension term $2S/R_o$ is equal to $p_v - p_\ell$ and therefore for a bubble in a m ta-stable equilibrium with the surrounding liquid, both equations (6.8) and (6.11) seem to be identical.

6.2 Scale Effects of Cavitation

The 'classical laws' of cavitation imply that cavitation will occur whenever the static pressure in the region of minimum pressure reaches the vapour pressure of the liquid at the existing temperature. Any departure from these laws is given the terminology 'cavitation scale effects' [60]. A very useful scaling parameter expressing the degree of cavitation is the cavitation number σ defined as follows;

$$\sigma = \frac{p_\infty - p_v}{\frac{1}{2}\rho_\ell V_\infty^2} \qquad (6.12)$$

Cavitation scale effects are numerous and according to Holl [63] and Billet [18], two major types can be distinguished. Type one are scale effects acting on the flow outside the cavitation bubbles and thus are associated with changes in the flow field caused by variations in Reynolds number Re, Froude number Fr, Mach number Ma and boundary conditions. Type two are scale effects acting on the bubble growth process thus causing the bubble wall pressure p_R to depart from the equilibrium vapour pressure corresponding to the bulk temperature of the liquid. These type two effects are primarily due to the following [18, 55];

- Time effect
- Heat transfer effect
- Surface tension effect
- Transport of non condensable gases
- Cavitation nuclei.

The bubble growth has been expressed in equation (6.5) by assuming that the bubble wall temperature is not much different from the bulk liquid temperature; which is an approximation valid for cold water [66]. However, if liquids of high vapour pressures such as hot water or cryogenic fluids are involved, then this assumption cannot be valid [128] and equation (6.5) takes the form;

$$\ddot{R}R + \frac{3}{2}\dot{R}^2 = \frac{1}{\rho_\ell}\left(p_v\,(T_R) + p_g - p_\ell - \frac{2S}{R} - 4\mu\,\frac{\dot{R}}{R}\right) \tag{6.13}$$

$p_v(T_R)$ is the equilibrium vapour pressure at the bubble wall. Introducing a pressure and a temperature coefficient defined by;

$$C_p = \frac{p_\infty - p_\ell}{\frac{1}{2}\,\rho_\ell\,V_\infty^{\,2}} \tag{6.14}$$

$$C_T = \frac{p_v\,(T_\infty) - p_v\,(T_R)}{\frac{1}{2}\,\rho_\ell\,V_\infty^{\,2}} = \frac{\Delta p_v}{\frac{1}{2}\,\rho_\ell\,V_\infty^{\,2}} \tag{6.15}$$

and inserting into equation (6.13), Holl [65] arrived at the following equation;

$$\ddot{R}R + \frac{3}{2}R^2 = \frac{1}{\rho_\ell}\left[p_g - \frac{2S}{R} - 4\,\frac{\mu\dot{R}}{R} + (C_p - \sigma - C_T)\,\frac{1}{2}\,\rho_\ell\,V_\infty^{\,2}\right] \tag{6.16}$$

Multiplying equation (6.16) by dt and integrating over a typical time interval of the cavitation process t, Billet [18] arrived at the following expression for the cavitation number;

$$\sigma = C_p + \frac{p_g - 2\,S/R}{\frac{1}{2}\rho_\ell V_\infty^2} - \phi - C_T \qquad (6.17)$$

All parameters of equation (6.17) are average values over the time interval t. The bubble dynamic parameter ϕ is given by;

$$\phi = [\frac{1}{t}\int_0^t (\frac{4\mu\dot{R}}{R} + \rho_\ell (R\ddot{R} + \frac{3}{2}\dot{R}^2))\,dt] \,/\, \frac{1}{2}\rho_\ell V_\infty^2 \qquad (6.18)$$

To include the effect of turbulence and boundary layer condition, Daily [39] and Holl [64] found that the liquid pressure p_ℓ at the boundary is lower than the mean local pressure $\bar{p}_\ell$ by an amount Δp_{TR} due to turbulence and roughness losses at the boundary and therefore;

$$p_\ell = \bar{p}_\ell - \Delta p_{TR} \qquad (6.19)$$

Substituting p_ℓ in equation (6.14);

$$C_p = \bar{C}_p + \Delta p_{TR} \,/\, \frac{1}{2}\rho_\ell V_\infty^2 \qquad (6.20)$$

and finally equation (6.17) takes the form;

$$\sigma = (\bar{C}_p + \frac{\Delta p_{TR}}{\frac{1}{2}\rho_\ell V_\infty^2}) - (\phi + C_T + \frac{2\,S/R}{\frac{1}{2}\rho_\ell V_\infty^2} - \frac{p_g}{\frac{1}{2}\rho_\ell V_\infty^2}) \qquad (6.21)$$

The first bracket of the right hand side of equation (6.21) represents type one scale effects which influence the flow outside the cavity. The second bracket represents type two scale effects produced by the thermal and dynamic action at the bubble wall. Examination of equation (6.21) shows that increased pressure coefficient $\bar{C}_p$, increased boundary layer losses Δp_{TR} and higher gas pressures p_g are likely to increase σ and hence

promote cavitation. Thermodynamic effect C_T, surface tension and bubble dynamics seem to favour a reduced σ and hence suppress cavitation. In the absence of a significant dynamic action within the cavitation region ($\phi \to 0$) implying a stabilized bubble radius, equation (6.21) represents the same form of equation presented by Holl [64] for pseudo equilibrium limited cavitation.

In the next two sections the thermodynamic effect of cavitation will be analysed in more detail, for both the pure liquids and for the binary mixtures. The influence of the gas pressure p_g will be discussed in the next chapter.

6.3 Thermodynamic Effect and the Fixed Cavity Theorem

In considering the thermodynamic effect on the performance of centrifugal pumps the heat transfer across a boiling vapour bubble during its growth is to be analysed first. Then the theory of the fixed cavity is to be explored. This theory deals with the concept of an attached cavity of appreciable size of the vapour phase persisting at the low pressure region of the hydro-dynamic machine.

Consider a spherical bubble in superheated liquid with an initial radius R_o according to equation (6.9). Then according to Plesset [128], the bubble starts to grow very slowly under the restraining effect of surface tension if the equilibrium of that equation is disturbed. If the initial superheat is sufficiently large the bubble radius will reach the asymptotic value of equation (6.11) governed by the inertial effect. A state will be reached where the vapour inflow into the bubble is so large as to produce a substantial cooling of the surrounding liquid. At this point, both inertial and thermal effects limit the growth rate. The growth rate then begins to decrease making inertial effects less and less important until the radius has grown so large that the growth process is limited only by the rate at which heat can be supplied to the bubble wall.

The rate of mass of vapour $\dot{m}_v$ flowing into the bubble is given by;

$$\dot{m}_v = (4\pi R^2)\ \dot{R}\ \rho_v \qquad (6.22)$$

The heat influx h_q corresponding to $\dot{m}_v$ is given by;

$$h_q = \dot{m}_v\ L = 4\pi R^2\ \dot{R}\ \rho_v\ L \qquad (6.23)$$

The heat transfer across the bubble boundary can occur in two ways; convection and conduction. Convection heat transfer requires a translational motion between the bubble and the liquid. Due to small pressure gradients existing in the reduced pressure region, Jackobson [81] neglected the convective heat transfer part which is a reasonable assumption for pump application.

For a thin heat transfer layer, the conductive heat flux into the bubble according to Plesset [128] and from figure 6.1, is as follows;

$$h_q = (4\pi R^2)\ k\ \theta_o\ /\sqrt{\alpha t} \qquad (6.24)$$

k is the thermal conductivity of the liquid, θ_o is the initial superheat $(= T_\infty - T_s)$ and α is the heat diffusivity $(= k/C_{p_\ell}\rho_\ell)$.

Combining equations (6.23) and (6.24), and introducing an adjustment constant in order to obtain an asymptotic value, the bubble growth velocity according to Plesset [128] reads as follows;

$$\dot{R} = \left(\frac{3}{\pi}\right)^{\frac{1}{2}}\ \frac{k}{L\ \rho_v}\ \frac{\Delta T}{\sqrt{\alpha t}} \qquad (6.25)$$

ΔT is the temperature difference between that of the bulk liquid and the temperature at the bubble wall. The equilibrium pressure at the bubble wall is that of the bulk liquid and therefore the bubble surface temperature reaches the saturation temperature T_s and therefore ΔT is equivalent to the

superheat θ_o.

Solving for ΔT gives;

$$\Delta T = (\frac{\pi}{3})^{\frac{1}{2}} \dot{R} \rho_v \frac{L}{k} \sqrt{\alpha t} \qquad (6.26)$$

Bonnin [21, 22, 23] elaborated on equation (6.26) to find an expression for the pressure depression Δp_v corresponding to ΔT, by equating;

$$\frac{\Delta p_v}{\Delta T} = \frac{dp_v}{dT} \qquad (6.27)$$

From which;

$$\Delta p_v = (\frac{\pi}{3})^{\frac{1}{2}} \dot{R} \rho_v \frac{L}{k} \sqrt{\alpha t} (\frac{dp_v}{dT}) \qquad (6.28)$$

and by integrating over the time interval of the cavitation process t, Bonnin obtained for the average bubble radius R;

$$\Delta p_v = (\frac{\pi}{12})^{\frac{1}{2}} \frac{R \rho_v L}{k} (\frac{\alpha}{t})^{\frac{1}{2}} (\frac{dp}{dT}) \qquad (6.29)$$

The thermal depression $\Delta p_v (= \rho_\ell \Delta E_v)$ is obviously a function of the thermodynamic properties of the liquid, the bubble radius at the point of observation R, and the residence time available for the growth (t).

In trying to establish a correlation prediction for the thermodynamic effect on the performance of small centrifugal pumps running with different liquids and liquid mixtures, both heat transfer across the bubble boundary and those associated with the attached cavity are to be considered. Because small pumps of side suction design are likely to be associated with a free vortex cavitation at impeller hub (see next chapter) with a strong velocity gradient inside the vortex, the assumption to ignore the convective heat transfer effect at the bubble surface [81] may be erroneous. However

a treatment with a combined conductive, convective heat transfer is beyond the scope of this work.

The bubble growth approach discussed above assumes a bubble surrounded completely by liquid with a very thin conduction heat transfer layer ($\sqrt{\alpha t} \ll R$). This is true in the case of cavitation inception where the bubble density is only small and the bubble is therefore completely surrounded by superheated liquid. When a stage is reached where the cavitation is well developed, an attached cavity will persist at the low pressure region and hence a modified form of thermal approach is needed. The entrainment theory developed by Holl [68] and Billet [19] is one of these approaches as outlined below.

To maintain an attached cavity (figure 6.2), a constant supply of vapour across the boundary of the cavity is necessary. The rate of heat flux h_q is given by;

$$h_q = \dot{m}_v L = \rho_v \dot{q}_v L \qquad (6.30)$$

whereby $\dot{q}_v$ is the vapour volume flow influx. Also for conductive heat transfer across the cavity wall;

$$h_q = C_h A_w \Delta T \qquad (6.31)$$

C_h is a film heat transfer coefficient and A_w is the cavity surface area. Combining equations (6.30) and (6.31);

$$\Delta T = \frac{\rho_v \dot{q}_v L}{C_h A_w} \qquad (6.32)$$

Introducing a vapour flow coefficient C_q and area coefficient C_a defined by [19, 68];

$$C_q = \frac{\dot{q}_v}{V_\infty D^2} \qquad (6.33)$$

$$C_a = A_w / D^2 \qquad (6.34)$$

whereby V_∞ is the free stream velocity and D is the model diameter. Combining equations (6.32), (6.33) and (6.34) gives;

$$\Delta T = \frac{C_q}{C_a} \frac{\rho_v}{C_h} L V_\infty \qquad (6.35)$$

Noting that $Pe = V_\infty D/\alpha$ $(= V_\infty D/\frac{k}{C_{p\ell}\rho_\ell})$ and $Nu = C_h D/k$, equation (6.35) can be expressed in the form;

$$\Delta T = \frac{C_q}{C_a} \frac{Pe}{Nu} \frac{\rho_v}{\rho_\ell} \frac{L}{C_{p\ell}} \qquad (6.36)$$

Billet [19] attempted to solve equation (6.36) empirically by determining the unknown parameters C_q, C_a and Nu. He suggested the final empirical form;

$$\Delta T = C(\ell_c/D)^k \, Re^\ell \, Fr^m \, We^n \, Pr^p \, Pe \, \frac{\rho_v}{\rho_\ell} \frac{L}{C_{p\ell}} \qquad (6.37)$$

This form of equation shows the tremendous difficulties associated with this approach; however exact the solution may be, for one case it cannot be immediately generalised.

A much simpler approach can be obtained by considering the following thermodynamic relationships at the cavity wall;

$$\Delta h_f = C_{p\ell} \Delta T \qquad (6.38)$$

also

$$\Delta h_f = \frac{\dot{m}_v}{\dot{m}_\ell} L \qquad (6.39)$$

and;

$$\Delta h_f = \frac{V_v}{V_\ell} \cdot \frac{\rho_v}{\rho_\ell} L \qquad (6.40)$$

Combining equations (6.38) and (6.40) gives;

$$\Delta T = B \frac{\rho_v}{\rho_\ell} \frac{L}{C_{p_\ell}} \qquad (6.41)$$

Whereby B is the vapour to liquid volume ratio (V_v/V_ℓ) passing through the low pressure zone per unit time, also known as Stepanoff's B factor [155, 158, 159]. Comparison between equation (6.41) and (6.36) yields;

$$B \cong \frac{C_q}{C_a} \frac{Pe}{Nu} \qquad (6.42)$$

which shows that the simple form of the cavitation tendency given by B has a much more complex origin.

The pressure depression Δp_v corresponding to ΔT can be established from the Clapeyron equation;

$$\frac{\Delta p_v}{\Delta T} T = \frac{-L}{v_\ell - v_g} \qquad (6.43)$$

Noting that $V_v >> V_\ell$ so that it can be ignored and that $\Delta p_v = \rho_\ell \Delta E_v$; then

$$\Delta E_v = \Delta T \frac{\rho_v}{\rho_\ell} \frac{L}{T} \qquad (6.44)$$

Substituting for ΔT from equation (6.41) gives;

$$\Delta E_v = B/\beta \qquad (6.45)$$

whereby β is a new (thermal) parameter;

$$\beta = C_{p\ell} T \left(\frac{\rho_\ell}{\rho_v} \frac{}{L}\right)^2 \qquad (6.46)$$

Ward and Sutton [179] showed that most approaches to the attached cavity phenomena such as those by Stepanoff [158], Salemann [145], Jacobs [80], Spraker [154] and Barenboin [13] reduce to the same form of equation (6.45).

Floyancic [46] considered an attached cavity supplied by bubbles growing from an initial radius R_o upstream of the low pressure region to a much larger stabilized radius R inside the cavity (figure 6.3).

By assuming that independent spheres of equal radius are involved, then the total vapour volume passing per unit time can be expressed by the simple formula;

$$V_v = Z \left(\frac{4}{3} \pi R^3\right) \quad (m^3) \tag{6.47}$$

From experience [46] the average number of bubbles Z changes only slightly ($\sim$ 5%) for any one liquid of low gas content over the temperature range normally encountered in the test programme. Assuming a similar initial radius and similar time available for the bubble growth, then equation (6.11) can be used for the bubble radius R. Hence equation (6.47) is reduced to;

$$V_v = K_1 \left(\sqrt{\frac{S}{\rho_\ell}}\right)^3 \tag{6.48}$$

The constant $\sqrt{S/\rho_\ell}$ is proportional to the Laplace constant ($\sim \sqrt{S/g(\rho_\ell - \rho_v)}$), which is of decisive importance for the theory of bubbles and drops in liquid/vapour biphase systems [46].

By using $a = \sqrt{S/g\,\rho_\ell}$ for $\rho_\ell >> \rho_v$ we have;

$$V_v = K_2\, a^3 \tag{6.49}$$

The volume flow rate V_ℓ is normally constant for the test and hence;

$$B = \frac{V_v}{V_\ell} = K_3 a^3 \qquad (6.50)$$

with the constant K_3 taking the final form;

$$K_3 = \frac{Z}{V_\ell} \frac{4}{3} \pi \left(\frac{4g}{3R_o}\right)^{3/2} \qquad (6.51)$$

The applications of equation (6.50), however, is doubtful because it includes parameters such as Z and R_o which are difficult to determine and may vary during the test. Its significance lies however, in the importance of the number of bubbles (and nuclei) and their growth rate, which is of great importance for cavitation in binary mixtures (see Chapter 9).

From the principle of conservation of energy to the bubble during its growth and from the energy equation of a single bubble in an infinite liquid, Jacobson [81] showed that ΔE_v is proprtional to $R^2/2$, and therefore is proportional to a^2 [46]. This may lead to the final conclusion of $\Delta E_v \sim B^{2/3}$ [81].

The internal pressure p_i of equation (6.4) can be modified to accommodate for the thermal depression in the form;

$$p_i = p_v + p_g - \Delta p_v \qquad (6.52)$$

Therefore exact measurement of the cavity pressure p_i would lead to a precise determination of Δp_v. Hutton [75] supported by the work of Furness [51] made an attempt to measure p_i in a fixed cavity and found that using p_i as a scaling factor instead of p_v would in fact result in reduced scaling effect and therefore they suggested the use of the modified cavitation number;

$$K_p = \frac{p_\infty - p_i}{\frac{1}{2} \rho_\ell V_\infty^2} \qquad (6.53)$$

Application of this theory to pumps, using data from Chivers [32, 33] for water and Freon 11 in the temperature range 10 - 110°C showed good similarity within ± 3%.

6.4 Boiling Heat Transfer of Binary Mixtures

The rate of bubble growth in a pure component depends on heat flow toward the bubble boundary to satisfy the heat requirements for evaporation. In liquid mixtures, on the other hand, heat diffusion is linked with mass diffusion of the more volatile component, which is rapidly exhausted in the liquid immediately adjacent to the bubble. The result of this is a low concentration and mass diffusivity of the more volatile component, which leads to a slowing down of bubble growth, because the mass diffusivity is an order of magnitude smaller than the thermal diffusivity [172, 173].

Consider first the bubble growth of a pure liquid given for the heat conduction case in equation 6.24, whereby the bubble wall temperature has reached the equilibrium saturated vapour temperature T_s and hence $\Delta T = \theta_o$; by integrating over the growth time and considering that $R(t) >> R_o$, hence [173];

$$R = \left(\frac{3}{\pi}\right)^{\frac{1}{2}} \frac{k\ \Delta T}{L\ \rho_v\ \sqrt{\alpha}} \left(2t^{\frac{1}{2}}\right) \qquad (6.54)$$

Multiplying the right hand side of equation (6.54) by $\sqrt{\alpha}/\sqrt{\alpha}$ and replacing α by $k/C_{p\ell}\ \rho_\ell$ we obtain;

$$R = \left(\frac{12}{\pi}\right)^{\frac{1}{2}} \frac{\rho_\ell C_{p\ell}}{\rho_v L}\ \Delta T\ \sqrt{\alpha t} \qquad (6.55)$$

The final radius R can also be expressed as a function of the Jacob's number, Ja ($= \rho_\ell\ C_{p\ell}\ \Delta T/\rho_v L$);

$$R = \left(\frac{12}{\pi}\right)^{\frac{1}{2}}\ Ja\ \sqrt{\alpha t} \qquad (6.56)$$

or more conveniently by;

$$R = F \Delta T t^{\frac{1}{2}} \tag{6.57}$$

in which F is a growth factor dependent on fluid properties only, and for the pure liquid is defined by;

$$F = \left(\frac{12}{\pi}\right)^{\frac{1}{2}} \frac{C_{p\ell}}{L} \frac{\rho_\ell}{\rho_v} \sqrt{a} \tag{6.58}$$

On figure 6.1, the temperature depression across the conduction layer for the pure liquid was assumed to be equal to the superheat of the liquid, once the bubble wall has reached the saturation pressure of the liquid, or, $\Delta T = \theta_o = T_\infty - T_s$. For the binary fluid mixture (figures 6.4 and 6.5), the dew temperature of the liquid adjacent to the bubble wall is increased by ΔT_s due to the increase in the saturation temperature of the boundary layer which is of a higher mass concentration of the less volatile component than the bulk concentration. This means that the actual depression across the boundary layer for the binary mixutre is less than that for the pure liquid according to;

$$\Delta T_{mix} = \Delta T - \Delta T_s \tag{6.59}$$

If one assumes the heat transfer to reach an equilibrium steady state, with slow changes for the vapourous cavity, then according to Van Stralen [172, 173], the bubble radius of equation (6.56) is also applicable for the binary mixture with a new modified Jacob's number;

$$(Ja)_{mix} = \frac{\rho_\ell}{\rho_v} \frac{C_{p\ell}}{L} \Delta T_{mix} \tag{6.60}$$

Since ΔT_{mix} is difficult to determine, it is more convenient to express the bubble radius for the mixture in a similar fashion to equation 6.57; or;

$$R_{mix} = F_{mix} \Delta T t^{\frac{1}{2}} \tag{6.61}$$

Several authors [25, 150, 153, 172, 175] have investigated the bubble growth phenomenon in superheated binary mixture in order to arrive at a theoretical value for F_{mix}. Scriven [150] considered the case for a spherical

vapour bubble expanding in a superheated binary mixture whereby the growth is governed by the vapour inflow into the bubble and therefore the radius expansion occurs at a steady rate. To account for the radial convection effects resulting from unequal densities as a result of phase changes, he modified the heat conduction equation for any point at distance r from the bubble radius (r/R > 1);

$$\frac{\partial T}{\partial t} = \alpha\left(\frac{\partial^2 T}{\partial r^2} + \frac{2}{r}\frac{\partial T}{\partial r}\right) - \varepsilon \dot{R} \frac{R^2}{r^2}\frac{\partial T}{\partial r} \qquad (6.62a)$$

whereby $\varepsilon = 1 - \rho_v/\rho_\ell$. Similarly for the concentration gradient in the surrounding liquid, he obtained the analogue equation;

$$\frac{\partial x}{\partial t} = \alpha_m\left(\frac{\partial^2 x}{\partial r^2} + \frac{2}{r}\frac{\partial x}{\partial r}\right) - \varepsilon \dot{R} \frac{R^2}{r^2}\frac{\partial x}{\partial r} \qquad (6.62b)$$

whereby x is the mass concentration of the more volatile component in the liquid mixture, and α_m is the mass diffusivity of the more volatile component into the less volatile component.

Van Stralen [173] modified the theories given by Scriven [150]; Van Wijk [175] and Brujin [25] to find an analogy between the heat and mass diffusion into the vapour bubble of a binary mixture. The mass flow equation takes the form;

$$\rho_v \; y \; R_{mix} = \rho_\ell \; \alpha_m \left(\frac{\partial x}{\partial r}\right)_{r=R_{mix}} \approx \rho_v \; (y-x) \; R_{mix} \qquad (6.62c)$$

whereby y is the mass fraction of the volatile component in the vapour phase (for EG/W mixture $y \to 1$ for concentration below 50% and below say 100°C).

Defining a bubble growth factor $\kappa = R/2\sqrt{\alpha t}$, Van Stralen was able to show that for $x(R_{mix}(t)) \to x$, that is, the concentration at the bubble boundary approaches a constant value, then from analogy of the asymptotic heat diffusion equation ($\Delta T_R \to 0$ as $t \to \infty$), we obtain;

$$x(R_{mix}(t)) - y = x_o - x - [x_o - x(R_{mix}(t))]$$

$$= x_o - x - [2(\frac{\pi}{12})^{\frac{1}{2}} \frac{\rho_v}{\rho_\ell} (y-x) (\frac{\alpha}{\alpha_m})^{\frac{1}{2}} \kappa]$$

(6.62d)

Equating 0 for the left hand side of equation (6.62d) and introducing a vapourized mass diffusion fraction for the binary mixture G (see figure 6.5b) in the form;

$$G = \frac{x_o - x}{y - x} \qquad (6.62e)$$

then from equation (6.62d);

$$G = 2(\frac{\pi}{12})^{\frac{1}{2}} \frac{\rho_v}{\rho_\ell} (\frac{\alpha}{\alpha_m})^{\frac{1}{2}} \kappa \qquad (6.62f)$$

For relatively large κ, i.e. sufficiently large superheat, it follows from equation (6.60) that [173];

$$\Delta T_s = T_s(x) - T_s(x_o) = (1 - \frac{F_{mix}}{F_p}) \Delta T \qquad (6.63a)$$

whereby F_p is given to the pure liquid. From both equation (6.60) and (6.62f) we also have;

$$G = (\frac{\alpha}{\alpha_m})^{\frac{1}{2}} \frac{F_{mix}}{F_p} \frac{C_{p\ell}}{L} \Delta T \qquad (6.63b)$$

The ratio $\Delta T_s/G$ (see figure 6.5b) simplifies in the asymptotic growth; i.e., vaporous growth at $t \to \infty$.

$$\frac{\Delta T_s}{G} = \left(\frac{\alpha_m}{\alpha}\right)^{\frac{1}{2}} \frac{L}{C_{p\ell}} \left(\frac{F_p}{F_{mix}} - 1\right) \tag{6.64}$$

From which we obtain;

$$F_{mix} = F_p \Big/ \left(1 + \frac{C_{p\ell}}{L} \left(\frac{\alpha}{\alpha_m}\right)^{\frac{1}{2}} \frac{\Delta T_s}{G}\right) \tag{6.65a}$$

and by substituting for F_p from equation (6.58) we obtain;

$$F_{mix} = \left(\frac{12}{\pi}\right)^{\frac{1}{2}} \frac{\sqrt{\alpha}}{(\rho_v/\rho_\ell)\left[\left(\frac{L}{C_{p\ell}}\right) + \left(\frac{\alpha}{\alpha_m}\right)^{\frac{1}{2}} \frac{\Delta T_s}{G}\right]} \tag{6.65b}$$

Solving for R_{mix} from equation (6.61);

$$R_{mix} = \left(\frac{12}{\pi}\right)^{\frac{1}{2}} \frac{\Delta T \sqrt{\alpha t}}{(\rho_v/\rho_\ell)\left[\left(\frac{L}{C_{p\ell}}\right) + \left(\frac{\alpha}{\alpha_m}\right)^{\frac{1}{2}} \frac{\Delta T_s}{G}\right]} \tag{6.66}$$

The assumptions for estimating R_{mix} may not be wholly justified, however, it is worth considering in order to obtain a lead into theoretical developments capable of furnishing predictive information.

Substituting ΔT of equation (6.55) by ΔT_{mix} for the mixture, we obtain;

$$R_{mix} = (\frac{12}{\pi})^{\frac{1}{2}} \frac{C_{p\ell}}{L} \frac{\rho_\ell}{\rho_v} \Delta T_{mix} \sqrt{\alpha t} \qquad (6.67)$$

Equating the right hand sides of equations (6.66) and (6.67) and solving for ΔT_{mix};

$$\Delta T_{mix} = \Delta T/[1 + \frac{C_{p\ell}}{L} (\frac{\alpha}{\alpha_m})^{\frac{1}{2}} \frac{\Delta T_s}{G}] \qquad (6.68)$$

or

$$\Delta T_{mix} = \Delta T/\psi_{mix} \qquad (\psi_{mix} > 1) \qquad (6.69)$$

This expression is very useful for the temperature depression associated with the thermal cooling of binary mixtures, which imples that ΔT_{mix} can readily be calculated from the mixtures physical properties.

Replacing R of equation (6.28) by R_{mix} of equation (6.67) will mean a reduction in the thermodynamic depression of the binary mixtures as a result of restricted bubble growth according to;

$$(\Delta p_v)_{mix} = \Delta p_v/\psi_{mix} \qquad (\psi_{mix} > 1) \qquad (6.70)$$

Hence the pressure depression of the binary mixture is a fraction of that of the pure liquid (of similar properties). The proportionality factor $1/\psi_{mix}$ is a complex function of the physical properties of the binary liquid, the mass diffusivity of the volatile component in the less volatile component, and the ratio $\Delta T_s/G$.

Tests performed by Scriven [150] and Benjamin [15] on the binary mixture Ethylene-glycol and water showed that from atmospheric boiling with various degrees of superheat the bubble growth of the mixture is

reduced below that of the volatile component (water), and reaches a minimum at a mass concentration of $\sim$ 5% water in the mixture. At this concentration, Ja(mix) reaches almost half that of the volatile component and about two-thirds of the less volatile component (Ethylene glycol), (see also figure 9.14).

A different approach to the reduced bubble growth in boiling binary mixtures is proposed by Stephan [160] based on convective pool boiling of these mixtures. Shock [152] also reviews all pertinent literature in this field.

Heat transfer in convection boiling of binary mixtures is known to be usually lower than that of the pure component of the mixture; which is related to the mass diffusion resistance to the volatile component due to increased concentration of the less volatile component at the vapour liquid interface.

Following the finding that heat flux densities for boiling of a binary mixture do not show a linear change with molar change, Stephan [160] elaborated on a theory to introduce a correction factor to the molar fraction relationship, which can be simplified as follows [27];

Defining an ideal heat transfer coefficient of the mixture $(h_{mix})_{id}$ which varies linearly with molar fraction ratios of the pure liquids. The reciprocal of h_{mix} is the superheat ΔT_{mix} and for unit heat flux it takes the form;

$$(\Delta T_{mix})_{id} = X_1 \Delta T_1 + (1 - X_1) \Delta T_2 \qquad (6.71)$$

The subscripts 1 and 2 describe the volatile and the less volatile compound respectively.

The actual superheat of the mixture is suggested to take the form [160];

$$\Delta T_{mix} = \phi_{mix} (\Delta T_{mix})_{id} \qquad (\phi_{mix} > 1) \qquad (6.72)$$

and for the heat transfer coefficient (for similar ΔT);

$$h_{mix} = (h_{mix})_{id}/\phi_{mix} \qquad (6.73)$$

whereby in both cases;

$$\phi_{mix} = 1 + K_{mix} (Y_1 - X_1) \qquad (6.74)$$

Y_1 is the molar fraction of the more volatile component in the vapour phase ($Y_1 > X_1$) and K_{mix} is an experimental value for the particular mixture.

Equation (6.73) bears a similarity to equation (6.69) in that in both cases a limited heat transfer rate across the vapour phase boundary is produced with the result of restricted bubble growth.

Stephan [160] showed from experiments on various binary mixtures that h_{mix} is lower than $(h_{mix})_{id}$ depending on the type of the mixture and the saturation pressure. For the mixture acetone-n-butanol, convection atmospheric boiling at a constant heat flux of 10^5 Watt/m^2, gave a heat transfer coefficient of almost half that of both the volatile and less volatile components for a mass concentration of $\sim$ 40% of the volatile component.

The application of equations (6.69) and (6.73) seem to depend on the ability to estimate the factors ψ_{mix} and ϕ_{mix} for the mixture and the flow conditions concerned. In our case equation (6.73) seems to be less useful because of the difficulty in obtaining a representative super heat ΔT or heat flux for the cavitation process. The bubble growth theory leading to equation (6.69), on the other hand, seems to be more appropriate to use for the cavitation bubbles, since both conductive and convective effects at the bubble wall as a result of the mass concentration gradient are considered.

FIGURES 6.1 to 6.4

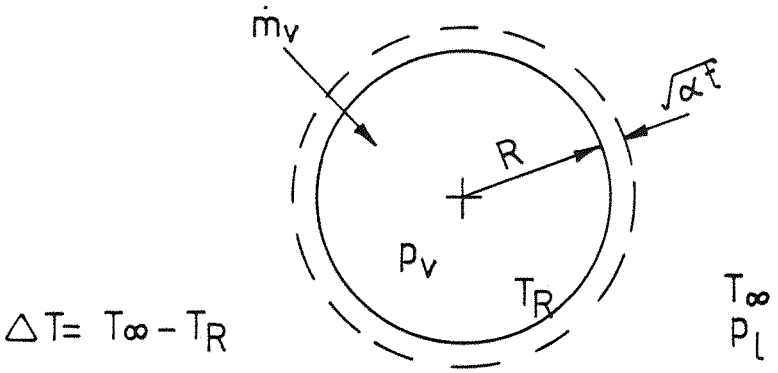

FIG 6.1 SPHERICAL VAPOUR BUBBLE WITH A THIN CONDUCTION LAYER IN SUPERHEATED PURE LIQUID

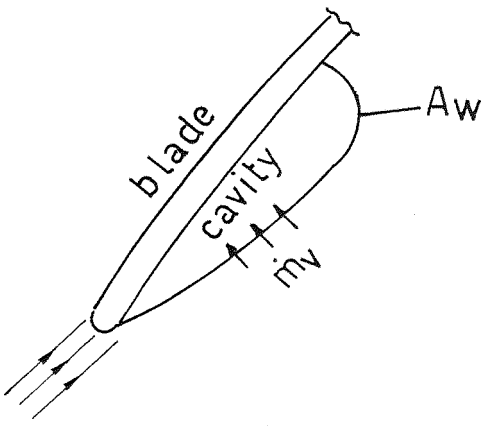

FIG 6.2 ENTRAINMENT THEORY CAVITY MODEL

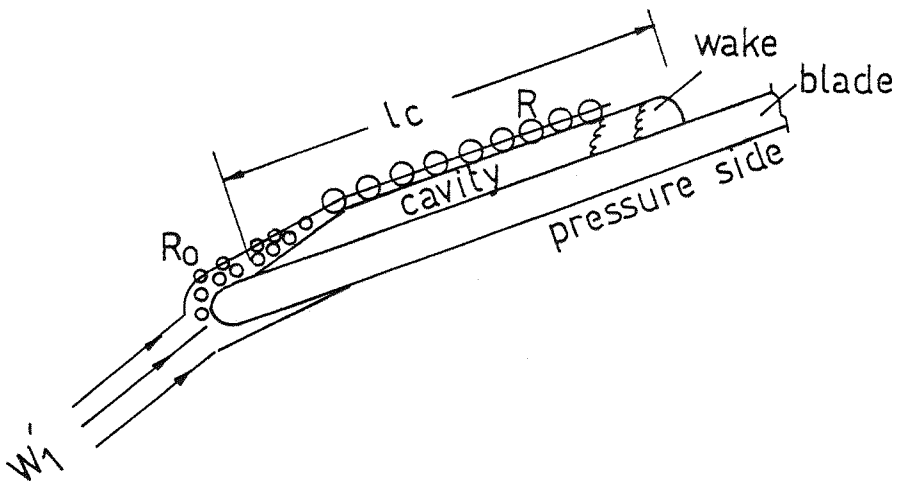

FIG 6.3 CAVITY FLOW MODEL WITH VAPOUR BUBBLES GROWING FROM INITIAL RADIUS R_o

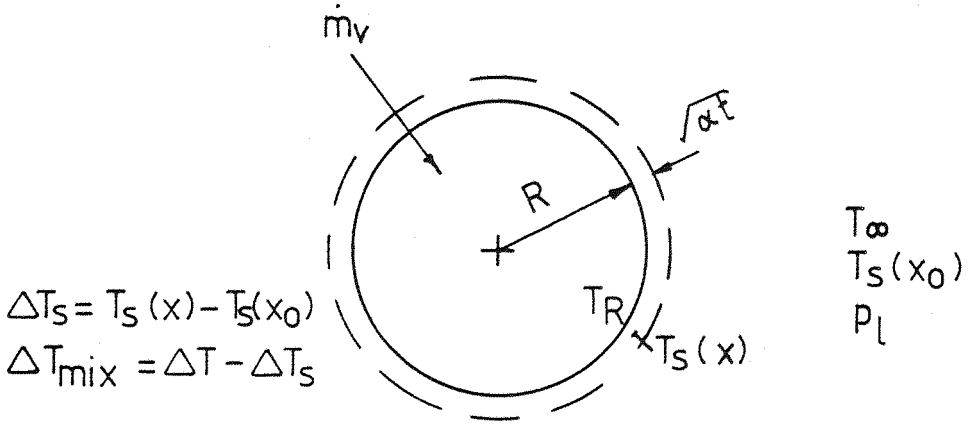

FIG 6.4 SPHERICAL VAPOUR BUBBLE WITH A THIN CONDUCTION LAYER IN SUPERHEATED BINARY LIQUID MIXTURE

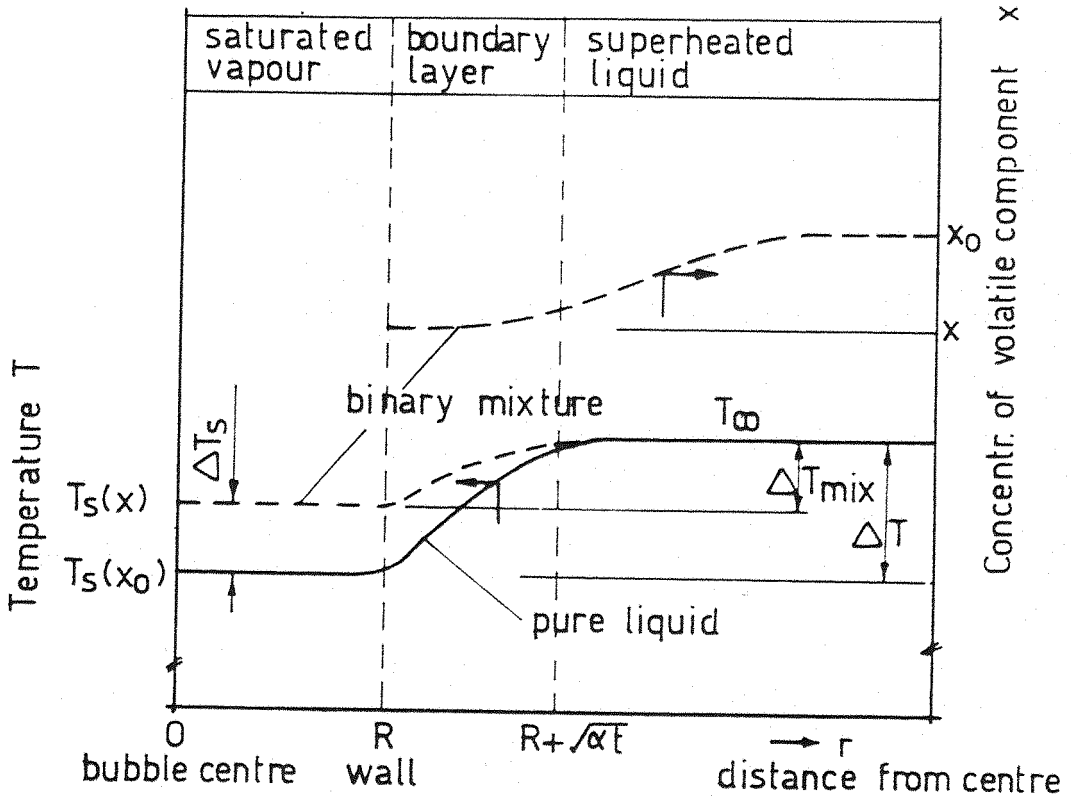

a) Temperature and mass concentration distribution in and around the vapour bubble

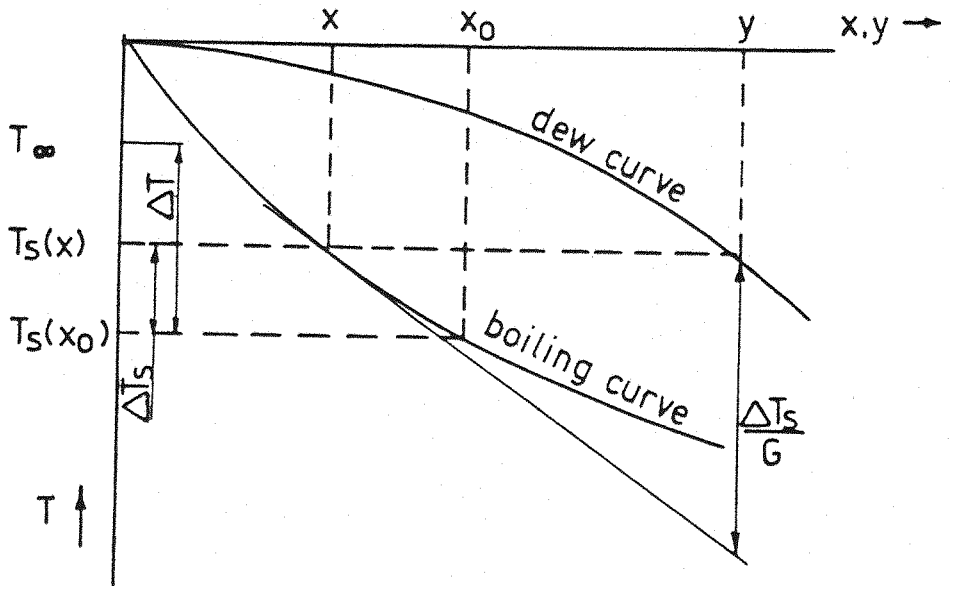

b) Isobaric equilibrium diagram

FIG 6.5 HEAT AND MASS EQUILBRIUM DIAGRAMS FOR THE BINARY LIQUID MIXTURE (173)

CHAPTER 7

GAS SOLUBILITY AND CONTENT EFFECTS ON CAVITATION

7.1 Introductory Background

In Chapter 6 it was mentioned that in order to initiate cavitation without producing a significant tensile pressure in the liquid, gas filled bubbles which act as cavitation nuclei, must be present in the system. The amount and distribution of these nuclei in the flowing system depend on the amount of gas in the liquid and the history of the cycle. Changes in the total gas content of the liquid are known to influence the cavitation inception and performance of the hydraulic machines [60]. An increase of $\sim$ 100% in the inception cavitation number was recorded in a closed cycle as a result of increased air content in cold water. In the field of pump cavitation, several authors [32, 46, 86, 107, 130, 131, 147] have shown the unfavourable effect of high gas content presence in the liquid on the cavitating flow performance of hydraulic machines. These effects were found to be most pronounced at the inception point when cold saturated water was handled.

The effect of the total gas content is two fold [66], namely the free gas can act as cavitation nuclei and the dissolved gas can influence the size of the nuclei and the growth of gaseous cavitation bubbles. The total gas content m_T is the sum of the free gas content m_F and the dissolved gas content m_D, or;

$$m_T = m_F + m_D \tag{7.1}$$

The free gas content has a decisive role in the cavitation process, and more precisely the size distribution of the free gas bubbles largely determines the cavitation inception in a system [60, 66]. Experiments have shown that in different facilities or at widely different velocities and pressures in the same facility, at the same total air content would not supply the same size and distribution of nuclei [104].

Ripken et al. [135] found that even for water of low dissolved air content, the shear force produced by the vortex motion of the centrifugal impeller is likely to promote the generation of gas bubbles which are stabilized in the liquid downstream to serve as cavitation nuclei in the closed system. According to their experiments, although the amount of free gas content could be less than 1% of the dissolved gas content, the effect of the free gas bubbles is decisive in producing a significant increase in σ_i with both increased m_F and flow velocity.

Vapourous cavitation occurs whence the liquid local pressure drops to a value below the vapour pressure at the saturation temperature, so that the initial bubble is observed to grow explosively and is caused by the rapid conversion of liquid to vapour. If however, the bubble starts to grow at pressures above the vapour pressure of the liquid, then this can lead to a pseudo cavitation, whereby the constant mass of gas in the bubble is merely responding to the change in liquid pressure outside of the bubble, so that the bubble grows to a larger equilibrium radius. If the liquid is super-saturated with gas and transport of gas across the interface takes place, then the bubble will grow mainly due to increased gas mass in the bubble. This type of cavitation is termed gaseous and is usually a slow process [64]. Both pseudo and gaseous cavitation can also extend below the vapour pressure of the liquid.

For liquids saturated with air, a highly super-saturated state can be reached locally as the liquid enters a low pressure region in the machine. If sufficient time is allowed, gaseous cavitation can occur at pressures above the vapour pressure of the liquid. Assuming that at the bubble wall, the gas concentration has reached the saturation level (C_s), then according to Arndt [8] the gradient of concentration between that of the bulk (single component) liquid (C_∞) and that at the bubble wall will initiate a gaseous diffusion. The diffusion rate can be expressed using the Epstein-Plesset [44] theory by neglecting the convection effects. For a single spherical bubble it is expressed by:

$$\frac{dm_g}{dt} = 4\pi R^2 \alpha_g (C_\infty - C_s) [\frac{1}{R} + \frac{1}{\sqrt{\pi \alpha_g t}}] \qquad (7.2)$$

where α_g is a coefficient expressing the gas diffusivity in the liquid.

The gas mass m_g at the time t can be found from the perfect gas law;

$$p_g V_g = K m_g T \qquad (7.3)$$

whereby K is the gas constant. Equating for the partial pressure p_g from equation (6.6), we obtain for the gas mass

$$m_g = \frac{4}{3}\pi R^3 (\frac{p_\ell - p_v + 2S/R}{KT}) \qquad (7.4)$$

Differentiation of equation (7.4) and equating to the right hand side of equation (7.2) will give:

$$\dot{R} = \frac{KT \alpha_g (C_\infty - C_s)}{p_\ell - p_v + \frac{4}{3}\frac{S}{R}} [\frac{1}{R} + \frac{1}{\sqrt{\pi \alpha_g t}}] \qquad (7.5)$$

Experimental results [44] have shown that a 10 times increase in size from an initial bubble radius R_o due to gas diffusion, by neglecting convective effects according to equation (7.5), requires about 30 seconds for a reasonably high concentration ratio C_∞/C_s of ~ 5. This implies that significant gaseous diffusion in flow through hydraulic structures is highly unlikely because of the short time residency of the bubble in the low pressure zone. However, if a velocity gradient does exist at the low pressure region then convective effects become important. Some authors [44, 176] extended the theory of gaseous diffusion to include convective effects. Their results showed that the time required for the bubble to increase its size 10 times from R_o is reduced by a factor of $\sim 2\sqrt{Pe}$ if convective effects are included. Pe being the gaseous diffusion Peclet number ($= uR_o/\alpha_g$) and is in the order of 4×10^4 [44], for cold water. This will mean that for a strong super-

saturation of the liquid, a fraction of a second may be sufficient to allow some gaseous diffusion, if convective effects are dominant.

Earlier experiments in this Department [192] with oil flow through a venturi have shown that largely gaseous cavities in the throat grew in a fraction of a second (1 - 5 ms) to a large enough size to choke the flow. Although the gas solubility of oil is considerably higher than water, the main reason behind the high gas diffusion rate is most likely linked to the convective effects associated with turbulant flow at the throat.

7.2 Oxygen Monitor as a Gas Content Meter

The measurement of the gas content in liquids has been the subject of numerous investigations. An excellent review on this subject is given in Ref. [14]. The Van Slyke apparatus [125] is widely used to measure the total gas content. Originally devised to measure the dissolved gases in blood, this instrument uses the principle of subjecting the agitated liquid sample to torricellian vacuum thus allowing the dissolved gas to escape. By measuring the partial pressure of the escaping gases, the volume of these can be estimated using the perfect gas law.

The use of the Van Slyke apparatus for a flowing system however, is hampered by the small sample volume and in obtaining a representative sample, and in its introduction into the instrument [32, 57]. These difficulties are made even worse when its use is linked with a hot circulating fluid in a presurized system.

Ideally one would like to know both the dissolved and the free gas content for the reasons discussed previously. Morgan [104] listed all important methods for the measurement of both total and free gas content.

One method to estimate the total air content in a liquid is by estimating the amount of oxygen present in that liquid. Dry air contains 20.95% oxygen by volume regardless of pressure, and since for liquids

saturated with air the solubility of the various components of air in the liquid is proportional to their partial pressures above the liquid, hence by knowing the saturation partial pressure of oxygen in the liquid, the air content can be easily estimated.

Using Henry's law, we obtain for the saturation partial pressure of the dissolved gas;

$$p_g = C_s \beta \tag{7.6}$$

The Henry's constant β is temperature dependent and is given by [7];

$$\beta = \frac{17032400\ \rho_\ell}{MW_\ell\ \alpha} + p_g \tag{7.7}$$

whereby both β and p_g are in mm Hg, α is the Bunsen solubility coefficient.

For water, the oxygen concentration at equilibrium (C_s) can be found if the partial pressure of O_2 is known. At 20°C and a partial pressure of 160 mm Hg (atmospheric), this concentration was found to be 5.12×10^{-6} in mole basis (Appendix II). Knowing that the dissolved oxygen comprises about 33.3% of the air volume dissolved in water [84]; the concentration of saturated air in water at 20°C is found to be 15.38×10^{-6} in mole basis (Appendix II).

The drawbacks of the oxygen measurement method emerge when conditions are away from an equilibrium (saturation) state. If conditions are such that a considerable amount of free air is circulated in the system, then percentage of nitrogen and oxygen in the dissolved and free air may vary depending on the cycle history [104]. Therefore a straightforward conversion of oxygen content to total air content may be erroneous. Similar doubts were expressed by Furness [51], commenting on results obtained by Chivers [32].

Of the various methods for measuring O_2 solubility, the Winkler chemical method [182] and the Polographic electrochemical method [62] are mostly prominent.

The Winkler method and modifications of it have been among the most popular and the most accurate [14]. It involves the oxidation of freshly precipitated manganous hydroxide by the dissolved oxygen to form manganic hydroxide. The solution is then made acidic under which condition the manganic ion oxidizes iodide.

The Winkler method although very accurate is a slow chemical process suitable for laboratory work. In testing the O_2 content of liquids in a flowing system a quick and easy method is required and therefore the polographic method provides the answer.

The advantages of this method are mainly the ease of calibration (on atmospheric air) and the ability to measure the oxygen content directly and continuously due to the quick response of the amperometric sensor. The drawbacks of this instrument are the temperature limitation (up to $\sim$ 40°C) and the pressure at the sensor which cannot respond to negative pressures and hence measurement at sub-atmospheric pressures of the cavitation region cannot be done.

The description and installation of one such instrument used in this research (Beckmann 7003) is given in Chapter 2.

7.3 Discussion of Gas Content Test Results

7.3.1 Change of O_2 Concentration During the Test

In a closed circulation system, the level of gas content is likely to change with test time. If the liquid is saturated with air, then as it passes through the low pressure region of the pump, some gas will come out of solution. Some of this liberated gas will redissolve again as it enters the high pressure zone at pump discharge, and some of it may circulate around the system as free gas bubbles.

The present test series of gas content in water and 3 different concentrations of EG/W mixtures has been limited to a liquid temperature of 20°C for two main reasons. The first is the low vapour pressure of the liquids tested at this temperature which do not influence the measured partial pressure of oxygen significantly. The second and more important reason was the intention to measure the O_2 content at the same calibration temperature of 20°C to avoid excessive errors of the instrument.

A constant flow cavitating test was applied according to the test procedures outlined in Chapter 2. A constant flow rate of 240 L/min, corresponding to $\sim Q_{opt}$ at 4000 rpm was used throughout the test series. The pressure level and control was done by increasing or decreasing the main reservoir pressure as outlined in Chapter 2.

Calibration of the oxygen monitor was done at a room temperature of 20°C and a barometric pressure of 752 mm Hg. 100% saturation was obtained by exposing the sensor to air and adjusting the instrument to read 21% O_2.

Every test started by pressurizing the rig to achieve non-cavitating conditions at pump inlet and then reducing the pressure level in the system gradually until cavitation started and then progressing towards head breakdown. Oxygen content was measured at an interval of $\sim$ 5 minutes at a point in the discharge pipe vicinity (figure 2.4). Total duration of the test was about 45 - 50 minutes.

On figure 7.1a, the O_2 concentration readings for water and 2 liquid mixtures were recorded with respect to test time. These liquids were used without any treatment. Tap water was pumped into the rig and left for 48 hours to reach equilibrium. EG/W mixtures were kept inside the storage barrels for a long period with ample air contact.

On figure 7.1b, the same three liquids were treated before the test. By heating these liquids up to a temperature of about 95°C overnight, most of the dissolved gas was expelled. By cooling them down to 20°C over a

period of 48 hours, without significant contact to air, partial de-aeration is obtained.

From these two figures, several interesting features can be outlined. For water the influence of test time is two fold. The first is to decrease the oxygen content for the saturated liquid and the second is to increase it for the partially de-aerated liquid as time passes. Eventually they end up both at the same level of about 60% saturation after the passing of about one hour. The behaviour of water saturated with air seemed to nearly agree with that obtained by Chivers [32] on cold water. A reasonable suggestion for the cause of it lies in that the liberated air tends to collect at the top of the main reservoir and therefore the test rig will be acting a large Van-Slyke apparatus down to a stable partial saturation level. The stabilization time is thought to depend strongly on the rig geometry.

Partially de-aerated water seems to redissolve some air as time goes by, eventually to reach the same stable saturation level of $\sim$ 60% (in the rig used). This is easily explained as free air is available through the free surface created at the top of the main reservoir in order to create low pressures for the purpose of reducing pump inlet NPSE. This free air is absorbed by the liquid of low air content as a result of the non-equilibrium condition.

As for the EG/W mixtures, the influences of test time on the O_2 saturation level for the saturated liquids (figure 7.1b) is less important within the period of test. 25/75 EG/W solution seems to increase its O_2 content with time until it reaches full saturation then starts to decrease slightly again. Similar increase of O_2 content is also visible for the 45/75 EG/W solution, although the limit of 70% saturation is nearly maintained throughout the test. This seems to suggest that for the EG/W mixture the effect of test time is less important than it is for water. A possible reason for this is that liberated air bubbles do not rise to the reservoir top in order to escape, but rather, they recirculate in the system as free gas bubbles, a phenomenon confirmed from visual observation. As these undissolved gases appear in bubble form, the O_2 meter will record the same reading for the

total O_2 content although the ratio of free to dissolved content may increase as the test progresses.

Partially de-aerated EG/W mixtures (figure 7.1b) seem to behave similarly, but to a lesser extent than water. As the concentration of EG in the mixture increases so does the changes of O_2 content with time become less pronounced. This is probably related to the anti-foaming substance present in the commercial Ethylene glycol used here, which is expected to collect at the interface and therefore reduces the gas diffusion coefficient.

The test results of figure 7.1b have been replotted in figure 7.2 as a function of the pump inlet pressure. It is interesting to note from this figure that as long as the system remains closed to the atmospheric air, the influence of the system pressure does not seem to influence the absolute O_2 saturation significantly for all liquids. Since the local pressure at the sensor is $\sim$ 0.8 bar above the inlet pressure at 240 L/min, this pressure is all the time above atmospheric for the closed rig and one would expect from Henry's law that air saturation would rise with pressure at any given liquid temperature. However since no additional air can enter the rig, the partial pressure of the original dissolved air cannot rise due to the incompressibility of the liquid (in the limit of pressure dealt with in the hydraulic machines). As the reservoir is opened to atmospheric air needed for the control of reservoir pressure, the saturation level of the liquid starts to pick up because more air for solution is available at the interphase. The diffusivity rate depends of course on the amount of Ethylene glycol in the mixture, being higher for water.

The influence of the free surface in the reservoir is clearly seen on figure 7.3 when reservoir pressure control is compared to inlet valve control, whereby the inlet NPSE to the pump is reduced by throttling on the inlet valve. In this case the reservoir has no free surface but rather a 10 mm diameter vent pipe to keep it under atmospheric pressure all the time. Here it is clearly seen that system pressure has only little influence on O_2

saturation for the valve method over the whole test period, because air cannot enter or leave the rig in sufficient quantities.

It should be noted from this figure that although the valve method was found to be inferior to the reservoir control method for the saturated liquid [57], it is for the same reason superior ro the reservoir method, when liquids of low air content are handled. Whereas for the saturated liquid the absence of the free surface in the reservoir does not allow for liberated gas to escape and hence recirculate in the system, it helps to minimize the inflow of free gas into the system when de-aerated liquids are being handled.

7.3.2 Gas Content Effect on Cavitating Flow Performance

The influence of the gas content on pump cavitation can be divided into two categories, limited and extensive. By limited it is meant that the increase is gas content (mainly dissolved) influences the pump performance only at a certain stage in the cavitation process, namely at inception and a small head drop. Extensive gas content effect is the case where the high amount of gas present in the liquid (both dissolved and free) does influence the pump performance over the whole cavitation process, i.e. from inception to performance break-down.

In the present rig complete de-aeration of the cold liquid is not possible. However, partial de-aeration can be performed by heating up the fluid to near boiling so that most of the gases are allowed to escape. By cooling it down to room temperature with little or no access of atmospheric air to the system, a low gas content level can be obtained.

On figure 7.4, limited gas content effect is shown for a) water and b) 50/50 EG/W mixture. The influence of increased gas content for both cases is limited to the range 0 $\sim$ 7% head drop. Extensive gas content effect is shown on figure 7.5 for a) 25/75 EG/W and b) 50/50 EG/W mixtures. Increased air content seems to influence the developed head over the whole cavitation

process from the point of inception to complete head break-down.

As the liquid of known gas content enters a region of low pressure and high velocity gradient where vortices are present, then the liquid will reach a saturation state even for very low gas content. If the gas content is high enough then a super-saturated state is likely to occur, and if the residence time of the gaseous bubble in the low pressure zone is long enough, gas will diffuse into these bubbles with the result of a singificant bubble growth.

From equation (7.5) if conditions at the pump inlet, such as liquid pressure, temperature and residence time are unchanged, then the bubble growth is merely dependent on the size of the gas bubble and the concentration gradient between the bulk liquid and the bubble wall ($C_\infty - C_s$).

For water it is widely accepted that gas content effects do not influence the cavitation performance at break-down [131, 147]. This seems to agree with the results of figure 7.4a. Chivers [32] however, found from tests on a small pump that pump cavitation with cold water can be influenced by the amount of the gas content even at an advanced stage (break-down). This contradiction can only be related to the different test facilities used by the various authors. Free stream gas bubbles serving as nuclei are very much dependent on the type of pump test facility and duration of test, even if water saturation level is the same to start with [135].

In our case, whereby a free surface is created above the liquid in the reservoir in order to produce a low pressure, the saturation level of both saturated (non-degassed) and degassed water approach nearly a similar value ($\sim$ 60% saturation) as the pump approaches break-down. Although this does not mean a similar level of free gas bubbles for both conditions, the effect of the gas content ceases to exist while the vapourous cavities are mainly operative.

Extensive gas content effect is established when tests are carried out using EG/W mixtures of different concentrations (figure 7.5). Contrary to

water of similar concentrations, the cavitation process is affected throughout the test from inception to complete head break-down. The gas concentration of these mixtures seems to be only slightly changed as the test time progresses. Gases liberated as a result of the low pressure and shear forces produced by the pump vortices do not escape via the free surface, but rather recirculate in the system, hence free stream bubbles increase in number and size as time progresses, a phenomenon confirmed from visual observation. The reason for this is not easy to explain, but a suggestion can be made with regard to the higher viscosity of those mixtures which diminishes the buoyancy of the free gas bubble in the main reservoir.

If convective effects were included in the gas diffusion formula of equation (7.5), then according to Arndt [8] a fraction of a second may be sufficient to promote gaseous diffusion, if a strong super-saturation zone is reached. This suggests that something like that is likely to happen when non-degassed EG/W mixtures are circulated in the rig, knowing that for the test pump used here the vortex motion around the drive shaft and seal may produce a comparatively long residence time of the gaseous bubbles.

If we consider a limit (L) between the limited and extensive gas content effect, then for a known saturated concentration C_s and residence time t, the limit can be expressed by using the relationship of equation (7.5):

$$\frac{C_\infty - C_s}{R} = K_c \qquad \begin{matrix} <L & \text{limited effect} \\ >L & \text{extensive effect} \end{matrix} \qquad (7.8)$$

whereby K_c is a gaseous bubble growth constant.

Following this assumption, the different behaviour of the 50/50 EG/W mixture on figure 7.4b and 7.5b could be explained. For nearly the same concentration reading of $\sim$ 50%, the only difference between the non-degassed mixture (figure 7.6b) and the degassed one (figure 7.5b) can only be related to higher super-saturation C_∞ due to the increased number of free gas bubbles recirculating in the system and eventually are collected in the low pressure

zone, when non-degassed mixtures are being used. A high value of K_c in equation 8.11 will results in an appreciable gas diffusion with the effect of the pump performance dropping sharply due to increased amount of air blocking the impeller entrance.

The results of figure 7.5b and 7.6b also suggest that the use of the oxygen amperometric monitor is not suitable for measuring the change in balance between the free and dissolved gas content. Ideally one would require to measure both dissolved and free gas content simultaneously. Morgan [104] lists most of the available methods available for measuring the free air in water, of which the capacitance sensor provides the highest accuracy.

The scale effect due to the gas content defined by the increase in the cavitation number by an amount of $\Delta\sigma_g$ due to an increase in the gas content is shown on figure 7.6 as a function of the Ethylene glycol concentration in the mixture. For a head drop of 3%, the scale effect is due to the total air content in the liquid, whereas at head break-down it is mainly due to the free bubbles which contribute to the impeller entrance blockage. This seems to be confirmed from photographs taken with 45/55 EG/W mixtures at an advanced stage of cavitation, with the gas nuclei increasing in number so that their density is high enough to block the vision through the sight glass (Chapter 10).

Increased size and number of gas nuclei in the mixture which largely contribute to the extensive cavitation effect are probably related to the surface properties of these particular mixtures, which allow the gas nuclei to increase sufficiently in size, to reach a stable equilibrium radius even at the high pressure region of the system.

7.3.3 Inlet Vortex Cavitation Inception

From visual observation of the flow field at impeller entrance of pump J, a free vortex was found to establish itself around the impeller hub as

a result of the peculiar inlet pipe design and the high speed rotation of the shaft and seal. Cavitation bubbles start to appear inside the vortex core very early on in the cavitation process.

In figure 7.7, the incipient cavitation numbers were recorded at the first appearance of the bubbles inside the vortex. Tests were conducted with pump J at various pump speeds both with water and EG/W mixture, keeping both liquid temperature and flow coefficient constant. From this figure, two obvious conclusions are immediately apparent. The first is the linear increase of the inception cavitation number σ_i with pump speed, and the second is a higher cavitation number for the EG/W mixture over the whole pump speed range.

Similar results were obtained on a second impeller of the same pump, using similar flow coefficient and fluid temperature (figure 7.8a). Comparison of the cavitation number for the two impellers, however, showed that the impeller with the nearly radial blades (J-8-70) produces a lower cavitation number for the same liquid and liquid temperature, than the impeller with back swept blades J-6-50, thus suggesting a strong influence of geometry (figure 7.8b).

Core formation in swirling flow has been shown to be a function of the swirl angle [12]. The core radius r_c on figure 7.7 was also shown to vary from r_h to r_1 depending on the strength of the swirl and the meridional velocity component of the flow.

The minimum pressure inside the vortex is best described by the minimum pressure coefficient C_{pmin} defined by:

$$C_{pmin} = \frac{p_\infty - p_{min}}{\frac{1}{2}\rho V_\infty^2} \qquad (7.9)$$

and can be predicted from a Rankine model [8, 16]:

$$C_{pmin} = 2 \left[\frac{\Gamma}{2\pi r_c u}\right]^2 \qquad (7.10)$$

whereby Γ is the circulation in the flow. Both Γ and r_c are difficult to estimate because of the many dependent variables involved. Billet [16] showed from his experiments on secondary flow generated vortices in a 48 inch water tunnel, that predicted values according to equation (7.10) agree well with actual test results. He also showed that desinent cavitation numbers are Reynold number dependent (with respect to flow velocities) and increase proportionally. This is a phenomenon also confirmed by other authors [8, 67], and the following proportionality was suggested:

$$\sigma_i \sim Re^n \qquad (7.11)$$

Similar proportionality seems to be evident from the results of both figures 7.7 and 7.8.

The local pressure at which vortex cavitation appear, are normally significantly higher than the vapour pressure of the liquid and therefore bubbles appearing at that early stage of cavitation are mainly of the non-vapourous (gaseous) type. In fact vortex flows tend to be good collectors of gas bubbles [16]. Therefore, in the absence of any significant dynamic actions, Holl [67] suggested that the gas pressure is a dominant factor in the estimation of the vortex cavitation number. By neglecting the thermodynamic term C_T at the point of inception in equation (6.17), in addition to the bubble growth term ϕ, we obtain;

$$\sigma_i = C_{pmin} + \frac{p_g}{\frac{1}{2}\rho_\ell V_\infty^2} - \frac{2\,S/R}{\frac{1}{2}\rho_\ell V_\infty^2} \qquad (7.12)$$

The surface tension term in equation 7.12 is of significance only for bubbles of very small initial radius R_o. For a visible bubble at the point of cavitation inception, the bubble diameter is in the order 0.1 - 1 mm, and therefore the surface tension term $2S/R \;/\; \frac{1}{2}\rho V_\infty^2$ barely reaches 1% of

the cavitation number. This suggests that the influence of the surface tension can be neglected and therefore equation (7.12) reduces to:

$$\sigma_i = C_{pmin} + \frac{p_g}{\frac{1}{2} \rho_\ell V_\infty^2} \tag{7.13}$$

This is the general form of the inception cavitation number of the vortex found in the literature [8, 67]. Billet [8] and Holl [67] found that for the same Cp_{min}, σ_i is likely to depend on the dissolved gas concentration in the liquid. For low gas content, σ_i is likely to increase with flow velocity simply because C_{pmin} is Re number dependent and tends to increase according to equation (7.11).

In comparing water with EG/W mixture at the same pump speed and flow coefficient, C_{pmin} is expected to be lower for the mixture because the circulation Γ is likely to reduce with increased viscosity [16]. However, if the change in C_{pmin} is considered to be only small for the viscosity range encountered here, then the difference in σ_i for both liquids is mainly dependent on the gas pressure.

The saturation gas pressure can be found from equation (7.6). For gasses which are not in equilibrium with the liquid, this equation can be modified as follows [67]:

$$p_g = K_s C_s \beta \tag{7.14}$$

whereby K_s is a constant expressing the percentage of saturation in the liquid.

For gasses in contact with the liquid, applying the Henry-Dalton's law for the equilibrium condition, then equation (7.14) can be presented in the following form:

$$p_g = K_s (p_{tot} - p_v) \tag{7.15}$$

The total pressure of the gasses above the liquid p_{tot} is $\sim$ 1 bar for dry atmospheric air. At low temperatures (< 20°C), p_v for water and EG/W mixtures can be ignored as being too small to consider. As the temperature of the liquid increases so does p_v and eventually at the boiling point, p_g is zero and the liquid is de-aerated.

Following the assumption of equation (7.13), for similar C_{pmin}, the increase of σ_i for EG/W mixture on figures 7.9 and 7.10 can be related to the difference of the gas pressure of the dissolved gasses at 90°C, or;

$$\Delta\sigma_i = \frac{\Delta p_g}{\frac{1}{2} \rho_\ell V_\infty^2} \tag{7.16}$$

To establish a quantitative solution for equation (7.16) one would require to apply equation (7.15) for both water and the mixture EG/W. From actual tests the local static pressure at the point of inception was found to be nearly the same for water and 45/55 EG/W mixture, and therefore p_{tot} of that equation can be assumed to remain unchanged for both conditions. Assuming the percentage saturation K_s takes a similar average value, then equation (7.16) can be represented in the form;

$$\Delta\sigma_i = \frac{K_s}{\frac{1}{2} V_\infty^2} \left[\left(\frac{p_v}{\rho}\right)_{water} - \left(\frac{p_v}{\rho}\right)_{EG/W} \right] \tag{7.17}$$

From figure 7.1, K_s takes an equlibirum value of $\sim$ 0.7 for water and 45/55 EG/W after the passing of $\sim$ one hour at 20°C. If K_s is assumed to remain unchanged while heating up the liquid from the saturated state, then the application of equation (7.17) can be attempted at 90°C with $K_s \cong 0.7$.

The results as calculated from this equation are plotted on figure 7.9 at different pump speeds. Actual values of $\Delta\sigma_i$ taken from figures 7.7 and 7.8 are also plotted on figure 7.9 for both impellers J-8-70 and J-6-50.

The agreement between the calculated and measured values of $\Delta\sigma_i$ is reasonable enough within the test accuracy limit. This may suggest that the assumption of equation (7.16) holds well for this particular pump. The difference in gradient between the predicted and actual $\Delta\sigma_i$ lines may be related to the Re number effect.

In reality both K_s and P_{tot} may vary for each liquid, and equation (7.17) must be altered to take an average value. However, at present the assumption made for water and 45/55 EG/W mixture seems to agree reasonably well with the actual test results.

Hub vortices of conventional pumps without a bare shaft inside the flow field are not expected to be of great significance compared to the pump discussed above. However some degree of vortex is likely to occur at low Q_{cav}/Q_{opt} values.

7.3.4 Comments on the Gas Solubility of Polar Liquid Mixtures

In considering the solubility of gasses in a liquid, the relationship between the Ostwald solubility coefficient γ and the surface tension of the liquid provides a sucessful correlation for most liquids and liquid mixtures [14]. According to the theory presented early on by Uhlig [171] and confirmed more recently by other investigators [14], if a spherical gas molecule of radius r is to enter the solvent, a spherical cavity must be produced in the solvent of essentially the same radius. A certain amount of work is done in producing this cavity since any increase in surface of a liquid is associated with a definite energy change, which is simply equal to $4\pi r^2 S$. In addition to this surface energy, there exist some energy terms which arise because of interaction of solvent and solute molecules. Given the term E for these interaction energies, the total energy change due to the transfer of the gas molecule takes the form:

$$\Delta u = 4\pi r^2 S - E \qquad (7.18)$$

And from the equilibrium theorem for the concentrations of solute molecules in the two phase, Uhlig [171] expressed the gas solubility in the following form:

$$\ell n\ \gamma = \frac{E - 4\pi r^2 S}{KT} \qquad (7.19)$$

Equation (7.19) indicates that if E remains constant for a certain gas, then the greater the radius of the solute molecule and the surface tension of the solvent, the smaller will be the solubility γ. From his own experience, Uhlig found that for the common gasses O_2, N_2 and CO, E is small compared to the term $4\pi r^2 S$ and does not change significantly from one solvent to another. Hence $\ell n\ \gamma$ is expected to be a linear function of the surface tension for most cases.

This is confirmed by Schläpfer [148] who tested the solubility of O_2 in several organic liquids and water. However, his test results of O_2 solubility in Ethylene glycol and glycerine does not seem to agree with the surface tension concept, with Ethylene glycol taking up only half the amount of O_2 taken up by water. More recent results [140] however, showed that several bench tests for pure saturated Ethylene glycol gave a total air content almost twice that of water, which seems to agree well with the surface tension concept. This may suggest that Schläpfer test results for EG are incorrect due to the non suitability of this liquid for the Winkler method, or perhaps because the Ethylene glycol used could have been contaminated by the higher glycols. Gjaldback [54] also found that the Bunsen absorption coefficient of N_2 in Ethylene glycol is 0.032 compared to 0.016 in water at 20°C. This again agrees well with the results obtained by NASA [140] for the air content in this liquid. Therefore it can be rightly concluded that the surface tension theory is also applicable for Ethylene glycol.

Some reservations in the application of the surface tension concept arise when liquid mixtures are considered, because the surface tension may not represent a property of the bulk solvent because of the enrichment of

the surface by the component of lower surface tension. Experiments have shown however, that surface active components present in the mixture do not influence the equilibrium solubility of the gas in the mixture but rather the rate of attaining equilibrium [14]. Test results obtained by Kretschmer [91] on organic mixtures showed that the solubility of O_2 and N_2 in iso-octane is about 4 times that of ethanol (based on molar fraction) for a decrease is surface tension of about 5×10^{-3} N/m. The solubility of these two gasses in a 50/50 mixture of these two liquids was half way between those of the pure liquids. Similar results were also obtained on a 50/50 mixture of Acetone/Ethanol mixture, which seems to confirm the applicability of the surface tension concept for the solubility of gasses in liquid mixtures. In figure 7.11 the solubility of O_2 in various Alcohol-water mixtures seems to indicate reasonable agreement with the surface tension theory [148].

Of particular interest here is the effect of temperature on the solubility of gas in liquid mixtures. From equation (7.19) it will be observed that if $4\pi r^2 S > E$ then the solubility of the gas increases with temperature T, and vice versa [171]. Pure water is known to have decreasing solubility of O_2 with increased temperature [148]. On the other hand the organic mixture Acetone/Ethanol showed some increased solubility of O_2 and N_2 with temperature [91]. No information is obtained on the mixture EG/W from the literature. On figure 7.12 the surface tension of pure Ethylene glycol and water is plotted against temperature [20]. One value for the mixture 50/50 EG/W is available at 25°C [6], from which a line is extrapolated to show approximate relationship with temperature. Higher gas solubility of the mixture compared to water at all temperatures is expected following the assumptions of the surface tension theory.

On figure 7.10, the % O_2 saturation of the mixture EG/W at 20°C is plotted against concentration of EG. Assuming an instrument accuracy of ± 3% at 20°C, this figure indicates that mixtures of higher concentrations which are supposed to be in equilibrium with atmospheric air, seem to be under-saturated. The only explanation for this behaviour can be found from the fact that mixtures stored inside the barrel for a long period of time

are likely to allow the anti-foaming agent to float on the surface and hence reduce the amount of air diffused into the liquid. Further experiments in the future are necessary to verify this behaviour. By stirring the mixture before circulation or better by using Ethylene glycol without any additives may help to push the gas solubility of the mixture nearer to full saturation.

EG/W mixtures are used for other industrial purposes like drying natural gas. Additives like anti-foaming and anti-corrosion inhibitors can be different from those required for the cooling system, and therefore test results obtained with the latter might not be completely true for other mixtures. However, the general trend of gaseous diffusion is likely to remain nearly similar in most cases.

7.4 Concluding Remarks

The test results on the effect of gas content on pump cavitation are by no means conclusive. Their importance however cannot be underestimated. Especially where a binary polar liquid mixture is handled the amount and the size distribution of the gas bubbles in the mixture seem to produce a significant scale effect throughout the cavitation test procedure. From the preceeding discussion of these test results, the following points of interest are outlined.

1. Measurements of dissolved gas in water and EG/W mixtures were obtained by measuring the percentage saturation of oxygen. A Beckman amperometric sensor responding to the partial pressure of O_2 in the solvent was used for continuous monitoring of the oxygen content during the test. Pressure and temperature limitation of this device made it necessary to make all measurement at 20°C and at a sample pressure of 1 - 1.8 bar, abs.

2. As the O_2 measurement was carried out directly at a point near the discharge of the pump, it was possible to assess the level of O_2 saturation as the test progressed from non-cavitating conditions to complete head breakdown. For water, the existence of a free surface in the main reservoir,

created to produce low pressures in the system, has a two sided effect. The first is to allow some of the dissolved gasses to escape when saturated water is circulated. The second is to help to redissolve some air when de-aerated water is handled. Eventually an equilibrium percentage saturation of $\sim$ 60% is reached (in the particular rig used) for both cases after the passing of about one hour. Removing the free surface by using the suction valve to control the inlet pressure to the pump, these effects seem to diminish with degassed water retaining almost the same percentage saturation during the test.

3. The level of O_2 saturation change during the test is also influenced by the type of circulated liquid. For EG/W mixtures these changes are less pronounced than those obtained with water. 45/55 EG/W mixtures seem not to be influenced by the presence of the free surface for both the saturated and the degassed state. As this mixture passes the low pressure zone of the pump some air will be released and stabilized as gas bubbles downstream of the pump. As the sensor is expected to respond to the total gas partial pressure of the oxygen, the same reading at the start and the end of the test may mean similar total gas content. However the amount of free gas bubbles may have increased tremendously. A phenomenon confirmed from visual observation. Therefore the O_2 monitor is not a relaible source of distinguishing between dissolved and free gas content.

4. Two types of gas content effects on the cavitating flow performance of pump J could be distinguished. The first is a limited effect influencing the generated head at inception and small head drops, and the second is extensive, influencing the pump performance from inception to head breakdown. The first effect is believed to be mostly due to dissolved gas content and the second effect due to both dissolved and free gas content. Saturated water and degassed 50/50 EG/W mixture fall under the limited effect category and all saturated EG/W mixtures fall under the extensive effect category.

5. From theoretical considerations, if convective effects are included gaseous cavitation can occur with the results of a significant scale effect

due to gas content. If the concentration gradient between the gas bubble and the bulk liquid $(C_\infty - C_s)$ is large enough and the bubble radius is small, then significant gaseous diffusion is likely to happen, even for relatively short residence time. Defining a limit L between the limited and the extensive gas content effect, then

$$\frac{C_\infty - C_s}{R} = K_c \qquad \begin{cases} <L & \text{limited effect} \\ >L & \text{extensive effect} \end{cases}$$

EG/W mixtures of high gas content with a large amount of visible gas bubbles circulated in the system are likely to produce high K_c with the result of extensive effect of the gas content.

6. The side suction design of pump J is likely to promote pre-rotation at the impeller entrance in the same direction as pump rotation. This pre-rotation is further accentuated by the swirling action of the drive shaft and seal with the result of a free vortex forming around the hub of the impeller; a phenomenon confirmed from visual observations. Cavitation bubbles appear inside this vortex at pressure significantly higher than the vapour pressure of the liquid, hence suggesting that these bubbles are of the gaseous type. Recording the inception point for water and 45/55 EG/W mixture showed that σ_i increase linearly with pump speed for 2 impeller geometries of pump J. Apart from the geometrical effect, the EG/W mixture seems to give about 20% higher σ_i than water at all speeds. By neglecting the thermodynamic effect due to the absence of the vapour bubbles and for insignificant surface tension effect, the difference between σ_i of water and 45/55 can only be related to higher gas pressure of the mixture.

An approximation of the difference $\Delta\sigma_i$ for these two liquids is found from the Henry-Datton's law;

$$\Delta\sigma_i = \frac{K_s}{\frac{1}{2} V_\infty^2} \left[\left(\frac{p_v}{\rho}\right)_{\text{water}} - \left(\frac{p_v}{\rho}\right)_{\text{EG/W}} \right]$$

where K_s is an average percentage saturation for both liquids. The agreement between the calculated and measured $\Delta\sigma_i$ for two impeller geometries is reasonable with an average value of $K_s = 0.7$.

7. By considering a linear relationship between the solvent surface tension and the solubility of gases, EG/W mixtures are expected to dissolve more gases than pure water. Instrument reading of $\sim$ 50% saturation for 50/50 EG.W in equilibrium with air can only be explained in the context of the anti-foaming aditives present in the commercial Ethylene glycol. If the mixture is stored for a lengthy period (which is normally the case), these additives would float on the surface and reduce the amount of air diffusion into the liquid. Pure Ethylene glycol or those used for other industrial purposes are not expected to show similar behaviour.

FIGURES 7.1 to 7.12

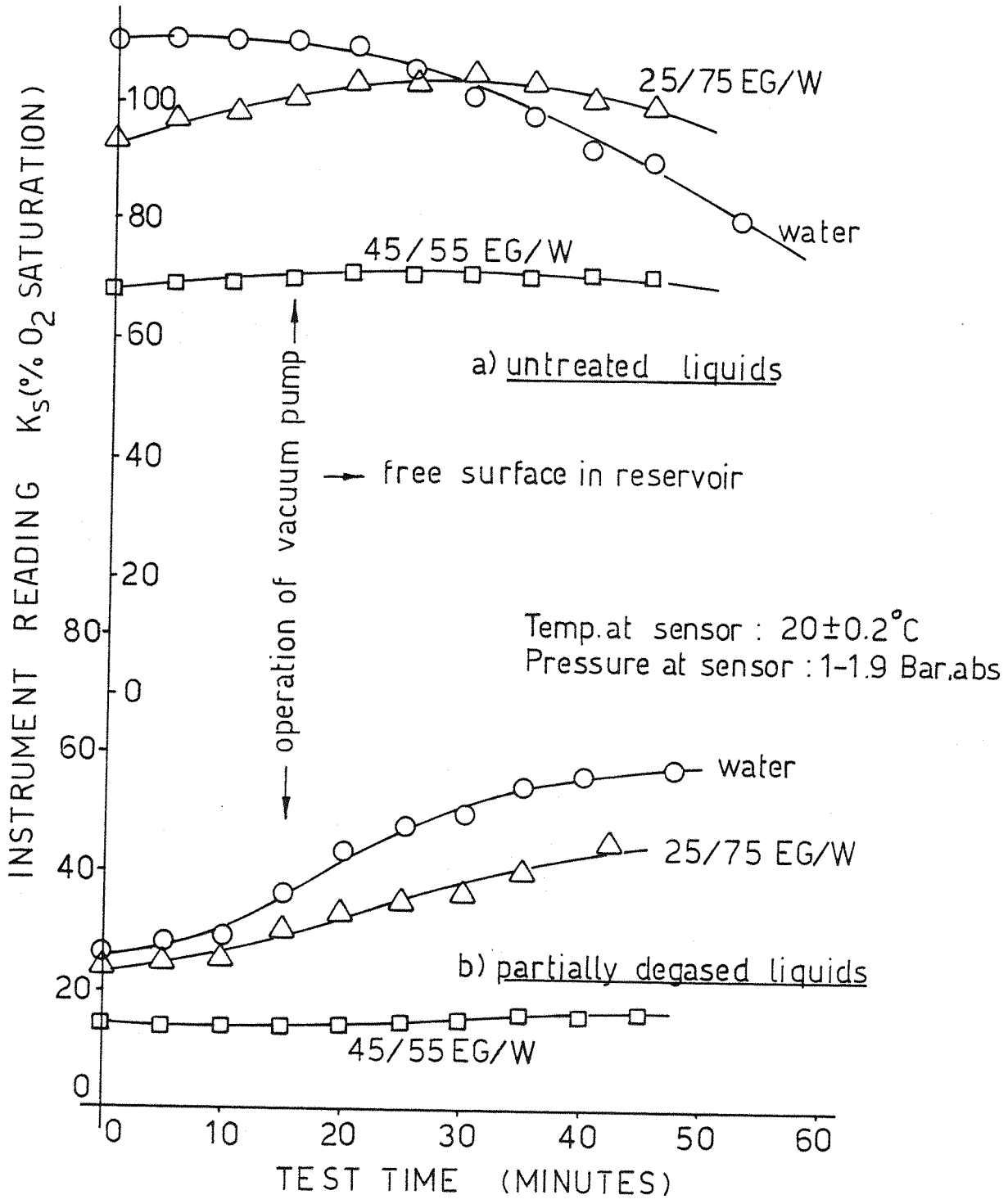

FIG 7.1 CHANGE OF OXYGEN CONCENTRATION WITH TEST TIME FOR WATER AND EG/W MIXTURES

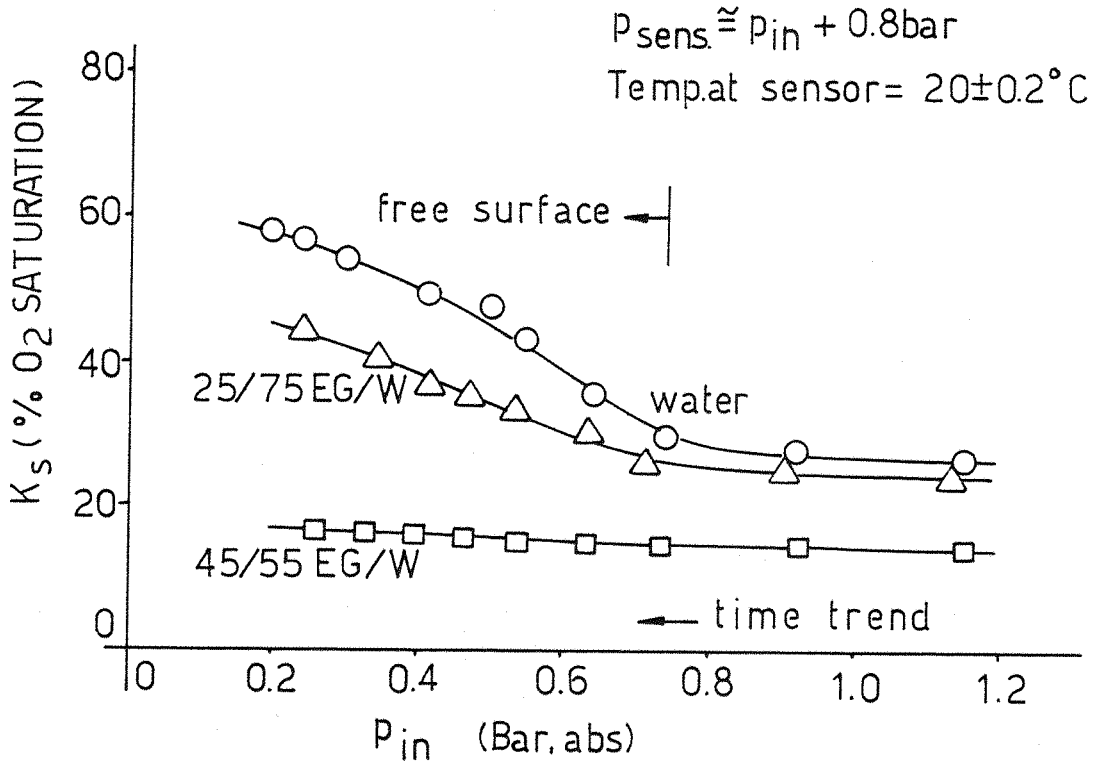

FIG. 7.2 CHANGE OF O_2 CONCENTRATION AS FUNCTION OF TEST PRESSURE FOR WATER & EG/W MIXTURES

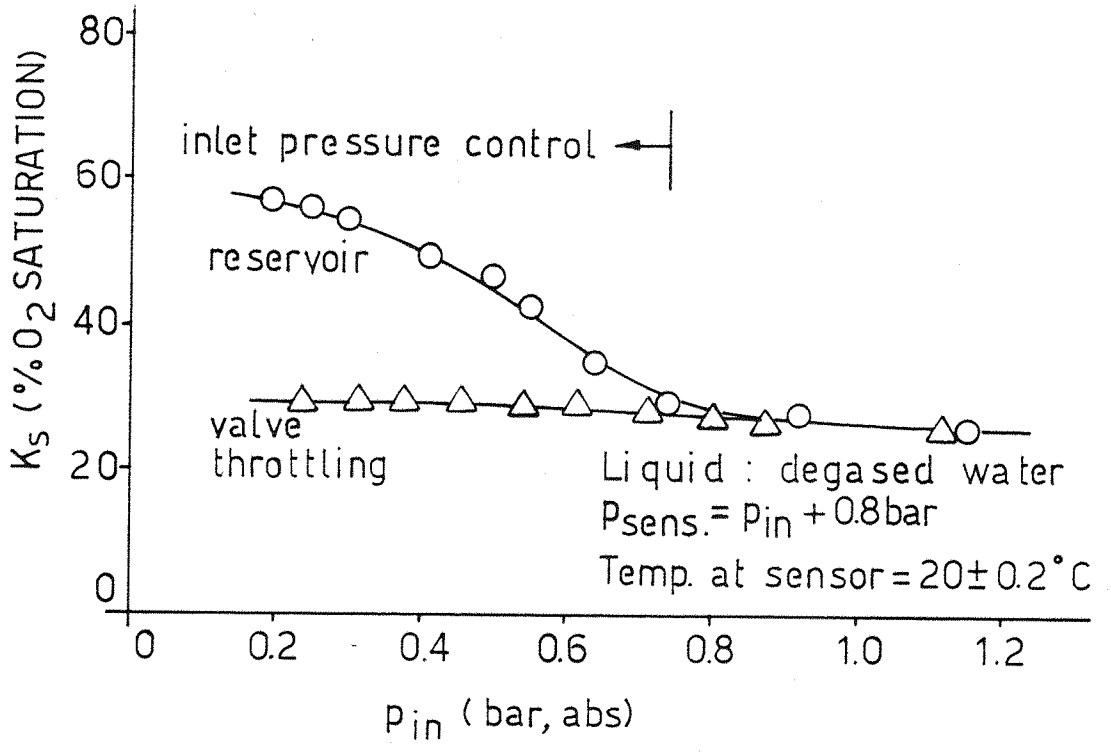

FIG. 7.3 TEST TYPE INFLUENCE ON THE VARIATION OF O_2 CONCENTRATION DURING THE TEST

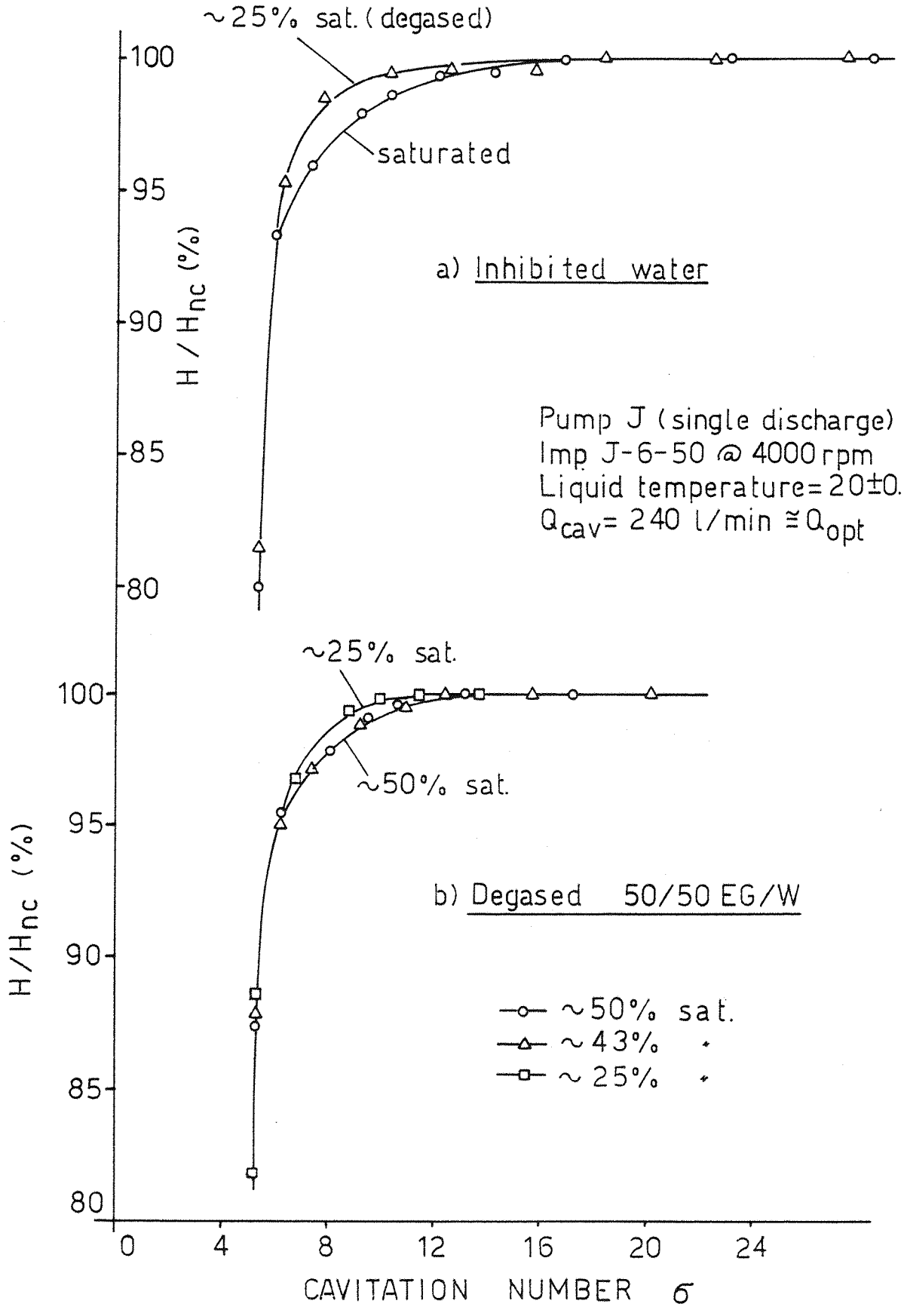

FIG 7.4 LIMITED GAS CONTENT EFFECT ON THE CAVITATION OF PUMP J WITH WATER AND EG/W MIXTURE

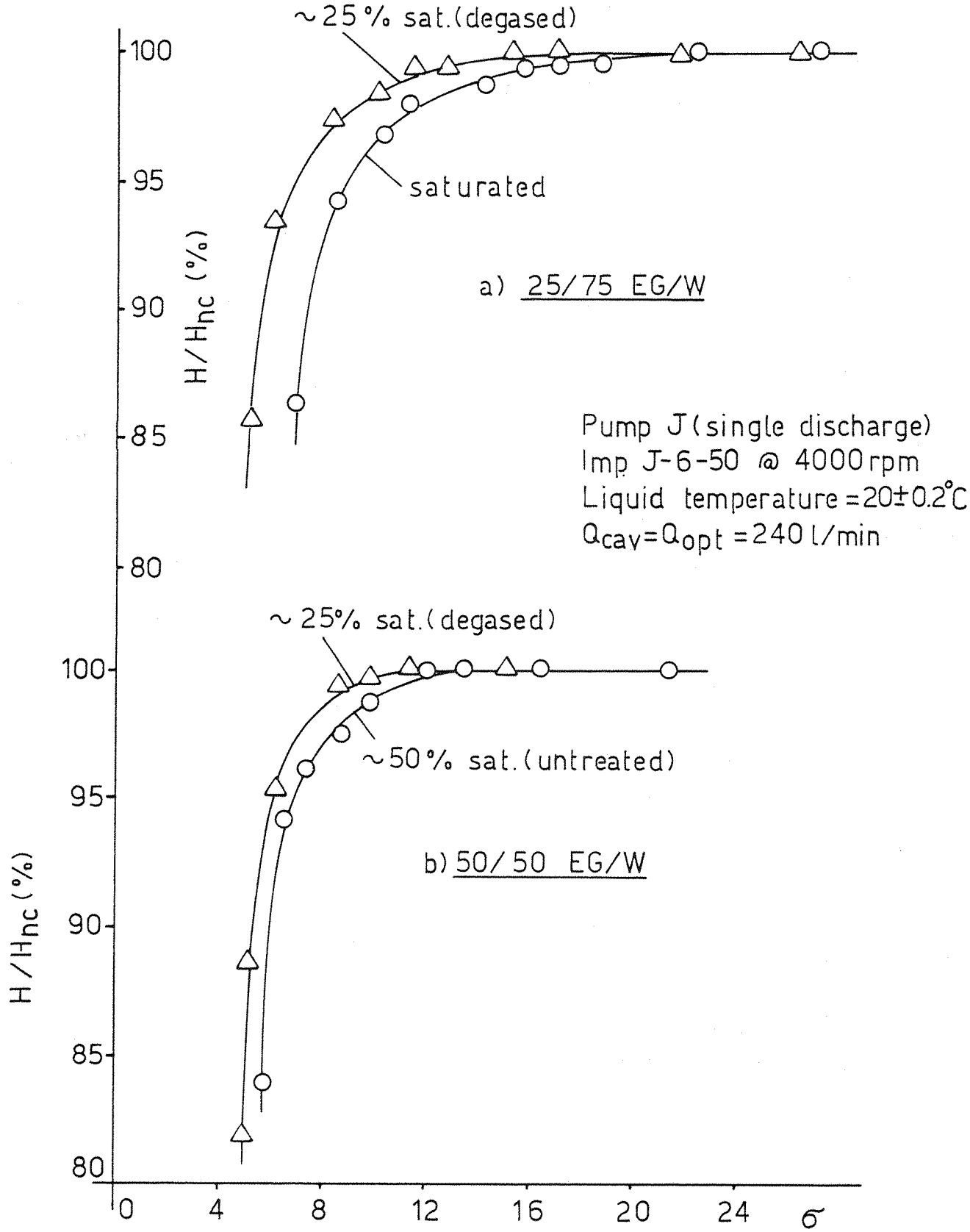

FIG 7.5 EXTENSIVE GAS CONTENT EFFECT ON PUMP J's CAVITATION FOR TWO EG/W MIXTURES

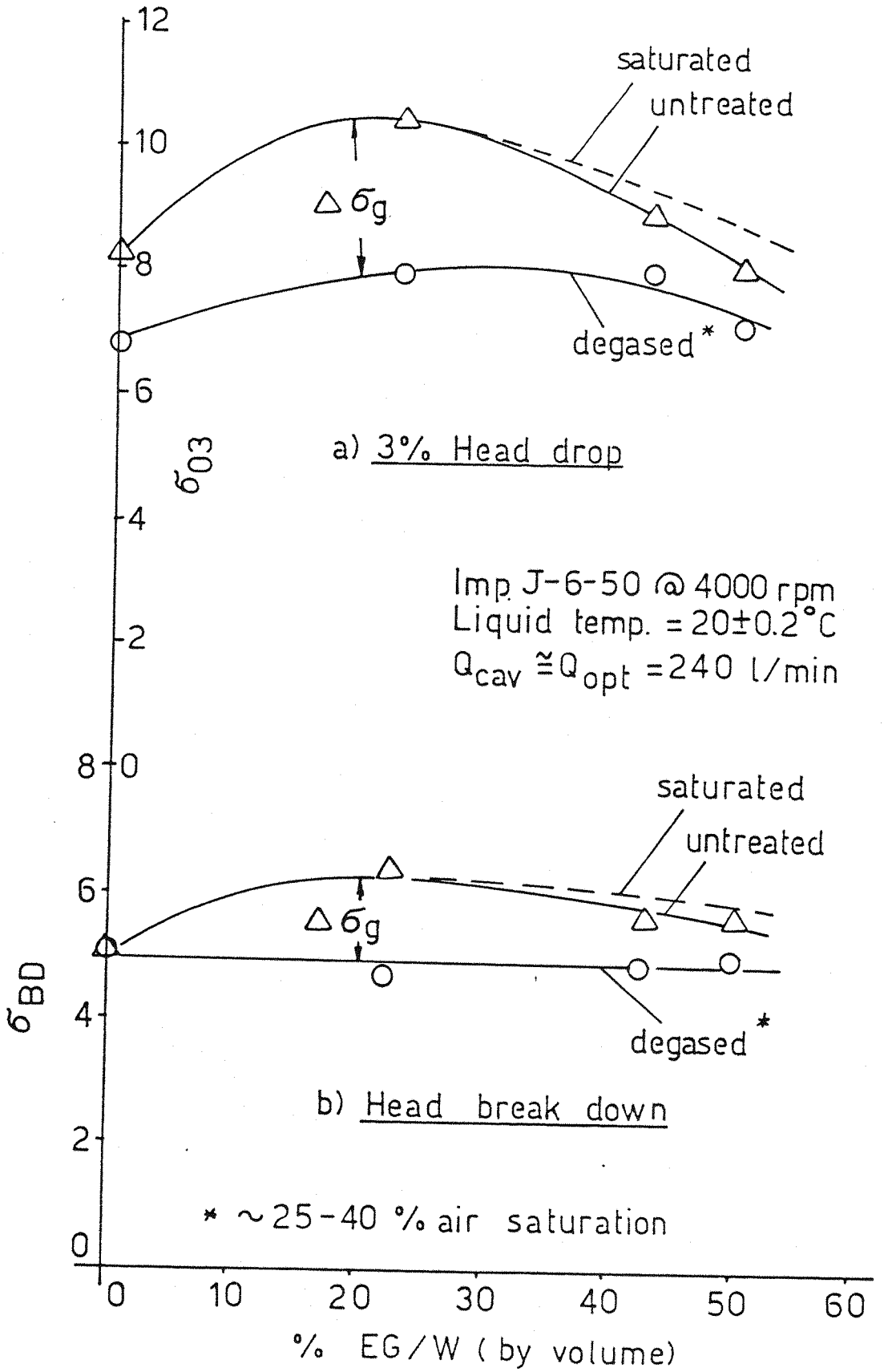

FIG 7.6 GAS CONTENT EFFECT ON PUMP Js CAVITATION AS FUNCTION OF EG CONCENTRATION AT 20°C

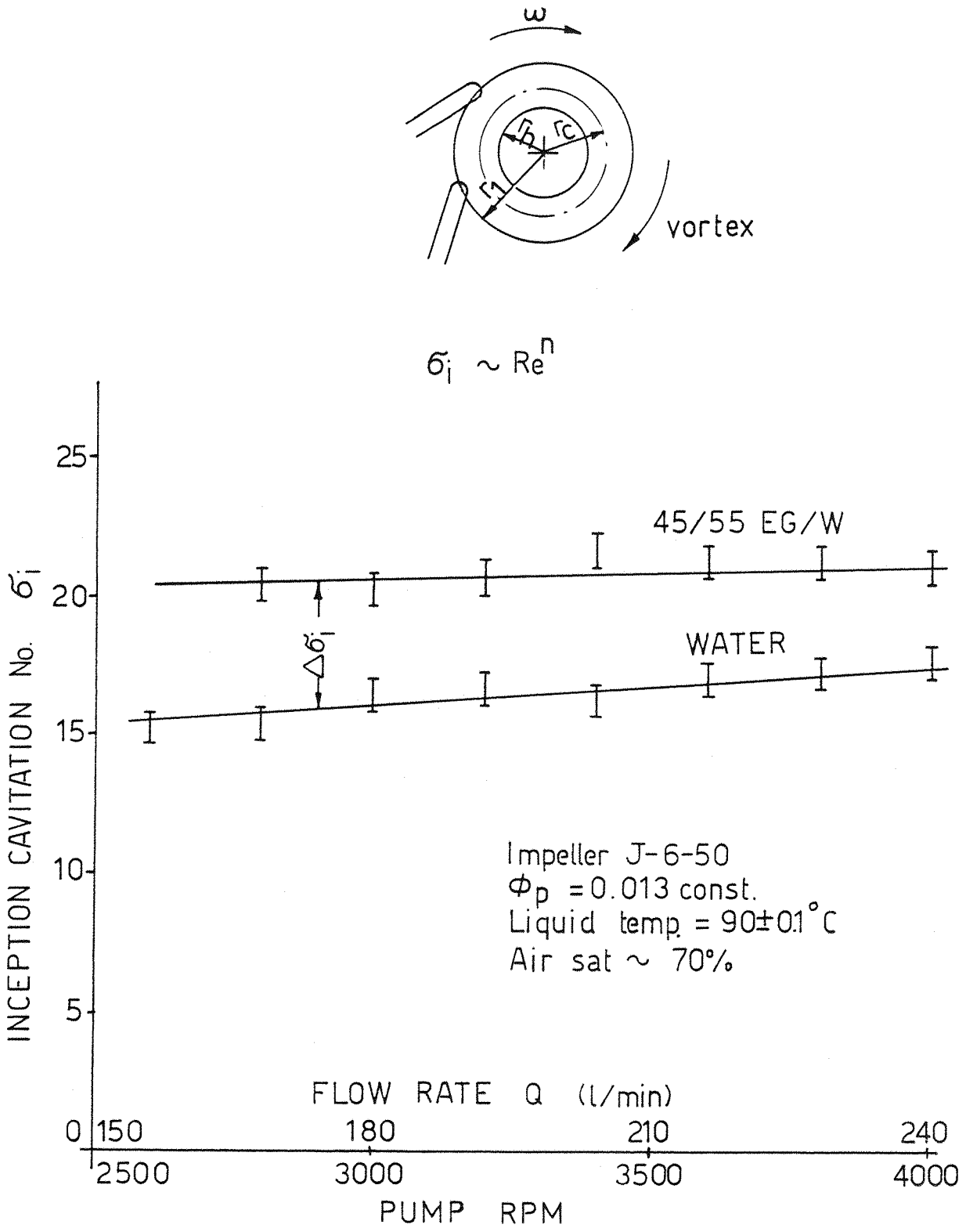

FIG 7.7 VORTEX INCEPTION CAVITATION AT IMPELLER HUB OF PUMP J FOR WATER AND EG/W MIXT. AT 90°C AND VARIOUS PUMP SPEEDS

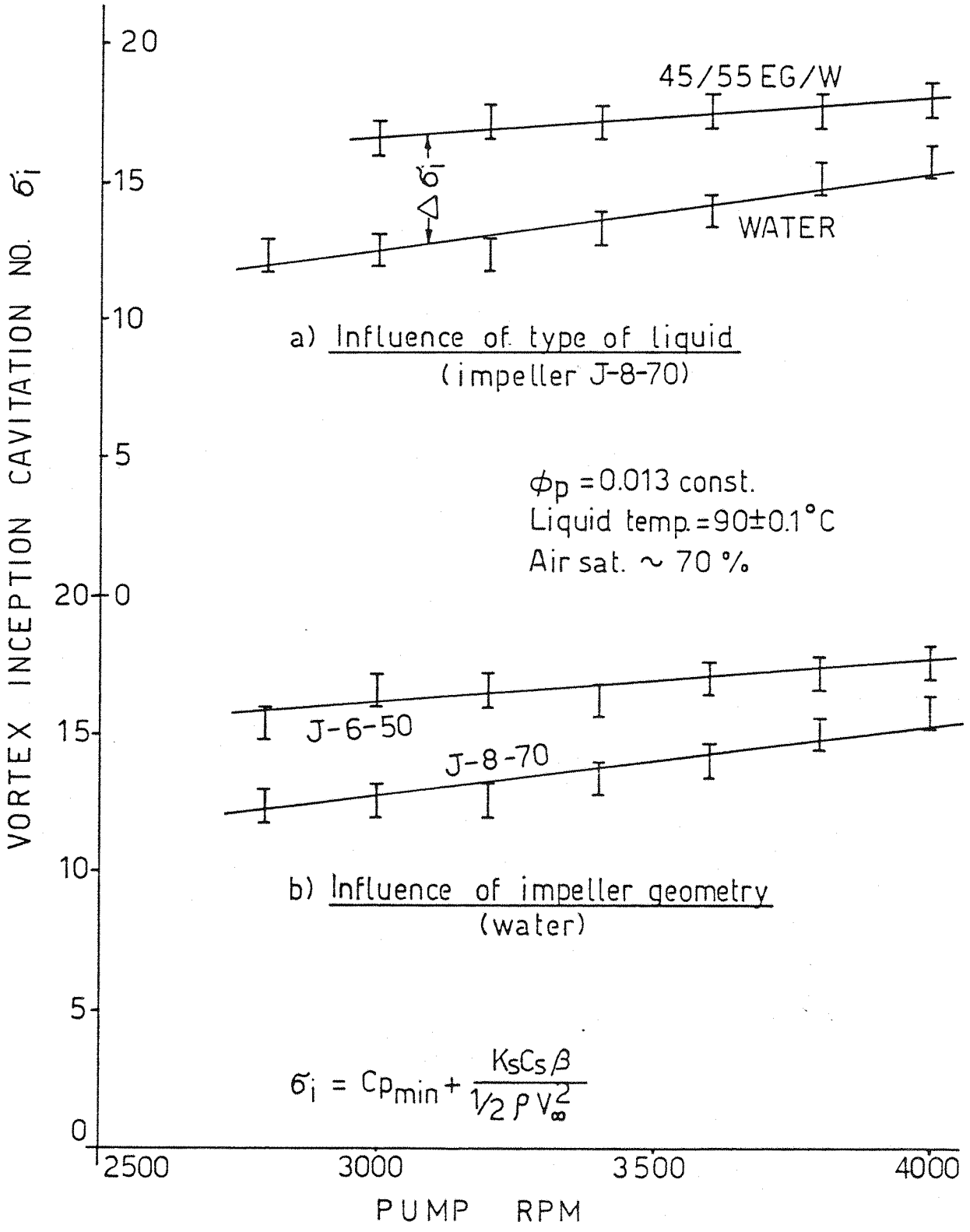

FIG. 7.8 COMBINED FLUID PROPERTIES AND IMPELLER GEOMETRY EFFECT ON THE CAVITATION INCEPTION INSIDE THE HUB VORTEX OF PUMP J

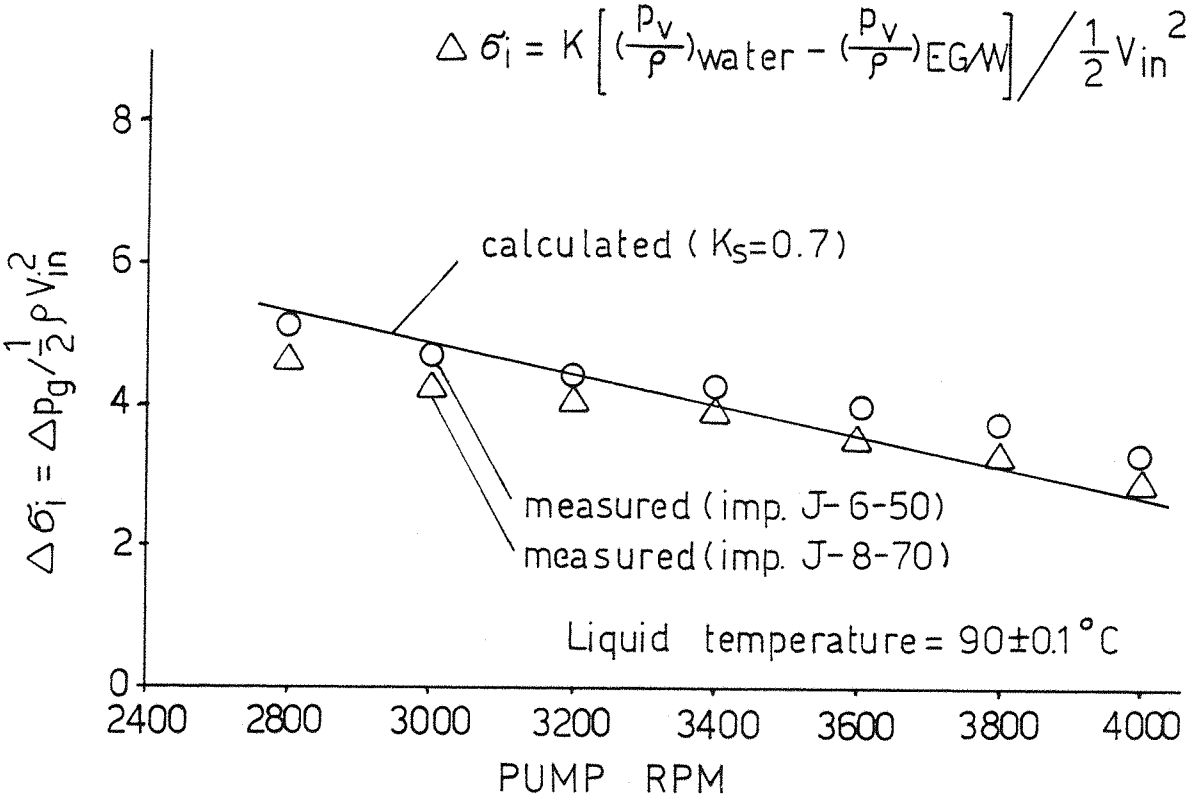

FIG 7.9 PREDICTED AND MEASURED INCREASE IN THE VORTEX CAVITATION INCEPTION NUMBER OF EG/W OVER THAT OF WATER DUE TO INCREASED P_g

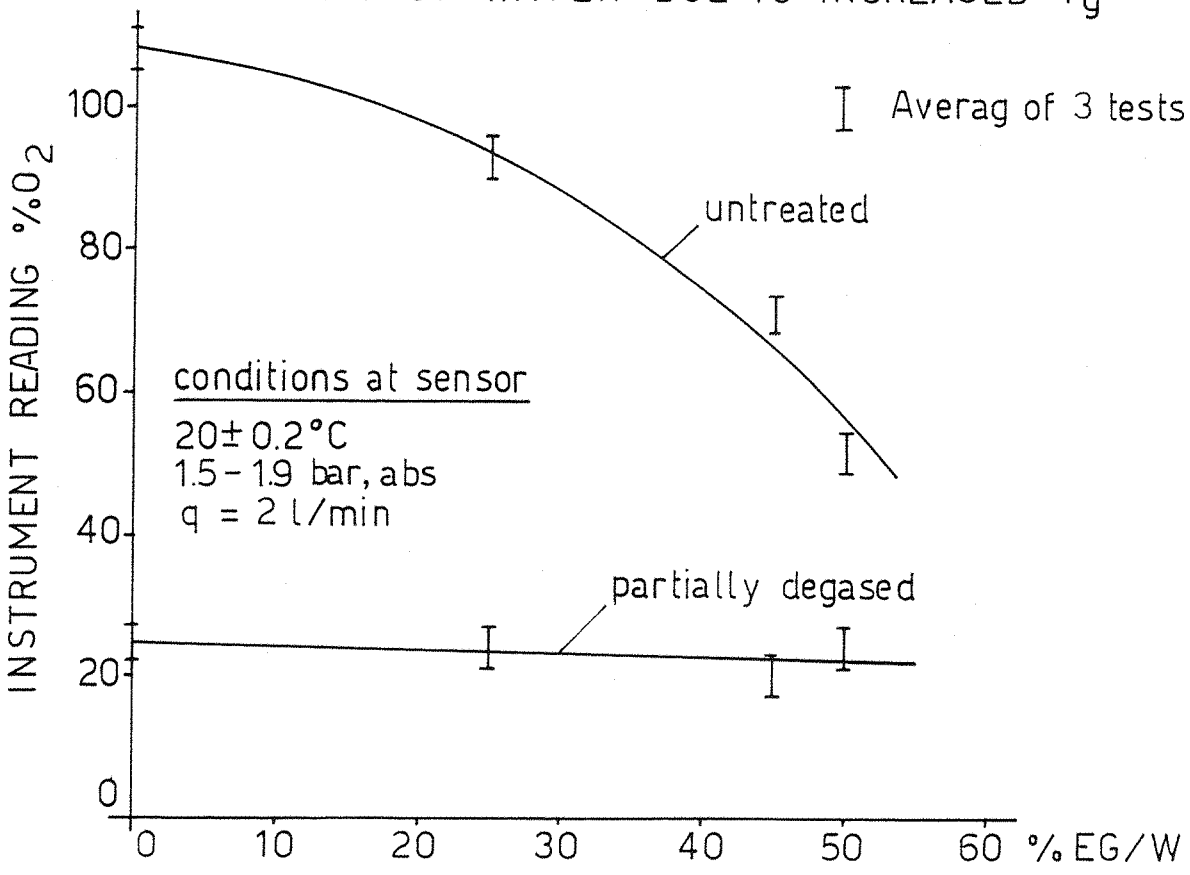

FIG. 7.10 OXYGEN METER READING FOR THE UNTREATED AND DEGASED COOLANTS AT THE START OF THE TEST

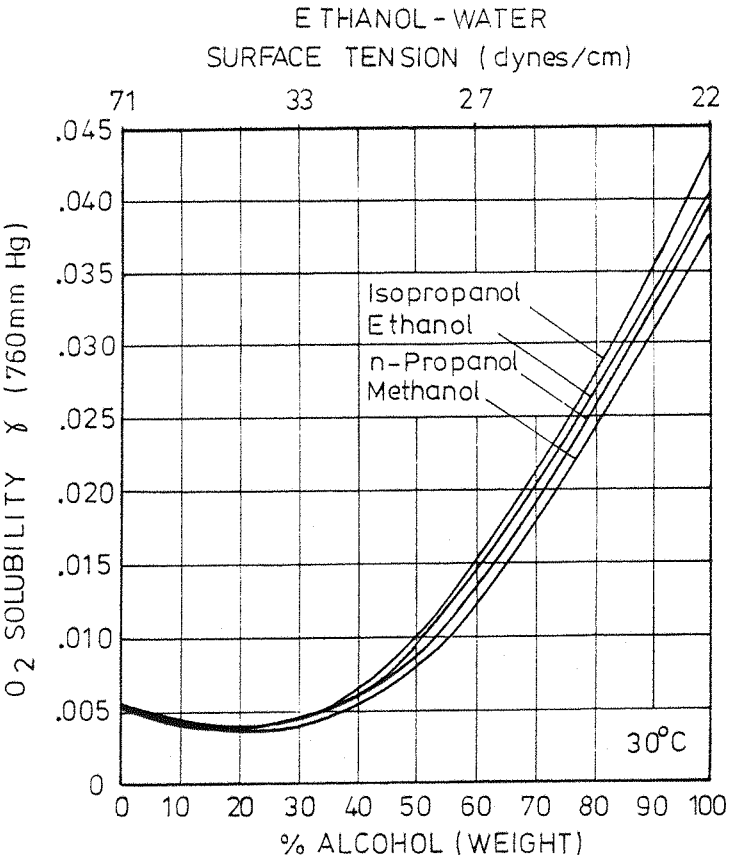

FIG 7.11 GAS SOLUBILITY OF ALCOHOL - WATER MIXTURES AS FUNCTION OF ALCOHOL CONCENTRATION AND SURFACE TENSION[148]

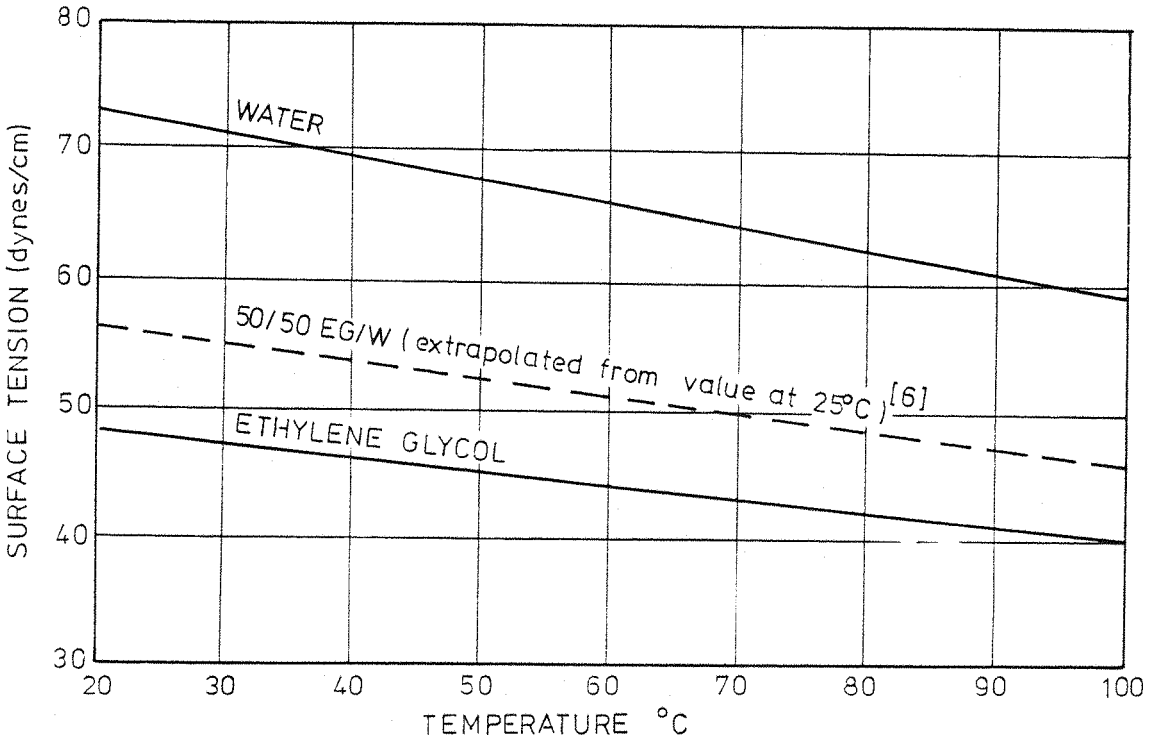

FIG 7.12 SURFACE TENSION OF PURE WATER AND ETHYLENE GLYCOL AND EXTRAPOLATED DATA FOR THE MIXTURE 50/50 EG/W[7,20]

CHAPTER 8

THERMODYNAMIC EFFECT AND THE PROPERTIES OF LIQUIDS: DISCUSSION OF TEST RESULTS

8.1 Temperature Effect on Pump Cavitations

In order to maintain adequate pump operation, the net positive suction energy (NPSE) defined by the difference between the total pressure energy at the suction flange and the vapour pressure energy (equation 5.1), must not be reduced significantly below that required for cavitation free operation. In Chapter 5 the suction performance of the small pumps was discussed in detail, and it was shown that the required NPSE depends largely on pump design and the flow conditions at impeller inlet. Equation (5.6) is a general form of the required NPSE, whereas equation (5.11) is a more reliable source for its estimation, although much more difficult to apply.

Let us consider equation (5.1) for the estimation of the available NPSE at the suction flange of the centrifugal pump. As the circulating liquid temperature rises so does its vapour pressure and hence in order to maintain the same NPSE at all temperatures, the inlet pressure p_{in} must be increased simultaneously as p_v rises.

The equilibrium vapour pressure of water, Ethylene glycol and their mixtures are plotted in figure (8.1) at elevated temperatures (80 - 120°C) [37]. On figure (8.2) the same vapour pressure values are replotted as function of percentage Ethylene glycol for any particular elevated temperature. From both two figures it should be obvious that EG/W mixtures have lower vapour pressure at any one temperature depending on the concentration of EG in the mixture. Hence to produce the same required NPSE of equation (5.1), the mixture requires less inlet pump pressure. 80/20 EG/W mixture for example has a vapour pressure of less than half that of water at temperatures 90 - 120°C and therefore apparently needs nearly 50% less inlet pressurization to maintain similar NPSE than that for water.

This is quite good from the operational point of view, because it reduces the need for extra high inlet pressures, which also means cheaper fittings and less leakage problems. The other advantage arises where inlet pressurization is reduced or diminished for some reason. In this case the EG/W mixtures would perform better, because for the same low inlet pressure which may prove inadequate for water, is likely to be sufficient to maintain some degree of pump performance adequacy. This was found to be true from tests on a constant geometry system using both water and EG/W mixtures [29, 35]. At an inlet pressure of 0.8 bars, abs, pump J operated near its Q_{opt} was approaching complete performance breakdown when water at 90°C was handled. When 50/50 EG/W mixture at the same temperature was handled, the same inlet pressure proved to be quite sufficient to maintain adequate pump operation, with only minor performance drop.

Pump cavitation is the result of a vapour cavity forming in the lowest pressure region of the pump, normally at the suction side of the blade. A fixed vapour cavity in the flow passage of the impeller has the effect of both reducing the blade loading capacity of the impeller and of producing a restriction to the flow passage, with the result of performance drop both in developed head and overall efficiency.

In Chapter 6 it was assumed that in order to maintain a fixed cavity in the low pressure region, a continuous vapour mass flow across the cavity boundary must be always present. This mass transfer is associated with heat transfer and therefore a temperature gradient ΔT must exist at the wall to satisfy the equilibrium condition. This is normally termed the thermodynamic effect. Theories dealing with the thermodynamic effect associated with the fixed cavity are reviewed in section 6.3. Basically these theories assume a pressure depression Δp_v corresponding to the temperature depression ΔT, which is largely dependent on the equilibrium vapour pressure gradient dp_v/dT at the cavity wall. Practically all these theories have been shown to be related in some way or another to the B-factor theory [155], which correlates the cavitation tendency of the pump to the vapour to liquid volume ratio (V_v/V_ℓ).

For the cold liquids water and EG/W mixture the thermodynamic effect produces only negligible pressure depression Δp_v as compared to the hot liquid, because of the low dp_v/dT ratio at low temperature. As an example, a temperature depression ΔT of only 2°C for water at 20°C produces a depression Δp_v of 0.003 bar compared to 0.07 bar at 100°C, an increase of 23 times. This led to the conclusion of treating cold water as the liquid with the worst cavitation performance [155].

Earlier test results on water [46, 81, 145, 154, 155, 158] showed that as the liquid temperature rises so does ΔT and Δp_v, with the result of improved pump performance correspondingly. In the early stage of this research some tests on water were performed at temperatures up to 110°C. Pump J was operated at 5000 rpm at a constant test flow of 0.86 Q_{opt}. The deterioration of both developed head and overall efficiency as a result of NPSE reduction were plotted on figure 8.3. The effect of temperature rise is to improve the cavitation performance of the pump by delaying both inception point and performance breakdown and therefore the same performance drop can be achieved at a lower available NPSE than that of the cold water, mainly due to improved thermodynamic effect. This agrees well with the results obtained by other authors mentioned above. In the next chapter we shall try to compare our test results with some other people's results and correlate them with respect to the B-factor theory.

Binary liquid mixtures of the polar type such as Ethylene glycol and water have lower vapour pressures and lower dp_v/dT ratio than water at any particular temperature, therefore the thermodynamic effect is expected to be less pronounced than water. Earlier test results [43, 57, 167] showed that this is true, however, they also showed that temperature rise produces an opposite trend at least up to $\sim$ 110°C, with the cold mixture giving the superior cavitation performance.

One of the main purposes of this research was to investigate this phenomenon further using three different centrifugal pumps of the automotive type. 50/50 EG/W mixture (by volume) was used in all cases. To reduce the

effect of test flow, all tests were performed at or above the BEP flow rate, which is in most cases the same as Q_{opt}. Due to rig limitations, tests could not be performed above 120°C. On figures 8.4 to 8.6, the test results are plotted for pumps J, H and K correspondingly.

By looking at these 3 figures it is possible to establish a common feature for all three pumps. That is, some thermodynamic effect is obtained at a temperature of 90 - 95°C above which it starts to diminish and in some cases (pump K at 110°C), the thermodynamic effect is practically non-existent.

Pump H (figure 8.5) provides another interesting feature of temperature effect. Here, as the inception point of cavitation is passed, there appears to be a rise in both developed head and overall efficiency before the pump performance starts to deteriorate again towards full breakdown. Temperature effect before the peak performance seems to suggest a positive thermodynamic effect up to 115°C. It is only when the cavity is fully developed, the thermodynamic effect at 115°C seems to diminish toward head breakdown.

The performance improvement of pump H can only be explained in the context of improved frictional factor at the boundary layer due to the presence of a thin vapour cavity at an early stage of cavitation, a phenomenon also found to be true by other authors [60, 90]. Pump H, is the only one of the three pumps tested which has a mixed flow portion at the impeller entrance with increased boundary layer contact to the entering liquid (see figure 2.11).

In order to obtain a clearer picture of the temperature effect on pump performance, the cavitation numbers of all three pumps tested were recorded at 5% head drop and plotted in figure 8.7 as a function of the bulk liquid temperature. Water data for pump J at a lower flow rate were taken from figure 8.3 and plotted on figure 8.7 for comparison.

For the 50/50 EG/W mixture, the drop in the cavitation number at ∿ 90°C due to the thermodynamic effect cannot be maintained at temperatures above 100°C. However after passing a relative maxima at ∿ 105 - 110°C, the cavitation numbers start to decrease again with further temperature rise. This is especially pronounced at 120°C for pump K. The relative maxima is also found by previous authors [57, 167]. Water, on the other hand, seems to give a progressive thermodynamic effect with increased temperature, as would be expected.

The deterioration of the thermodynamic effect above 90°C has not been explained fully so far. Thew and Hadji Sheikh [167] suggested a possible higher influence of surface tension and gas pressure of equation (6.21) as a counter balance to the thermodynamic effect, which may render the latter less effective at a certain temperature range. The same authors also suggested that because the fixed cavity consists mainly of vapour of the more volatile component of the mixture (water), the liquid surrounding the cavity will be depleted of the volatile component and therefore vapour mass transfer across the cavity boundary is reduced, followed by reduced heat transfer and thermodynamic effect.

The heat transfer problem associated with the binary mixture analysed in Chapter 6 seems to be the most significant of these suggestions, since both surface tension and disolved gas influences are less important for the well developed cavity. Free gas bubbles acting as nuclei, however, may be also of significance, because they provide the possibility of gaseous diffusion for highly saturated liquids and increase the number of vapour bubbles in the low pressure region with the result of reduced bubble growth and heat transfer across the boundary. In the next chapter these factors are discussed in full.

8.2 The Influence of the Gas Content

In Chapter 7, the influence of the gas content has been shown to be of great importance for the cold binary EG/W mixtures. Contrary to water, the influence of the saturated cold mixture showed a persistent cavitation effect

from the point of inception down to the head breakdown (figure 7.5). The suggestion has been made that free small gas bubbles of high population and unexpectedly long life observed during the test, promote the diffusion of gases due to highly super-saturated state at the low pressure region.

As the thermodynamic effect is estimated at a certain head drop (normally 3 - 5%) according to the following simple formula

$$\Delta E_v = (NPSE)_{cold} - (NPSE)_{hot} \qquad (8.1)$$

then any significant change in the estimated NPSE due to gas content both for the cold and hot liquid is bound to lead to some discrepancy in the estimation of ΔE_v.

This is best demonstrated on figure (8.8), whereby the mixture 50/50 EG/W was tested at 2 temperatures and different air contents. Test A was performed with a cold mixture taken from a freshly mixed batch of liquids, after settling down for a lengthy period. Hence it is assumed to be nearly saturated with air. Test A' was performed with the same mixture after heating it up to 95°C and then leaving it to cool down to 20°C over a period of 48 hours with little air contact. Oxygen meter reading for this liquid indicated about 40% saturation with air.

Test B' was performed with the same liquid of test A' after heating it up to 90°C, therefore it is plausible to assume that its percentage saturation remains unchanged. Lastly test B was performed with the liquid of test B' heated up to boiling and then cooled down to 90°C under vacuum. Hence this liquid is assumed to be nearly free of dissolved gas.

The resulting picture from these 4 tests shows that the application of equation (8.1) is highly uncertain if the exact amount of gas content is not known for the mixture, for both the hot and cold condition. If for example the thermodynamic effect is estimated from tests A and B, then we obtain an

extremely high value for ΔE_v. On the other hand, the application of equation (8.1) between test B' and A' would result in a much lower value for ΔE_v. This however, is believed to be more reliable because the gas content remains nearly constant between the two tests. Ultimately one would require to test the mixture at conditions of no gas content which corresponds nearly to that of test B. However the present rig is not suitable for such tests at the moment.

On figure 8.9, the effect of the air content on the estimation of ΔE_v is shown for water and three different concentrations of EG/W mixtures. 3% and 10% head drop was used in this figure. In both cases, the upper curve represents the evaluation of ΔE_v between the hot liquid of low gas(25-40%sat) content and the cold nearly saturated liquid, which corresponds to test B' and A of figure 8.8 respectively. The lower curve is obtained by estimating ΔE_v for the hot and cold liquid of similar low air content ($\sim$ 25 - 40%).

Figure 8.9 shows clearly that the margin of error between the saturated and the de-aerated curves is quite high and can reach as high as 200% of ΔE_v of the lower curve. In the last chapter it was shown that partially de-gased liquids (water and EG/W mixtures) do not show any measurable gas content below 7% head drop, and therefore it seems to be safer to use a 10% head drop for the purpose of thermodynamic result correlations.

Finally the conclusion is to be made from both figure 8.8 and 8.9 as to limit the thermodynamic effect where air content is both small and similar for both the cold and the hot liquid. Since gas free liquids cannot be obtained in our rig, at the moment, a percentage saturation of $\sim$ 25% seems to be sufficient to produce reasonably reproduceable test results.

8.3 The Influence of the Test Flow Ratio Q_{cav}/Q_{opt}

In section 5.2, the test flow rate was shown to influence the tendency of the centrifugal pump to cavitate. The lower the flow rate below the optimum value Q_{opt}, the sharper the $\sigma - \psi$ curve will fall as a result of NPSE reduction. Therefore σ_{cr} is likely to increase. The magnitude of these changes were also found to be influenced by the liquid temperature.

In applying equation (8.1) for estimating the thermodynamic effect, changes in σ_{cr} as a result of changes in the test flow rate are likely to influence the value of ΔE_v.

Let us first consider the combined effect of fluid properties and the test flow at a bulk liquid temperature of 25°C. Water and 50/50 EG/W mixtures were used for the test with pump J running at a speed of 4500 rpm. Both fluids were heated to 90°C and cooled down before the test, hence a moderate gas content effect for both liquids is expected. The test results are plotted on figure 8.10, with respect to the ratio Q_{cav}/Q_{opt}. Using the term $\Delta NPSE_\ell$ to express the difference in the required NPSE to produce similar head drop (3% in this case) due to the change in the liquid properties at the same flow rate and liquid temperature, it should be obvious from this figure that the liquid mixture fares better especially at flows significantly below Q_{opt}. At the Q_{opt} and above it $\Delta NPSE_\ell$ reduces to a small positive value.

If one assumes that all liquids of negligible air content have similar inception cavitation number, then according to Stepanoff [158] all liquids require an additional $\Delta NPSE_\ell$ drop below that of cold water to produce the same head drop as that of water. Then according to this, the positive $\Delta NPSE_\ell$ of figure 8.10 at Q_{opt} can be explained in this context. Knowing however that the mixtures of EG and water produce higher B-factor for the same head drop or in other words lower head drop for the same B-factor as we shall see in Chapter 9, then cold water is expected to behave better than the EG/W mixture, and therefore the positive $\Delta NPSE_\ell$ of the mixture cannot be explained in the context of the thermodynamic effect.

As a matter of fact, more recent results showed that EG/W mixtures of low gas content show an increase in σ_{cr} up to a concentration of 45/55 EG/W (figure 7.6a), above which σ_{cr} becoming lower than that of water, hence suggesting a strong viscosity effect.

The explanation for this seems to be related to the inlet hub vortex discussed in section 7.3.3, rather than the thermodynamic effect. If the dissolved gas pressure p_g of equation (7.16) is assumed to be nearly the same for cold water and 50/50 EG/W mixture, then the cavitation inception is likely to be dependent on the minimum pressure coefficient C_{pmin}, which according to equation (7.14) is Re number dependent. Knowing that the mixture is about 4 times more viscous than water, then it is obvious that at low flows the mixture is likely to operate at a relatively low Re number with the result of a significant drop in both C_{pmin} and σ_i. This seems to justify the appreciable $\Delta NPSE_\ell$ encountered in figure 8.10.

The thermodynamic effect is of more importance when operating centrifugal pumps with liquids of high vapour pressure like hot water and cryogenic fluids. On figure 8.11 the combined effects of test flow rate and fluid properties on the thermodynamic effect of pump J at 90°C are shown at 3% head drop. At flows around the Q_{opt}, the thermodynamic effect of water is higher than that of the liquid mixture 50/50 EG/W. As the flow rate is reduced, the difference between the two increases progressively with the thermodynamic effect of the mixture becoming non-existent at low flows. This seems to agree with earlier results [43, 57] obtained from tests on EG/W mixtures at flows appreciably lower than Q_{opt}. The reason behind this seems also to be coupled to the viscosity effect which produces low cavitation numbers for the cold mixture at low flows as shown on figure 8.10. In the absence of significant thermodynamic effect for this type of impeller, the effect of temperature rise does not produce the required improvement to counteract the viscosity effect and hence negative values of ΔE_v are produced. This may suggest that for the EG/W mixtures thermodynamic effect values ought to be obtained at sufficiently high Re numbers to avoid excessive viscosity effect. This is best done by testing the pump at flows near or above Q_{opt}.

8.4 The Influence of Impeller Geometry

The thermodynamic effect is likely to be influenced by the type and geometry of the test pump [154]. To assess the importance of the geometry, the present research looked at the variations of the thermodynamic effect due to changes in the impeller geometries of three pump types, in some detail. In Chapter 5, geometrical influences were discussed in the context of the general suction performance of the test pumps, which is to be extended here to include the thermodynamic effect due to temperature rise.

Two main geometrical categories were found to be of special interest for the pumps handled here. The first is the influence of the presence and size of the tip-to-casing clearance at the open end of the impeller. The second is the influence of the blade number and shape for similar inlet and outlet diameter.

The tip clearance presence was found to promote some improvement in the suction performance of the centrifugal pump at any given flow rate (section 5.3). These improvements were also found to reach a maximum at a certain tip clearance, above which the pump suction performance starts to decrease again.

With regard to the thermodynamic effect, changes in the suction performance are likely to reflect on the net value of the thermal depression of equation (8.1). This is shown on figure (8.12) for pump J operated with the closed and the semi-open impeller as a function of the test flow. Although the scatter of the test results is understandbly high, which can be related to the pronounced air content effect of the circulating liquid (50/50 EG/W), a marked increase in the thermal cooling can be traced for the semi-open impeller, nearly at all test flows.

On figure 8.13, the same two impellers were examined for the thermodynamic effect at different tip clearances near the optimum flow rate, again using 50/50 EG/W mixtures. Apart from the marked thermodynamic effect of

the semi-open impeller of larger tip clearance (1 mm), the influences of the type of shroud and the size of the clearance seems to be only slight nearly at all head drops. This suggests that the thermal cooling is only a weak function of the type of shroud, especially for EG/W mixtures where the thermal cooling is low any way. For water greater variations could be established (figure 8.17).

Extending the thermodynamic effect to a higher temperature, the semi-open impeller of pump K was tested near Q_{opt} up to a temperature of 120°C. 50/50 EG/W mixture was used again with similar amount of air content (40 - 60% saturation). In figure 8.15 the test results of the semi-open impeller are compared to those of the closed impeller given on figure 8.7. Cavitation number and suction specific speed were measured at 5% head drop and plotted as a function of the liquid temperature for both impeller types. The resulting picture seems to indicate an improved cavitation performance at temperatures above 90°C. At temperatures below that the performance is not changed significantly, although some improvement is expected for the semi-open impeller as was discussed in Chapter 5. Since this comparison was done at the same flow of 90 L/min, then the improved thermodynamic effect is partly because this flow rate comprises about 1.1 Q_{opt} for the semi-open impeller compared to $\sim$ 0.9 Q_{opt} for the closed impeller. However, when comparing at a single flow rate, the semi-open impeller shows an improved (larger) thermodynamic effect at elevated temperatures.

The blade shape and number was shown to influence the suction performance of the pump (section 5.4) and therefore the critical cavitation number could be successfully correlated to the contraction number (figure 5.16) or even better to a geometry ratio ℓ/w (figure 5.17).

On figure 8.16, the thermal cooling ΔE_v was estimated according to equation (8.1) at various head losses for three different blade shapes but of the same blade number of pump J. 50/50 EG/W mixture was used at a test flow near Q_{opt}. Some water test data for two similar blade shapes were also included for comparison. Examination of this figure reveals that for both

liquids, the thermal cooling is a strong function of the impeller shape, improving with increasing blade length and reduced inlet angle (increased solidity).

Examination of the test results of the cold liquids for the three impellers in question (figure 5.15) suggests that the impeller with the highest σ_{03} of the liquid produces higher ΔE_v. As a matter of fact, test results of the three impellers at 90°C produce similar cavitation numbers, which mean that geometrical influences obtained with the cold liquid do not apply when the pump is operated with hot liquids, simply because factors such as the thermodynamic effect are largely influenced by the inlet geometry of this particular pump.

Since from visual observations (Chapter 9), the cavitation bubbles are likely to block the entrance to the impeller with a fixed cavity (or cavity cloud) extending to the pressure side of the blade, impeller J-8-30 with significantly smaller inlet area is likely to produce high vapour bubbles per unit volume of the flowing liquid with a better distribution. Hence the thermal cooling effect although normally small with the EG/W mixture, will be more pronounced with this impeller, which in turn allows for a better blade loading.

To explore this phenomenon further, pumps J and H were tested with 6 different impellers each with 50/50 EG/W mixtures near Q_{opt}. The resulting thermal cooling at small head drop was estimated in the temperature range 25 - 95°C and plotted against the geometry ratio ℓ/w on figure 8.14. The resulting adjoining curves seem to indicate a gradual thermal cooling improvement with increased ℓ/w ratios (and solidity). It must be noted here however, that this figure is not to show absolute terms of thermal cooling for pumps, but rather a tentative suggestion of the increased tendency of pumps to promote thermal cooling with increased solidity. Liquid type and temperature, pump speed, gas content effect are likley to influence the absolute value of the thermodynamic effect, however the general trend of figure 8.14 is believed to be operative if conditions are maintained the same

throughout the test. This is of special interest to the pump user, since a better impeller tested with cold water may prove less efficient at elevated temperatures when operating with some degree of cavitation.

Finally, the combined effect of blade shape, tip clearance and test flow rate is shown for water on figure (8.17). The blade shape effect is obviously obtained when comparing the semi-open impellers J1 and J2 of similar tip clearance (0.5 mm), with J-8-30 giving significantly higher thermal cooling at all flows. The influence of the type of shroud and the tip clearance size, seems to indicate a better result with the closed impeller with the semi-open impeller with smaller clearance (0.5 mm) fairing worst, although the latter was estimated a higher pump speed. In general it can be said that the tip clearance effect on the thermal cooling is only marginal at 95°C, for both water and 50/50 EG/W mixture.

For the same mixture the results of the shrouded and two different clearances of the semi-open impeller J-8-48 are presented as an envelope on the same figure. Obviously, the downward trend of ΔE_v with reduced test flow is quite strong which again confirms the results of figure (8.12).

8.5 Concluding Remarks

Thermodynamic effect of cavitation for the small, simple design, high speed centrifugal pumps is likely to depend on several parameters such as the test flow rate, the pump and impeller geometry, the fluid properties and most prominently, the liquid temperature for water and EG/W mixtures. The discussion of the test results can be summarized as follows.

1. Contrary to inhibited water, the mixture 50/50 EG/W does not give a progressive rise in the thermodynamic as the temperature of the liquid rises. Tests with three different small centrifugal pumps at Q_{opt} showed that some thermodynamic effect is obtained at $\sim$ 95°C and diminishes as the temperature rises further. Eventually a minimum is reached at $\sim$ 105 - 110°C for this mixture, above which a marked tendency to promote thermodynamic effect with further increase in temperature sets in.

2. Tests performed with cold water and 50/50 EG/W mixtures at different Q_{cav}/Q_{opt} ratios show that the required NPSE for 3% head drop is lower for the mixture, and therefore it cannot be related to the thermodynamic effect because of the higher vapour pressure of water. The reason behind this seems to be related to the vortex influence at the impeller inlet, which is strongly dependent on Re number. Relatively low Re numbers for the more viscous mixture at low Q_{cav} seems to promote low σ_{03}.

3. In Chapter 7, it was shown that EG/W mixtures are greatly influenced by the amount of disolved gas content, so that pump cavitation is significantly promoted when the gas content is sufficiently high. Because the thermodynamic effect is normally compared at a small head drop, it follows that any great variation in σ can lead to great discrepancies in the estimation of ΔE_v. Thermodynamic effect test results obtained at relatively low gas content ($\sim$ 25% sat.) and at sufficiently large head drop ($\sim$ 10%) seem to give much lower margin of error, and better repeatability of the test data.

4. The influence of the test flow ratio Q_{cav}/Q_{opt} on the thermal cooling of the small pumps is less pronounced with water than with the mixture 50/50 EG/W. Tests at relatively low Q_{cav}/Q_{opt} ratio seem to promote higher viscosity effect on the cold mixture as discussed under (2) above, and therefore, the thermodynamic effect is counter-balanced by the viscous effect at low flows, with the result of negative ΔE_v values in some cases.

5. Most small, commercial pumps are fitted with semi-open impellers to reduce maintenance and cost. Compared to a fully shrouded impeller of the same design, these impellers seem to promote an improvement in the thermodynamic effect of the pump. At 90°C, these improvements are only marginal when compared at the same flow rate, but as the temperature increases, a marked improvement is recorded for pump K.

6. Impellers of high geometry ratio ℓ/w (or solidity) produce higher thermodynamic effects. Since from visual observations, the vapour cavity is likely to occupy the whole entrance to the impeller, smaller inlet area is likely to promote higher vapour bubbles per unit volume of the flowing

liquid with better distribution, with the result of improved heat transfer and thermodynamic effect.

7. In general, the absolute values of ΔE_v were found to be larger than one would expect in this range of temperatures. High gas content effect of the cold liquid, which is very pronounced at small head drops, is one reason. The other is believed to be related to the particular impeller inlet flow field of the test pumps. A vortex formed at the impeller entrance is likely to promote a longer residence time of the vapour bubble in the low pressure zone, which help to promote bubble growth, with the result of improved thermal depression.

FIGURES 8.1 to 8.17

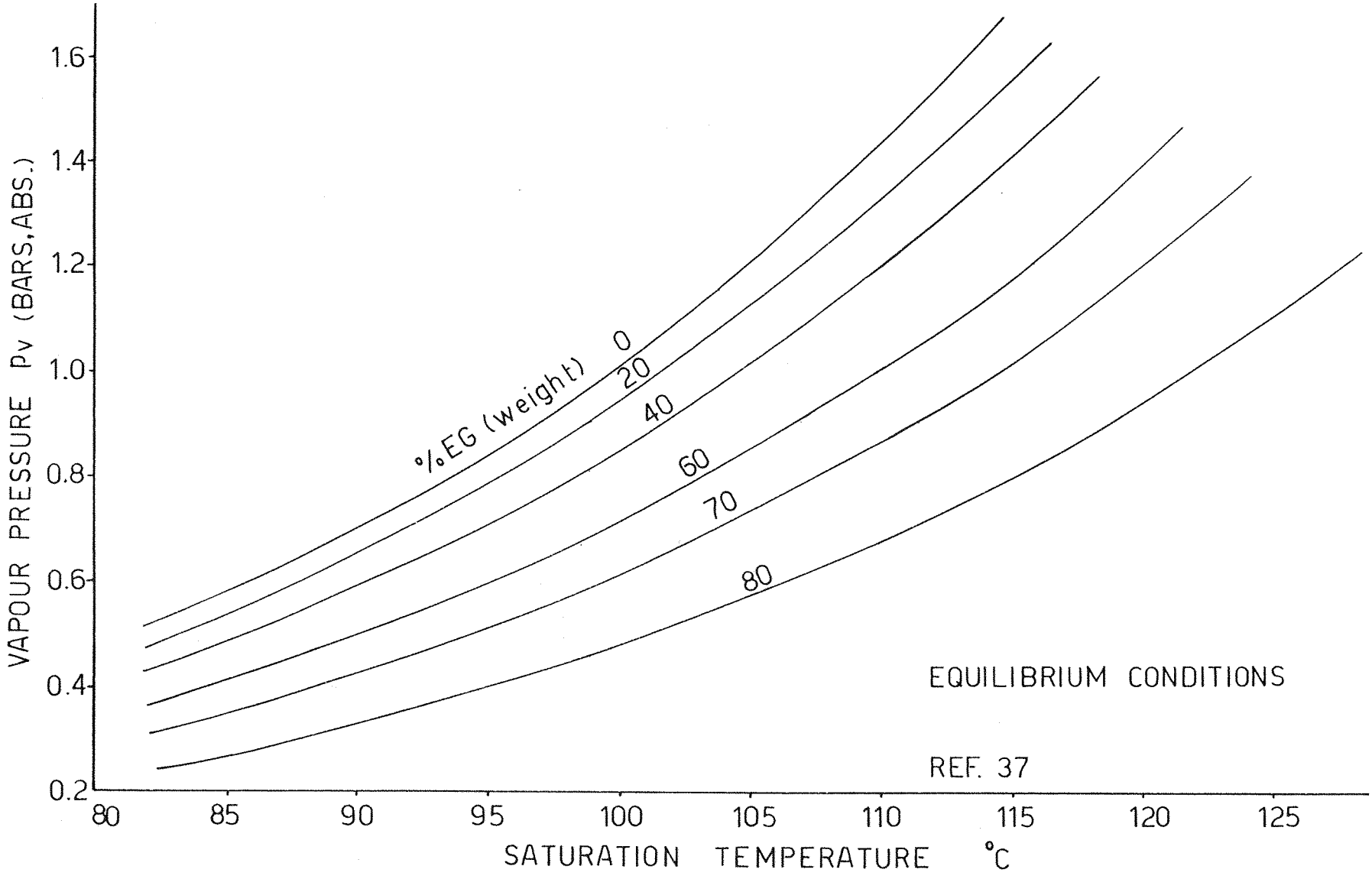

FIG 8.1 VAPOUR PRESSURES OF ETHYLENE GLYCOL-WATER SOLUTIONS

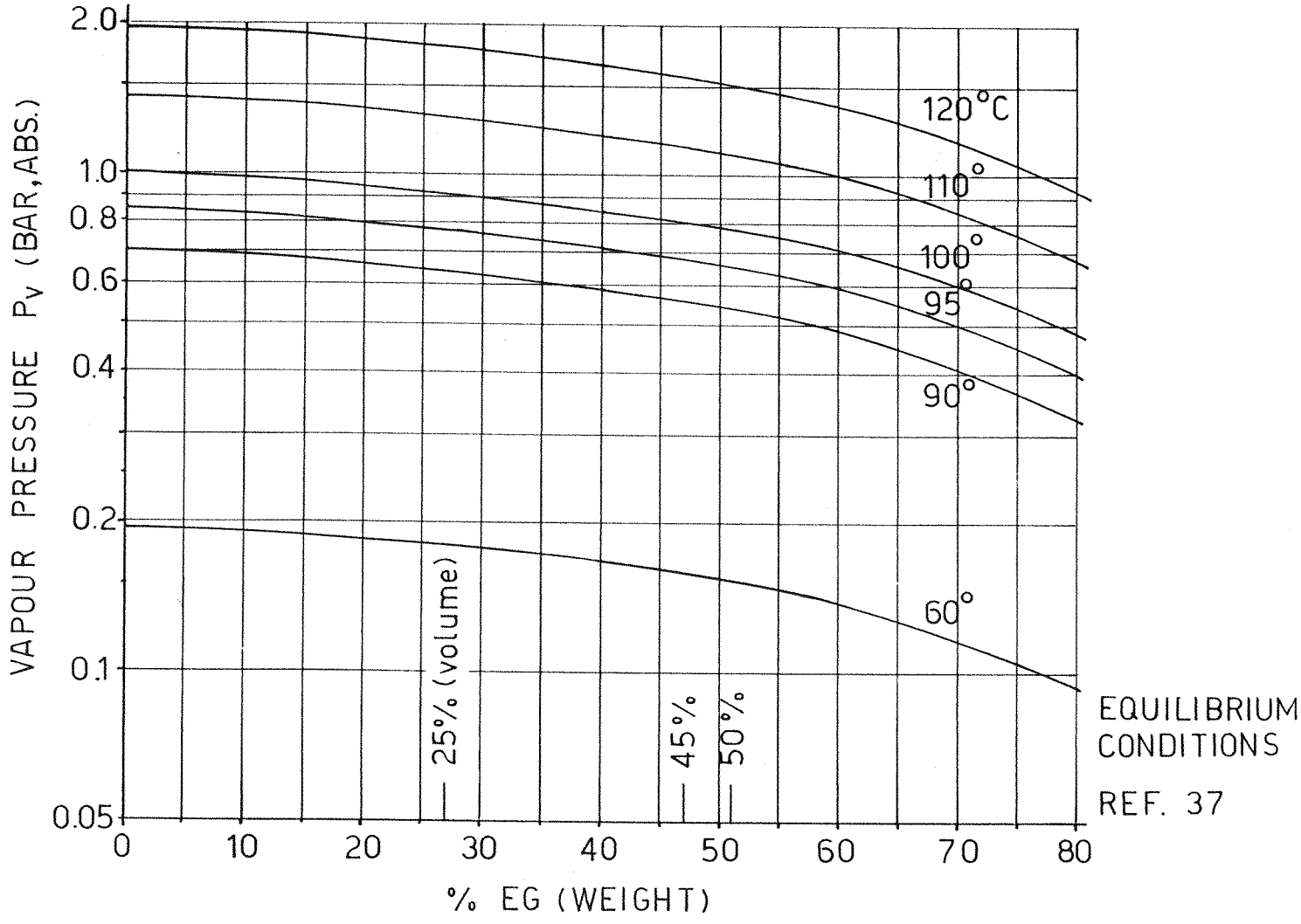

FIG. 8.2 VAPOUR PRESSURES OF EG/W MIXTURES AT VARIOUS TEMP.

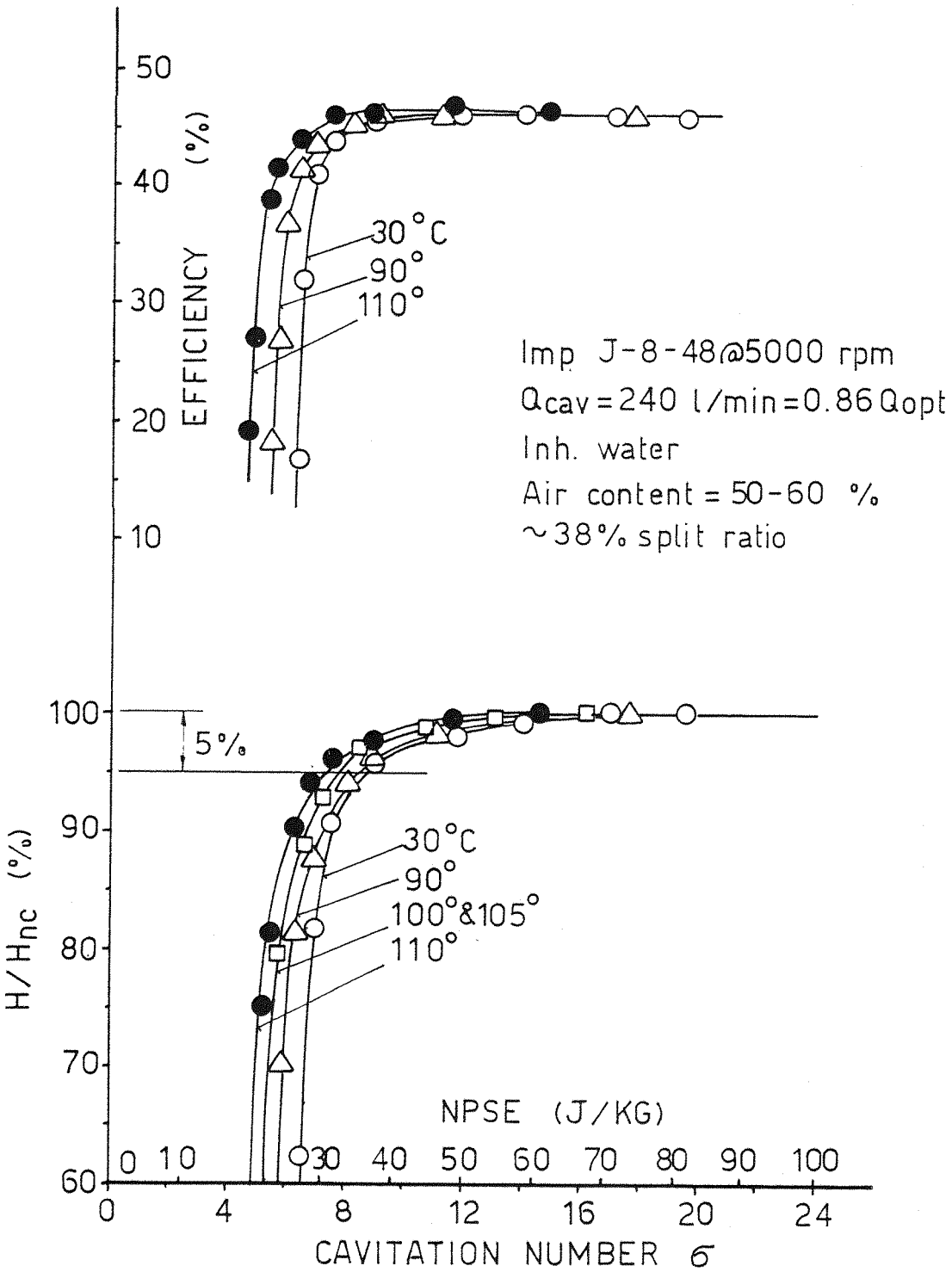

FIG 8.3 CAVITATING FLOW PERFORMANCE OF PUMP J WITH INH. WATER AT VARIOUS TEMPERATURES

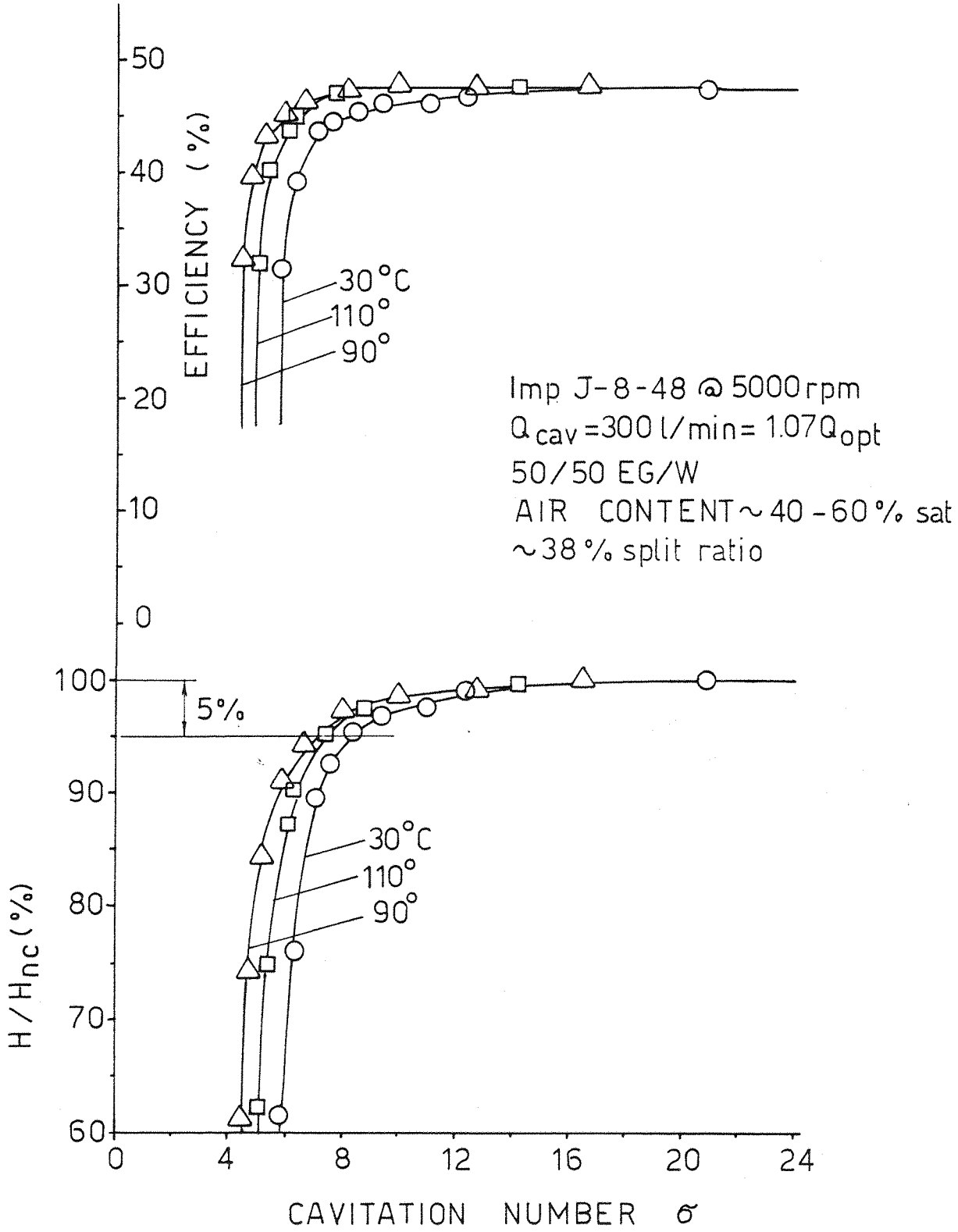

FIG 8.4 CAV. FLOW PERFORMANCE OF PUMP J WITH 50/50 EG/W AT VARIOUS TEMPERATURES

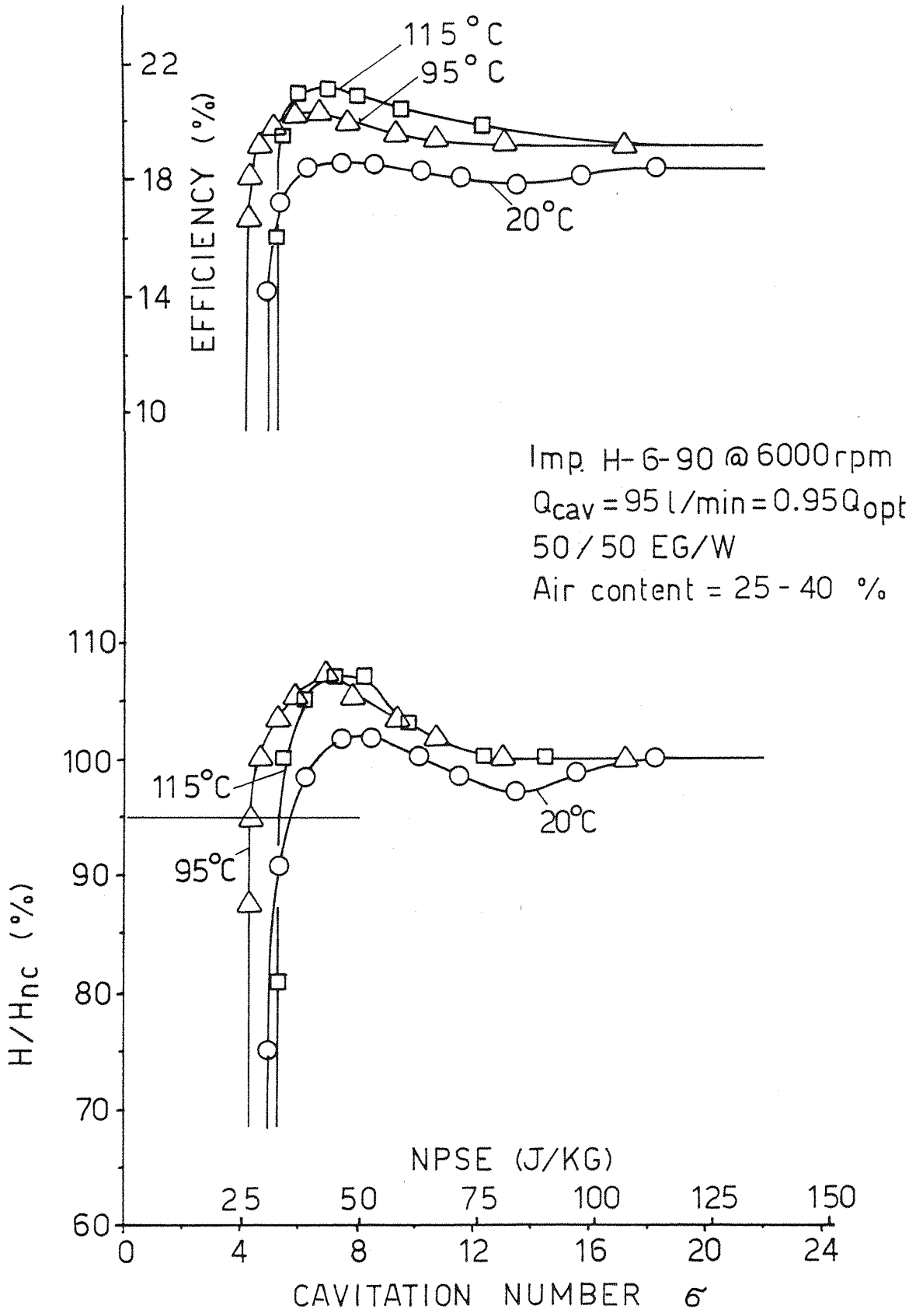

FIG. 8.5 CAVITATING FLOW PERFORMANCE OF PUMP H WITH 50/50 EG/W AT VARIOUS TEMPERATURES

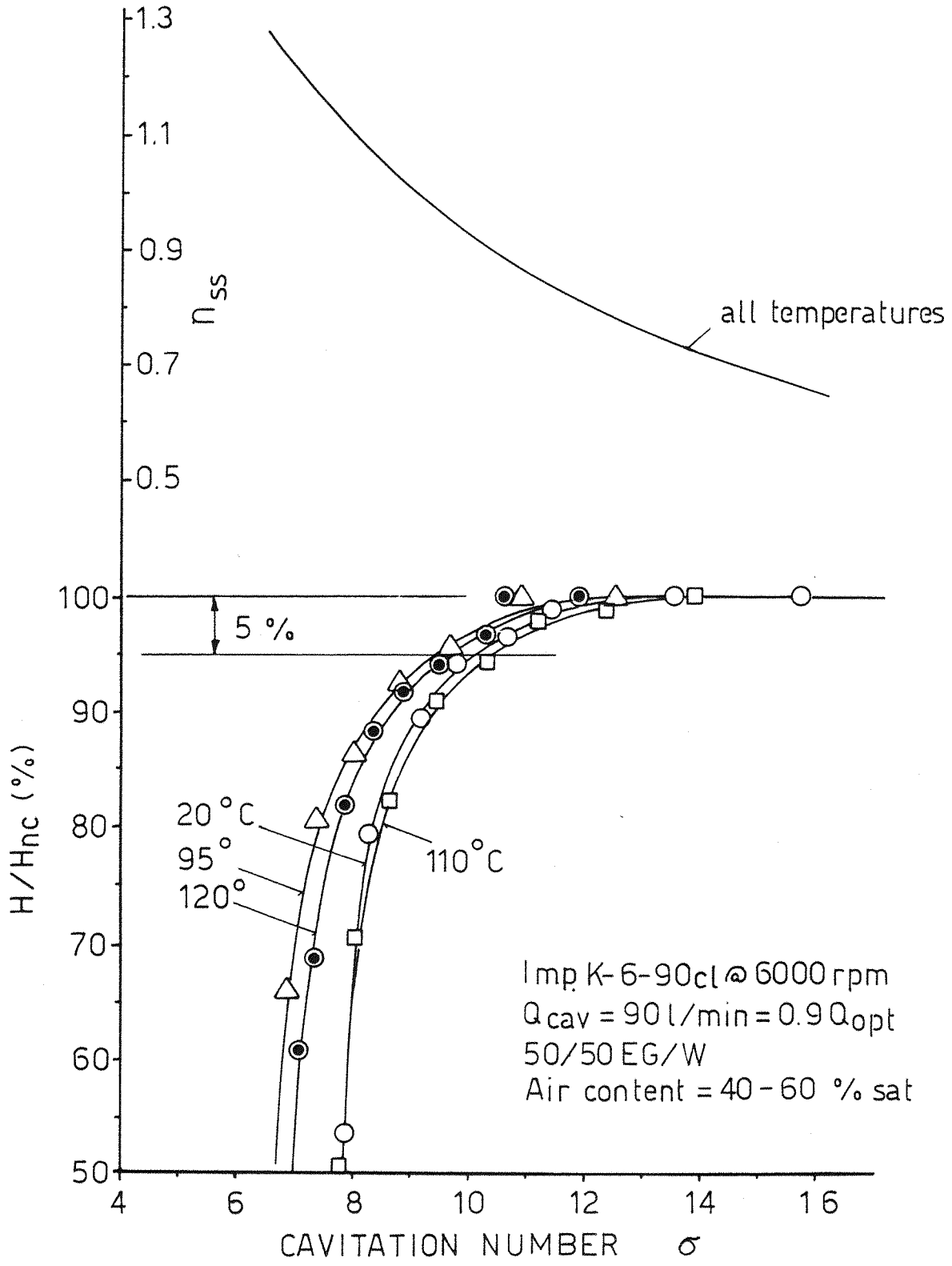

FIG. 8.6 CAV. FLOW PERFORMANCE OF PUMP K WITH 50/50 EG/W AT VARIOUS TEMPERATURES

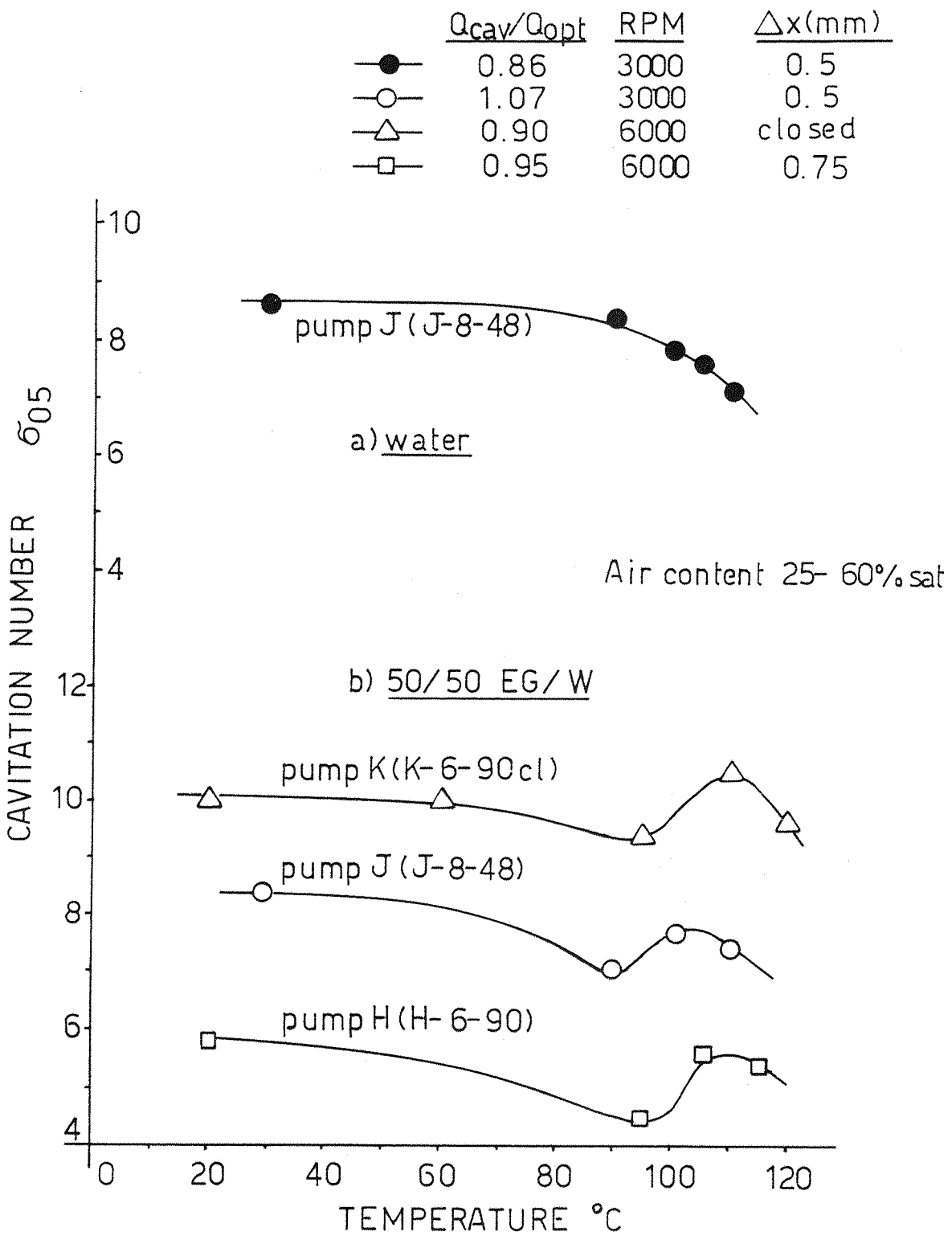

FIG. 8.7 VARIATION OF THE CAVITATION NUMBER WITH LIQUID TEMPERATURE FOR 3 PUMPS

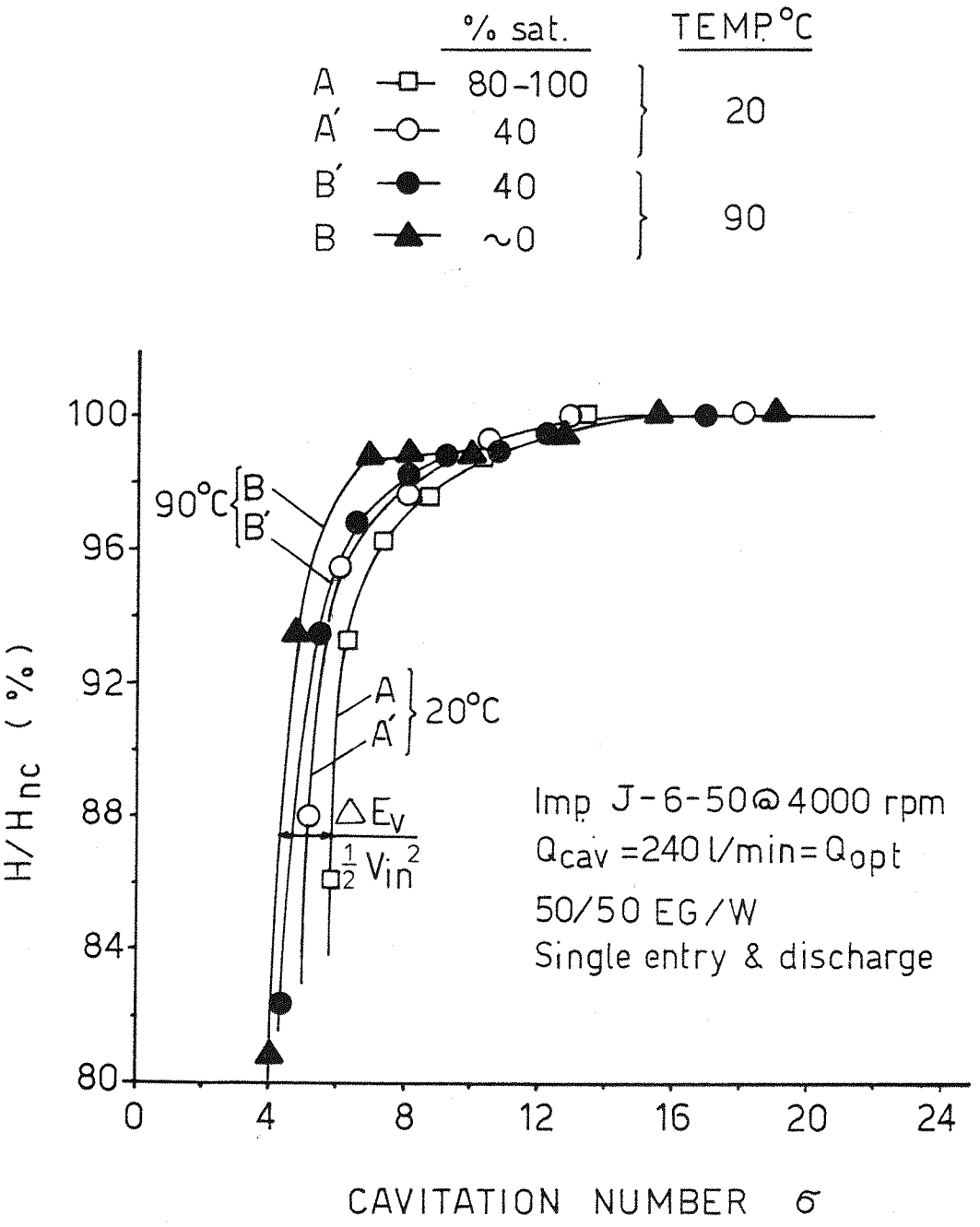

FIG. 8.8 COMBINED GAS CONTENT AND LIQUID TEMP. EFFECTS ON THE CAVITATION OF PUMP J

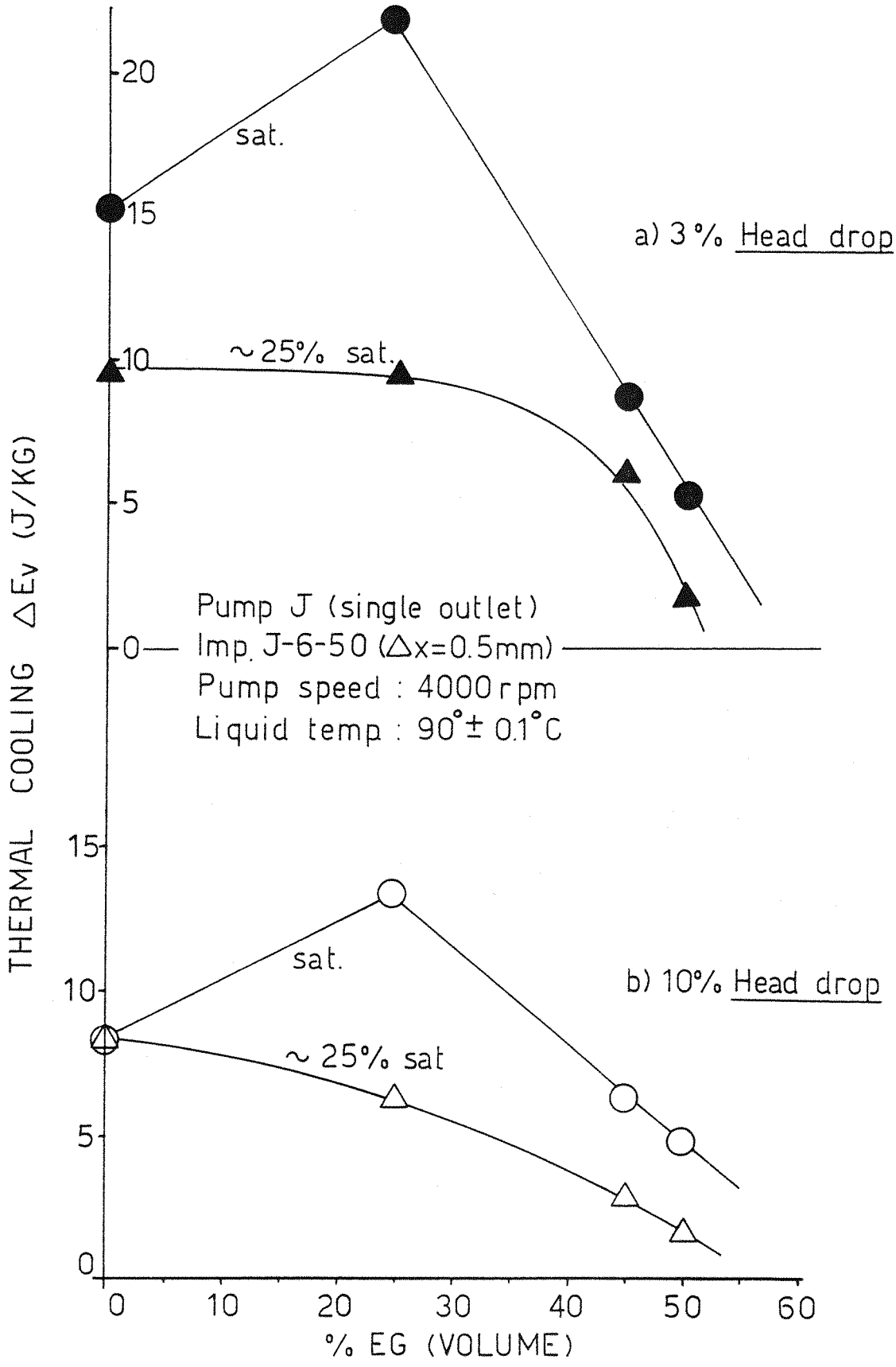

FIG.8.9 INFLUENCE OF AIR CONTENT AND EG CONCENTRATION ON THE THERMAL COOLING OF PUMP J AT 90°C

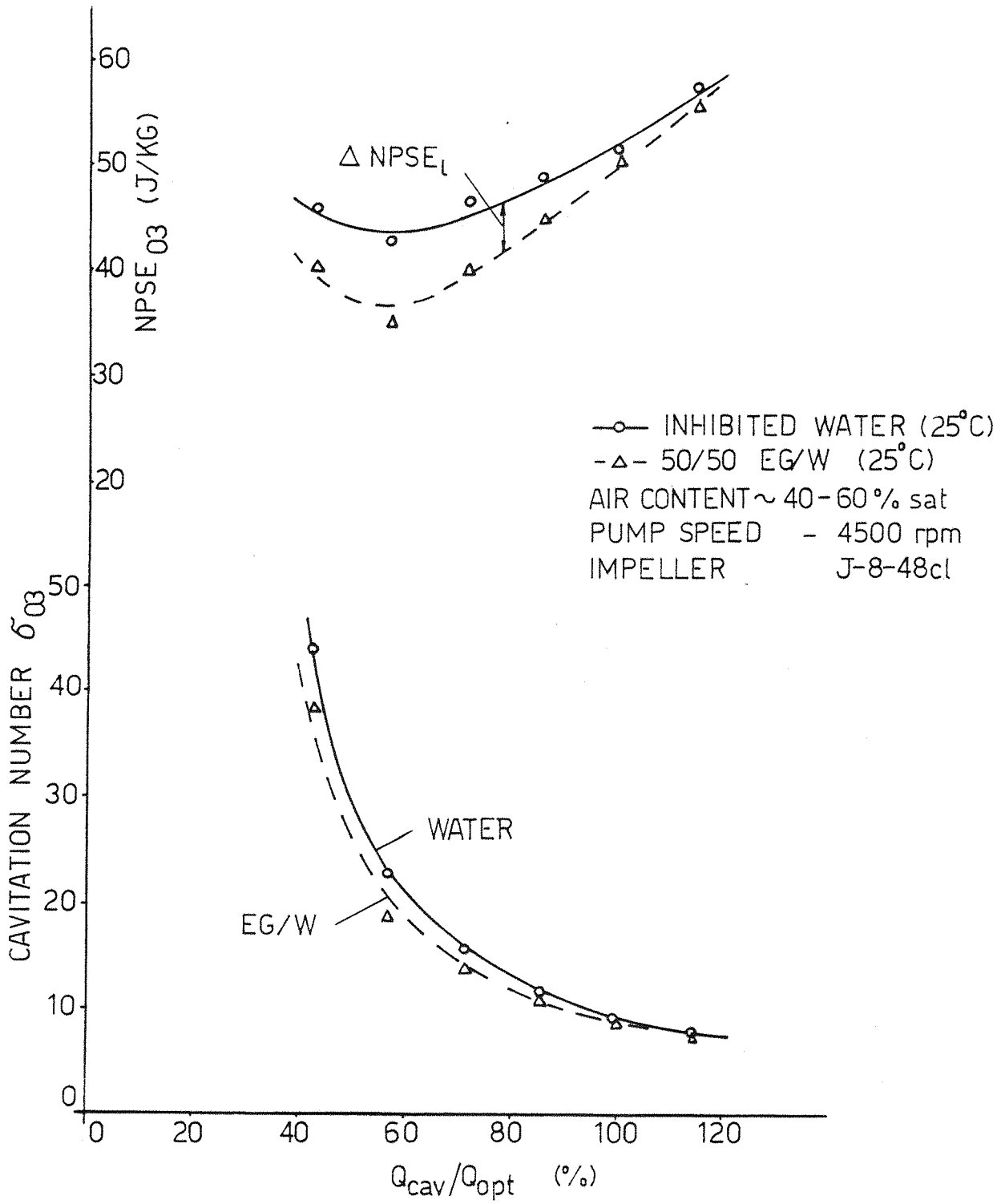

FIG.8.10 THE EFFECTS OF TEST FLOW AND LIQUID PROPERTIES ON PUMP CAVITATION AT 25°C

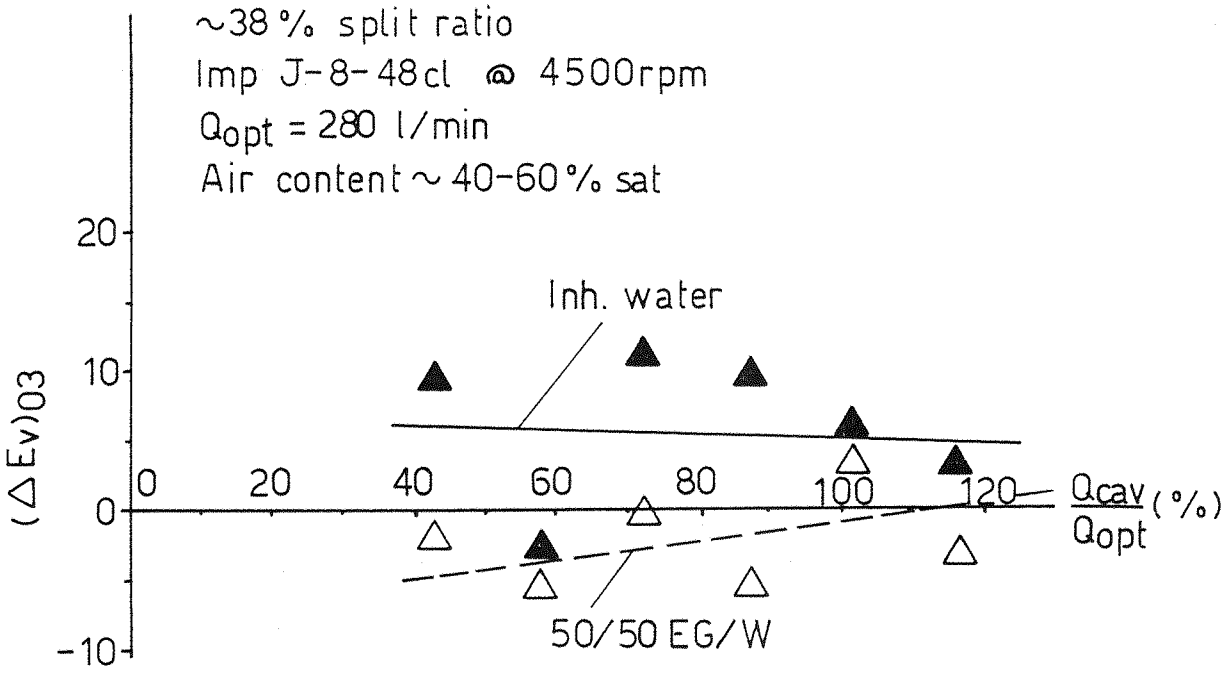

FIG. 8.11 COMBINED EFFECT OF TEST FLOW AND LIQUID TYPE ON THE THERM. COOLING OF PUMP J AT 90°C

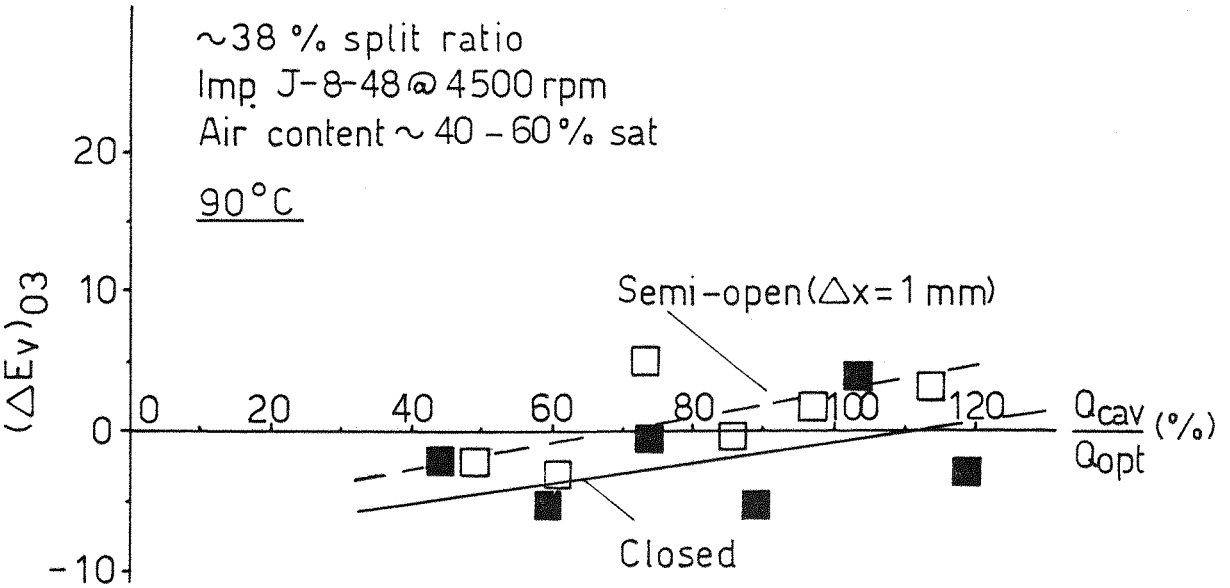

FIG 8.12 COMBINED EFFECT OF TEST FLOW AND TYPE OF SHROUD ON THE THERM. COOLING OF PUMP J

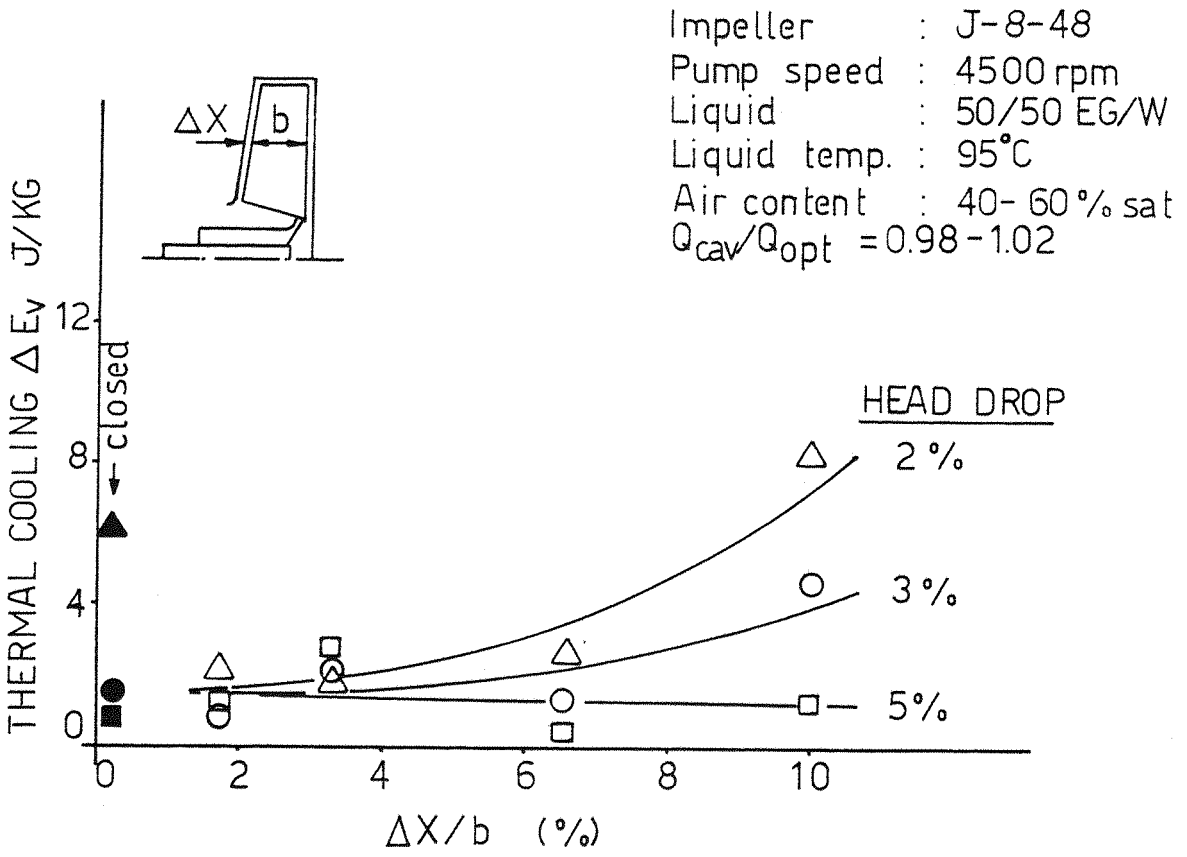

FIG. 8.13 TIP CLEARANCE EFFECT ON THERMAL COOLING FOR THE SEMI-OPEN CENTRIFUGAL IMPELLER

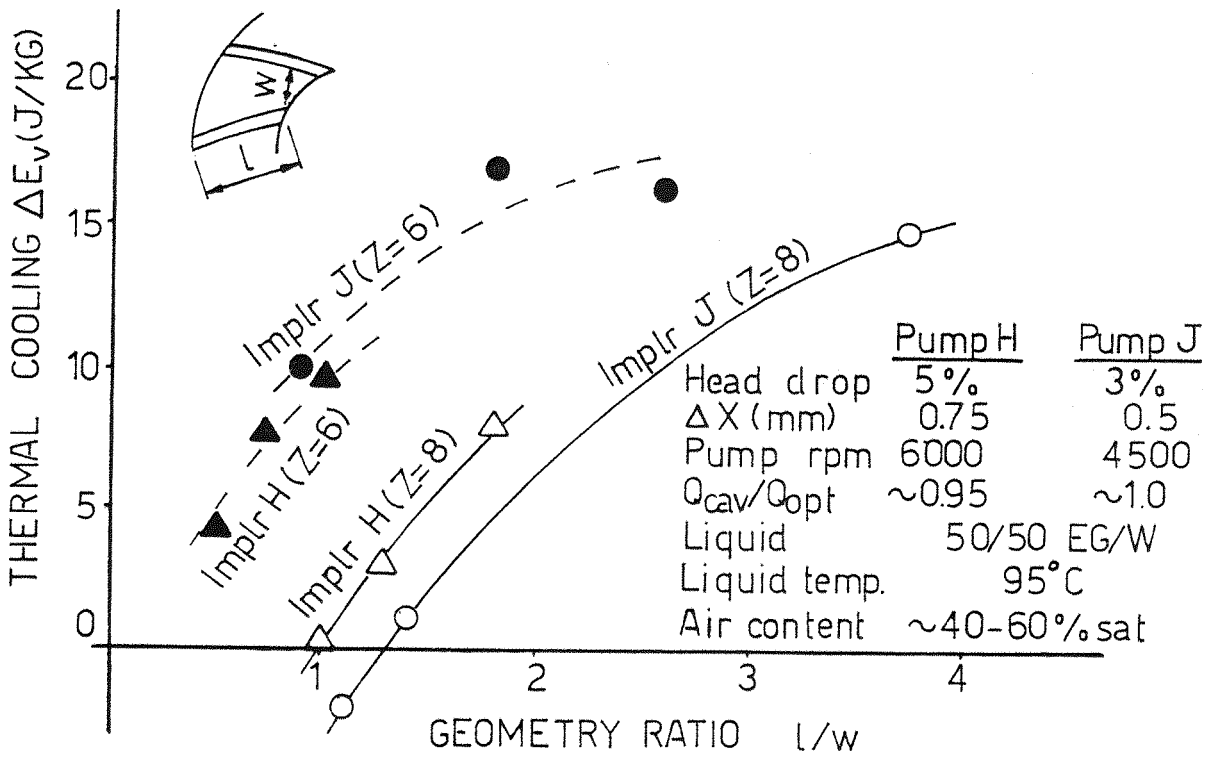

FIG. 8.14 THE EFFECT OF IMPELLER GEOMETRY ON THERMAL COOLING FOR 2 DIFFERENT CENTRIFUGAL PUMPS AND 12 SEMI-OPEN IMPELLERS

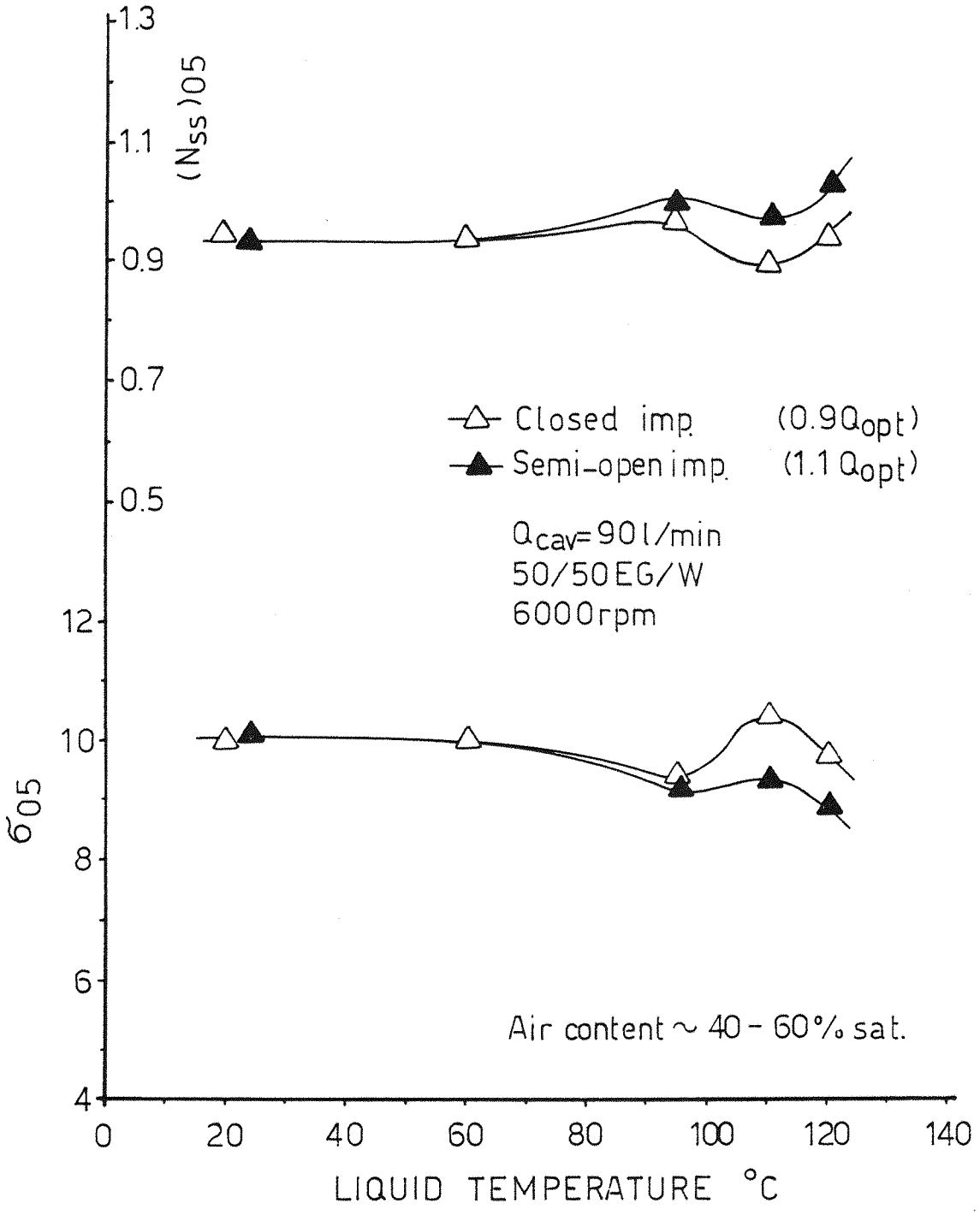

FIG.8.15 THE INFLUENCE OF THE TYPE OF SHROUD ON THE CAVITATION OF PUMP K AT VARIOUS TEMPERATURES

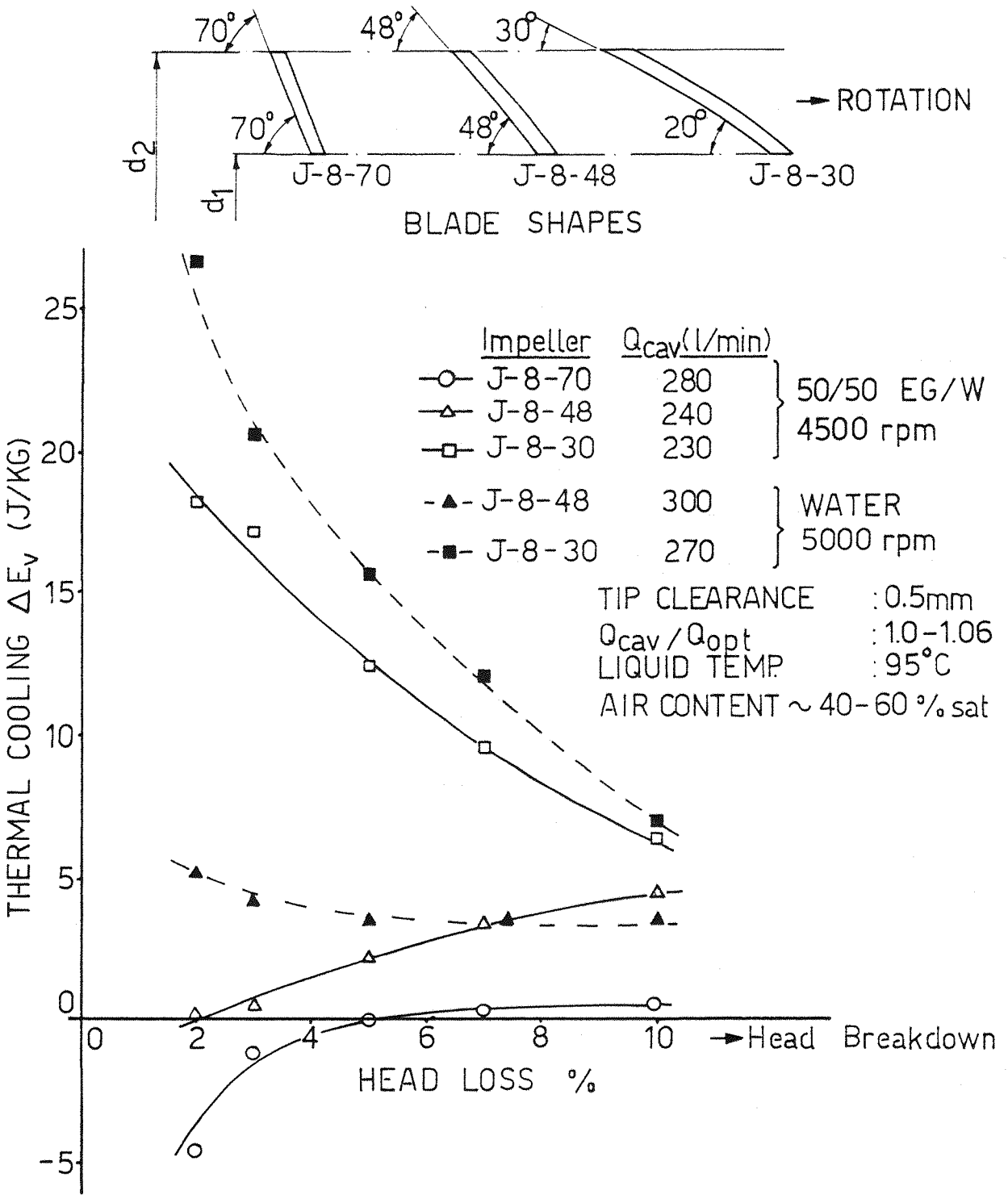

FIG. 8.16 THE EFFECT OF BLADE SHAPE ON THE THERMAL COOLING OF PUMP J WITH 8-BLADED SEMI OPEN IMPELLERS

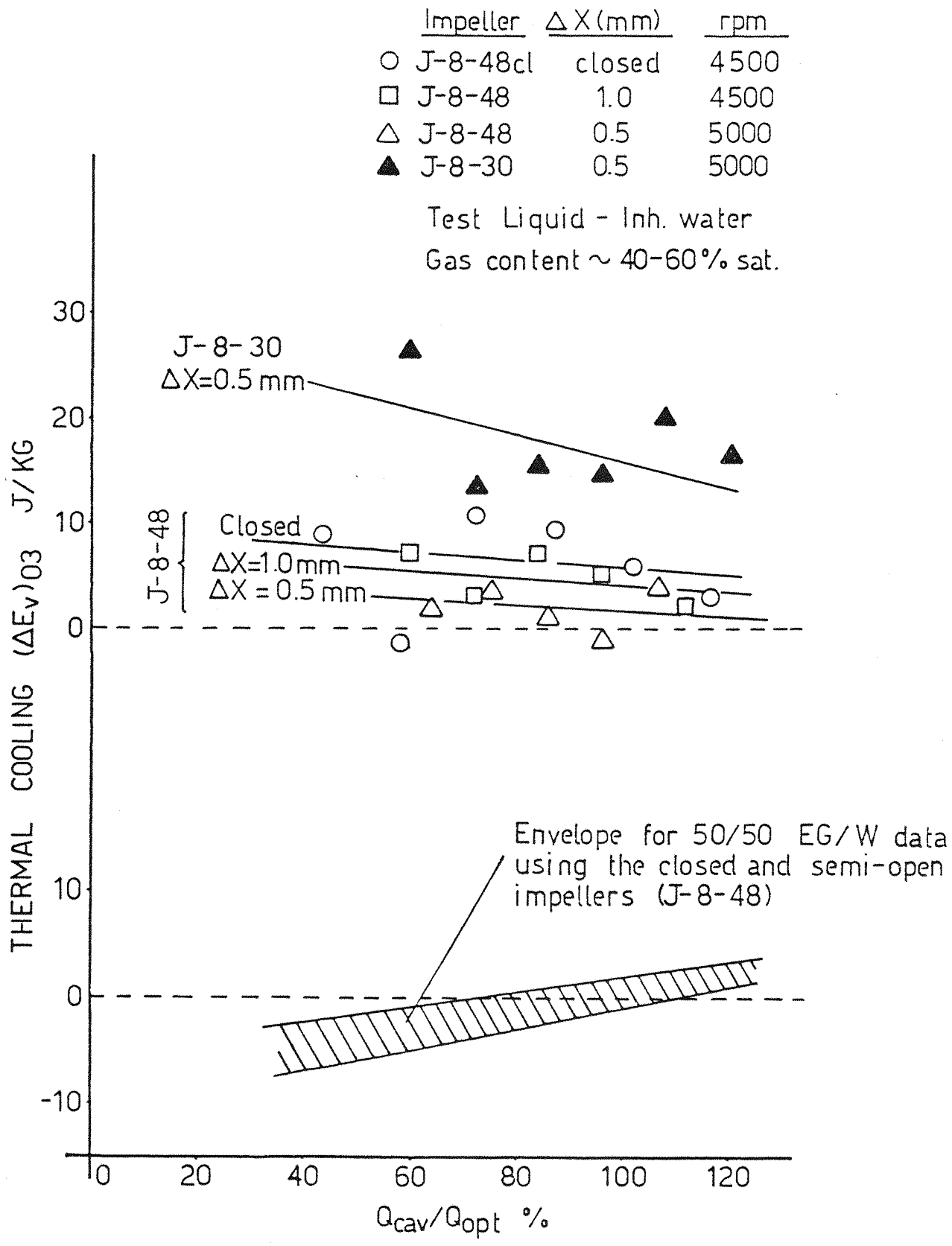

FIG.8.17 THE INFLUENCE OF THE TEST FLOW AND IMPELLER GEOMETRY ON THERMAL COOLING FOR TWO LIQUIDS AT 95°C

CHAPTER 9

CORRELATION OF THE THERMODYNAMIC EFFECT TEST RESULTS

9.1 The B-Factor Theory

In section 6.3 the various theories connected with the fixed cavity concept were reviewed. Among the very first and simplest is the B-factor theory [155, 158], which correlates the cavitation tendency of the pump to the vapour to liquid volume ratio (V_v/V_ℓ). The basic idea behind this theory is that in order to produce a certain performance drop for the same pump and flow conditions, a similar size fixed cavity is required. The same rate of vapour formation at different temperatures or for different liquids of the same temperature produces different thermodynamic effects depending on the physical properties of the liquid at test conditions.

Because of the simplicity of the B-factor theory, its application provided some controversy and therefore several other investigators [13, 80, 145, 154] sought to find an alternative more elaborated correlation factor to suit their test results. However, a review by Ward and Sutton [179] showed that most of these approaches can be related to a single thermal parameter β, which is related to the B-factor by equation (6.45). Jacobson [81] and Florjancic [47] used a combined bubble growth and fixed cavity model to arrive at a correlation which can be expressed as a function of the B-factor. NASA [102, 141] developed a modified version of the B-factor which seems to give good prediction for the hydrodynamic machines. This, however, was disputed by Bailey and Wykes [9] as being "singularly unconvincing" and that it provides no real improvement to the conventional B-factor theory. Hammitt [60] also noted that the application of the NASA modified B-factor for untested liquids requires some information which can only be assumed.

A more recent approach by Holl [68] and Billett [19] applying a ventilated cavity in a rotating component showed that the B-factor can be expressed

as a complex function of several parameters outlined in equation (6.37). The application of this approach however is far from being simple and requires highly sophisticated experimentations.

Combining equations (6.41) and (6.44) will give the following expression for the thermal depression ΔE_v;

$$\Delta E_v = \frac{B}{C_{p\ell} T} L^2 \left(\frac{\rho_v}{\rho_\ell}\right)^2 \qquad (9.1)$$

The application of equation (9.1) for pure (single component) liquids is no problem since the physical properties at equilibrium are well defined. As for a binary mixture, the formation of vapour is associated with a mass transfer gradient as well as a temperature gradient across the boundary layer, as mentioned in section 6.4, which makes the equilibrium assumption rather inappropriate. However it seems to be worthwhile to apply the B-factor theory first in its elementary form of equation (9.1) in order to establish the degree of departure from the real thermodynamic behaviour of the binary mixture and then try to modify it with respect to the special heat transfer characteristics of these mixtures.

The physical properties of the binary mixture EG/W are not fully known and some properties like the latent heat of vapourization must be estimated from thermodynamic laws. Liquid specific heat $C_{p\ell}$, thermal conductivity k, and relative density of this mixture are given on figures 9.1 to 9.3 respectively [6]. When EG/W mixture is brought to the boil the vapour formed is usually predominantly that of the more volatile component (water). This is clearly indicated on figure 9.4 [170] where the percentage of EG mass in the vapour is negligibly small up to a concentration of 60% in the liquid. It is therefore plausible to use water vapour data for both L and ρ_v of equation (9.1) by applying a correction factor with respect to the local pressure according to the perfect gas law. Alternatively,similar results would be obtained by using L of the bulk liquid mixture and by estimating ρ_v from the Clapeyron equation (6.43). The latter is perhaps more appropriate to use since the B-factor theory is closely connected to the Clapeyron equation. As shown by the data derived in Appendix VI both methods seem to give closely similar results in the range 0 - 50% EG/W concentrations.

The latent heats of vapourization for pure water and Ethylene glycol are known [37]. On figure 9.5 they are plotted against temperature in the range 0-120°C. The latent heat of the mixture of these pure liquids cannot be found from the literature. Santrach [146] suggests a method of prediction for the binary mixture based on empirical relationship along the mixture

liquid-vapour saturation curve over the entire liquid range. A simpler method is to use a similar approach to estimate the vapour pressure of the mixture [150]:

$$L_{mix} = \gamma_1 X_1 L_1 + \gamma_2 (1 - X_1) L_2 \qquad (9.2)$$

Suffices 1 and 2 refer to the two pure liquid components, γ is an activity constant and X_1 is the molar fraction of component 1 in the mixture. In figure 9.4 [170], the molar fraction of EG in the liquid mixture is given as a function of the percent concentration. The activity constants for both water and EG are difficult to determine and therefore they are assumed to be unity for the equilibrium conditions. This may be unrealistic but for the approximate solution of the thermodynamic effect of this assumption is likely to give only a marginal error for this mixture.

On figure 9.6, the latent heat at 20°C and 90°C as estimated from equation (9.2) is plotted against EG concentration in the mixture. Also on this figure $C_{p\ell}$ values at 20°C and 90°C as extracted from figure 9.1 are plotted against concentration.

Once the physical properties of the mixture are sorted out, equation (9.1) can be applied for the estimation of the B-factor at any particular fluid temperature or EG concentration. This is done on figure 9.7 for the inhibited water and the mixture 50/50 EG/W at 90°C and 100°C. As a comparison, the more accurate ΔE_v values obtained by Hord [69], using a "quasi-static" model* are plotted for water at 90.5°C and 102°C on the same figure. A close agreement between the calculated data and those estimated by Hord could be found for the two temperatures, thus suggesting that equation (9.1) provides a reasonable source of estimating ΔE_v from the B-factor theory, in this range of temperatures.

---

* This model features a unit mass of saturated liquid completely filling an insulated cylinder with a tightly fitted piston. When the piston is lifted some of the liquid is vapourized. Using this method the B-factor can be correctly estimated by accounting for changes in fluid properties with temperature depression.

To obtain a general picture of the applicability of the B-factor theory for the small size pumps, thermodynamic effect test results of pump J obtained with inhibited water from figure 8.3 are correlated in figure 9.8, with the B-factor theory in the temperature range 90 - 110°C. 5% head drop was chosen for the purpose of correlation in order to avoid excessive air content effect according to figure 7.4. Constant B-factor curves were drawn using equation 9.1 to estimate ΔE_v at different temperatures.

To obtain a clearer picture of the correlation, the values of the thermal parameter β are estimated from figure 9.8 using the relationship of equation (6.45). On figure 9.9 the thermal cooling values of figure 9.8 were replotted as a function of β on a log-log scale. Constant B-factor lines were drawn according to the relationship of equation (6.45). Furthermore, also on this figure, the correlation results of 2 pumps obtained by Stepanoff [158] and Spraler [154] with water, were also drawn for the purpose of comparison.

From figure 9.9 it should be obvious that the B-factor thoery provides a reasonable correlation for water, with the test results aligning themselves on a line parallel to the constant B-factor lines. This is in accord with the results obtained by other investigators, two sets of which are shown on this figure. However, the ΔE_v values of pump J are significantly higher than those obtained by nearly all other investigators [179]. The reason behind this is two fold. The first is related to the special inlet design of pump J, with the inlet hub vortex probably allowing for increased residential time, and hence vapour bubble growth is promoted. The second reason is believed to be connected to the pronounced air content effect which increases σ_{05} of the cold water even for moderate dissolved air content of the liquid.

Moving on to the correlation of the binary EG/W mixture, the thermodynamic effect test results for 3 pumps and a concentration of 50/50 EG/W were estimated at 5% head drop and about 40 - 60% air saturation from figures 8.4 to 8.6, and plotted as functions of the liquid temperature on figure 9.10. Using equation (9.1), the B-factor was estimated with respect to the bulk liquid equilibrium physical properties at different temperatures. From these estimations, the constant B-factor curves were constructed and drawn on the

same figure. Once this is done the thermal parameter β values for two pumps (J and H) were estimated from this figure using the relationship of equation (6.45). Finally the ΔE_v test results for pumps J and H were replotted on figure 9.11 as a function of the thermal parameter β.

The resulting picture on figure 9.11 indicates clearly that the B-factor theory does not provide a good correlation for the binary mixture 50/50 EG/W. Some correlation is obtained at low values of β (high temperatures) but the sudden drop of the thermodynamic effect at $\beta \sim 1$ cannot be explained or justified in the light of the conventional B-factor theory.

To understand the possible reasons behind the abnormal behaviour of the EG/W mixture with respect to the thermodynamic effect, it was decided to correlate the thermodynamic effect of the EG/W mixture in the range of 0 - 50% EG concentration at a single temperature and hence obtain a clear picture of the influence of the fluid properties on the B-factor correlation. To do so the following pre-conditions were considered.

1. Pump geometry: It has been shown that pump geometry such as type of shrouding, tip clearance size and blade number and shape, does influence the thermodynamic effect. Also the size and casing design is likely to influence the cavitating flow performance of the pump. Therefore it was decided that the more conventionally designed pump J is to be used for the purpose of test results correlation. A 6 bladed semi-open impeller of a strongly backward curved blade with an axial tip clearance of 0.5 mm to be used for the test. Furthermore, to avoid excessive disturbance to the flow at pump discharge, one of the twin discharge ports was blocked and flow is allowed to exit through the more streamline *oil* cooler outlet.

2. Test flow: To avoid excessive viscosity effect of the vortex, the test flow rate was kept both high and equal to the BEP flow, which is at 4000 rpm is nearly equal to Q_{opt} of 240 L/min.

3. Air content: In section 8.2, the strong influence of the gas content was shown to produce extremely high discrepancies in the determination of

the thermodynamic effect of the binary liquid mixtures. Therefore it was decided that testing for correlation should be performed at a low content of dissolved air (preferably ∿ 25% saturation). In order to minimise further gas content effect even at a low gas content, it was thought that according to figure 7.4, correlations ought to be made at a head drop higher than 7%. A 10% head drop is expected to give good prediction values.

Once these pre-conditions were met the test results were obtained and plotted on figure 8.9b (lower curve), and are used again to correlate the thermodynamic effect as a result of the change in fluid properties to the B-factor. This is done on figure 9.12, from which figure 9.13 is constructed. (Since no similar work could be found in the literature the author believes such correlation for the binary (polar) mixtures are the first of its kind).

Figure 9.13 shows clearly that the significant drop in ΔE_v with increased EG concentration cannot be correlated successfully to the B-factor at this particular temperature. This is clearly seen on the adjoining ΔE_v curve which seems to provide a poor alignment with the constant B-factor lines. If one assumes rightly, that the same size cavity (or cavity closed) is required to produce a similar head drop for two different liquids, then for the mixture 50/50 EG/W, only one third of the vapour cavity is involved in the thermodynamic process compared to 100% in the case of water, and hence the B-factor cannot provide a satisfactory correlation for the binary mixture.

9.2 The Modified B-Factor for the Binary Mixtures

In the previous section it was shown that the conventional B-factor theory based on the bulk liquid physical properties does provide a useful tool for correlating the thermodynamic effect of water but fails to do so for the binary mixture 50/50 EG/W at a certain range of temperature. At 90°C, it was shown that the B-factor theory is not suitable for correlating the thermodynamic effect with respect to fluid properties, using water and 3 different concentrations of the mixture EG/W. In this section, the correlations of figure 9.13 are to be discussed in the light of the heat and mass transfer phenomenon of the binary mixtures discussed in section 6.4. Then a modified

B-factor for the mixture is to be introduced which takes into account these additional factors.

In a boiling binary mixture, the vapour is predominently that of the more volatile component (water for the EG/W binary mixture). In order to maintain a vapour cavity of a "fixed" size, vapour must be drawn from the liquid adjacent to the cavity wall. As a result a condition will be reached, whereby a layer of higher concentration of the less volatile component than that of the bulk liquid, with a higher saturation temperature, surrounding the vapour cavity, thus a reduction in the overall temperature depression compared to that of the bulk liquid will result with a reduced thermodynamic effect.

In equation (6.72), the author has shown that due to the phenomenon associated with the mass and heat transfer of the binary mixture, the temperature depression of the mixture ΔT_{mix} is less than that based on the bulk liquid properties. Therefore equation (6.41) can be modified as follows:

$$\Delta T_{mix} = B_{mix} \frac{\rho_v}{\rho_\ell} \frac{L}{C_{p\ell}} \tag{9.3}$$

If ΔT_{mix} is related to ΔT of the bulk liquid by the relationship $\Delta T_{mix} = \Delta T / C_{mix}$, whereby C_{mix} is a correction factor, then,

$$B_{mix} = \frac{\Delta T}{C_{mix}} \frac{\rho_\ell}{\rho_v} \frac{C_{p\ell}}{L} \qquad (C_{mix} > 1) \tag{9.4}$$

Using the Clapeyron equation with $\Delta P_{mix}/\Delta T_{mix}$ gradient for the mixture, and modifying equations (6.43) and (6.44) accordingly will yield the following equation of the modified B-factor:

$$B_{mix} = \frac{\Delta E_v}{C_{mix}} \frac{C_{p\ell} T}{L^2} \left(\frac{\rho_\ell}{\rho_v}\right)^2 \tag{9.5}$$

The temperature correction factor C_{mix} for the binary mixtures is a complex function of both the bulk liquid properties and of the heat and mass transfer rate of the volatile component in the less volatile component. If

one uses the bubble growth theory in a superheated binary mixture with both conductive and convective influences at the bubble wall as the main reason for the reduced temperature depression of the mixture according to equation (6.68) then:

$$C_{mix} = \psi_{mix} = 1 + \frac{C_{p\ell}}{L} \left(\frac{\alpha}{\alpha_m}\right)^{\frac{1}{2}} \left(\frac{\Delta T_s}{G}\right) \qquad (9.6)$$

In order to find a solution for C_{mix} from equation (9.6), it is necessary to find the exact values of α_m and $\Delta T_s/G$ for the binary mixture EG/W. Because such values are not easily obtained for this binary mixture, one would simply derive it from existing test results on atmospheric boiling [15, 150], as follows.

Defining a growth factor κ similar to the Ja number of equation (6.56) the bubble radius can be expressed by [150];

$$R = 2 \kappa \sqrt{\alpha t} \qquad (9.7)$$

From atmospheric boiling Scriven [150] and Benjamin [15] obtained some experimental values of the growth factor κ at different superheats ΔT of the liquid, which are plotted on figure 9.14.

If we introduce a factor τ, defined by:

$$\tau = \frac{\rho_v}{\rho_\ell} \left[\left(\frac{L}{C_{p\ell}}\right) + \left(\frac{\alpha}{\alpha_m}\right)^{\frac{1}{2}} \frac{\Delta T_s}{G}\right] \qquad (9.8)$$

then from both equations (6.66) and (9.7) we obtain:

$$\tau \cong \frac{\Delta T}{\kappa} \qquad (9.9)$$

Using equation (9.9) and figure 9.14, τ values can be estimated for the various concentrations of EG in the mixture and for different values of the super heat ΔT at a reference temperature of 100°C. On figure 9.15 the mean values of τ as estimated for five different ΔT are plotted against mass concentration of EG.

Dividing equation 9.6 by equation 9.8 yields:

$$\psi_{mix} = \frac{\rho_\ell}{\rho_v} \frac{C_{p\ell}}{L} \tau \qquad (9.10)$$

ψ_{mix} values were calculated using equation (9.10) for the different values of τ of figure (9.15) and were plotted on the same figure against concentration.

Once ψ_{mix} is estimated from atmospheric boiling, it can only be assumed, that it does not change considerably with saturation pressure of the test, which is only true if the local pressure is not appreciably different from atmospheric pressure because the heat transfer rate is pressure dependent [160]. Following this assumption the ψ_{mix} values of figure 9.15 are used to estimate the modified B_{mix}-factor values from equation (9.5) for the different concentrations of EG at 90°C. The results are plotted on figure 9.16 together with the actual thermodynamic effect test results of pump J as applied before in figure 9.12. From figure 9.16, the thermal parameter of the mixture β_{mix} is obtained using the relationship:

$$\beta_{mix} = B_{mix}/\Delta E_v \qquad (9.11)$$

After this has been done, the thermodynamic test results are replotted on figure 9.17 as a function of the thermal parameter β_{mix}.

Compared to figure 9.13, figure 9.17 seems to indicate a better correlation of the thermodynamic effect of the binary mixture with respect to the modified B_{mix}-factor, which takes into consideration, heat transfer factors associated with the concentration change at the cavity wall. However, this modified correlation, although better than before, it does not provide a fully satisfactory correlation with respect to the B-factor! Two main reasons are believed to be responsible for this behaviour. The first is that C_{mix} values are obtained from atmospheric boiling with the bulk liquid at rest and heat transfer is mainly through conduction. In pump cavitation where a strong vortex is operative with substantial velocity gradients and strong mixing with

convective influences and local pressure could influence the value of C_{mix} and may push it up considerably. The second is connected to the nuclei density approaching the low pressure region which may help to increase the numbers of vapour bubbles and therefore reduce their growth.

From visual observation (see next chapter), it was evident that when EG/W mixture at 90°C was circulated around the rig, visible gas bubbles released at the low pressure zone of the pump do not redissolve completely but recirculate in the system. Dissolved gas of low concentration may not influence the developed cavitation considerably, but its presence helps to increase the number of nuclei in the liquid. Photographs taken for the mixture 45/55 EG/W at the low pressure region showed that the increasing number of nuclei approaching the low pressure region is so high that they block the vision when a head drop of $\sim$ 10% is reached. For water at 90°C on the other hand, the number of the nuclei is much less and pictures could be taken easily down to a head drop of more than 22%.

Since the bubble growth rate is not dependent on the number of nuclei but rather on their size, the influence of the increased number of nuclei is that the same volume of vapour V_v of equation (6.50) is reached at a shorter growth time t. If however, the residence time t is the same at the correlation point, then a smaller bubble radius R is produced. Since the growth factor κ of equation (9.7) is equivalent to the Ja number of equation (6.56), then from equation (6.67), a smaller bubble radius at the end of the growth time t necessitates a lower temperature depression ΔT_{mix} with a lower thermodynamic effect.

Therefore if one neglects the convective effects at this stage, the correction factor C_{mix} of equation (9.5) can be assumed to depend on the number of nuclei Z as well as the heat transfer factor ψ_{mix}, or:

$$C_{mix} = f(\psi_{mix}, Z) \qquad (9.12)$$

Using this concept it is possible to demonstrate its usefulness on figure 9.17. Assuming the influence of nuclei number as being of the same magnitude of the heat transfer effect, the correlation curve for the EG/W mixture would have a better alignment with the constant B_{mix}-factor lines (broken curve on figure 9.17). Eventually a similarity could be obtained between this new correlation of the EG/W mixture and that of the inhibited water of figure 9.9, although the absolute values of ΔE_v of figure 9.17 are higher, merely because a different geometry impeller has been used here.

This correlation also shows that the EG/W mixture at 90°C behaves like water at lower temperatures depending on the EG concentration. As the concentration of EG/W increases so does the thermodynamic effect decrease and eventually 50/50 EG/W of figure 9.17 behaves like cold water.

Finally, the same concept of equation (9.12) is applied on figure 9.19 to explain the minimum ΔE_v value obtained at T_{crit} of the mixture 50/50 EG/W. The test results of pump H were taken from figure 9.10 as an example and re-plotted on this figure at the range 100 - 115°C for the purpose of demonstration. For the same B_{mix} of 4 for this mixture, the constant curves for the different C_{mix} values were plotted using equation (9.5).

The resulting picture on figure 9.19 is to demonstrate that it is possible for the same B_{mix} or for the same amount or size of the vapour cavity, lower ΔE_v are possible at higher temperature depending on the value of C_{mix}. Although this figure is not a definitive solution, it is possible to gain a picture of the importance of the factor C_{mix}, when a binary mixture is being handled.

Critical temperatures were also established for other concentrations [167] as tabulated below:

EG content %	0	7	12	50	100
T_{crit} °C	20	70	80	105	115

These figures were established at an early stage and therefore they should be treated with reservations for two main reasons. The first is the low Q_{cav}/Q_{opt} ratio at which these tests were performed ($\sim$ 60%) which is likely to involve some Re number effect for these type of pumps. The second is the neglegence of the air content effect at that time which is likely to allow for high test discrepancies.

All this seems to promote further experimentation in the field of binary mixtures cavitation, in order to verify the validity of C_{mix} at a wider range of temperatures and mixture concentrations. A special attention is to be paid to the importance of the number of gas nuclei entering the low pressure zone.

9.3 Inertial Effect

It was shown in the last section, that for the same growth time t, the binary mixture EG/W produces a lower growth constant κ than water and therefore the bubble radius R is not allowed to grow at the same rate, thus smaller bubbles are produced. This phenomenon is also confirmed by some other investigators from atmospheric boiling of EG/W mixtures [98, 169], associated with a sudden increase in the heat flux for the nucleate boiling.

It was also shown that if the nuclei density upstream from the low pressure region is extremely high, further reduction in the growth of the vapour bubbles is necessary to obtain the same volume size of vapour cavity for increased numbers of bubbles.

Both these factors are believed to be operative for the mixture EG/W and therefore the determination of the thermodynamic effect is largely dependent on the estimation of these two factors.

Consider equation (6.21) for the limited cavitation number σ_L. As the vapour bubble increases in size, both the soluble gas content and the surface tension effects become less and less important, and if C_p is assumed to change little with temperature or liquid, equation (6.21) can be expressed in the following form:

$$\sigma = K - \phi - C_T \qquad (9.13)$$

whereby C_T represents the thermodynamic effect expressed by equation (6.15) and ϕ represents the inertial (dynamic) effect expressed by equation (6.18), and both are acting to reduce the cavitation number. Neglecting the viscosity term of equation (6.18), Bonnin [22] arrived at an approximate solution for the energy depression due to inertial effects, given by the following equation:

$$\Delta E_{dyn} = \frac{3}{2} \left(\frac{R}{t}\right)^2 \qquad (9.14)$$

The energy depression of equation (9.14) is usually small and is only of importance if the thermodynamic effect is not dominant (cold liquid).

The bubble growth restraints of the binary mixture, which result in a smaller bubble radius R at the end of the growth time t, will also mean a reduction in the energy depression due to inertial effects. If compared to water, the ratio of the inertial effect of the mixture is simply proportional to $(R_{mix}/R_w)^2$ for the same t. Applying equation (9.7) for the binary mixture and its volatile component (water), we obtain for the bubble size ratio:

$$\left(\frac{R_{mix}}{R_w}\right)^2 = \left(\frac{\kappa_{mix}}{\kappa_w}\right)^2 \frac{\alpha_{mix}}{\alpha_w} \qquad (9.15)$$

Using figure 9.14 with the data for the thermal diffusivity α at atmospheric boiling [150], the ratio $(R_{mix}/R_w)^2$ is estimated at different EG/W concentrations and plotted on figure 9.18 for an arbitrary superheat of ΔT = 15 °C. Here it is demonstrated that due to heat transfer effects only, the effects of the mixture are reduced appreciably below that of water, and is about half of it at a concentration of 50/50.

If one includes the number of nuclei Z in the bubble growth process of the mixture, then a further reduction in bubble radius is exprected to result. For a similar size effect of nuclei number to that of the heat transfer correction factor ($C_{mix} = \psi_{mix}^2$), then from figure 9.18 (broken line), the energy depression due to inertial effects of the mixture is further reduced below that for pure water. At 50/50 EG/W it reaches almost 20% of it.

9.4 Concluding Remarks

In this chapter, the thermodynamic effect results of 3 centrifugal pumps have been correlated to the B-factor in the temperature range 90 - 120°C. Some correlation was possible for pump J operated with water in the temperature range 90 - 110°C which seems to suggest that this theory is quite reasonable for single component liquids first hand prediction. As for the binary mixture 50/50 EG/W, B-factor corretation of the thermodynamic effect with increased temperature were not possible, with the mixture reaching a minimum ΔE_v at a critical temperature T_{crit} of $\sim$ 105 - 110°C. To examine this behaviour of the mixture further, ΔE_v is examined at 90°C with respect to changes in the EG/W concentration in the range 0 - 50% EG/W. To avoid excessive errors in the estimation of ΔE_v, the following pre-conditions had to be made.

1. To avoid excessive geometrical influences, pump J of the more conventional design was used with single streamline inlet and outlet.

2. To reduce the influence of the vortex flow at impeller inlet, the test flow was maintained at Q_{opt} and at sufficiently high Re number.

3. To minimize the dissolved gas content, tests were carried out at a low gas concentration for both the cold and the hot liquid ($\sim$ 25% saturation). Also, to avoid further gas content effect at this concentration, correlations were made at a head drop of 10%.

The test results obtained from pump J at 90°C and different EG/W concentrations, at 10% head drop showed only poor correlation to the B-factor, thus indicating the non-suitability of this theory to the binary mixtures at this temperature.

Considering the phenomenon associated with the mass and heat transfer properties of the binary mixtures, a modified B-factor for the mixture was introduced with takes the form:

$$B_{mix} = B/C_{mix} \qquad (C_{mix} > 1)$$

The correction factor C_{mix} for the binary mixture is a complex function of the bubble growth mechanism of these mixtures and cannot be measured directly. From existing results on atmospheric boiling of EG/W mixtures, C_{mix} values were estimated with respect to reduced bubble growth effect and correlation of test results were made with respect to the modified B_{mix}-factor. Here we obtained an improved correlation although not completely satisfactory.

To modify on the correlation procedure further, it was suggested that the number of nuclei approaching the low pressure region also contribute to a further decrease in the temperature depression of the EG/W mixtures. From visual observations it was found that the nuclei density and size at the pump inlet is much higher than that of water for similar flow conditions.

Therefore, the correction factor C_{mix} is thought to depend not only on the heat transfer factor ψ_{mix} but also on the number of nuclei, in the form:

$$C_{mix} = f(\psi_{mix}, Z)$$

Using this concept, a similar influence of Z to that of the heat transfer factor brings the correlation of the test results of pump J nearer to the acceptable range in the $\Delta E_v - B_{mix}$ diagram.

Also it is possible to show that for pump H, the minimum ΔE_v at T_{crit} of $\sim$ 110°C can be explained in the same context of changing C_{mix} with test temperature.

Since, the bubble growth *results* in both a thermodynamic and inertial effect, the decrease in the growth rate of the binary mixture, produces both a reduction in the temperature depression and in the inertial effect, which is related to R^2.

Therefore it could be said, that for the binary EG/W mixture, extremely low ΔE_v values are associated with the restraint on bubble growth both due to reduced temperature depression at the vapour bubble wall, and due to increased

number of nuclei. As a result both the thermodynamic and inertial effects are reduced considerably depending on the growth restraint factor C_{mix}.

Further experiments are required to verify the validity of the correction factor C_{mix} concept for the binary mixtures. The importance of both the heat transfer reduction and the number of nuclei are to be investigated separately. Making use of pure deareated mixtures is likely to help reduce the number of gas nuclei significantly and therefore a better correlation with ψ_{mix} only may be possible.

TABLE 9.1

FIGURES 9.1 to 9.19

Table 9.1 Conventional and modified B-parameters for the binary mixture EG/W at different concentrations and at 90°C.

Pump J, impeller J-6-50, pump speed 4000 rpm.

% EG (weight)	ΔE_v* (J/kg)	Cavitation parameter based on bulk liquid properties		Inclusion of binary mixture bubble growth restraint $C_{mix} = \psi_{mix}$			Inclusion of both growth restraint and nuclei density $C_{mix} = \psi_{mix}^2$		
		B	β	ψ_{mix}	B_{mix}	β_{mix}	C_{mix}	B_{mix}	β_{mix}
0	8.4	13.2	1.6	1.0	13.2	1.6	1.0	13.2	1.6
25	6.2	11.4	1.84	1.14	12.8	2.1	1.30	14.5	2.3
45	2.7	6.2	2.3	1.38	8.8	3.3	1.90	11.8	4.4
50	1.7	4.5	2.65	1.46	6.8	4.0	2.13	9.6	5.7

* Measured at 10% head drop and ∿ 25% air saturation.

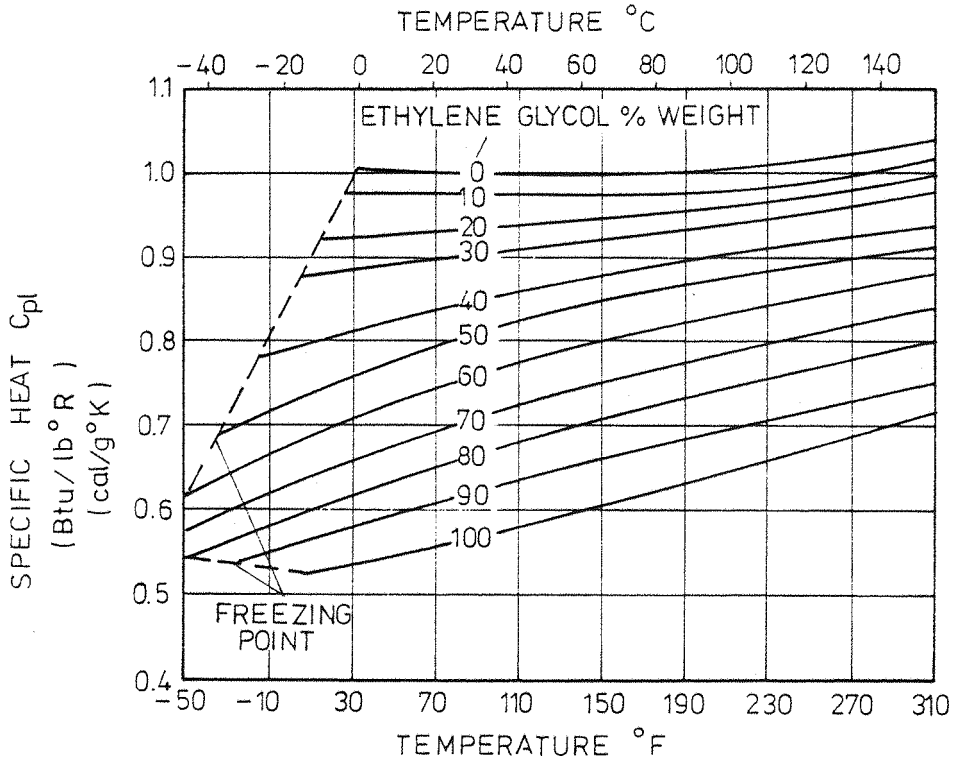

FIG 9.1 SPECIFIC HEATS OF AQUEOUS ETHYLENE GLYCOL SOLUTIONS[6]

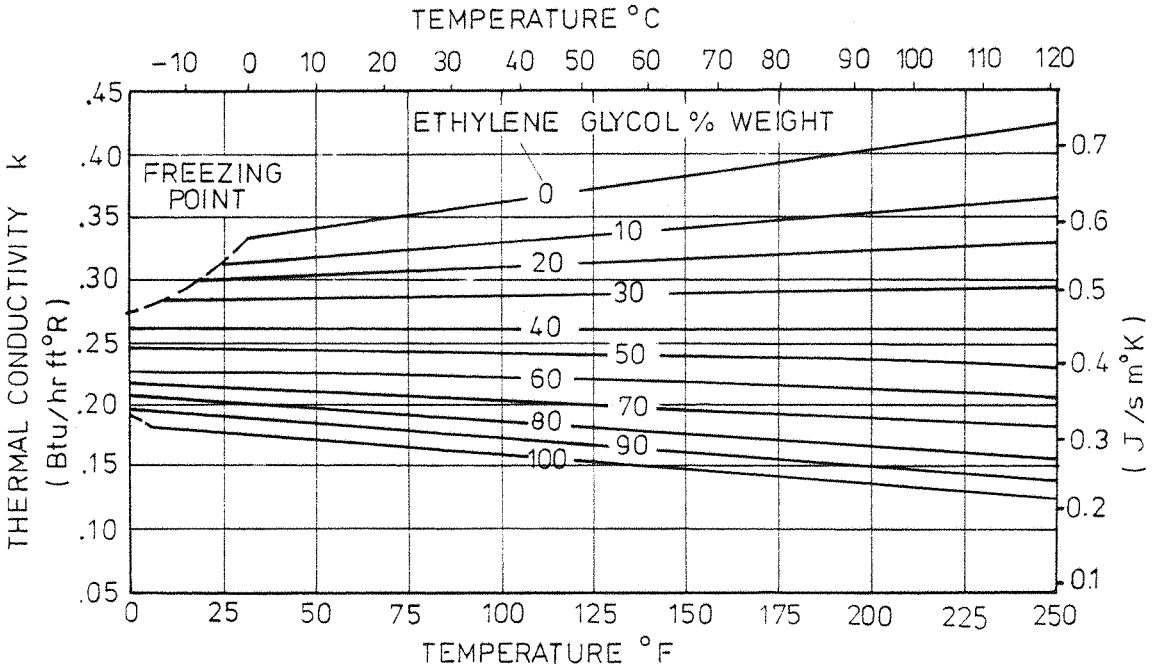

FIG 9.2 THERMAL CONDUCTIVITIES OF AQUEOUS ETHYLENE GLYCOL SOLUTIONS[6]

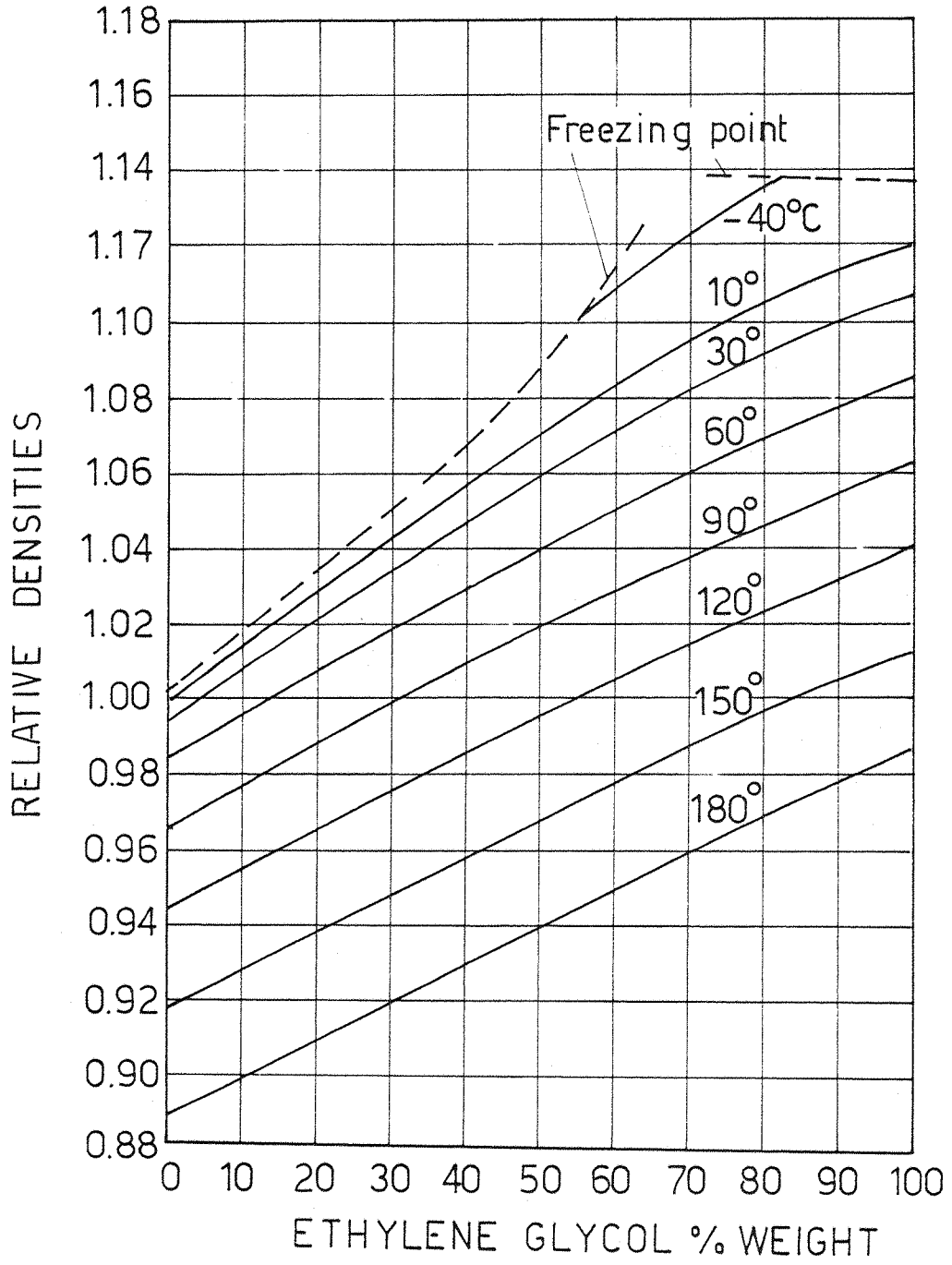

FIG 9.3 SPECIFIC GRAVITIES OF AQUEOUS ETHYLENE GLYCOLS SOLUTIONS (6)

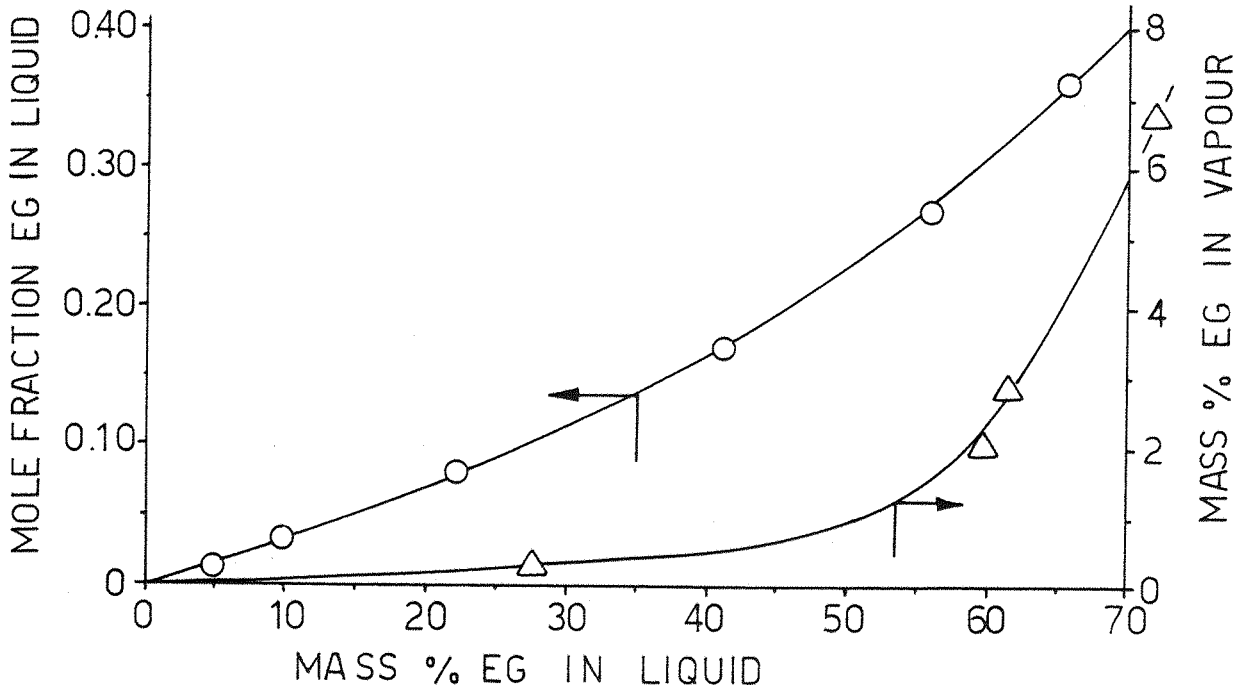

FIG 9.4 MASS RELATIONSHIPS OF EG/W MIXTURE IN THE LIQUID AND VAPOUR STATE(170)

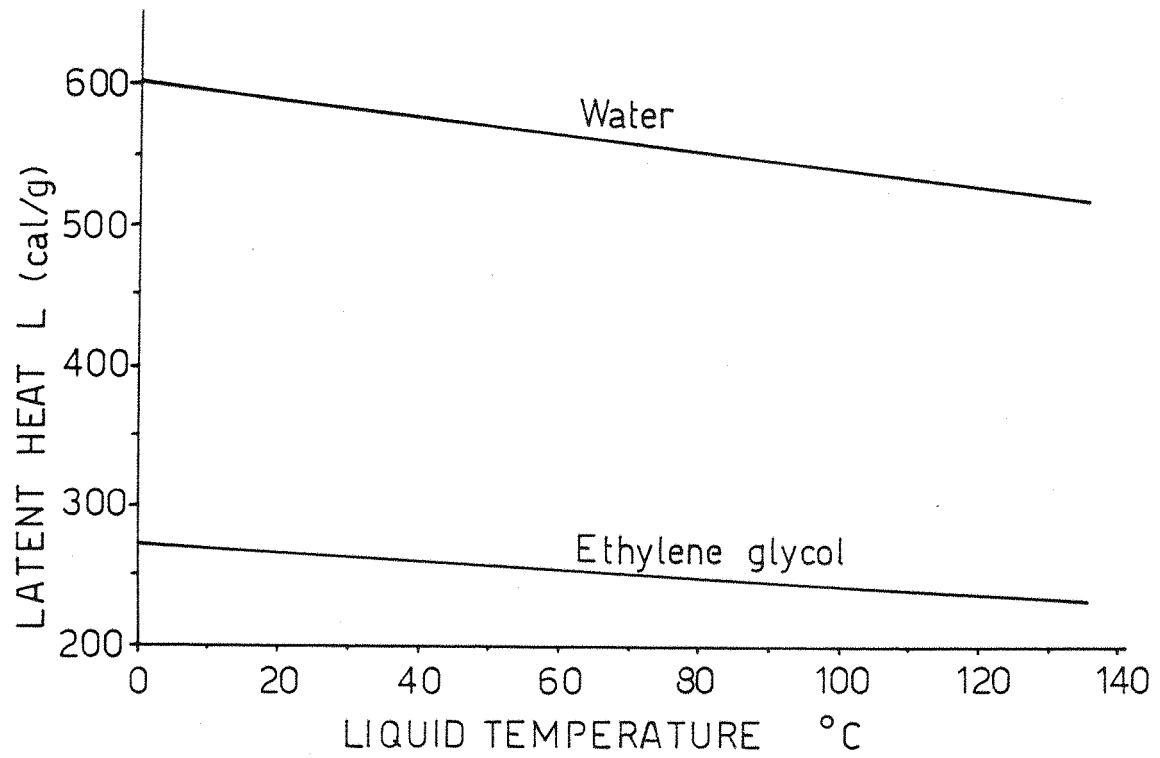

FIG 9.5 LATENT HEAT OF VAPOURIZATION FOR THE PURE LIQUIDS WATER AND ETHYLENE GLYCOL(37)

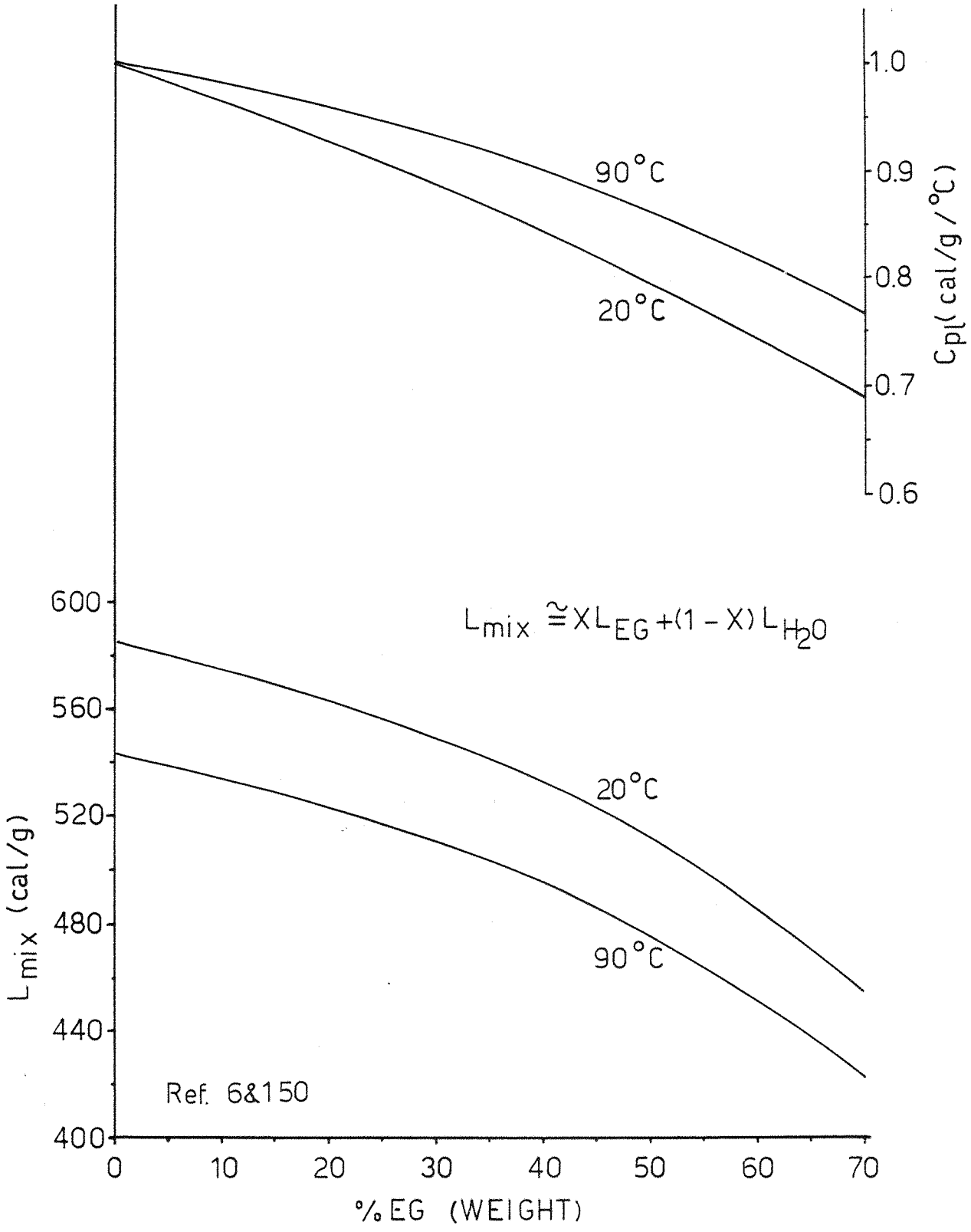

FIG 9.6 LATENT HEAT OF VAPOURIZATION AND SPECIFIC HEAT FOR THE MIXTURE EG/W AT 20°C AND 90°C

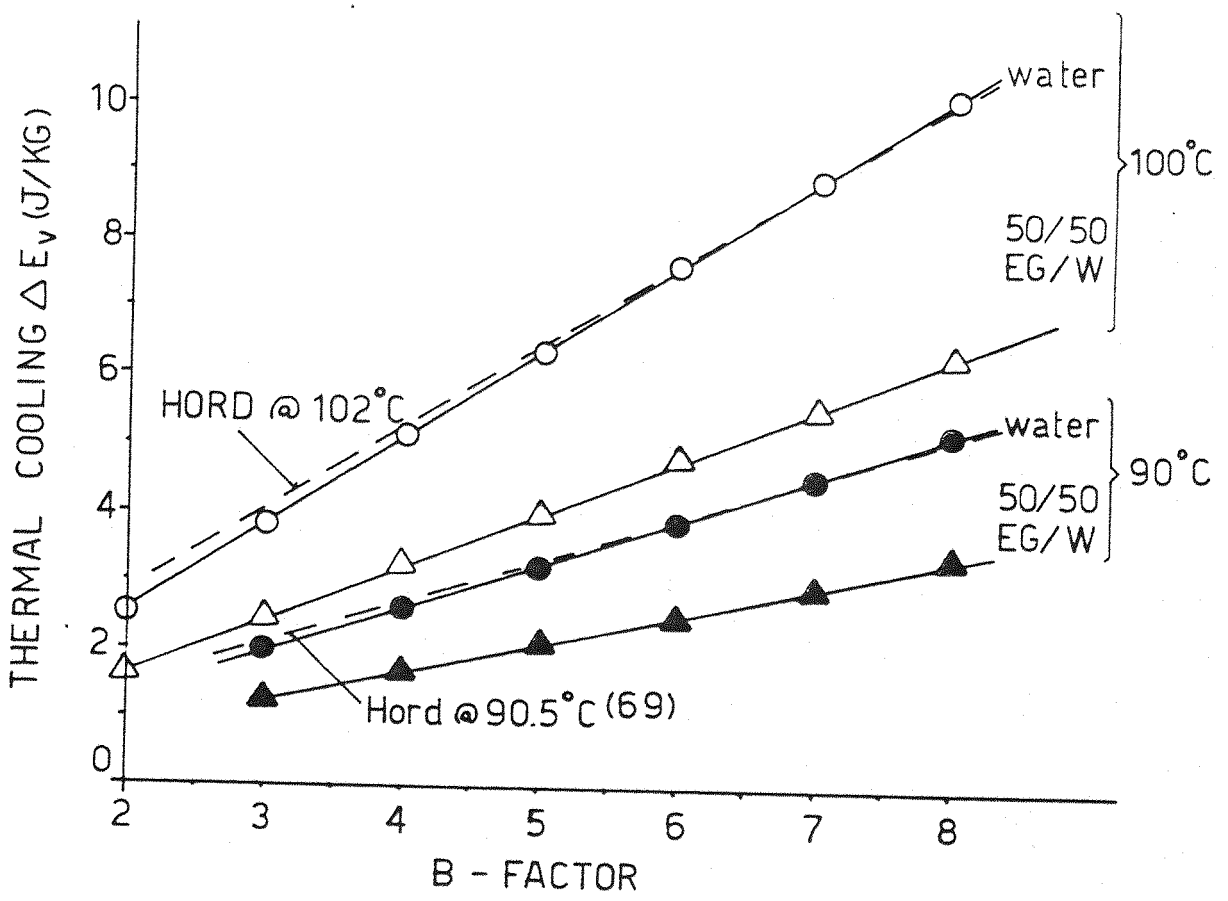

FIG. 9.7 THERMAL COOLING AS FUNCTION OF THE B-FACTOR

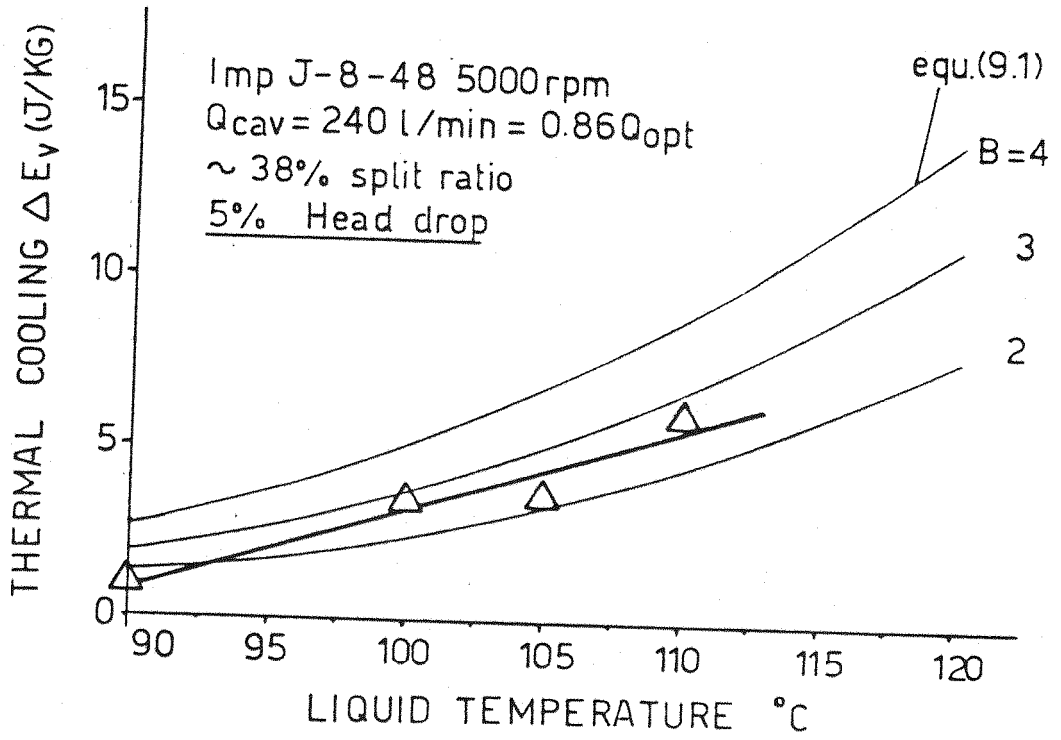

FIG. 9.8 THERMO DYNAMIC EFFECT OF PUMP J OPERATED WITH INHIBITED WATER

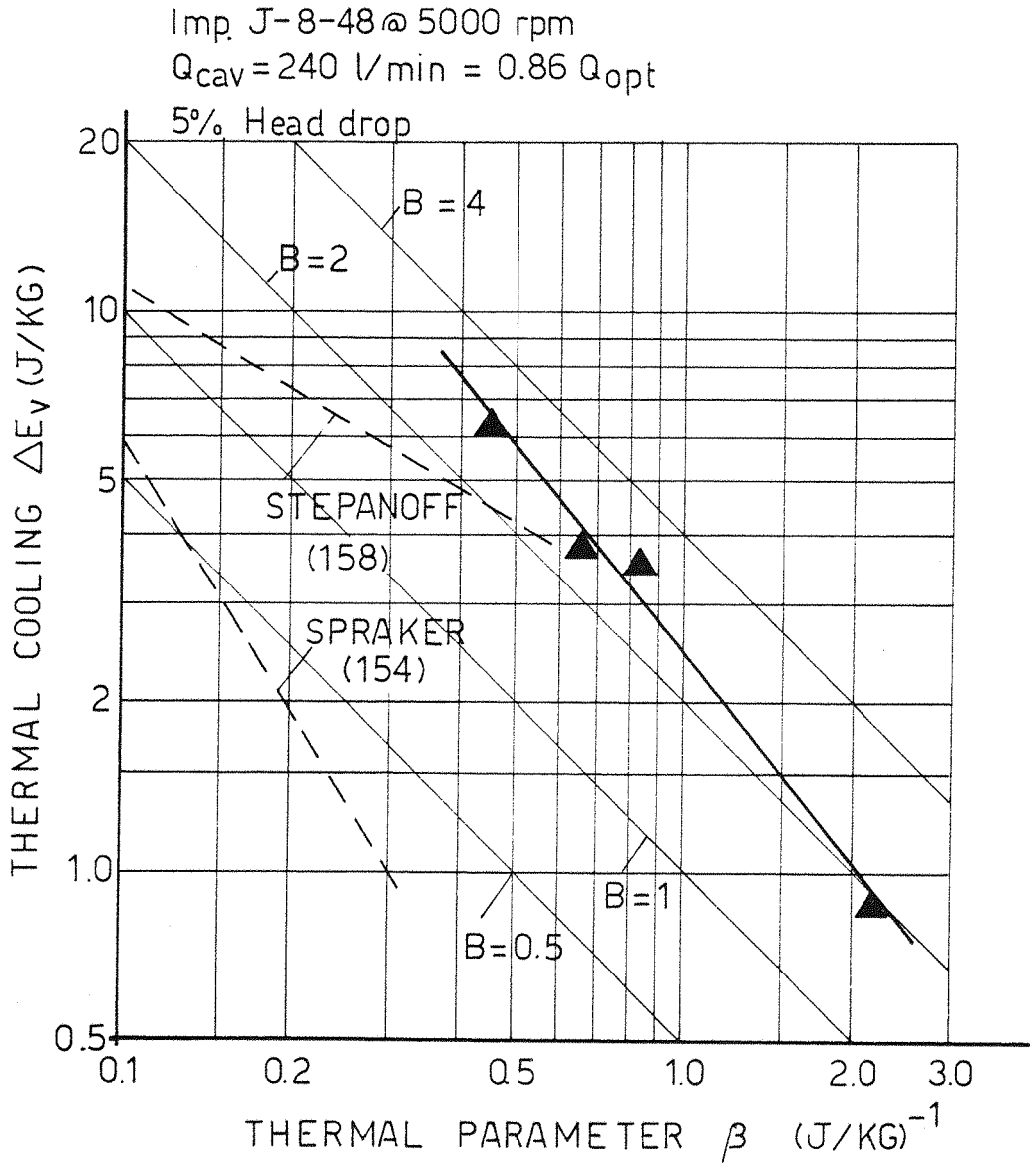

FIG. 9.9 CORRELATIONS OF THERMO DYNAMIC TEST RESULTS OF PUMP J WITH INHIB. WATER (RE-PLOTTED FROM FIG 9.8 IN THE RANGE 90°-110°C)

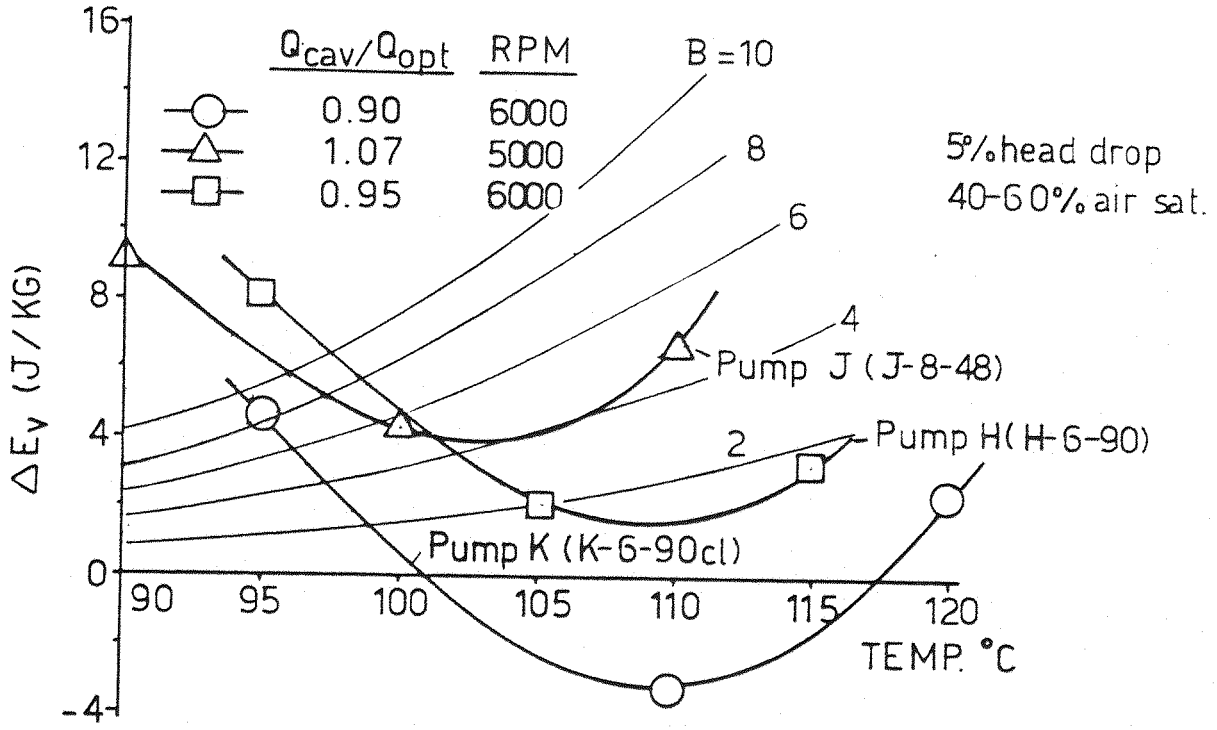

FIG. 9.10 THE INFLUENCE OF TEMPERATURE ON THE THERMO-DYNAMIC EFFECT OF THE BINARY MIXT. 50/50 EG/W

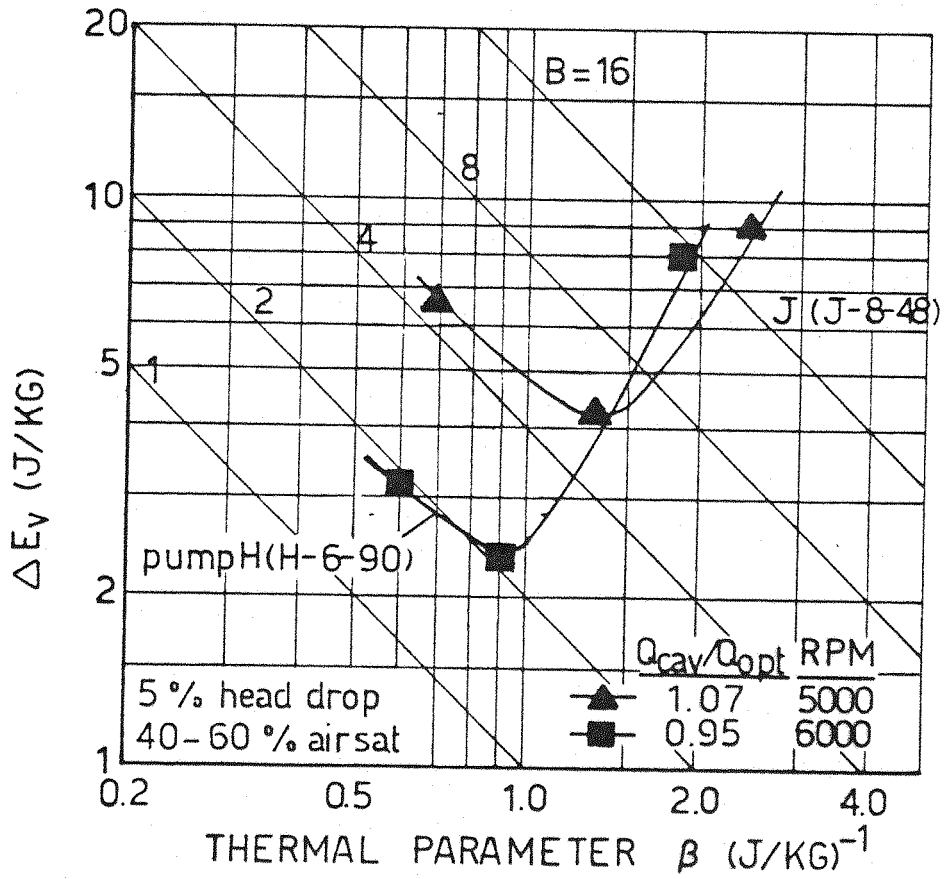

FIG. 9.11 CORRELATIONS OF THERMO DYNAMIC TEST RESULTS OF 2 PUMPS WITH 50/50 EG/W MIXTURE

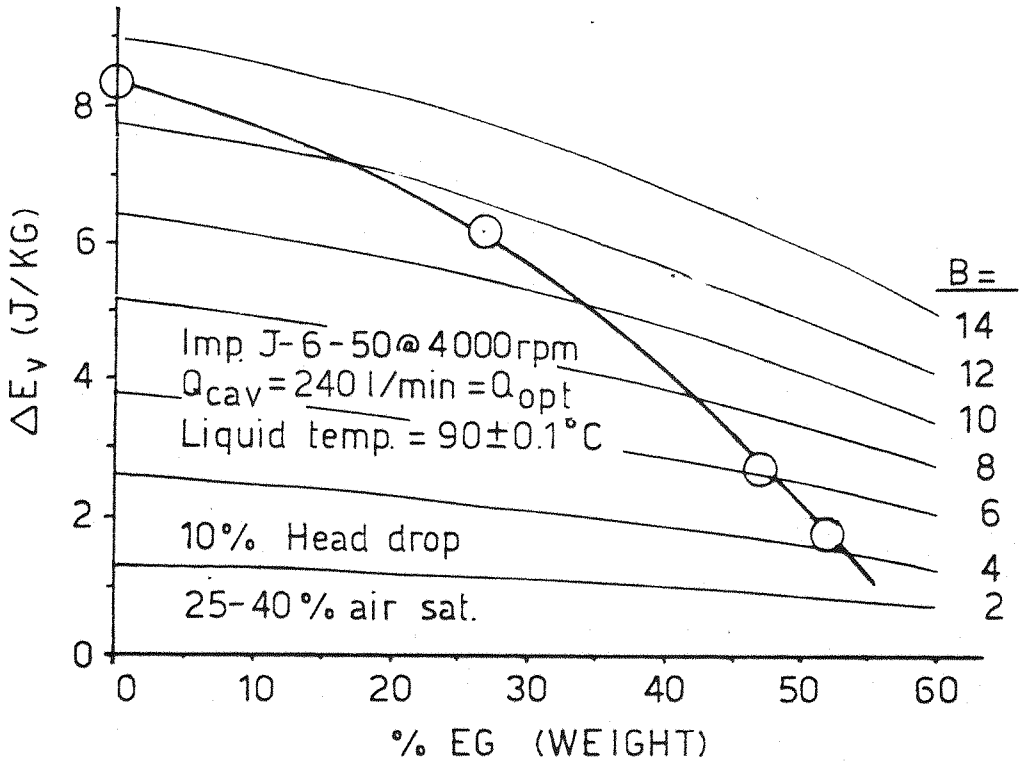

FIG 9.12 THE INFLUENCE OF EG CONCENTRATION ON THE THERMAL COOLING OF PUMP J AT 90°C

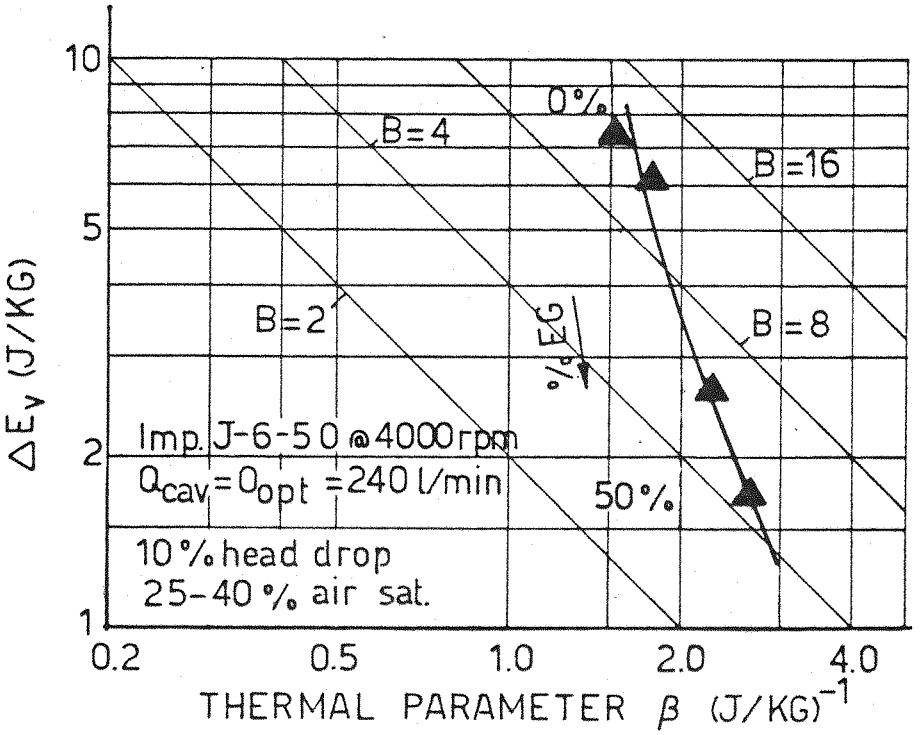

FIG 9.13 CORRELATION OF THERMO DYNAMIC TEST RESULTS OF PUMP J WITH BINARY MIXTURES OF ETHYLENE GLYCOL AND WATER AT 90°C

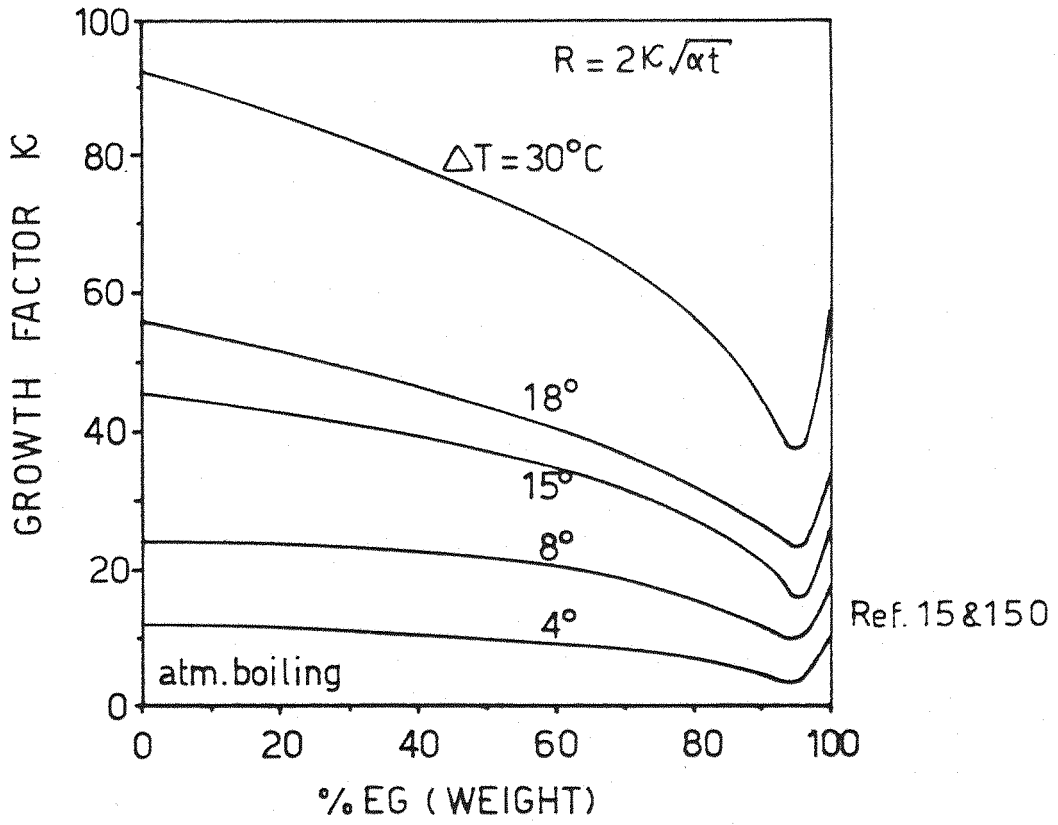

FIG 9.14 EXPERIMENTAL VALUES OF THE GROWTH FACTOR FOR EG/W MIXTURES FROM ATMOSPH. BOILING

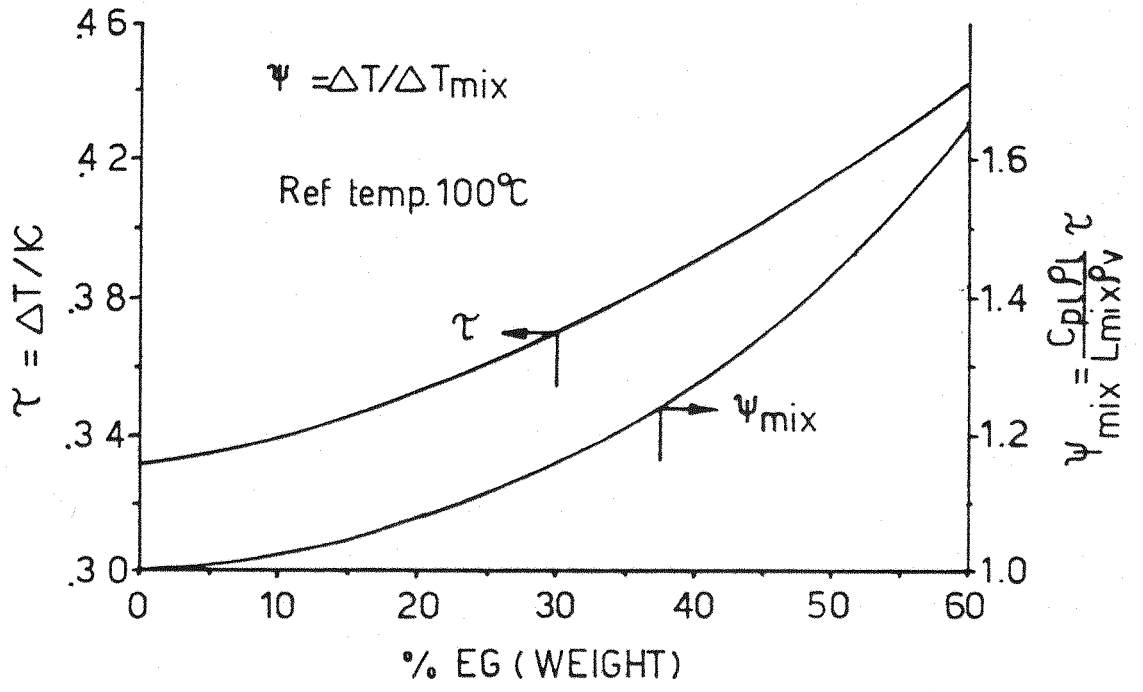

FIG 9.15 MEAN VALUES OF τ AND Ψ_{mix} OBTAINED FROM EXPERIMENTAL K VALUES OF EG/W MIXTURES

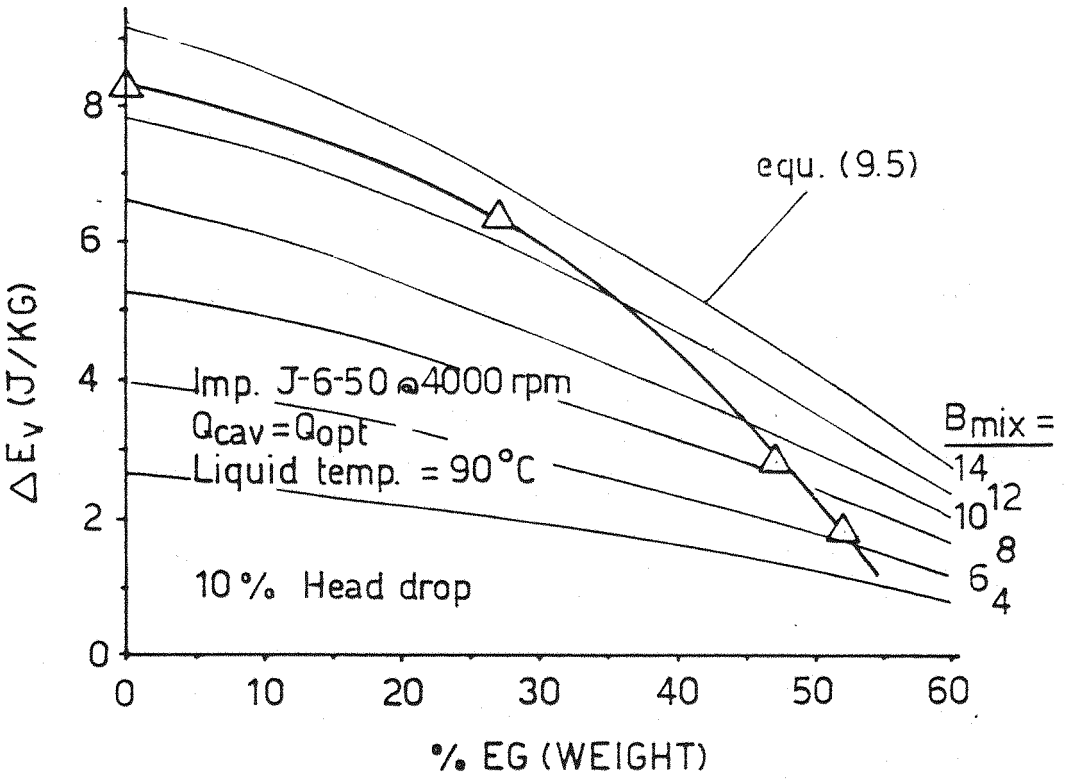

FIG. 9.16 THE INFLUENCE OF % EG ON ΔE_v AND B_{mix} FOR PUMP J

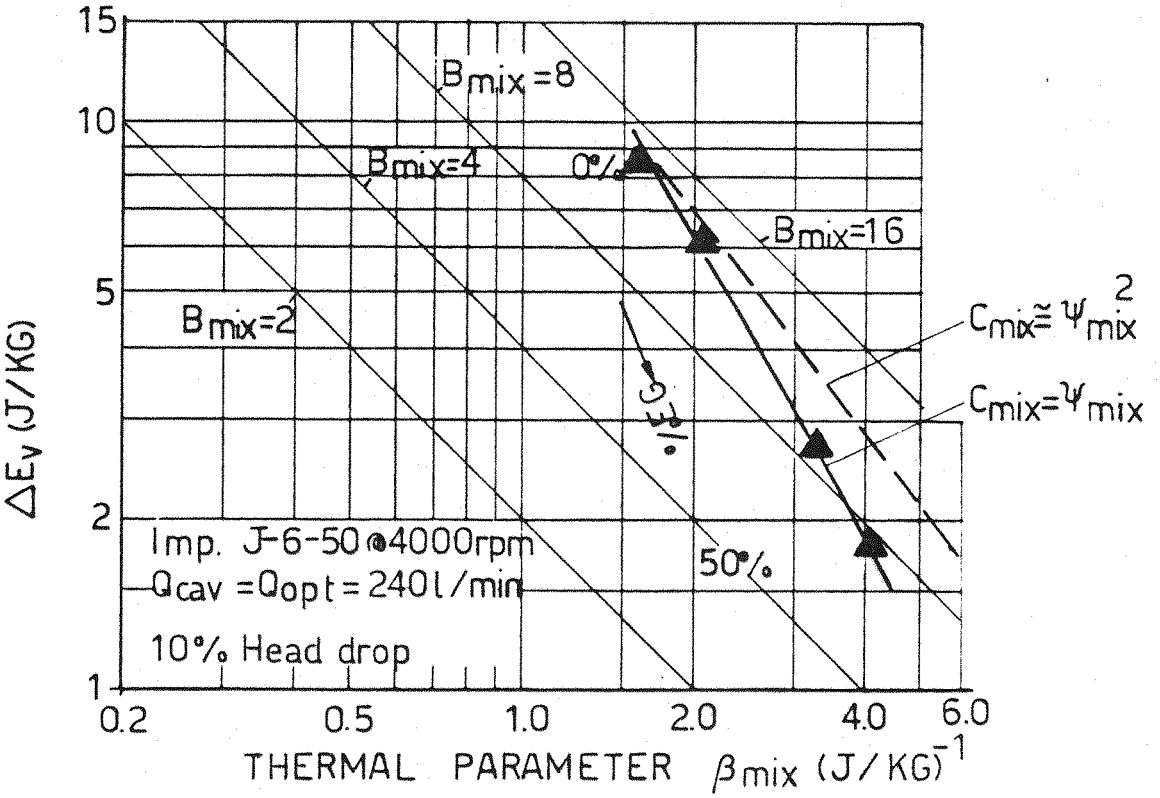

FIG. 9.17 CORRELATION OF ΔE_v VALUES FOR EG/W MIXTURES AT 90°C WITH RESPECT TO B_{mix} & β_{mix}

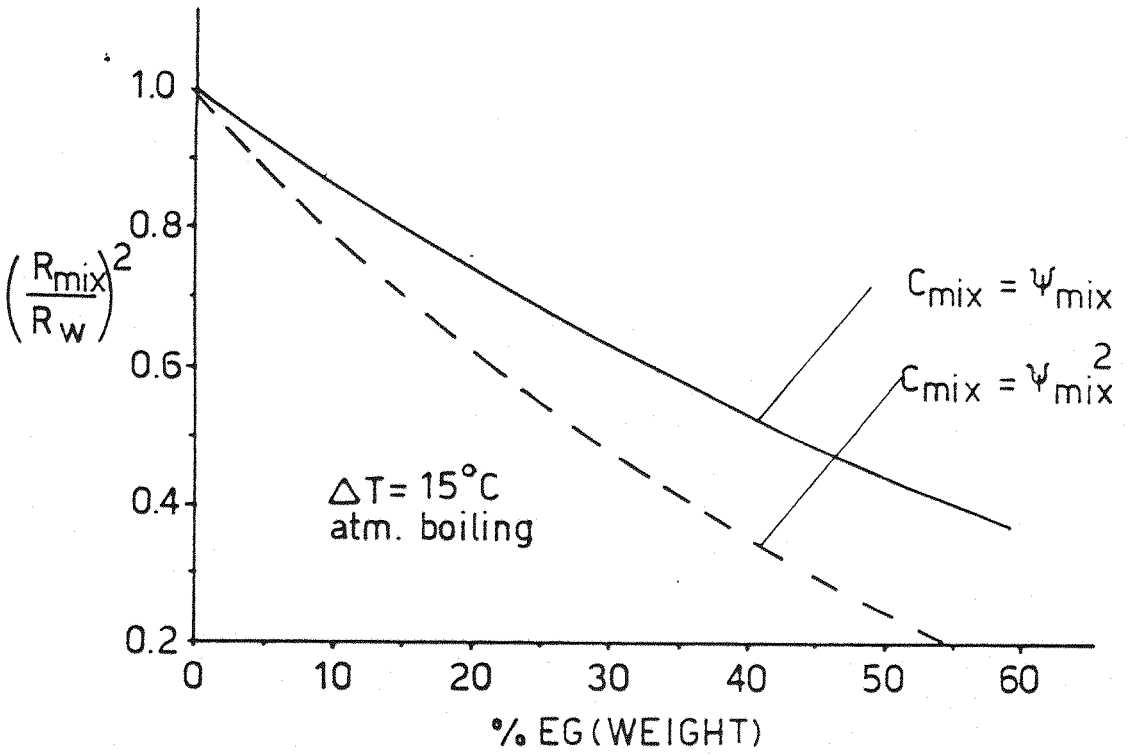

FIG 9.18 INERTIAL EFFECT RATIO OF EG/W MIXTURES TO THAT OF WATER FROM ATM. BOILING TEST RESULTS

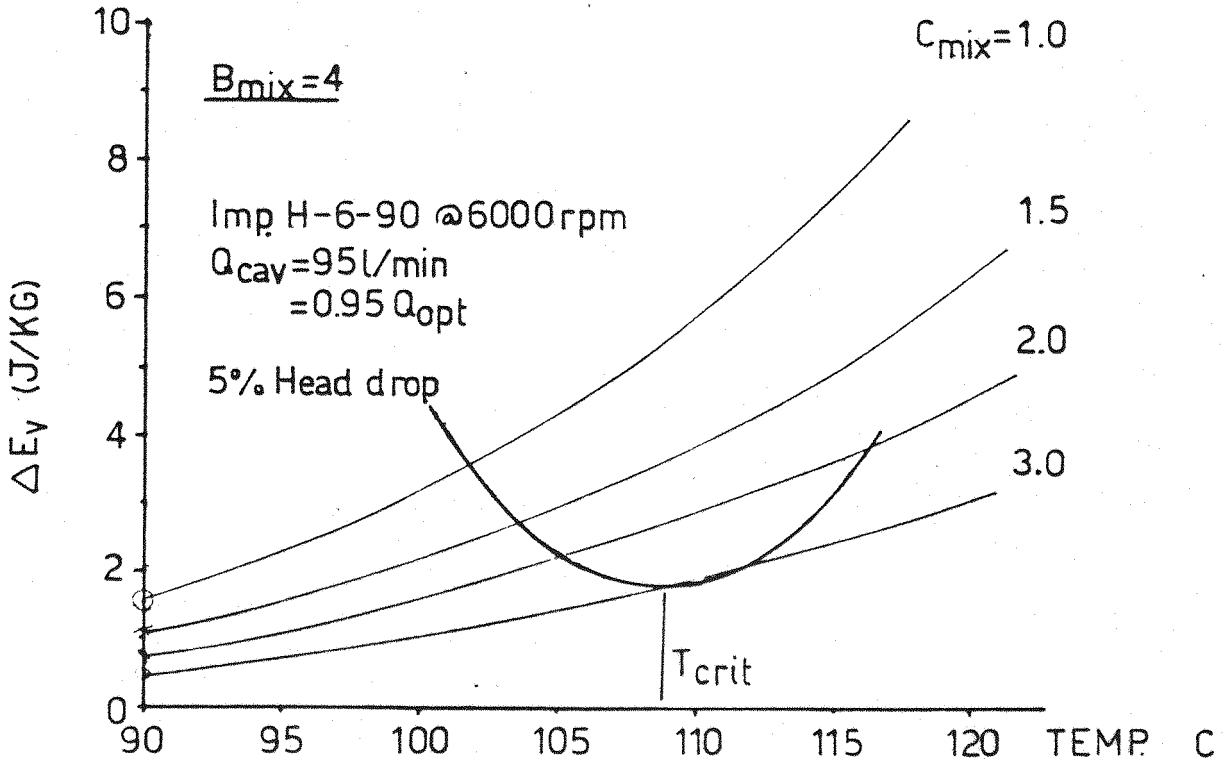

FIG. 9.19 CORRELATION OF ΔE_v FOR PUMP H NEAR T_{crit} OF THE MIXT. 50/50 EG/W FOR B_{mix}=4 AND 4 VALUES OF C_{mix}

CHAPTER 10

VISUAL OBSERVATION AND PHOTOGRAPHY

10.1 Experimental Technique

In order to gain a better understanding of the flow pattern and cavity development at pump inlet channel and impeller entrance, it was decided to fit some glass windows to the cast iron body of the relatively large automotive pump J. In figure 10.1 the dimensions of the glass windows and their placement in the body is given schematically. In figure 10.2, the pictures of the pump body fitted with the glass windows are shown.

From both figures 10.1 and 10.2, the external glass windows A, B and C are required to introduce sufficient lighting into the pump inlet flow channel and allow for visual observations and photographs to be taken. The internal glass ring D replacing the pump body part immediately near the open end of the impeller is to allow an insight into the impeller channels and therefore cavity development can be observed during pump operation.

In figure 10.3 the installation of the test pump is shown. In order to avoid any damage to the turbine flow meter mounted at pump discharge, the twin discharges of pump J were cut down to a single discharge pipe which is provided with a fine mesh strainer (picture) to collect glass debris in the case of an accident.

Visual observations were made using two different light sources. The first is a 150 W (microscope) light source employing two fibre optic light discharges (figure 10.3). Since this source provides a continuous light, its application was limited for observation of the flow pattern at the pump inlet chamber and the first appearance of the cavitation bubbles (inception). The second light source used for the purpose of observation is of the stroboscope type which can be adjusted to match the speed of the impeller. If successful matching is obtained, the impeller blades can be frozen in space

and the cavity development around the blade can be studied during pump operation.

Photographic work was performed by using a Pentax camera with a focal extension piece which allows the camera to be installed $\sim$ 15 cm from glass B (figure 10.1) looking foward into the impeller channel through glass ring D.

The exposure time was set by the pump speed to avoid any distortion to the picture. At a standard pump speed of 4000 rpm, the blade speed inside the frame range varies between 12 and 20 m/sec. Therefore an exposure time of no more than 5 μsec (corresponding to $\sim$ 0.1 mm maximum dislocation of the blade) was thought to be required to avoid any significant distortion of the picture. A specially acquired Zenon strobe was therefore used with the facility to give a single flash with an exposure time of 2 μsec and at a strobe power of 10 Joule.

The application of this flash however, provided some difficulties. Since a sufficient amount of light is required to enter the pump through window B in order to obtain a reasonable focal depth at the cavitating region, the strobe light had to be collected by two lenses installed between the strobe and the pump. Space limitations at window B which had to accommodate the camera made it extremely difficult to obtain sufficient light into the pump to produce wholly satisfactory pictures.

10.2 Visual Observations

Hub vortex: The design of pump J (and perhaps most automotive type centrifugal pumps) allows the flow to enter the suction cavity in front of the impeller from the side and parallel to the impeller (figure 10.1). The location of the inlet pipe is not concentric (figure 10.2) but set rather at an angle because of space limitation. All this is likely to promote some degree of pre-rotation of the flow entering the inlet cavity. Furthermore, the rotation of the drive shaft and the near side of the mechanical seal

turning in the same direction as the initial swirl is likely to add to the strength of the flow whirl and therefore a free vortex near the impeller hub is created. Such a vortex was clearly visible when observing through the glass windows of pump J, using the microscope type light source.

Inside the core of the free vortex (usually near the rotating shaft boundary where the velocity is maximum), the local pressure is expected to be exceptionally low and therefore cavitation bubbles (mostly gaseous) were visible even at relatively high suction pressures (and NPSE).

Examination of the inception cavitation number σ_i of the vortex revealed that σ_i is dependent on several factors such as flow velocity, impeller geometry and the type of fluid. In Chapter 7 the theoretical analysis of the vortex cavitation is discussed in some detail. In general it was found that σ_i is influenced by the circulation strength of the vortex which is Re number dependent, and by the soluble gas pressure.

Gas nuclei: In Chapter 7, the amount of gas content in the liquid was found to be of major importance for the cavitation process of pump J, especially when cold EG/W mixtures were being circulated.

As the liquid enters a low pressure region in the system, then depending on the gas concentration of the liquid, some gas will come out of solution and form gaseous bubbles which can act as cavitation nuclei. Earlier test results [135] showed that the vortex flow field associated with the centrifugal impeller acts as an excellent gas bubble generator. Some of these bubbles redisolve as they enter a high pressure region in the system, but some of them persist much longer and stabilize as cavitation nuclei, the amount of which depends on the air saturation and the pressure field around the system.

Pump J has an optimum flow rate of $\sim$ 240 L/min at a pump speed of 4000 rpm. Bearing in mind that the total liquid capacity of the test rig (reservoir and piping) is in the region of $\sim$ 250 Lit. , then at Q_{opt} the total

circulation time does not exceed 1 minute. Although this time seems quite a lot compared to actual cooling systems (average circulation time about 2 seconds), it is doubtful that it is long enough to allow all gas bubbles to redissolve again, especially those of larger diameter [66].

In figure 10.4 the cavitation test results of pump J were plotted in terms of percentage head drop against inlet (suction flange) static pressure at Q_{opt}. Two conditions were considered, the first (upper curve) is that of the mixture 25/75 EG/W mixture having a relatively low air content. The second is of the same mixture being fully saturated with air (lower curve).

As the liquid passes the glass window B before entering the low pressure region of the pump, it was possible to observe the amount of gas bubbles (nuclei) carried around the system depending on the inlet pressure and the gas content of the liquid (nuclei size observed is in excess of 100 μm). Three concentrations of nuclei intensity were recorded on figure 10.4 for both soluble air contents. (1) is the condition where only few visible bubbles appear in the liquid, (2) is that when a significant amount of gas nuclei (in the range 0.1 - 1.0 mm in diameter) are circulated around the system, and (3) is when the amount of bubbles entering the pump is so great that they block the sight to the internal parts of the pump.

Two features can be established from figure 10.4. The first and obvious one is that the lower the inlet pressure becomes the more gaseous bubbles are released and recirculated in the system. The second and more important feature is the significant influence of the dissolved gas content of the mixture on the amount of gas nuclei generated and recirculated as cavitation nuclei. As the first few bubbles appear when the degassed liquid mixture is circulated, at the same inlet pressure ($\sim$ 0.6 bar, abs), the saturated liquid would have developed so many gas nuclei that they block the view to the inside of the pump completely. Hence cavitation breakdown of the saturated liquid is accelerated due to promotion of gaseous diffusion (see Chapter 7).

Similar effects of the dissolved gas content were less pronounced with water. The reason behind this seems to originate from the surface properties

of the EG/W mixtures which allows for the gas bubbles generated inside the low pressure zone to expand sufficiently in size to be stabilized as cavitation nuclei in the high pressure region in the flow system. As for water, on the other hand, the higher surface activity helps to restrain the growth of these bubbles and redissolve most of the smaller size ones, as they enter the high pressure region.

Fixed cavity development: Cavitation bubbles (mostly gaseous) appear inside the core of the hub vortex at an early stage of the cavitation process (at relatively high NPSE). As the NPSE reduces, the number of cavitation bubbles (both vaporous and gaseous) inside the vortex increase in number and eventually a stage will be reached where a permanent cloud of cavities is created at the impeller entrance even before any performance drop can be detected.

Observations of the cavity formation and development were made using pump J running at 4000 rpm and delivering 240 L/min (corresponding to Q_{opt}). Inhibited water and three different mixtures of Ethylene-glycol and water were used. From all test liquids, hot water was found to be the one which allows for a better observation, mainly because the recirculated cavitation nuclei are less in number and therefore the developed cavity could be clearly seen when viewed from glass B (figure 10.1) down to near performance breakdown.

This was not found possible when using hot EG/W mixture because of the increasing cavitation nuclei passing glass B at low inlet pressures although the red colour dye also helped to reduce the visibility. Eventually the view is completely blocked whence 10% head drop is reached and observation was not possible beyond that point.

In figure 10.5, visual observation of the developing cavity was recorded for the cavitation process of pump J using hot water (at 90°C) at a constant flow test.

Positions 1 and 2 on this figure show how the cavity develops inside the vortex at an early stage of the process without any detectable performance drop but with some increase in the noise level of the pump.

When the inlet energy is reduced further, the vortex cavity pushes nearer to the impeller entrance (position 3) and partly extends along the suction side of the blade. When position 4 is reached the cavity has pushed more inside the impeller channel and nearly covers the whole channel width. At this stage the first sign of performance drop is recorded (∿ 1% head drop).

As the inlet pressure drops further, the fixed cavity has pushed itself well inside the impeller channel (positions 5 and 6). At the same time the fixed cavity no longer extends along the suction side of the blade. A shift toward the pressure side is noticed here, with the cavity taking an oval shape. This is evidently shown in position 6, where the head drop has reached ∿ 5%.

When cavitation progresses towards full (∿ 20%) head breakdown (position 7), the fixed cavity has pushed itself almost completely inside the impeller channel. At the same time the shift from the suction side is more pronounced with the cavity almost covering the whole length of the pressure side of the blade.

As far as the visual observation allowed, the general appearance of the cavity cloud observed with water seems to hold also for the mixture EG/W down to a head drop of 10%, below which the visibility deteriorates sharply due to the great number of nuclei entering the inlet cavity and blocking the view when looking through glass B. The only difference seems to originate from the fact that due to limited bubble growth of the mixture as discussed in the previous chapter, smaller bubbles are produced than with water and therefore the fixed cavity does not show a similar continuity of the vapour phase as observed with water, but rather more bubbles in abundance can be observed.

10.3 Photography

The photographic work was done in two phases. The first phase was to explore the shape of the cavity at impeller entrance without considering the particular details of the impeller. This phase was performed at an earlier stage of the test series at a time when the Zenon fast flash was not available

for the test. Instead of that a Medical Nikkor flash of an exposure time of $\sim$ 200 μsec was used.

In figure 10.6, two sample photographs of this first phase are shown. Impeller J-6-50 was run at 4000 rpm and delivering 240 L/min. Inhibited water at 90°C was used for the test. At low head drop (a), the fixed cavity is mostly outside the impeller channel and inside the free vortex at impeller hub, therefore blocking the entrance to the impeller. As the cavitation advances (b) the fixed cavity pushes more and more inside the impeller channel.

The second phase of the photographic test was performed with the Zenon flash and therefore pictures could be taken with 100 times less exposure time (2 μsec) and therefore the internal details of the impeller could be easily distinguished. However, some problems were associated with the use of this flash because of its bulky size and the high scatter of its light rays, which necessitated in the use of two collecting lenses. This however made it difficult to get sufficient light directly through glass B because of space limitations.

Hot inhibited water and 45/55 EG/W mixtures were examined in this test series using impeller J-8-70 running at 4000 rpm and delivering 240 L/min. In figure 10.7, the fixed cavity is photographed for the hot water at a small head drop (corresponding to position 6 on figure 10.5). Two frames at different focal depth were used at a similar exposure time of 2 μsec. Although the blade is clearly identified here, the fixed cavity is not very well defined. The main cavity seems to build up at the impeller entrance and extend inside the channel not necessarily attached to the suction side of the blade.

The picture is much clearer when looking at figure 10.8 where the fixed cavity for the hot water has reached an advanced stage thus producing a significant 22% head drop (corresponding to position 7 of figure 10.5). Here again two frames are presented, from which one can identify (with some difficulty) the whole channel between two adjacent blades. Here it should be obvious that the fixed cavity has pushed well inside the impeller channel and is firmly attached to the pressure side of the blade. It is also worth mentioning here that the blade in frame (b) is covered parly with a vapour

layer. This is to be related to the flow across the tip clearance from the high pressure to the low pressure side of the blade, thus a reduction in the cavity size may occur.

Photographic work with the hot EG/W mixture was hampered by two obstacles. The first is the red dye of the mixture which reflects some of the light. The second and more important is the amount of recirculated bubbles in the systems which block the view through window B (figure 10.1) below a head drop of $\sim$ 10% (similar bubble population was also observed at the sight glass about 1 metre upstream the pump suction pipe).

In figure 10.9, two frames taken of the hot mixture 45/55 EG/W are shown for a head drop of $\sim$ 10%. The external shape of the fixed cavity does not vary much from that of the hot water, with the cavity pushing nearer to the pressure side of the impeller. However, the density of the vapour phase is less accentuated than in the case of water. The reason behind this can be related to the retardation in bubble growth of the mixture due to the main concentration gradient at the bubble wall, thus giving more bubbles of smaller size. Also with EG/W the amount of larger size bubbles recirculated in the system, which appear in the picture of an average size of $\sim$ 0.5 mm, do contribute to a further increase in bubble number in the fixed cavity. All this seems to be responsible for the significant drop in the thermodynamic effect of the mixture.

10.4 Concluding Remarks

Visual observation and photography of the fixed cavity at the impeller channel of the automotive pump J provides with some very useful information on the inception and development of the cavity for both water and EG/W mixtures studied at Q_{opt}. The main points of interest are listed below.

1. A free vortex is formed at the impeller hub due to the side suction pipe design and the high speed rotation of the drive shaft and seal, which are situated inside the flow channel. First cavitation bubbles appear inside this vortex at an early stage of the cavitation process. As the inlet NPSE reduces, a fixed cavity inside this vortex is created, the downstream end of which blocks the entrance to the impeller.

2. Dissolved gas released from the liquid in the low pressure zone of the pump recirculate in the system, the amount and size distribution of which depends largely on the percent saturation of the liquid with air, but also on the particular liquid of the test. EG/W mixtures were found to be especially affected by air content. Recirculated gas nuclei reach such a high number that they block the view at NPSE as high as 60 J/kg for the saturated 25/75 EG/W mixture. Much lower effect was established with saturated water.

3. After the cavity has developed well at the impeller entrance, the attachment to the suction side of the impeller becomes weaker with further NPSE drop and eventually below $\sim$ 3% head drop the fixed cavity starts to detach itself from the suction side of the impeller, and as the cavitation process advances, the cavity becomes fully attached to the geometrical pressure side of the blade.

4. Vapour mass transfer across the tip clearance of the semi-open impeller could be established at an advanced stage of cavitation (22% head drop). The transfer from the pressure side to the suction side of the impeller may help to reduce the size of the fixed cavity and hence improve the suction performance of the pump.

5. Advanced stage of cavitation (above 10% head drop) for the hot EG/W mixture could not be photographed because of the increasing amount of recirculated nuclei which block the sight to the impeller. Bubble sizes in the range 0.1 - 1.0 mm in diameter could be established from the photographs.

6. Increased nuclei number and reduced heat transfer across the bubble wall of the mixture are believed to be responsible for the reduced bubble size and the increase in their number inside the fixed cavity. This may explain the more broken up pattern of the vapour phase of the fixed cavity in the case of the mixture EG/W as compared to that of water. Although the coloured dye used with these mixtures may also influence the picture, it is however believed that in the case of the mixture more bubbles appear in abundance.

FIGURES 10.1 to 10.9

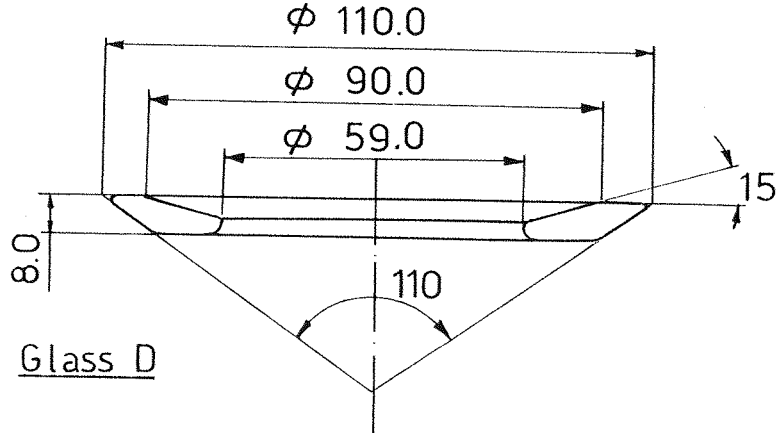

Glass D

Dimensions in mm

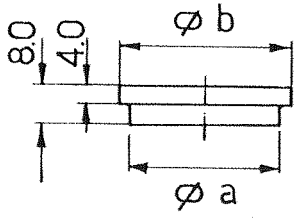

Glass -C

Window	a	b
A	30.0	34.0
B	23.0	27.0
C	18.0	22.0

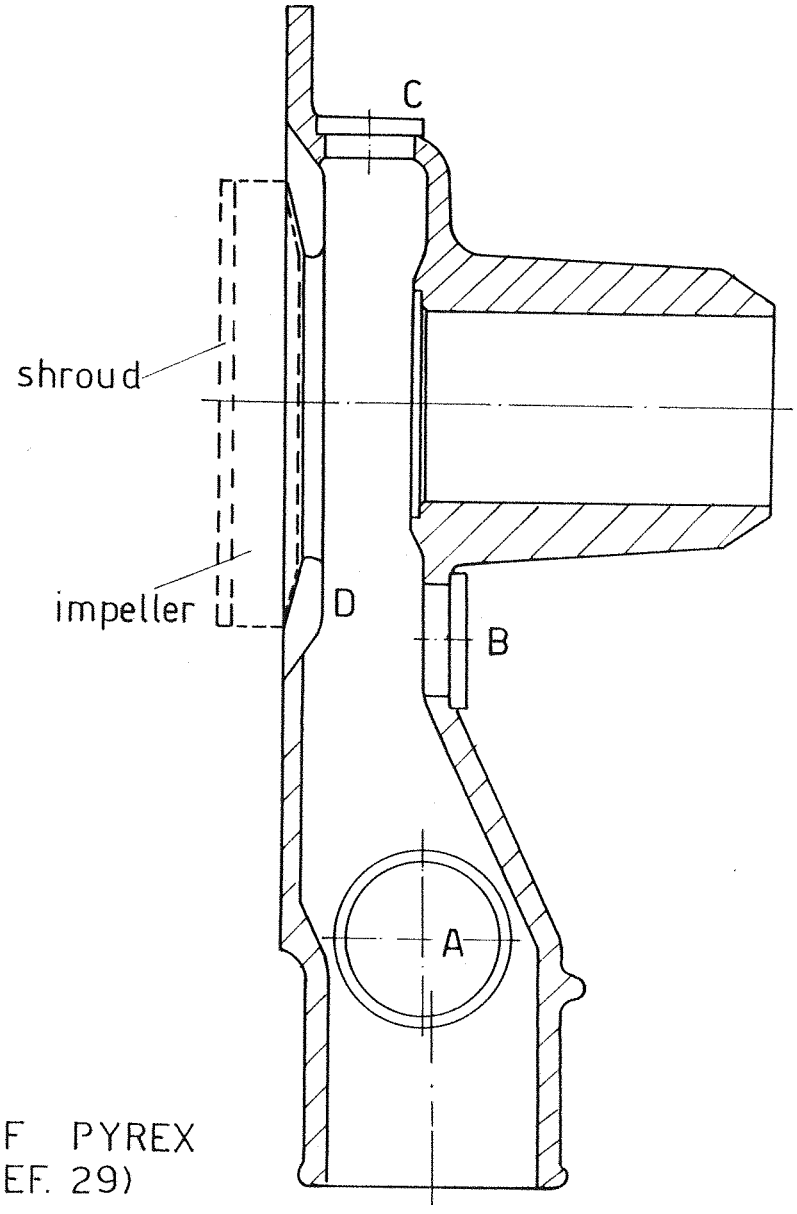

FIG 10.1 DIMENSIONS AND PLACEMENT OF PYREX GLASS WINDOWS IN PUMP J (REF. 29)

Fig. 10.2 Photographs of pump J's body fitted with the glass windows.

a. Glass ring fitted inside the pump adjacent to the impeller.

b. Three external glass windows fitted to the pump at the vicinity of the inlet flow channel.

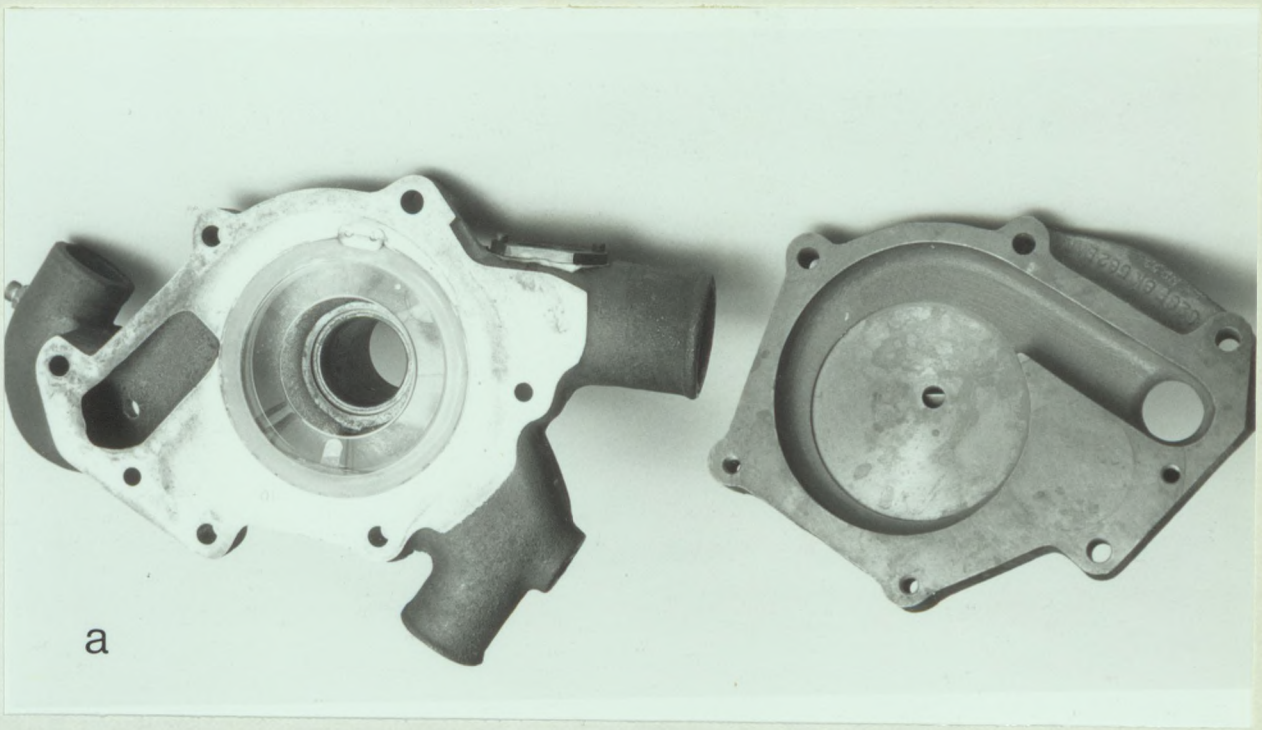

a

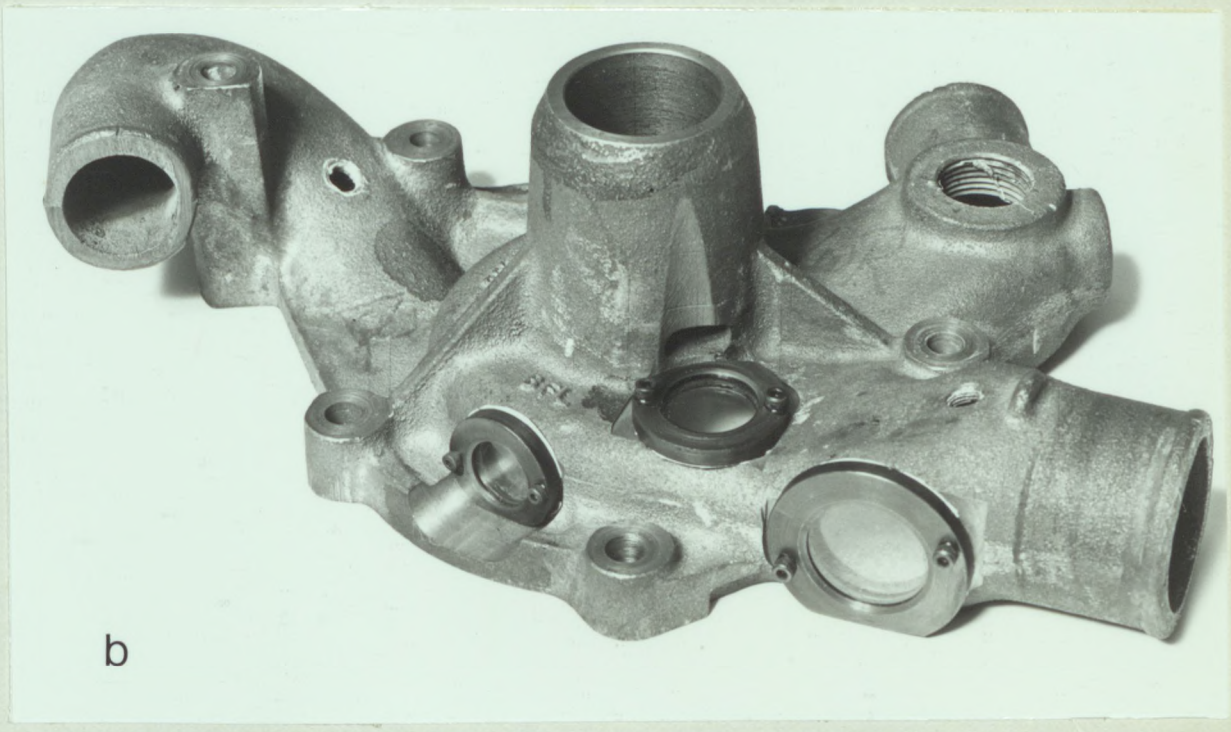

b

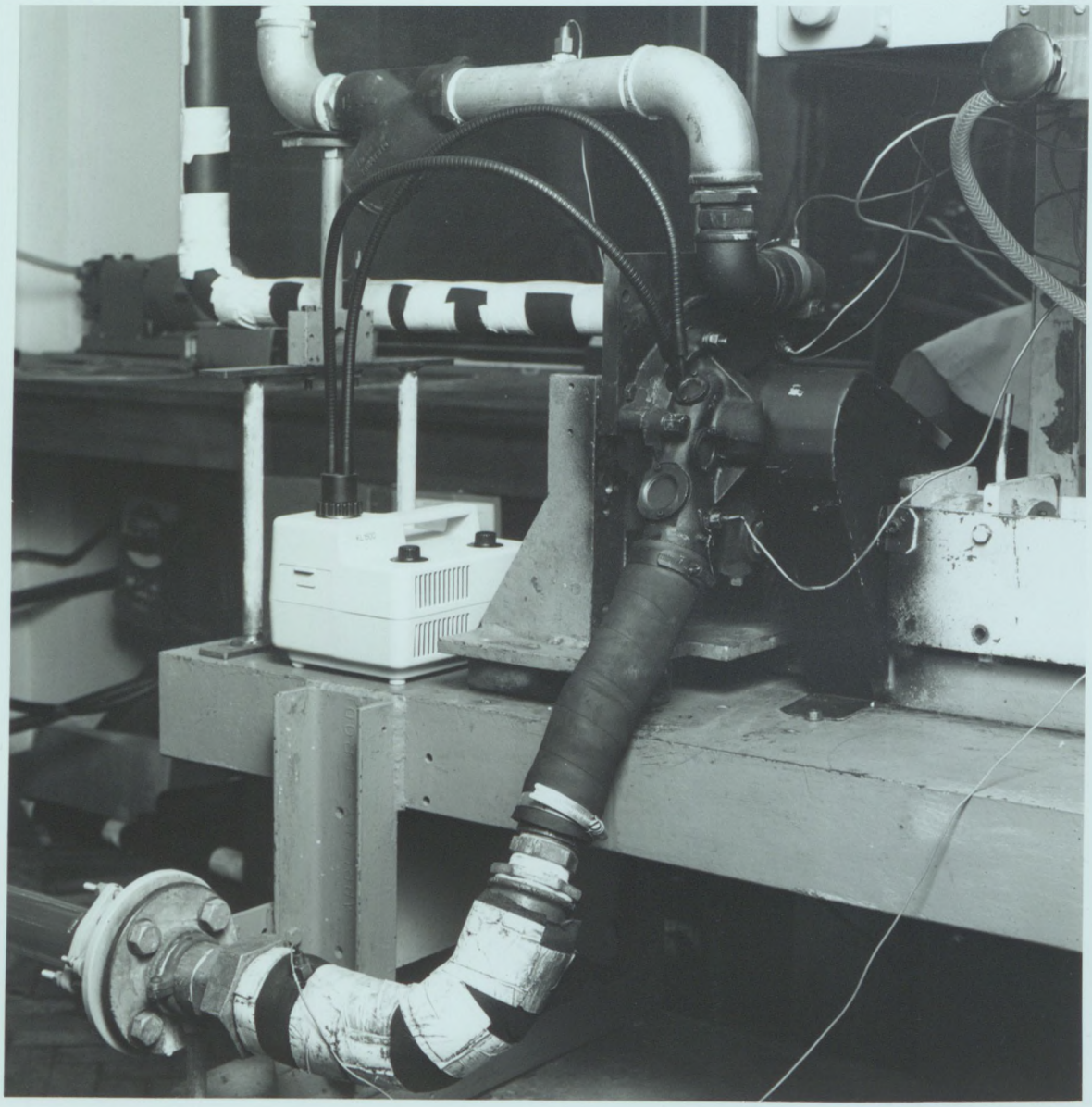

Figure 10.3 Rig arrangement for the observation work with pump J installed in place.

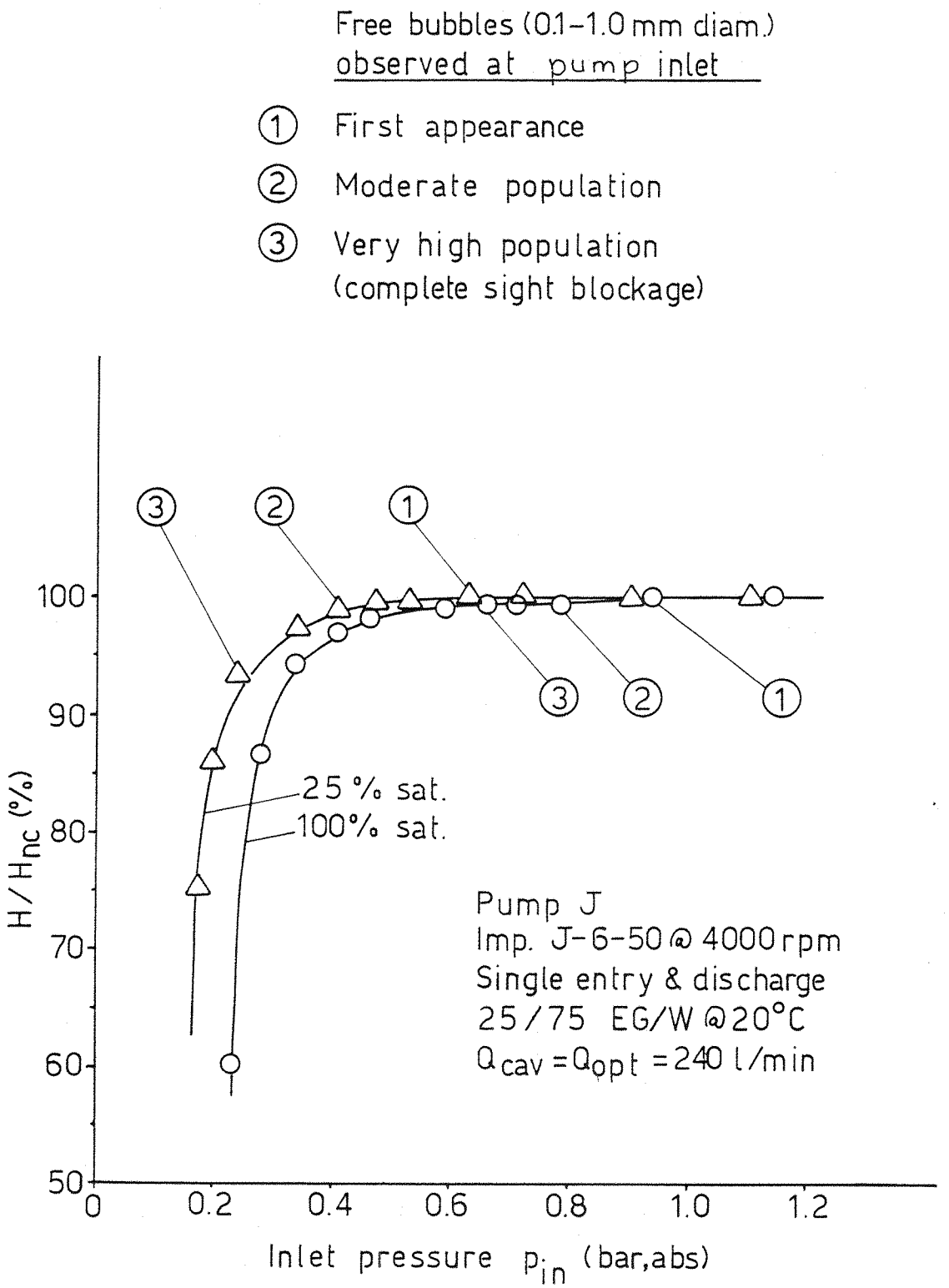

FIG. 10.4 THE INFLUENCE OF THE TOTAL AIR CONTENT ON THE DEVELOPMENT OF FREE GAS NUCLEI FOR THE BINARY MIXTURE EG/W

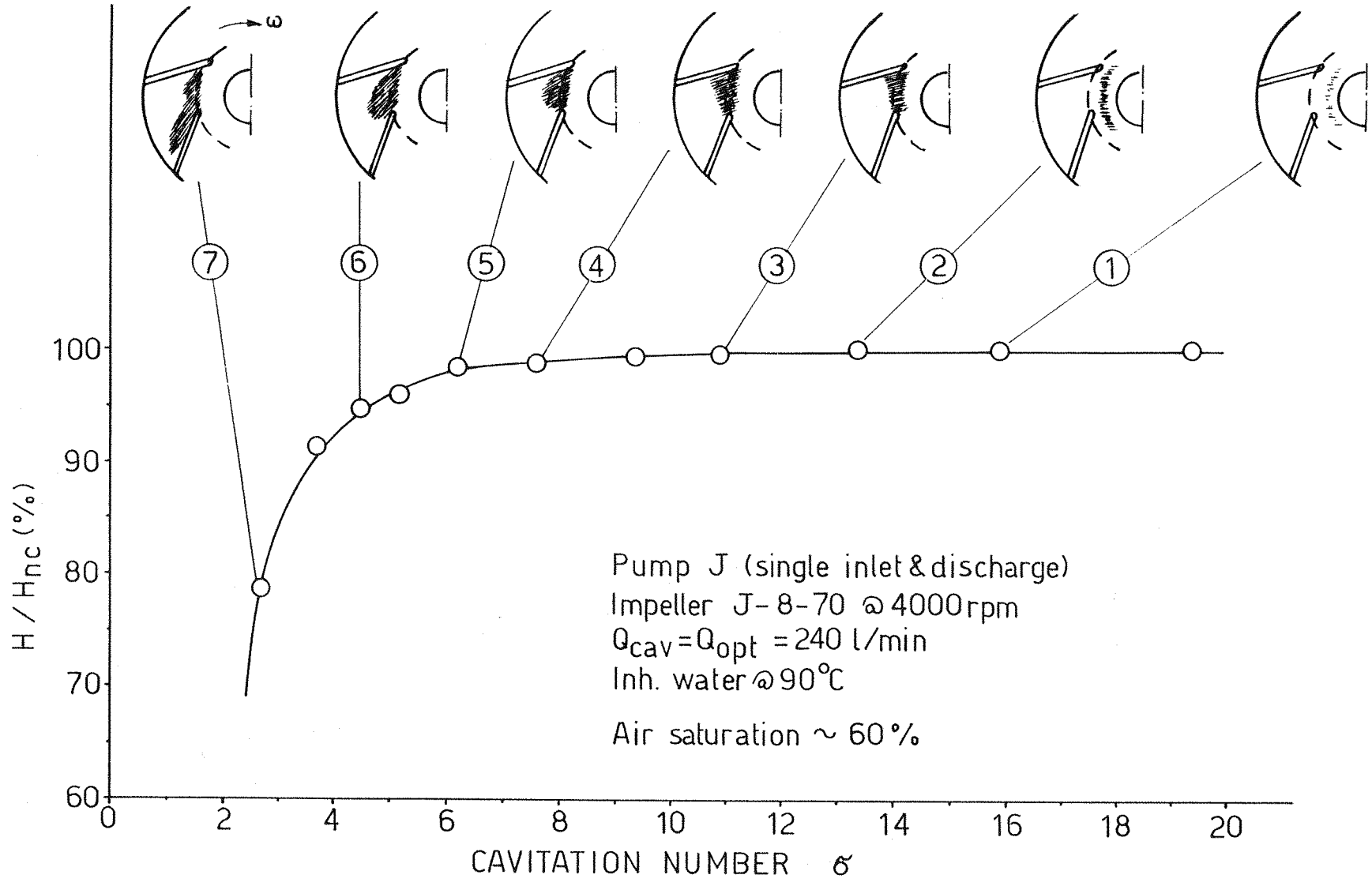

FIG 10.5 FIXED CAVITY DEVELOPMENT AT THE IMPELLER ENTRANCE OF PUMP J

Fig. 10.6 Development of the vortex cavity cloud at small head drops.

Pump J, impeller J-6-50

Pump speed 4000 rpm

$Q_{cav} = Q_{opt} = 240$ lit/min

Inhibited water at 90°C

Gas content ∿ 60% sat.

a. 2% head drop
F16, exposure time 200 μsec
6 times enlargement

b. 5% head drop
F16, exposure time 200 μsec
6 times enlargement

a

b

Fig. 10.7 Photographs of the developed cavity at small head drop with water.

Pump J - impeller J-8-70

Pump speed - 4000 rpm

$Q_{cav} = Q_{opt} = 240$ lit/min

5% head drop

Inhibited water at 90°C

Gas content ∿ 60% sat.

a. F8, exposure time 2 μsec
4 times enlargement

b. F 5.6, exposure time 2 μsec
4 times enlargement

a

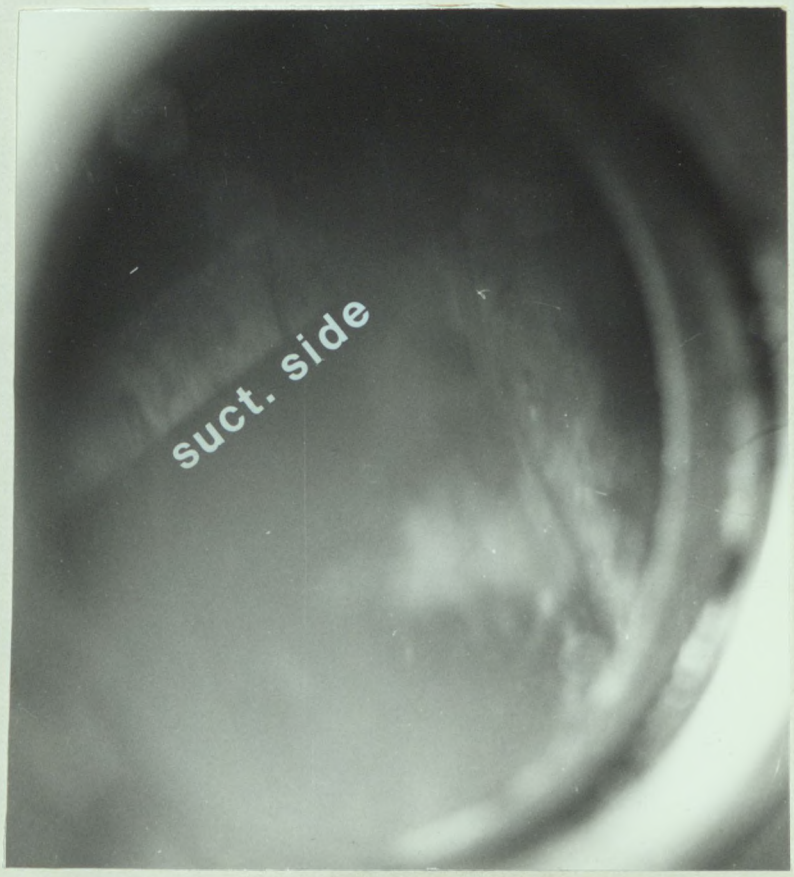

b

Fig. 10.8 Photographs of the developed cavity at advanced stage with water.

Pump J, impeller J-8-70

Pump speed - 4000 rpm

$Q_{cav} = Q_{opt} = 240$ lit/min

22% head drop

Inhibited water at 90°C

Gas content ∿ 60% sat.

a. F8, exposure time 2 μsec
4 times enlargement

b. F 5.6, exposure time 2 μsec
4 times enlargement

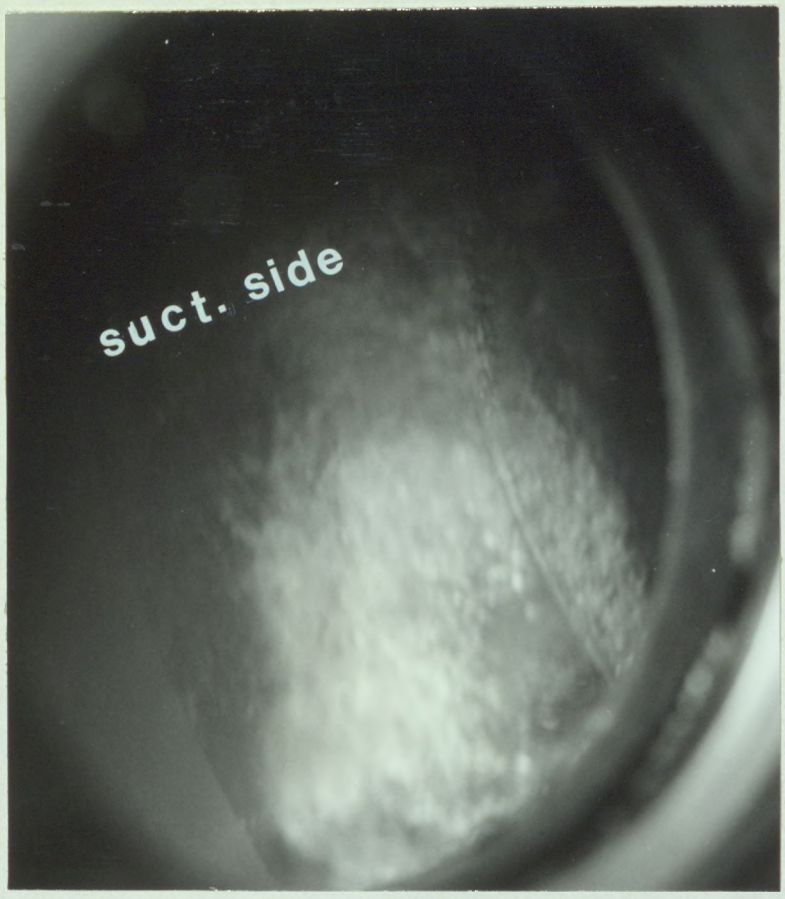

a

b

Fig. 10.9 Photographs of the developed cavity at advanced stage with 45/55 EG/W.

Pump J, impeller J-8-70

Pump speed - 4000 rpm

$Q_{cav} = Q_{opt} = 240$ lit/min

45/55 EG/W mixture at 90°C

Gas content ∿ 70% sat.

a. 7% head drop
F8, exposure time 2 μsec
4 times enlargement

b. 12% head drop
F8, exposure time 2 μsec
4 times enlargement

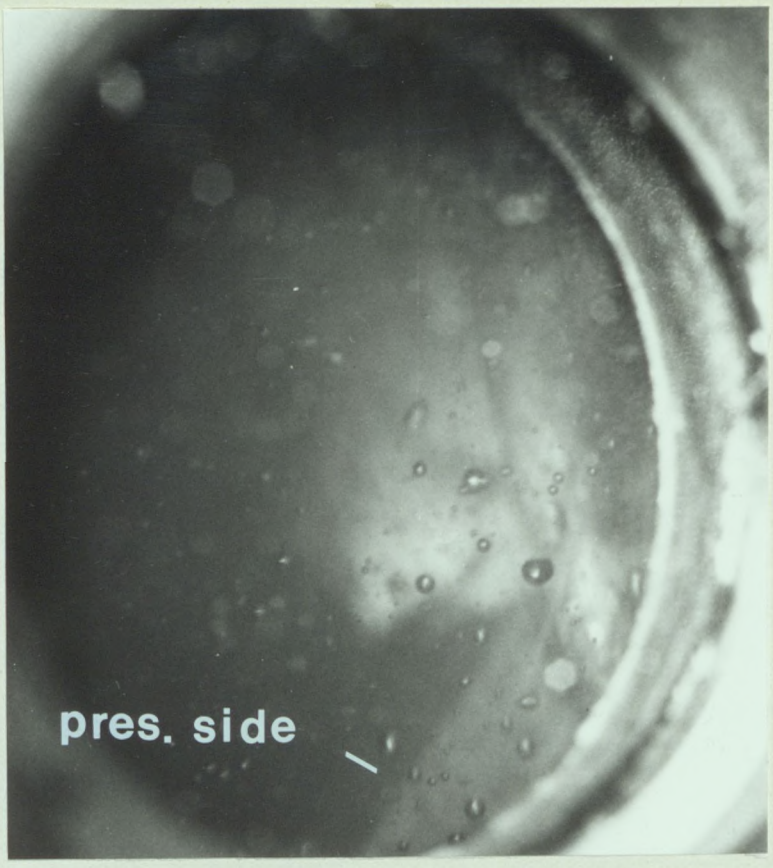

a

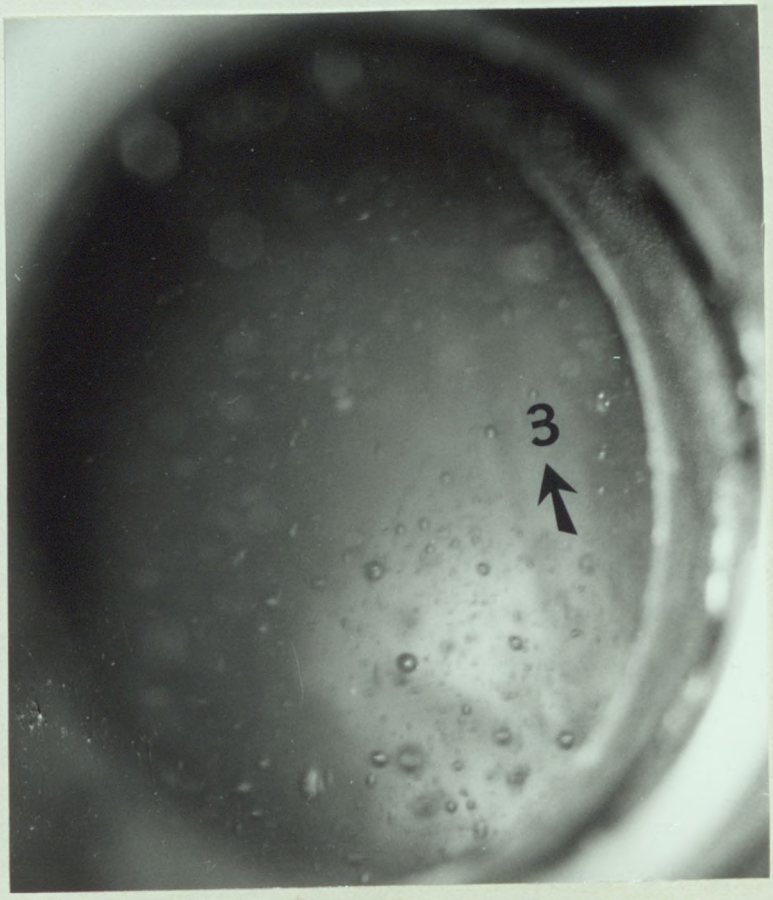

b

CHAPTER 11

CONCLUSIONS

Three small, automotive type centrifugal pumps were tested, using both inhibited water and binary (polar) mixtures of Ethylene glycol and water. Use of an amperometric oxygen monitor was made to measure the total air content of the liquid directly during the test. One body of pump J was fitted with glass windows which made it possible to examine the flow pattern at pump inlet and take some photographs of the fixed vapour cavity inside the impeller channels.

Concluding remakrs were made at the end of each chapter. Below are the summaries of those remarks:

A. Efficiences and Scale Effects

1. Overall efficiences of the test pumps are low ($\sim$ 20% for pumps H and K and $\sim$ 50% for pump J). Improving the hydraulic design of the impeller such as blade number and shape gave reasonable performance improvements for the volute type pump J, and only marginal improvements for the voluteless pump H.

2. Volute to impeller matching of pump J using slip factor according to Wiesner [181], showed that impellers of larger β_2 are more suited to this type of volute and therefore performance optimization is obtained using more radial vanes.

3. Developed head and overall efficiency were found to be influenced by the presence and size of the axial tip clearance at the open end of the impeller. However for these small pumps the presence of the tip clearance proved to be more important than its size with the shrouded impeller having the superior generated head and efficiency.

4. Predicted input power estimated from $\rho g Q_i H_i$ was found to be lower than the actual P_i (= P_s - P_m) in almost all cases. The difference between the two is assumed to be consumed to overcome the recirculatory flow in the impeller channel. This P_{rec} was found to depend on the impeller and pump geometry and was successfully correlated to the solidity of the impeller of pump J.

5. High power scale effects were found to exist for all test pumps with respect to changes in pump speeds. Analysis of the various losses in the speed range 3000 - 6000 rpm for pumps H and K showed that these scale effects can be related mainly to δ_{rec} and δ_m. Re number effects due to surface roughness were found also important at speeds below 3000 rpm.

6. Using the Cordier plot it was possible to show that for the same pump diameter, geometrical improvements leading to increased ψ_p/ϕ_p ratio pushes the correlation point nearer to the optimum range of the diagram, thus suggesting optimization of the pump diameter for the duty it performs.

B. Suction Performance

1. Inlet conditions such as cramped inlet and the situation of the shaft and seal inside the flow channel make the suction performance of these pumps rather inefficient. Analysing the impeller inlet velocity triangle showed that for these pumps, pre-rotation, impact losses and various other energy losses are likely to reduce their suction performance appreciably below the optimum value.

2. The influence of the test flow ratio Q_{cav}/Q_{opt} for pump J showed that the cavitation number σ_{05} is likely to increase at low flows and approaches infinity at $\sim 0.5\ Q_{opt}$; below which it decreases again. The critical flow rate is accompanied by an increase in the required NPSE.

3. The presence of an axial tip clearance was found to improve the suction performance of the pump slightly when tested at the same flow rate. This improvement, however, was not necessarily proportional to the size of

the tip clearance. An optimum clearance of $\sim$ 0.7 mm could be established for pump J.

4. Impeller geometry influence such as inlet angle and number of blades was examined for pumps H and J using different impeller designs. In general large β_1 was found to improve the suction performance in all cases. Increased number of blades improved the performance at advanced cavitation, but proved less favourable at small head drops.

5. Using a contraction number C_n which correlates all the geometrical factors at impeller inlet, it was possible to show that σ_{05} rises steadily with increased C_n, although some scatter was apparent. By including the length of the blade and using a geometrical parameter ℓ/w instead, a better correlation with σ_{05} could be established for pump J.

C. Gas Content Effect

1. Use is made of an amperometric oxygen sensor to monitor the percentage air saturation in the liquid at 20°C. Installed in a loop, this monitor was made to measure the O_2 content continuously during the test. Reservations about its use arise from the fact that gases may redissolve in different rates to their percentage in air.

2. In the present rig, the level of O_2 saturation during the test was found to change depending on the type of liquid and the method of controlling the inlet NPSE. Using a free surface in the main reservoir for this purpose, results in an equilibirum O_2 saturation of 60% for water after one hour regardless of the initial saturation level. EG/W mixtures, on the other hand, were found to be less influenced by test time, with initial saturation retained during the test period depending on EG concentration.

3. Depending on the gas concentration gradient $(C_\infty - C_s)/R$ it was found that pump performance can be effected at various degrees. Saturated EG/W mixtures were found to produce high gas content scale effects with the suction

performance of pump J significantly impared. High gas concentration gradient is believed to promote gaseous diffusion for the mixtures, and to a much lesser extent with water.

4. Hub vortex observed at pump inlet was found to promote early cavitation bubble formation which are believed to be of the gaseous type. Testing for σ_i at various pump speeds with water at 90°C it was possible to show that $\sigma_i \sim Re^n$ and may be influenced by impeller geometry. Tests with 45/55 EG/W at 90°C showed that σ_i increases for similar impeller geometry and pump speed. Approximate theoretical solution showed that the difference in σ_i for the two fluids can be successfully related to increased partial gas pressure of the mixture.

D. Thermodynamic Effect

1. Contrary to water, the EG/W mixtures do not show a progressive increase in the thermodynamic effect with temperature rise up to a temperature of ∿ 110°C. Some thermodynamic effect is obtained for 50/50 EG/W at ∿ 95°C, above which it reduces and eventually reaches a minimum at ∿ 105°C for three pumps.

2. For pump J, operated with 50/50 EG/W, low values of Q_{cav}/Q_{opt} (< 0.7) is likely to produce negative value of ΔE_v. This is believed to be related to the Re number effect of the hub vortex which is found to produce low σ_{05} values for the more viscous cold mixture. This suggests that the ΔE_v is preferably estimated at high Re numbers.

3. Air content effect was shown to give high discrepancies in the estimation of ΔE_v, especially for the EG/W mixtures. To minimize these effects, correlations at low gas content (∿ 25% saturation) and 10% head drop were found to give reasonable accuracy for the mixtures.

4. Correlation of ΔE_v test results to the B-factor have shown that inhibited water can be reasonably correlated in the temperature range 20 - 110°C, although the absolute values of ΔE_v are higher than is expected in

this temperature range. Similar correlations for the mixture 50/50 EG/W from results obtained with three pumps up to 120°C were not possible, especially around the critical temperature of ∿ 105°C.

5. ΔE_v test results at 90°C obtained with water and three concentrations of EG/W mixtures at relatively low gas content and 10% head drop, could not be successfully correlated to the B-factor. By introducing a modified B-factor for the mixtures which includes the mass and heat transfer properties of the mixture, represented by the correction factor ψ_{mix}, better correlation could be obtained with respect to B_{mix} ($= B/\psi_{mix}$), but not fully satisfactory.

6. Gas filled nuclei circulated in the system was found to be highly pronounced when EG/W mixtures are handled. Including the influence of these nuclei as a second factor to reduce ΔE_v so that $B_{mix} = B/C_{mix}$ with the new correction factor $C_{mix} = f(\psi_{mix}, z)$, a better correlation for ΔE_v with B_{mix} is sought.

7. Using the concept of C_{mix}, better correlation for the mixtures could be demonstrated (although only tentatively). It is also possible to show that for the same B_{mix} and different C_{mix} values, the minimum ΔE_v at 105°C for 50/50 EG/W can be justified.

E. Visual Observations

1. Observations of the flow field at impeller inlet made it possible to observe the appearance of the first cavitation bubbles inside the hub vortex. Gas filled bubbles were observed to recirculate in the system in great numbers for the EG/W mixtures and much less for inhibited water. Unstable surface properties at the bubble interface are believed to allow initial gas bubbles to grow sufficiently in size to be stabilized at pump discharge and become travelling nuclei.

2. The attached cavity was observed to start forming inside the hub vortex and gradually pushes into the impeller channel as the NPSE is reduced.

Cavity cloud was found to cover the whole entrance to the impeller before any head or efficiency drop could be detected. At small head drops the fixed cavity extends only marginally along the suction side of the blade, and as the inlet pressure decreases it deflects from the suction side towards the pressure side. When 10% head drop and more is reached the fixed cavity was observed to be firmly attached to the pressure side of the blades.

CHAPTER 12

FUTURE RESEARCH

Discussions of the test results in this work suggest further research in the field of pump performance with binary liquid mixtures. Since the non-cavitating performance of the centrifugal pump is not much influenced by the type of the liquid for similar density but rather by its viscosity, only the cavitating flow performance is of interest here.

Suggestions for future work in this field are listed below according to priorities.

1. The use of the oxygen monitor is to be extended further to include testing at the maximum allowable sensor temperature ($\sim$ 45°C). By making use of the special cooler (figure 2.4) air content of circuit liquid temperatures up to about 100°C can be measured. Since the O_2 monitor cannot distinguish between free and dissolved gas, extra arrangements to measure the free gas content simultaneously with the O_2 monitor is desirable.

2. Thermodynamic effect test results were limited to the maximum temperature of 120°C with the present rig. To gain a better picture for the binary mixture, the temperature is to be extended to a higher temperature ($\sim$ 200°C). This of course necessitates major improvements to the present rig.

3. Correlations of the thermodynamic test results with respect to the fluid properties were attempted for three concentrations of EG/W mixtures in addition to water, and one temperature only. This is to be extended to include several more concentrations at higher temperatures and preferably for more than one pump geometry.

4. Photographic study of the fixed cavity for the binary mixtures is to be extended and improved by using larger windows and better lighting and photographic techniques. Colourless mixtures are required to eliminate the negative influence of the colour dye.

5. The correction factor to the B-factor of the mixture (C_{mix}) is of vital importance for the correlation of the thermodynamic effect of the binary mixtures. Its concept and theoretical background are to be further investigated and strengthened. Successful correlation with respect to the heat transfer problem only ($C_{mix} = \psi_{mix}$) is required to support the theoretical concept of ψ_{mix}. This can be done either by using gas free mixtures thus minimizing the free gas nuclei number or by measuring the number of nuclei and account for their presence.

6. Measurement of the gas nuclei in the flowing stream is of great importance for the successful correlation of the cavitating behaviour of the hydraulic equipment. This seems to be of additional importance for the binary mixtures. Light scattering method is to be attempted to measure the active nuclei.

7. On the theoretical front more information is required about the physical properties and heat and mass transfer phenomenon of the binary mixtures. Gas diffusion and surface activity at the bubble interface is to be analysed for the mixture in some more depth.

8. To extend the research further, pure Ethylene glycol (mixed with distilled water) is required to eliminate undesirable impurities. Few more binary (preferably polar) mixtures are also required to support the theory. Furthermore, a straight inlet, larger centrifugal pump of wider applicability may be required.

APPENDIX I

CENTRIFUGAL PUMPS DESIGN CONCEPTS

a) Theoretical Head

The theoretical (Euler) energy transfer per unit mass of the flowing liquid is given by the following equation:

$$gH_e = U_2 C_{u2} - U_1 C_{u1} \qquad (I\text{-}1)$$

For the shock-free entrance case ($C_{u1} = 0$), we have;

$$gH_e = U_2 C_{u2} \qquad (I\text{-}2)$$

Using simple trigonemetrical relationships of figure 3.1, we obtain;

$$gH_e = U_2^2 - U_2 C_{m2}/\tan \beta_2 \qquad (I\text{-}3)$$

and

$$\psi_e = 1 - \frac{\phi}{\tan \beta_2} \qquad (I\text{-}4)$$

b) Reaction Effect

Using trigonemetric relationships of figure 3.1, equation (I.1) can be represented as follows [156];

$$gH_e = \frac{U_2^2 - U_1^2}{2} + \frac{W_1^2 - W_2^2}{2} + \frac{C_2^2 - C_1^2}{2} \qquad (I.5)$$

Both terms $\frac{1}{2}(U_2^2 - U_1^2)$ and $\frac{1}{2}(W_1^2 - W_2^2)$ represent static energy gains, whereas the term $\frac{1}{2}(C_2^2 - C_1^2)$ represents the dynamic part of the energy transfer equation. The ratio of the static energy gain to the total energy transfer is termed the reaction effect [41]. For the radial entry case with $C_{u1} = 0$ ($W_1^2 = C_1^2 + U_1^2$), the theoretical reaction effect

will take the form;

$$T_e = \frac{U_2^2 - W_2^2 + C_1^2}{2U_2 C_{u2}} \qquad (I.6)$$

For $C_1 = C_{m1}$ and $C_{m1} \cong C_{m2}$, we obtain;

$$T_e = 1 - \frac{1}{2}\psi_e \qquad (I.7)$$

c) Slip Factor

Due to the presence of a finite number of blades, the whirl component of the absolute discharge velocity C_{u2} is reduced by an amount ΔC_{u2} due to head slip (figure 3.1b). For the radial entry case ($C_{u1} = 0$), we obtain for the input energy;

$$gH_i = U_2 (C_{u2} - \Delta C_{u2}) \qquad (I.8)$$

and;

$$gH_i = U_2 C_{u2} (1 - \frac{\Delta C_{u2}}{C_{u2}}) \qquad (I.9)$$

or;

$$H_i = \sigma H_e \qquad (I.10)$$

whereby;

$$\sigma = 1 - \frac{\Delta C_{u2}}{C_{u2}} \qquad (I.11)$$

According to Stodola [161] and from figure 3.1d, we obtain;

$$\Delta C_{u2} = \frac{1}{2} a \omega \qquad (I.12)$$

Substituting for $a \equiv \pi d_2/z$;

$$\Delta C_{u2} = \frac{\pi \sin \beta_2}{Z} U_2 \qquad (I.13)$$

Dividing both sides of equation (I.13) by U_2 and subtracting from one we get;

$$1 - \frac{\Delta C_{u2}}{C_{u2}} = 1 - \frac{\pi \sin \beta_2}{Z} = \sigma' \qquad (I.14)$$

Note that slip factor σ' is equal to σ for radial blades ($C_{u2} = U_2$).

Pfleiderer [126, 127] introduced another factor to represent the slip phenomenon as follows;

$$CP = \frac{\Delta C_{u2}}{C_{u2}'} = K \frac{r_2^2}{Z M_{st}} \qquad (I.15)$$

M_{st} is the static moment of the central stream line through the impeller passage; for the radial impeller;

$$M_{st} = \int_{r_1}^{r_2} r dr = \frac{1}{2} (r_2^2 - r_1^2) \qquad (I.16)$$

Therefore;

$$CP = \frac{1}{Z} \frac{K}{1 - (r_1/r_2)^2} \qquad (I.17)$$

According to Pfleiderer [126];

$$K = a + b \sin \beta_2 \qquad (I.18)$$

According to Eck [41];

$$K = a + b (\beta_2/90) \qquad (I.19)$$

APPENDIX II

GAS SOLUBILITY OF WATER

a) Oxygen Solubility

According to Henry's Law:

$$P_g = C_s \beta \qquad \text{(II-1)}$$

Whereby C_s is the concentration (mol gas/mol liquid) at saturation and β is the Henry's constant.

At 20°C, for water of low salinity the concentration of O_2 at a standard atmospheric pressure is 9.1 ppm, or

$$C_s(O_2) = \text{ppm } (O_2) \frac{MW\ (H_2O)}{MW\ (O_2)} \times 10^{-6}$$

$$C_s(O_2) = 9.1 \times \frac{18}{32} \times 10^{-6} = 5.12 \times 10^{-6} \text{ (mol } O_2/\text{mol } H_2O).$$

From critical tables [7] the Henry's constant for O_2 at 20°C is 3.043×10^7, hence for the partial pressure;

$$P_g(O_2) = 5.12 \times 10^{-6} \times 3.043 \times 10^7$$

$$\underline{P_g(O_2) = 156 \text{ mm Hg}} \quad \text{(in water)}$$

For dry air at standard pressure of 760 mm Hg, the partial pressure of the oxygen is proportional to its volume or;

$$P_g(O_2) = \frac{V\ (O_2)}{V\ (Air)} \times 760 = 0.2095 \times 760$$

$$\underline{P_g(O_2) = 159 \text{ mm Hg}} \quad \text{(in air)}$$

Hence the oxygen partial pressure above the liquid is equal to that in the liquid (with reasonable accuracy).

b) Air Solubility

Air is a mixture of gases. In a mixture of gases in contact with a liquid, each gas obeying Henry's Law, their solubilities will be proportional to their corresponding partial pressures.

From the definition of the Bunsen absorbsion coefficient α; we get for any gas;

$$\alpha = \frac{v_o}{V} \frac{760}{P_g} \qquad \text{(II-2)}$$

Where v_o is the volume of the dissolved gas reduced to N.T.P. and V is the volume of the liquid. The unit volume of dissolved air will contain a fraction of any one gas [84];

$$u_1 = \frac{\alpha_1 p_1}{\alpha_1 p_1 + \alpha_2 p_2 + \ldots \alpha_n p_n} \qquad \text{(II-3)}$$

Whereby 1, 2, ... n corresponds to the different gases constituting the air.

The Henry's constant for any gas can be found from the critical tables [7]. At 20°C, these constants are;

$$\beta(O_2) = 3.043 \times 10^7$$
$$\beta(N_2) = 5.9 \times 10^7$$
$$\beta(CO_2) = 0.107 \times 10^7$$

From the definition of β, we obtain:

$$\alpha = \frac{17032400\ \rho}{MW\ (\beta - P_g)} \qquad \text{(II-4)}$$

ρ and MW are those of the solvent. After substituting we obtain;

$$\alpha(O_2) = 0.031$$
$$\alpha(N_2) = 0.016$$
$$\alpha(CO_2) = 0.882$$

Substitution in equation (3) for the various gases;

$$u(O_2) = 33.28\%$$
$$u(N_2) = 64.85\%$$
$$u(CO_2) = 1.87\%$$

This shows that the percentage of O_2 in air increases from 20.95% in the gaseous state (standard) to the dissolved state (in water).

As for the concentration of the saturated air in water

$$C_s(\text{Air}) = \frac{\text{Number of moles (air)}}{\text{Number of moles } (H_2O)} = \frac{\text{moles } (O_2)/u(O_2)}{\text{moles } (H_2O)}$$

At 20°C, 9.1 ppm of O_2 concentration is equivalent to

$$\frac{9.1}{32} \times 10^3 = 2.84 \times 10^{-4} \text{ moles } O_2/\text{litre } H_2O$$

and hence

$$C_s(\text{air}) = \left(\frac{2.84 \times 10^{-4}}{0.3328}\right) / \left(\frac{1000}{18}\right)$$

$$C_s(\text{air}) = 15.38 \times 10^{-6} \quad (\text{moles air/moles } H_2O)$$

From critical tables [7], β for air at 20°C is 4.93×10^7, and hence

$$P_g(\text{air}) = 15.38 \times 10^{-6} \times 4.93 \times 10^7$$

$$\underline{P_g(\text{air}) = 758 \text{ mm Hg}}$$

which agrees well with standard atmospheric pressure.

As we have seen, the number of moles (air) in solution was found from;

$$\frac{\text{moles } (O_2)}{u(O_2)} = \frac{2.84 \times 10^{-4}}{0.3328} = 8.53 \times 10^{-4} \quad \text{(moles air/litre } H_2O\text{)}$$

To convert this ratio into ppm basis;

$$\text{ppm (air)} = 8.53 \times 10^{-4} \times 10^{3} \, (MW \times u(O_2) + MW \times u(N_2) + MW \times u(O_2))$$

$$\text{ppm (air)} = 0.853 \, (10.65 + 18.2 + 0.823)$$

$$\underline{\text{ppm (air)} = 25.31} \quad \text{(in water)}$$

For ρ(air) = 1.19 kg/m^3 at 20°C we obtain;

$$25.31 \text{ ppm} = \frac{25.31}{1.19} \times 10^{-3} = 2.1\% \text{ in volume.}$$

APPENDIX III

ACCURACY OF TEST RESULTS

The measurement of any test variables is associated with some errors which can be expressed either as random error or systematic error.

Random errors appear as scatter around the average value of the measured variable. These errors are caused by characteristics of the measuring systems and/or changes in the measured quantity. The standard deviation, SD, of the whole population of measurement is used to characterise errors. A small standard deviation would indicate high precision in the data.

For a small sample, the standard deviation can be estimated according to [99, 132]:

$$\text{Mean value } \bar{x} = \frac{\sum_{n} xi}{n} \qquad \text{(III.1)}$$

and

$$\text{Standard deviation } SD = \sqrt{\frac{\sum_{n} (x_i - \bar{x})^2}{n - 1}} \qquad \text{(III.2)}$$

Systemic errors are characterized by bias and are normally too high or too low with respect to the true value. If the bias can be quantified it may be used as a correction factor which can be applied to all measurements, or minimized by instrument calibration.

When repeat measurements are not available, which is generally the case for pump performance testing, where separate measurements are numerous and time consuming, the uncertainty in the individual reading must be estimated according to the maximum error to be reasonably associated with any measurement. Factors including the resolution, sensitivity and nominal accuracy of the measuring instrument, variation in the controlled input,

variation in the quantity being measured and reading errors should be considered.

In section 2.3, the most important instrument and reading errors for the test rig are listed. The combined effect of these errors on the final estimated performance parameters is discussed separately below.

1. Flow rate: Two turbine flow meters were used to measure the flow downstream the pump discharge. The measurement is displayed digitally in litre per minute with a resolution of 0.1 lit/min. Such instruments have an accuracy of ± 0.5% for 10 - 100% of the flow range for liquid viscosities below 5 cSt. If two meters are used simultaneously, the combined instruments error is ± 0.5% of the combined reading.

Reading errors due to test fluctuations take the maximum value of ± 0.5 litres/min. Hence for two meters operating in parallel,

$$\partial Q = \pm (0.5\% \, Q \pm 0.5) \text{ lit/min}$$

2. Pressure rise : Errors in the static pressure reading can arise from the location and shape of the pressure tapping, the pressure transmitting lines, the inaccuracy of the pressure gauge, and as a result of improper observation [132].

To minimize the partial sensing of any dynamic pressure in the static pressure reading, tappings of 1 mm diameter were used with their contact to the liquid stream being kept both tangential and smooth. Therefore dynamic pressure influence is believed to be only negligible.

Other dynamic influences such as pre-rotation in the suction line or velocity gradient in the test suction such as near an elbow were avoided by placing the tappings in a straight piece of pipe and not too close to the suction cavity of the impeller.

Errors due to the existence of pressure gradient in the lines between the 6-way valve and gauge were minimized by allowing ample time for pressure

equalization between readings. Precautions were always made not to allow for air to be trapped inside these lines.

The accuracy of the precision burdon tube gauge is given by the manufacturer as ± 0.1% of full scale. For a full scale of 7 bars, this accuracy amounts to ± 0.007 bar. A further ± 0.005 bar error is caused by reading and sample discrepancies and therefore a combined error for any single reading is about ± 0.012 bar.

For the pressure differential between pump discharge and inlet, the total error margin is twice that or:

$$\partial \Delta p = \pm 0.024 \text{ bar}$$

3. Pump speed: Speed was measured by an electro-magnetic pick-up in conjunction with a sixty toothed gear wheel on the drive shaft, and digitally displayed on an electronic counter, directly in rpm. Speed control was done through a magnetic coupling which has an accuracy of ± 0.05%.

Test fluctuations on the digital display unit amounts to ± 3 rpm. This error amounts to only ± 0.1% at 3000 rpm shaft speed, but reaches a significant ± 1% at 300 rpm. In general:

$$\partial N = \pm (0.05\% \, N + 3) \text{ rpm}$$

4. Shaft torque: The gross torque absorbed on the rig was measured with a strain gauge transducer, and directly displayed in Nm on a digital indicator reading to 0.01 Nm. An instrumental error of ± 1% over the range of test is given by the manufacturer. Further ± 0.03 Nm error is present which takes into account fluctuations during the test.

A further inaccuracy is the estimation of the pump torque lies in the uncertainty in the value of the parasitic torque absorbed by the shaft bearing. This torque is normally measured by running the rig with the pump

disengaged, and therefore a no-load condition is created [28]. This torque, however may change when load is applied. The random error during parasitic torque measurement is ± 0.02 Nm. Hence:

$$\partial Tp = (1\%\ Tp + 0.05)\ Nm$$

5. Liquid temperature: A five-way temperature recorder with matched thermistor is used to monitor the temperature of the liquid, and display the measurement digitially in degrees Celsius with a resolution of 0.1°C. Two temperature probes are used to measure the temperature near the pump. The first is placed ∿ 50 cm from the suction flange, and the second is some 50 cm downstream the pump discharge.

Instrument error in the range 0° - 150°C is given as ± 1°C. The accuracy of the thermostat is ± 2°C and is therefore not suitable for accurate pump testing. By using a controlled by-pass cooler flow with the reservoir heater continuously switched on an accuracy of ± 0.2°C can be easily maintained. Hence:

$$\partial T = \pm 1.2°C$$

6. Overall pump efficiency: This is normally expressed by the simple formula:

$$\eta = \rho\ g\ Q\ H\ Tp^{-1}\ \omega^{-1} \qquad \text{(III.3)}$$

and therefore errors associated with each of the non-dependent variables are likely to effect the total magnitude of the accuracy in the estimation of η. One way to express the relative error in η is given by [164]:

$$\partial\eta = \pm \sqrt{k\ (\delta\eta_Q^{\,2} + \delta\eta_\omega^{\,2} + \delta\eta_\rho^{\,2}) + \delta\eta_{Tp}^{\,2} + \delta\eta_H^{\,2}} \qquad \text{(III.4)}$$

Whereby K expresses the average value of the test points and is small for a high number of test points and a small standard deviation. Other

factors are those expressing the change in pump efficiency with respect to each individual test parameter.

For a single test point (k = 1), equation (III.4) can be simplied as follows:

$$\frac{\partial \eta}{\eta} = \pm \sqrt{\left(\frac{\partial Q}{Q}\right)^2 + \left(\frac{\partial N}{N}\right)^2 + \left(\frac{\partial \rho}{\rho}\right)^2 + \left(\frac{\partial T_p}{T_p}\right)^2 + \left(\frac{\partial H}{H}\right)^2} \qquad \text{(III.5)}$$

Example: Pump J at 2500 rpm torque-shaft speed (5000 rpm pump speed). Two turbine flow meters at pump discharge. Water at 95°C.

For 2500 rpm; $\partial N/N$ is 0.17% and can be neglected. For 1.2°C temperature error, $\partial \rho/\rho$ is only 0.1% and can also be neglected. Other parameters depend on the flow rate as follows:

Q (lit/min)	η (%)	$\frac{\partial Q}{Q}$ (%)	$\frac{\partial H}{H}$ (%)	$\frac{\partial T_{sg}}{T_{sg}}$ (%)	$\pm \frac{\partial \eta}{\eta}$ (%)	$\pm \partial \eta$ (%)
350	45.3	0.63	1.17	1.51	2.02	0.92
200	47.3	0.75	0.85	1.66	2.01	0.95
80	24.7	1.12	0.77	1.80	2.62	0.65

7. NPSE: The net suction energy is defined by equation (5.1), and according to reference [164], the relative error in measuring the NPSE is expressed by:

$$\partial NPSE = \pm \sqrt{\left(\frac{\partial p_{in}}{\rho}\right)^2 + \left(\frac{\partial p_v}{\rho}\right)^2 + \left(\frac{\partial V_{in}^2}{2}\right)^2} \qquad \text{(III.6)}$$

Inlet pressure reading error is found from 2 above to be ± 0.012 bar. The error in ∂P_v is dependent on the accuracy of the temperature measurement. Since $\partial P_v/\partial T$ rises with temperature, the absolute value for ∂P_v is only important at elevated temperature (above 60°C).

The accuracy of measuring the inlet velocity depends on the accuracy of the measured flow rate Q and the pipe section area.

Example: Pump J running with water at 95°C and Q_{cav} = 280 l/min, $NPSE_{05}$ = 39.0 m^2/sec^2.

$$\partial T = 1.2°C \rightarrow \partial p_v = 0.03 \text{ bar}$$
$$\partial Q = 1.9 \text{ l/min} \rightarrow \partial V_{in} = 0.024 \text{ m/sec}$$

$$\partial NPSE = \pm \sqrt{\left(\frac{0.012 \times 10^5}{962}\right)^2 + \left(\frac{0.03 \times 10^5}{962}\right)^2 + \left(\frac{0.024^2}{2}\right)^2}$$

$$\partial NPSE = \pm 3.4 \ m^2/sec^2$$

$$\frac{\partial NPSE}{NPSE_{05}} = 8.6\%$$

The gas solubility of the liquid has been assumed to be negligible influence in equation (III.6). If this is not the case, then a systematic error must be included to take into account the gas content effect. If the gas solubility can be measured, a correction to the required NPSE over that of the gas free liquid can be applied depending on the type of liquid and percentage saturation.

High combined errors in the estimation of $NPSE_{05}$ make the estimation of ΔE_v according to equation (8.1) highly risky. However it is believed that the instrumental errors of both differential pressure and fluid temperature cancel out since these errors are expected to have similar signs when estimating ΔE_v. Hence only reading errors are important here, which are normally kept small.

APPENDIX IV

PROGRAMME FOR PUMP PERFORMANCE ESTIMATION

1. Input Test Constants (data file)

Pump inlet pipe diameter	d_{in}	(m)
Impeller inlet diameter (tip)	d_1	(m)
Impeller exit diameter	d_2	(m)
Discharge angle	β_2	(°)
Percentage glycol in mixture	EG	(% volume)
Bulk liquid temperature	T	(°C)
Pump speed	N	(rpm)

2. Input Test Results (data file)

Input matrix with R = number of rows and M = number of columns.

Flow meter No. 1	Q_1	(lit/min)
Flow meter No. 2	Q_2	(lit/min)
Strain gauge torque	T_{sg}	(Nm)
Inlet pressure	p_{in}	(bar, abs)
Outlet pressure	p_{out}	(bar, abs)

3. Input Fluid Properties (20 - 120°C) (sub-routine)

Liquid density	ρ	(f(EG,T))	Ref. 6	(kg/m^3)
Liquid viscosity	μ	(f(EG,T))	Ref. 6	(cP)
Vapour pressure	p_v	(f(EG,T))	Ref. 37	(bar, abs)

4. Estimation of Dimensional Parameters

Total flow rate	$Q = (Q_1 + Q_2)/60 \times 1000$	(m^3/sec)
Pressure rise	$\Delta p = (p_{out} - p_{in})\ 10^5$	(N/m^2)
Generated head	$H = \Delta p/\rho g$	(m)
Pump torque	$T_p = \frac{1}{2}\ [T_{sg} - ((N - 2000)/5000)]$	(Nm)
Rotational velocity	$\omega = 2\pi N/60$	(1/sec)
Input power	$P_s = \omega\ T_p$	(watt)
Kineamtic viscosity	$\nu = \mu/1000\ \rho$	(cSt)
Inlet velocity	$V_{in} = Q/(\frac{\pi d_{in}^2}{4})$	(m/sec)
Relative velocity	$W \cong Q/0.8\ \pi d_2\ b_2\ \sin\beta_2$	(m/sec)
NPSE	$= (\frac{P_{in}}{\rho})\ 10^5 + \frac{V_{in}^2}{2} - (\frac{p_v}{\rho})\ 10^5$	(m^2/sec^2)
Inlet peripheral velocity	$U_1 = \omega \frac{d_1}{2}$	(m/sec)

5. Estimation of Non-Dimensional Parameters

Pump overall efficiency	$\eta = \Delta p\ Q/P_s$
Flow coefficient (ext.)	$\phi_p = Q/\omega d_2^3$
Head coefficient (ext.)	$\psi_p = gH/\omega^2 d_2^2$
Power coefficient (ext.)	$\lambda_p = P_s/\rho\omega^3 d_2^5$
Specific speed	$n_s = \omega\ Q^{\frac{1}{2}}/(gH)^{0.75}$
Free stream Re number	$Re = W\ \ell/\nu$
Cavitation number	$\sigma = NPSE/\frac{1}{2}\ V_{in}^2$
Thoma sigma	$\sigma_{TH} = NPSE/gH$

Inlet cavitation number	σ_{u1}	$= NPSE/\frac{1}{2} U_1^2$
Suction specific speed	n_{ss}	$= \omega Q^{\frac{1}{2}}/(NPSE)^{0.75}$
Head ratio	HR	$= H_{cav}/H_{nc}$
Flow ratio	FR	$= Q_{cav}/Q_{nc}$

6. Curve Plotting (X-Y digi-plot)

Non-cavitating flow:

X-plane	Flow rate	Q
Y-plane	Generated Head	H, input power P_s, and overall efficiency η.

Cavitating flow (constant Q_{cav})

X-plane	cavitation number σ	
Y-plane	Head ratio	HR and suction specific speed n_{ss}

Cavitating flow (variable flow-constant system)

X-plane	NPSE	
Y-plane	Head ratio	HR, Flow rate FR, and suction specific speed n_{ss}.

Example: Pump J, semi-open impeller J-6-50, single entry and discharge pipes.

d_{in}	=	0.042	(m)
d_1	=	0.0565	(m)
d_2	=	0.09	(m)
EG	=	50	(%)
T	=	90	(°C)
N	=	4000	(rpm)
Q	=	240	(lit/min) constant
ρ	=	1033	(kg/m^3)
μ	=	0.85	(cP)
p_v	=	0.535	(bar, abs)

ω	=	418.9	(1/sec)
ν	=	0.823	(cSt)
V_{in}	=	2.89	(m/sec)
W	=	2.00	(m/sec)
U_1	=	11.9	(m/sec)

Non-cavitation parameters ($Q = Q_{opt}$)

T_{sg}	=	5.52	(Nm)
p_{in}	=	1.43	(bar, abs)
p_{out}	=	2.96	(bar, abs)
Δp	=	$(1.53)\ 10^5$	(N/m^2)
H_{nc}	=	15.1	(m)
P_s	=	1150	(Watt)
η	=	53.4	(%)
Re	=	0.88×10^5	(non-dim.)
n_s	=	0.624	(non-dim.)

Cavitating flow parameters (∿ 3% head drop) $\frac{Q_{cav}}{Q_{opt}} = 1.0$

T_{sg}	=	5.52	(Nm)
p_{in}	=	0.78	(bar, abs)
p_{out}	=	2.26	(bar, abs)
Δp	=	$(1.48)\ 10^5$	(N/m^2)
H_{cav}	=	14.6	(m)
P_s	=	1150	(Watt)
η_{cav}	=	51.8	(%)
NPSE	=	27.9	(J/kg)
σ_{03}	=	6.65	(non-dim.)
σ_{TH}	=	0.195	(non-dim.)
σ_{ul}	=	0.099	(non-dim.)
n_{ss}	=	2.19	(non-dim.)
H_{cav}/H_{nc}	=	0.967	(non-dim.)

APPENDIX V

PROGRAMME FOR LOSS ANALYSIS

1. Input Test Constants (data file)

Pump inlet pipe diameter	d_{in}	(m)
Impeller inlet diameter (tip)	d_1	(m)
Impeller exit diameter	d_2	(m)
Percentage glycol in mixture	EG	(%)
Bulk liquid temperature	T	(°C)
Pump speed	N	(rpm)
Number of impeller blades	z	
Blade thickness	t	(m)
Impeller inlet channel depth	b_1	(m)
Impeller exit channel depth	b_2	(m)
Axial tip clearance	Δx	(m)
Impeller exit angle	β_2	(°)
Best efficiency flow	Q_{opt}	(l/min)
Best efficiency head	H_{opt}	(m)
Mechanical power losses	P_{sb}	(watt)
Disc clearance	e	(m)
Length of neck ring gap (equivalent)	L	(m)
Thickness of neck ring gap (equivalent)	s	(m)
Leakage factor for semi-open impeller	α	

2. Input Test Results (data file)

Input matrix with R = number of rows and M = number of columns

Flow meter No. 1	Q_1	(lit/min)
Flow meter No. 2	Q_2	(lit/min)
Strain gauge torque	T_{sg}	(Nm)
Inlet pressure	p_{in}	(bar. abs)
Outlet pressure	p_{out}	(bar, abs)

3. Input Fluid Properties (20 - 120°C) (sub-routine)

Liquid density	ρ (f(EG,T))	Ref. 6	(kg/m^3)
Liquid viscosity	μ (f(EG,T))	Ref. 6	(cP)

4. Estimation of Pump Performance Parameters

Test flow rate	$Q = (Q_1 + Q_2)/60 \times 1000$	(m^3/sec)
Developed head	$H = (p_{out} - p_{in})\ 10^5/\rho g$	(m)
Rotational velocity	$\omega = 2\pi N/60$	(1/sec)
Input power	$P_s = \frac{1}{2}\ \omega\ [T_{sg} - (\frac{N}{2000}/5000)]$	(watt)
Overall efficiency	$\eta = (\rho g H Q/P_s)$	

5. Estimation of Design Parameters for the Closed Impeller

Inlet peripheral velocity	$U_1 = \omega\ d_1/2$	(m/sec)
Exit peripheral velocity	$U_2 = \omega\ d_2/2$	(m/sec)
Leakage head	$H_L = 0.75\ (U_2^2 - U_1^2)/2g$	(m)
Leakage area	$A_L = \pi\ d_1 s$	(m^2)
Discharge constant	$C_d = (0.08\ L\ /2s)^{-\frac{1}{2}}$	
Leakage flow	$Q_L = C_d A_L\ (2gH_L)^{\frac{1}{2}}$	(m^2/sec)
Slip limit (Wiesner)	$\xi = 1/\ln^{-1}\ (\frac{8.16\ \sin\beta_2}{2})$	
Slip factor	$\sigma' = 1 - \frac{\sin\beta_2}{Z^{0.7}}\ [1 - (\frac{r_1/r_2 - \xi}{1 - \xi})^2]$	
Input flow rate	$Q_i = Q + Q_L$	(m^3/sec)
Impeller exit area	$A_2 = b_2\ (\pi d_2 - zt/\sin\beta_2)$	(m^2)
Exit meridi velocity	$C_{m2} = Q_i/A_2$	(m/sec)
Exit relative velocity	$W_2 = C_{m2}/\sin\beta_2$	(m/sec)
Exit abs. velocity	$C_2 = [C_{m2}^2 + (U_2 - \frac{C_{m2}}{\tan\beta_2})^2]^{\frac{1}{2}}$	(m/sec)
Flow coefficient	$\phi = C_{m2}/U_2$	
coefficient	$\psi = gH/U_2^2$	

Theoretical head $H_e = \frac{1}{g}\left[U_2^2 - \frac{U_2\, C_{m2}}{\tan\beta_2}\right]$ (m)

Input head $H_i = \sigma' \frac{U_2^2}{g} - \frac{U_2\, C_{m2}}{g \tan\beta_2}$ (m)

Input head coefficient $\psi_i = gH_i/U_2^2$

Reaction effect $\Upsilon_i = 1 - \frac{1}{2}\psi_i$

6. Correction for the Semi-Open Impeller

Tip clearance ratio $\lambda = \Delta x / \frac{1}{2}(b_1 + b_2)$

Leakage flow $Q_L = \alpha\lambda\, Q_{opt}/(1 - \alpha\lambda)$ (m^2/sec)

Head loss factor $\beta \cong 4\alpha/3$

Head loss (clearance) $\Delta H = \beta\lambda\, H_{opt}/(1 - \beta\lambda)$ (m)

Input head $H_i = \sigma' \frac{U_2^2}{g} - \frac{U_2\, C_{m2}}{g \tan\beta_2} - \Delta H$ (m)

7. Estimation of the Various Power Scale Losses

Kinematic viscosity $\nu = \mu/1000 \times \rho$ (m^2/sec)

Rotational Re number $Re_\omega = U_2 \left(\frac{d_2}{2}\right)^2/\nu$

Disc friction power losses:

Closed impeller: $P_d(cl) = 7.3 \times 10^{-4} \left(\frac{10^6}{Re_\omega}\right)^{1/6} \rho\, U_2^3\, d_2^2 \left(\frac{d_2 + 5e}{d_2}\right)$ (watt)

Semi-open impeller $P_d = \frac{1}{2} P_d(cl)$ (watt)

External (mehcanical) Power loss $P_m = P_{bs} + P_d$ (watt)

Mechanical scale loss $\delta_m = (P_{bs} + P_d)/P_s$

Volumetric power losses $P_v = \rho g\, Q_L\, H_i$ (watt)

Volumetric scale loss	$\delta_v = P_v/P_s$
Hydraulic power losses	$P_h = \rho g\, Q(H_i - H)$
Hydraulic scale loss	$\delta_h = P_h/P_s$
Predicted total scale losses	$\delta_{pred} = \delta_m + \delta_h + \delta_v$
Recirculation scale loss	$\delta_{rec} = \delta - \delta_{pred}$

Example: Pump H, semi-open impeller H-8-90

d_{in}	$= 24.0 \times 10^{-3}$	(m)
d_1	$= 41.2 \times 10^{-3}$	(m)
d_2	$= 56.6 \times 10^{-3}$	(m)
EG	= 50	(%)
T	= 95	(°C)
N	= 6000	(rpm)
z	= 8	
t	$= 4 \times 10^{-3}$	(m)
b_1	$= 12 \times 10^{-3}$	(m)
b_2	$= 9 \times 10^{-3}$	(m)
Δx	$= 0.75 \times 10^{-3}$	(m)
β_2	= 90	(°)
Q_{opt}	= 100	(lit/min)
H_{opt}	= 5.5	(m)
P_{sb}	= 80	(watt)
e	$= 3 \times 10^{-3}$	(m)
α	= 1	
ρ	= 1030	(kg/m^3)
μ	= 0.77	(cP)
Q	= 105/60 x 1000	(m^3/sec)
H	= 5.6	(m)
ω	= 628.3	(1/sec)
P_s	= 493	(watt)
η	= 20.3	(%)

Design parameters

U_2	=	17.8	(m/sec)
λ	=	0.071	
Q_L	=	7.7/60 x 1000	(m^3/sec)
σ'	=	0.62	
β	=	1.33	
ΔH	=	0.56	(m)
Q_i	=	112.7/60 x 1000	(m^3/sec)
A_2	=	1.31×10^{-3}	(m^2)
C_{m2}	=	1.4	(m/sec)
W_2	=	1.4	(m/sec)
C_2	=	17.8	(m)
ϕ	=	0.081	
ψ	=	0.175	
H_e	=	32.2	(m)
H_i	=	19.4	(m)
ψ_i	=	0.597	
T_i	=	0.7	

Scale losses

ν	=	0.748×10^{-6}	(m^2/sec)
Re_ω	=	0.673×10^{-6}	
P_d	=	16.8	(watt)
P_m	=	96.8	(watt)
δ_m	=	0.196	
δ_v	=	0.051	
δ_h	=	0.496	
δ	=	0.797	
δ_{pred}	=	0.743	
δ_{rec}	=	0.054	

APPENDIX VI

PROGRAMME FOR ESTIMATING THE B-FACTOR FOR BINARY MIXTURES

1. Input Liquid Properties

Bulk temperature	T	(°K)
Glycol concentration in the mixture	EG	(% weight)
Saturation vapour density	ρ_v	(kg/m^3)
Saturation liquid density	ρ_ℓ	(kg/m^3)
Specific heat of the liquid	$C_{p\ell}$	(J/g °K)
Equilibrium vapour pressure	p_v	(bar, abs)
Molar fraction glycol in mixture	X	
Latent heat of vapourization (EG)	L_{EG}	(J/g)
Latent heat of vapourization (H_2O)	L_{H_2O}	(J/g)
Thermal cooling	ΔE_v	(J/kg)
Saturation curve slope	dp_v/dT	(bar/°K)

ρ_ℓ from fig. 9.1, $C_{p\ell}$ from fig. 9.2, p_v from fig. 9.1 and 8.2, X from fig. 9.4, L_{EG} and L_{H2O} from fig. 9.5, dp_v/dT from fig. 8.1.

2. Estimation of Mixture Properties

$(\rho_v)_{water}$ corrected for local pressure $= (\rho_v)_{water} \times \dfrac{(p_v)_{EG/W}}{(p_v)_{H_2O}}$ $\left(\frac{kg}{m^3}\right)$

$(\rho_v)_{Clapeyron}$ $\rho_v = \dfrac{T}{L_{mix}} \dfrac{dp_v}{dT}$ $\left(\frac{kg}{m^3}\right)$

$L_{mix} = X\, L_{EG} + (1 - X)\, L_{H_2O}$ (J/g)

Growth restraint factor $\psi_{mix} = \dfrac{C_{p\ell}\ \rho_\ell}{L_{mix}\ \rho_v}\ \tau$

τ found from figures 9.14 and 9.15 (ref. 15 and 150).

Correction for growth restraint:

$$\beta_{mix} = \psi_{mix}\ \beta$$

$$B_{mix} = \Delta E_v\ \beta_{mix}$$

Correction for growth restraint and nuclei number:

$$\beta_{mix}' = C_{mix}\ \beta$$

$$B_{mix}' = \Delta E_v\ \beta_{mix}'$$

where $C_{mix} = \psi_{mix}^{\ n}$ $(n > 1)$

Example: Pump J, semi-open impeller J-6-50, 4000 rpm, 240 l/min, single entry and discharge, gas content ∿ 25% sat., 10% head drop.

T	$= 90$	(°C)
EG	$= 52$	(% weight)
$(\rho_v)_{clap.}$	$= 0.383$	(kg/m^3)
ρ_ℓ	$= 1020$	(kg/m^3)
$C_{p\ell}$	$= 0.87 \times 4.187$	(J/g °K)
p_v	$= 0.54$	(bar, abs)
X	$= 0.23$	
L_{EG}	$= 245 \times 4.187$	(J/g)
L_{H_2O}	$= 545 \times 4.187$	(J/g)
L_{mix}	$= 476 \times 4.187$	(J/g)
ΔE_v	$= 1.7$	(J/kg)
β	$= 2.65$	
B	$= 3.5$	
ψ_{mix}	$= 1.46$	
β_{mix}	$= 4.0$	
B_{mix}	$= 6.8$	
β_{mix}'	$= 5.7$ for $C_{mix} = \psi_{mix}^{\ 2}$	
B_{mix}'	$= 9.6$	

Comparison of 2 Methods to Estimate B

ΔE_v^* - based on L and ρ_v of water corrected for the local pressure of the liquid.

ΔE_v^{**} - based on L_{mix} according to equation 9.2 and ρ_v from the Clapeyron equation.

B = 4
90°C

% EG	ΔE_v^*	ΔE_v^{**} (J/kg)
10	2.45	2.50
20	2.29	2.31
30	2.21	2.15
40	1.89	1.83
50	1.62	1.69

REFERENCES

1. Altenburg, K. "Die Temperatur abhängigkeit der Ultraschal-geschwindigkeit und der oberflächenspannung des Äthylenglycols". Z.f. phys. Chem. 201, Nov. 1952, pp. 901-6 (In German).

2. Anderson, H.H. "Centrifugal pumps", Trade and Technical Press Ltd., First Edition, England 1962.

3. Anon. "ASTM Annual Book of Standards Part 30-Coolants", 1978, American Society of Testing and Materials, Philadelphia.

4. Anon. BSS 3150/1/2 "Corrosion inhibited Ethandiol Anti-freeze for water glycol engines 1959".

5. Anon. Beckman's instruction manual for dissolved O_2 monitor Model 715.

6. Anon. "Glycols", Pub. Union Carbide Co., New York, 1968.

7. Anon. "International Critical Tables", McGraw Hill 1928, Vol III, p. 254.

8. Arndt, R.A. "Cavitation in fluid machinery and hydraulic structures", Ann. Rev. Fluid Mech. 1981, Vol. 13, pp. 273-328.

9. Bailey, A.B. and Wykes, M.E.P. "Thermodynamic Aspects of Cavitation: A research project", Conference on Cavitation, Edinburgh, 3-5 Sept. 1974. Pub. J. Mech. E., London.

10. Baldwin, R.R. and Daniel, S.G. "A method for the determination of the solubility of gases in liquids with particular reference to viscous liquids". J. App. Chem 2, April 1952, pp. 161-165.

11. Balje, O.E. "A study on design criteria and matching of turbo machines: Part B - Comp. and pump performance and matching of turbo components", Trans ASME J. Eng'g f. Power 84, Jan. 1962, pp. 103-114.

12. Balje, O.E. "Turbo machines", John Wiley & Sons Inc. USA, 1981.

13. Barenboin, A.B. "Conditions for modelling cavitation phenomena in pumps for refrigeration liquids", BHRA Trans. No. T865, Oct. 1966 (Russian original 1965).

14. Battino, R. "The solubility of gases in liquids", Chemical Review, Vol. 66, pp. 395-463, 1966.

15. Benjamin, J.E. and Westwater, J.W. "Bubble growth in nucleate boiling of a binary mixture". International Developments in heat transfer. Proc. 1961, Int. Conf. Bouder.

16. Billet, M.L. "Secondary flow generated vortex cavitation", Naval Hydrodyn. Symp. 12th, Washington, 1978.

17. Billet, M.L. and Gates, E.M. "A comparison of two optical techniques for measuring cavitation nuclei". Trans ASME, J. Fluid Eng'g, Vol. 103, March 1981, pp. 8-13.

18. Billet, M.L. and Holl, J.W., "Scale effects on various types of limited cavitation", Trans ASME, J. Fluid Eng'g, Vol. 103, Sept. 1981, pp. 405-414.

19. Billet, M.L. et al. "Correlation of thermodynamic effect for developed cavitation", Trans ASME, J. Fluid Eng'g, Vol. 103, December 1981, pp. 534-542.

20. Bonnel, W.S. et al. "Surface tension of Ethyl-Alcohol-water mixture", Ind. & Eng. Chem. Vol. 32, No. 4, April 1940.

21. Bonnin, J. "Incipient cavitation in liquids other than cold water", 1971 Cavitation Forum, Fluid Engineering Conference 10-12 May, 1971, Pittsburg, Pennsylvania.

22. Bonnin, J. "Theoretical and experimental investigations of incipient cavitation in different liquids". ASME Publication No. 72-WA/FE-31, 1972.

23. Bonnin, J. "Thermodynamic effect in cavitation", Conference on cavitation, Edinburgh 3-5 Sept. 1974, Pub. Inst. of Mech. Engrs'. 1976, London.

24. Booth, T.C. et al. "Rotor-tip leakage, Part 1 - Basic methodology", Trans ASME, Vol. 104, Jan. 1982, J. Eng'g for Power.

25. Brujin, P.J. "On the assymptotic growth of vapour bubbles in superheated binary liquid mixtures", Physica, Vol. 26, 1960, pp. 326-334.

26. Busemann, A. "Das Förder-höhen Verhältnis radialer Kreiselpumpen mit logaritmisch-spiraligen Schaufeln", Z. angew. Math. Mech, Vol. 8, p. 372, 1928 (In German).

27. Butterworth, D. "Unresolved problems in heat exchanger design", Interflow 80: Proc. Symp. on fluid handling (1980), I. Chem. E. Symp. Series No. 60, pp. 231-248.

28. Chalaby, A.A. and Thew, M.T. "Rig for small pump performance testing, description and test procedure", University of Southampton, Dept. of Mech. Eng'g. Report No. ME/80/25, Nov. 1980.

29. Chalaby, A.A. "Performance of small centrifugal pumps with mixed liquids", University of Southampton, Dept. of Mech. Eng'g interim report No. ME/81/20, December 1981.

30. Chalaby, A.A. and Thew, M. T. "Cavitation in a small pump: Effect of some variation in impeller geometry and comparison of water with water-Antifreeze mixture", IAHR Symposium, Operating problems of pump sections and power plants, Amsterdam, 1982.

31. Chalaby, A.A. and Thew, M.T. "Cavitation in a binary mixture of polar liquid (water-antifreeze) in a small centrifugal pump", Paper to be read at the I. Mech. Eng. 2nd Conference on Cavitation, Edinburgh, Sept. 1983.

32. Chivers, T.C. "The effect of air content on advanced cavitation", The Engineer, 16 August 1980.

33. Chivers, T.C. "Temp. effects on cavitation in a centrifugal pump, theory and experiment", Proc. Inst. Mech. Engrs. Vol. 184, Part 1, No. 1, pp. 37-47, 1969/1970.

34. Chivers, T.C. "The correlation of cavitating performance for a centrifugal pump handling various liquids", Proc. Inst. Mech. Engrs. Vol. 184, Part 1, No. 2, pp. 48-64, 1969/1970.

35. Clark, Jr. J.B. "Cavitation-erosion damage control in aluminium water pumps for cars", SAE paper No. 680498 May 1968.

36. Cordier, O. "Similitude parameter for flow machines", Brenn staffe Warme-Kraft 5(10), pp. 337-340, Okt 1953 (In German). Trans. S. Merry Ed. M.T. Thew, Report ME/76/24, Southampton University (1976).

37. Curme, G.O. and Johnson, F. "Glycols", Reinhold Pub. Corporation, A.S.C. Monograph Series 1953.

38. Daily, J.W. "Hydraulic Machinery", Ch. 13 in 'Engineering Hydraulics', Ed. H. Rouse, Pub. Wiley, New York, 1950.

39. Daily, J.W. and Johnson, V.E. "Turbulance and boundary layer effect on cavitation inception from nuclei", Trans. ASME, Vol. 78, p. 1695, 1956.

40. Douglas, J.F. et al. "Fluid mechanics", Pitman Pub. Ltd., First Edition, London 1979.

41. Eck, B. "Fans", Pergamon Press, 1973.

42. Elmieh, F. "Car cooling systems and their pumps", M. Phil. thesis, 1975, University of Southampton, Mech. Eng. Dept.

43. Elmieh, F. and Thew, M.T. "Performance of automotive liquid coolant pumps", Intern. Conf. on pumps and turbines, NEL 1976.

44. Epstein, P.S. and Plesset, M.S. "On the stability of gas bubbles in liquid gas solution", The J. of Chem. Phys. Vol. 18, No. 11, pp. 1505-1509, Nov. 1950.

45. Fay, A. "On the high accuracy scaling-up for pumps and turbines", Int. Conf. on pumps and turbines, (Vol. I) NEL East Kilbridge, 1-3 Sept., 1976 (Paper 2-5).

46. Florjancic, D. "Experimentelle Untersuchungen an einer pumpe zur Feststellung der Änderung der Saugfähigkeit durch Oberflachenrauhigkeit, durch Michvorgänge auf Laufradeintrit und durch Heisswasserförderung", Thesis (in German), ETH Zurich No. 4406.

47. Florjancic, D. "Influence of water temperature on the suction capacity of centrifugal pumps", Sulzer Tech. Review, pp. 25-34, 1971.

48. Florshütz, L.W. "On the mechanics of vapour bubble collapse", Trans. ASME, J. Heat Transfer, May 1965, pp. 209-220.

49. Frank, F. "Water, a comprehensive treatise", Vol. 2, Plenum Press, New York, 1973.

50. Fujie, K. "Three dimensional investigation of flow in centrifugal impeller with straight-radial blades", JSME, Vol. 1, No. 1, 1958.

51. Furness, R.A. "Basic cavitation studies in a convergent/divergent nozzle", Ph.D. Thesis, University of Southampton 1973.

52. Gambil, W.R. and Bundy, R.D. "High flux heat transfer characteristics of pure ethylene glycol in axial and swirl flow", A.I. Ch. E., Vol. 9, No. 1, pp. 55-59, Jan. 1963.

53. Garcia, R. and Hammitt, F.G. "Cavitation damage and correlation with material and fluid properties", Trans. ASME J. Basic Eng'g Series D, Vol. 89, pp. 753-763, Dec. 1967.

54. Gjaldback, J. Chr. and Niemann, H. "The solubility of nitrogen, argon and ethan in alcohols and water", Acta. Chemica. Scand. 12 (1958), No. 5, pp. 1015-1023.

55. Grein, H. "Cavitation", Van Karman Institute for Fluid Dyn., Lecture Series 61, Recent progress in pump research", Vol. 1, December 1973.

56. Gülich, J. "Similarity characteristics for the suction capacity and bubble propagation of pumps", Sulzer Tech. Review, Feb. 1980.

57. Hadji-Sheikh, M. "The performance of water pumps for automotive cooling systems", M. Phil Thesis, University of Southampton 1977.

58. Hammitt, F.G. "Observation of cavitation scale and thermodynamic effect in stationary and thermodynamic components", Trans. ASME (D) 85, pp. 1-16, 1963.

59. Hammitt, F.G. et al. "Gas content, size, temperature and velocity effect on cavitation inception in a venturi", ASME paper 67-WA/FE-22, 1968.

60. Hammitt, F.G. "Cavitation and multi-phase flow phenomena", McGraw-Hill, USA, 1980.

61. Hicks, T.G. "Pump application engineering", McGraw-Hill, 1971.

62. Hitchman, M.L. "Measurement of dissolved oxygen", John Wiley & Sons, New York, 1978.

63. Holl, J.W. and Wislicenus, G.F. "Scale effect of cavitation", J. Basic Eng'g Trans. ASME, Vol. 83, 1961, p. 385.

64. Holl, J.W. "Limited cavitation", Cavitation state of knowledge, ASME, New York, 1969. Editors, J.M. Robertson and G.F. Wislecenus.

65. Holl, J.W. and Kornhauser, A.L. "Thermodynamic effect on disinent cavitation on hemispherical nosed bodies in water at temperature from 80 to 260°F", Trans. ASME J. Basic Eng'g, March 1970, pp. 44-58.

66. Holl, J.W. "Nuclei and Cavitation", ASME paper No. 70-FE-23, 1971, ASME publications.

67. Holl, J.W. et al. "Limited cavitation and the related scale effects problems", 2nd Int. JSME Symposium of Fluid Machinery and Fluidics, Tokyo, Sep. 1972.

68. Holl, J.W. et al. "Thermodynamic effects on developed cavitation", Trans. ASME, Vol. 97, J. Fluid Eng'g, Dec. 1975, pp. 507-514.

69. Hord, J. and Voth, R.D. "Tabulated values of cavitation β-factor for Helium, H_2, N_2, F_2, O_2, Refrigerant 114 and water", National Bureau of Standards, USA, Tech. Note. 397, Feb. 1971.

70. Howard, J.H. and Kittmer, C.W. "Measured passage velocities in a radial impeller with shrouded and unshrouded configuration", J. Eng. Power, Trans. ASME, April 1975, pp. 207-213.

71. Hsieh, Din-Yu. "Some analytical aspects of bubble dynamics", Trans. ASME, J. Basic Eng'g, 87, Dec. 1965, pp. 991-1005.

72. Hutton, S.P. "Component losses in Kaplan turbines and the prediction of efficiency from model tests", Proc. Instn. Mech. Engrs. 1954, 168(28), pp. 743-762.

73. Hutton, S.P. and Chivers, T.C. "Cavitation scale effects in pumps", Schweiz. Bauzeitung, 89 Jhg. H12, März 1971.

74. Hutton, S.P. and Fay, A. "Analysis of efficiency scale up for hydraulic machines". Water Power 1974 26(6), p.205.

75. Hutton, S.P. and Furness, R.A. "Thermodynamic scale effects in cavitating flows and pumps", Conf. on Cavitation, Edinburgh, 3-5 Sep. 1974, Pub. Inst. Mech Engr's, London 1976.

76 Irving, J.B. and Jamieson, D.T. "Thermal conductivity of binary liquid mixtures", NEL Report No. 567, Dept. of Industry, July 1964.

77. Ishida, M. and Senoo, Y. "On the pressure losses due to the tip clearance of centrifugal blowers", Trans ASME, J. Fluid Eng'g, Vol. 103, April 1981, pp. 271-278.

78. Iverson, H.W. "Volute pressure distribution", J. Eng. Power, April 1960, p. 137.

79. Jacobs, R.B. et al. "Direct measurement of NPSH", J. Basic Eng'g, Series D, Vol. 81, June 1959, pp. 147-152.

80. Jacobs, R.B. "Predictions of symptoms of cavitation", J. of Research NBS, Vol. 65, Series C, No. 3, 1961, p. 147.

81. Jacobson, J.K. "On the mechanism of head breakdown in cavitating inducers", Trans. ASME, J. Basic Eng. June 1964, p. 291.

82. Janigro, A. and Schiavello, B. "Pre-rotation in centrifugal pumps - design criteria", Van Karman Inst. Lecture Series, 1978 - 3(1).

83. Kamiyama, Sh. "One predicting method of gaseous cavitation occurrence in water and Na", Bull. JSME, Vol. 23, No. 183. Sept. 1980, pp. 1428-1434.

84. Kanellopolous, E.V. "New method for measuring the gas content of water", M.E.R.L. Fluids Report No. 69. East Kilbride, Glasgow, 1958.

85. Kannellopulous, E.V. "Cavitation tests on a small centrifugal pump", NEL Report No. 95, 1960.

86. Kannellopulous, E.V. and Pierie, D.A. "The effect of temperature and blade number on cavitation cessation in a small centrifugal pump", NEL Report No. 166, 1964.

87. Kassai, T. and Takamatu, Y. "Flow in radial impeller with cavitation", Bull. JSME, Vol. 7, No. 27, 1964.

88. Keenan, J.H. et al. "Steam Tables", John Wiley & Sons Inc., 2nd ed. 1978.

89. Kleinert, H. et al. "Experimental and theoretical investigation of the flow in radial impeller of centrifugal pumps at cavitation", Proc. of the 6th Conf. on fluid mech. Vol. 1, Budapest, 1979.

90. Knapp, R.T., Daily, J.W. and Hammitt, F.G. "Cavitation", McGraw-Hill Pub. Monographs Eng. Soc., 1970.

91. Kretschmer, C.B. et al. "Solubility of oxygen and nitrogen in organic solvents from -25° to 50°C", Ind. and Eng'g Chem. Vol. 38, No. 5, May 1946.

92. Lazarkiewicz, S. and Troskolanski, A.T. "Impeller pump", Pergamon Press, 1965.

93. Lobanof, V. "Designing the modern centrifugal pump", Pipe Line Industry, Vol. 6, pp. 36-40, 1957.

94. Mansel, C.J. "Impeller cavitation damage on a pump operating below its rated discharge", Conference on cavitation, Sept. 1974. Pub. Inst. Mech. Engrs. 1976.

95. Matsushimura, A. "Guide to automotive water pump seals", SAE Prepr. 780404 for meeting Feb. 27 - March 3, 1978.

96. Mayer, E. "Mechanical seals", Pub. Butterworth & Co. (Publishers) Ltd., 1972.

97. McNulty, P.J. and Pearsall, I.S. "Cavitation inception in pumps", J. Fluid Eng'g, March 1982, Vol. 104, pp. 99-104.

98. Mercer, A.D. "Laboratory research in the development and testing of inhibited coolant, in boiling heat transfer conditions". ASTM Special Publication 705, Ed. W.H. Ailer, pp 53-80, 1980.

99. Merry, S.L. "Scaling and performance comparison of a centrifugal pump with hydrodynamic disc seals running in water and mercury", Ph.D. Thesis, University of Southampton, 1982.

100. Miller, S.A. "Ethylene and its industrial derivatives", Pub. Ernest Benn Limited, London 1969.

101. Minami, S. et al. "Experimental study of cavitation in centrifugal pump impeller", Bull. JSME, Vol. 3, No. 9, 1960.

102. Moor, R.D. "Prediction of pump cavitation performance", Symposium at the Pennsylvania State University, August 31 - September 3, NASA Publication SP-304, 1970.

103. Moor, T. "Literature review on the effect of viscosity on the performance of centrifugal pumps", BHRA Report TN 1530, March 1979.

104. Morgan, Wm. B. "Air content and nuclei measurement", Intern. Towing Tank Conf. 13th (1972), USA, Rep. of cavitation Comm.

105. Murakami, M. and Heya, N. "Swirling flow in suction pipe of centrifugal pumps", Bull. JSME, Vol. 9, No. 34, 1966.

106. Murakami, M. and Minemura, K. "Effects of running clearance of semi-open impeller pumps under air admitting conditions". Bull. JSME, Vol. 19, No. 136, Oct. 1976, pp. 1141-1148.

107. Murakami, M. "Effect of entrained air on the performance of centrifugal pump under cavitation". Bull. JSME, Vol. 23, No. 183, Sept. 1980, pp. 1435-1442.

108. Murakami, M. et al. "Velocity and pressure distribution in the impeller passages of centrifugal pumps". Trans ASME, J. Fluid Eng'g, Vol. 102, Dec. 1980.

109. Myles, D.I. "An analysis of impeller and volute losses in centrifugal flows". Proc. Inst. Mech. Eng. Vol. 184, Pt. 1, No. 14, pp. 253-267, 1969/1970.

110. Myles, D.I. "Pump losses", Van Karman Inst. for Fluid Dynamics, Lecture Series 29, Dec. 1970.

111. Nixon, R.A. and Cairney, W.D. "Scale effects in centrifugal cooling water pumps for thermal power stations", NEL Report No. 505, April 1972.

112. Noorbaclsh, A. "A theoretical and real slip factor in centrifugal pumps", Van Karman Institute for Fluid Dynamics, Lecture Series 61, Dec. 1973.

113. Noskievic, J. "An application of the new calculus for NPSH of centrifugal pumps". Proc. 4th Conf. on Fluid Mech. 11-16 Sept., 1972, pp. 837-850, Budapest

114. Noskievic, J. "The suction ability of centrifugal pumps", Int. Conf. on pumps and turbines, NEL, East Kilbride, Scotland, 1976.

115. Okamura, T. and Miyashiro, H. "Cavitation in centrifugal pumps operating at low capacities", Polyphase flow in Turbomachinery, Edit. C. Brennen et al., 1978.

116. Oldenziel, D.M. "A new instrument in cavitation research: The cavitation susceptibility meter", Trans. ASME, J. Fluid Eng'g, Vol. 104, June 1982, pp. 136-142.

117. Osterwalder, J. and Etting, C. "Determination of individual losses and scale effect by model tests with a radial pump". I. Mech. E. Conf. publications 1977-7, Pub. Inst. Mech. Engrs. London, 1977.

118. Osterwalder, J. "Scale effects on performance and efficiency of hydraulic machines". Van Karman Institute for fluid Dyn. Recent progress in pump research, Lecture series, Dec. 1973.

119. Pantell, K. "The behaviour of centrifugal pumps operating with heavy oils", Erdöl und Kohle 6 Jahrg. No. 11, pp. 715-720, Nov. 1953.

120. Pearsall, I.S. "Design of pump impellers for optimum cavitation performance", Proc. Inst. Mech. Engrs. 187, pp. 55-73, 1973.

121. Pearsall, I.S. "Off-design performance of pumps - cavitation". Van Karman Institute for Fluid Mechanics, Lecture Series 1978-3(1), March 1978.

122. Peck, J.F. "Investigations concerning flow conditions in a centrifugal pump and the effect of blade loading on head slip". Proc. Inst. Mech. Engrs. V.164(1), pp. 1-15, 1951.

123. Peck, J.F. "Design of centrifugal pumps with computer aid". Proc. Inst. Mech. Engrs. Vol. 183, Pt. 1, No. 17, 1968/1969.

124. Petermann, H. "Einführung in die Strömungsmachinen". Springer Verlag, Berlin, 1974 (In German).

125. Peters, J. and Van Slyke, D. "Quantitative Clinical Chemistry - Vol. 2", Methods, Baltimore: William and Wilkins, 1932, pp. 106-229.

126. Pfleiderer, C. and Petermann, H. "Strämungsmachinen". Springer Verlag, 4th Ed., Berlin 1972 (In German).

127. Pfleiderer, C. "Die Kreisel pumpe". Springer Verlag, Berlin 1955 (In German).

128. Plesset, M.S. "Bubble dynamics and cavitation". Ann. Rev. Fluid Mech. 1977. 9: pp. 145-185.

129. Plutecki, J. and Skowronski, M. "Viscosity of the liquid and one-stage centrifugal pump parameters". Conf. on fluid mech. 6th Proc. Budapest, 1979, V2. pp. 868-877.

130. Prager, R. "Influence of the gas content of the delivered fluid on the suction performance of centrifugal pumps", 4th Conf. on fluid mech., Budapest 1972.

131. Raabe, J. "Cavitation effect in turbomachinery - European Experience". Cavitation State of Knowledge, ASME, June 16-18, 1969.

132. Raabe, J. and Dernedde, R. "Experimental techniques". Van Karmen Institute for fluid dynamics, Lecture Series 29, Dec. 1970.

133. Rayleight (Lord), "On the pressure developed in a liquid during the collapse of a spherical cavity", Philos. Mag. Vol. 34, pp. 94-98, 1917.

134. Reid, R.C., Prausnitz, J.M. and Sherwood, T.K. "The properties of gases and liquids". McGraw-Hill Book Co., 3rd Ed. USA, 1977.

135. Ripken, J.F. and Killen, J.M. "Gas bubbles: their occurrence, measurements and influence in cavitation testing". Proc. IAHR Symposium, Sendai, Japan, pp. 37-57, 1962.

136. Rohsenow, W.M. and Clark, J.A. "A study of the mechanism of boiling heat transfer". Trans. ASME, Vol. 73, 1951, p. 609.

137. Rohsenow, W.M. "Boiling". Ann. Rev. Fluid Mech. 1971, 3, pp. 211-236.

138. Rowe, L.C. "Automotive engine coolants, a review of their requirements and method of evaluation". ASTM special techn. pub. 705, Ed. W.H. Ailor, 1980.

139. Rowlinson, J.S. "Liquids and liquid mixtures". Butterworth & Co. (Pub) Ltd. 2nd edition, 1969.

140. Ruggeri, R.S. and Moore, R.D. "Incipient cavitation of ethylene glycol in tunnel venturi". NASA TND 2722, March 1965.

141. Ruggeri, R.S. "Experimental studies on thermodynamic effects of developed cavitation". Symposium at the Pennsylvania State University Aug. 31 - Sept. 3, NASA Publication SP-304, 1970, p.377.

142. Ruggeri, R.S. and Gelder, T.F. "Effects of air content and water purity on liquid tension at incipient cavitation in venturi flow". NASA TND - 1459, Washington, March 1973.

143. Rütchi, K. "Die Arbeitsweise von Freistrompumpen", Schweiz Bauzeitung 86 Jahrg. Heft 32, 8 Aug. 1968, (In German).

144. Sabeisky, R.H. and Acosta, A.J. "Fluid flow", Chapter 9, Pub. Collier MacMillan, New York, 1st ed., 1964.

145. Salemann, V. "Cavitation and NPSH requirement of various liquids". Trans ASME, J. Basic Eng. Vol. 81, No. 2, pp. 167-180.

146. Santrach, D. and Leilmezs, J. "The latent heat of vapourization prediction for binary mixtures". Ind. & Eng. Chem. Fund. Vol. 17, No. 2, May 1978.

147. Schiele, O. "Some views on the different cavitation criteria of a pump". Conf. on Cavitation, Edinburgh, 3-5 Sept. 1974, Pub. Inst. Mech. Engrs. 1976.

148. Schläpfer, P. and Audykowski, T. "Untersuchungen über die maximale sauer stoffaugnahme vermögen organisher Flussigkeiten und die jodemetrische Bestimmung der audgenommenen Sauerstuffe", Schweiz, Arch. Angew, Wiss. Tech. V.15, pp. 299-307, 1949 (In German).

149. Schulmeister, R. "Über die Wertstoffzertörung durch Kavitation und Korrosion in Athyleneglycol-Wasser gemishen", Werkstoffe und Korrosion, Jahrg. 1966, Heft 3 (In German).

150. Scriven, L.E. "On the dynamics of phase growth". Chem. Eng. Science, Vol. 10, Nos. 1/2, pp. 1-13, 1959.

151. Sen, M. "Pre-rotation in centrifugal pumps". Van Karman Inst. for Fluid Dynamics, Lecture Series 1978-3(1), March 1978.

152. Shock, R.A.W. "Boiling in Multi-component fluids". Multiphase Science and Technology, 1978.

153. Skinner, L. A. and Bankoff, S.G. "Dynamic of vapour bubbles in binary liquids with spherically symmetric initial conditions". The Phys. of Fluids, Vol. 7, No. 5, May 1964.

154. Spraker, W.A. "The effect of fluid properties on cavitation in centrifugal pumps". Trans. ASME, J. Eng. Power, Vol. 87, No. 3, pp. 309-318, July 1965.

155. Stahl, W.A. and Stepanoff, A.J. et al. "Thermodynamic aspects of cavitation in centrifugal pumps". Trans. ASME, Vol. 78(8), pp. 1691-1693, 1959.

156. Stepanoff, A.J. "Centrifugal and axial flow pumps". John Wiley & Sons Inc. 2nd ed. New York, 1957.

157. Stepanoff, A.J. "Dissimilarity laws in centrifugal pumps and blowers", Trans. ASME, J. Eng. Power, Paper No. 60-WA-145, 1960.

158. Stepanoff, A.J. "Cavitation in centrifugal pumps with liquids other than water". Trans. ASME, J. Eng. Power, Vol. 83, pp. 79-90, 1961.

159. Stepanoff, A.J. "Cavitation properties of liquids". Trans. ASME, J. Eng. Power, Vol. 86, No. 2 pp. 195-200, April 1964.

160. Stephan, K. "Natural convection boiling in multi-component liquids", Heat Exchangers, Thermal Hydraulic Fund. and Design. Pub. Hemisphere-McGraw Hill, 1981.

161. Stodola, A. "Steam and gas turbines". McGraw Hill Book Co., New York, 1927.

162. Surek, D. "Parameters for the performance analysis and scale up of turbomachines". Trans. from German by S.L. Merry, ed. M.T. Thew, University of Southampton, April, 1977.

163. Takamatsu, Y. "Improvement of suction performance of centrifugal pump impeller". Bull. JSME, Vol. 23, No. 177, March 1980.

164. Tarshish, M.S. and Demchinskii, B.F. "Combined errors in the results of tests on dynamic pumps". Russian Eng. J., Vol. 58, No. 3, pp. 5-10, 1978.

165. Taylor, S.R.G. "Recent research and development in truck engine cooling". Proc. I. Mech. Engrs. 1969/1970, V. 184(3a), p. 117.

166. Thew, M.T. "Comments on further development in the correlation of specific speed versus specific diameter". University of Southampton, Report ME/76/24, Pt. 2, 1976.

167. Thew, M.T. and Hadji-Sheikh, M. "Cavitation behaviour of water-glycol mixture in small centrifugal pumps", NEL Fluid Mech. Silver Jubilee Conf., Nov. 1979.

168. Thoma, D. "Bericht zue Weltkraft Konferenz, London 1924", Z. Ver. Deut. 129, Vol. 79, p. 329, 1935.

169. Tolubinskii, V.I. "Experimental investigation of the influence of pressure on the rate of heat transfer during boiling of water-Ethylene glycol mixture", Teplofiziha, Teplotechnika No. 22, pp. 19-21, Translated by L. Rosenfeld, Southampton University, 1978.

170. Trimble, H.M. and Potts, W. "Glycol water mixture, vapour pressure, boiling point-composition relation", Ind. Eng. Chem. Vol. 27, No. 1, pp. 66-68, Jan. 1935.

171. Uhlig, H.H. "The solubilities of gases and surface tension". The J. Phys. Chem. Vol. 41, No. 9, pp. 1215-1225, 1937.

172. Van Stralen, S.J.D. "The mechanism of nucleate boiling in pure liquids and in binary mixtures". Int. J. Heat and Mass Transfer, Vol. 9, Pt. 1, pp. 995-1020, Pt. 2, pp. 1021-1046, 1966.

173. Van Stralen, S.J.D. and Cole, R. "Boiling phenomena", McGraw Hill Book Co., New York, 1979.

174. Varley, F.A. "Effects of impeller design and surface roughness on the performance of centrifugal pumps". Proc. Inst. Mech. Engrs. Vol. 175(21), pp. 955-989, 1961.

175. Van Wijk, W.R. et al. "Heat transfer to boiling binary liquid mixtures", Chem. Eng'g Science, Vol. 5, pp. 68-80, 1956.

176. Van Wijngaarden, L. "On the growth of small cavitation bubbles by convective diffusion". Int. J. Heat Transfer, Vol. 10, pp. 127-134, 1967.

177. Wadia, A.R. and Booth, T.C. "Rotor tip leakage, Part II - design optimization through viscous analysis and experiment", J. Eng. for Power, Trans. ASME, Vol. 104, Jan. 1982.

178. Ward, A. "The performance of pumps and fans at peak efficiency". I. Mech. E. Conf. publication 1977-7, pp. 19-25, London 1973.

179. Ward, T. and Sutton, M. "A review of the literature on cavitation in centrifugal pumps with various liquids", BHRA report TN 892, Cranfield, April, 1967.

180. Weyer, H.B. "Measurements methods in rotating components of turbo-machinery". Joint Fluid Eng. Gas Turbine Conf. and Products Show - New Orleans, Louis. March 10-13, 1980, ASME Publ.

181. Wiesner, F.J. "A review of slip factors for centrifugal impellers", Trans ASME, J. Eng. Power, pp. 558-572, Oct. 1967.

182. Winkler, L. W. "Die Lösligkeit des Sauerstoffes in Wasser", Ber. Chem. Ges. 1889, 22, pp. 1764-1774 (In German).

183. Wislicenus, G.F. "Fluid mechanics of turbo machinery - Vol ", Dover Pub. 2nd Ed. 1965.

184. Wood, G.M. et al. "Tip clearance effects in centrifugal pumps". Trans ASME Vol. 97(D), pp. 932-940, 1965.

185. Worster, R.C. "The flow in volutes and its effect on centrifugal pump performance", Proc. Inst. Mech. Engrs, Vol. 177, No. 31, pp. 843-865, 1963.

186. Yedidiah, Sh. "Centrifugal pumps - theories and facts". Proc. Inst. Mech. Engrs. Vol. 179, Pt. 1, No. 20, pp. 615-626, 1964/1965.

187. Yedidiah, Sh. "Effect of inlet vane design on cavitation in a centrifugal pump". Fluid Eng. Conf. 10-12 May, 1971, Pittsburgh.

188. Yedidiah, Sh. "Some observations relating to suction performance of inducers and pumps", J. Basic Eng., Trans. ASME, pp. 567-574, Sept. 1972.

189. Zika, V.J. "A correlation of cavitating centrifugal pumps". Paper presented at ASME Summer meeting, Colorado, June, 1981.

Additional References

190. Eckardt, D. "Detailed flow investigations with a high speed centrifugal compressor", Trans. ASME, J. Basic Eng. Sept. 1976, pp 390-402.

191. Reddy, V.R. and Kar, S. "Optimum vane number and angle of centrifugal pumps with logarithmic vanes". Trans ASME J. Basic Eng. Setp. 1971, p 441.

192. Thew, M. Private communication, 1983.